

Diss. ETH No. 28909

# EIS applied to Li-Ion Batteries: Modelling Cell Aging for Comprehensive SoH Estimation

A thesis submitted to attain the degree of

Doctor of Sciences of ETH Zurich

(Dr. sc. ETH Zurich)

presented by

**Pietro Iurilli**

Laurea Magistrale in Energy Engineering, Politecnico di Milano

born July 6, 1993 citizen of Italy

accepted on the recommendation of

Prof. Dr. Vanessa Wood, examiner

Prof. Dr. Francesco Ciucci, co-examiner

Prof. Dr. Mario Paolone, co-examiner

Dr. Claudio Brivio, co-examiner

2022





Eidgenössische Technische Hochschule Zürich  
Swiss Federal Institute of Technology Zurich



Department of Information Technology and Electrical Engineering  
Institute for Electronics  
Materials and Device Engineering Group  
ETH Zürich  
Gloriastrasse 35  
8092 Zürich  
Switzerland



Sustainable Energy Center  
CSEM SA  
Jaquet-Droz 1  
2002 Neuchâtel  
Switzerland



“Eureka!”

– Archimede



# Abstract

Lithium-ion batteries represent an essential technology for accelerating the transition to sustainable energy systems and mobility. With the ramping-up of Li-ion batteries applications, it is crucial to accurately assess their states under operation to maximize performances while ensuring reliability and safety.

The *general objective* of this doctoral thesis is to expand the knowledge about Electrochemical Impedance Spectroscopy (EIS) when used to investigate and understand Li-ion battery aging. EIS is a powerful non-invasive technique that allows to identify and track the evolutions of cell processes within a short testing time, being a valid candidate to improve sensing capabilities of the new generation of Battery Management Systems (BMSs). In this perspective, this work has the following *specific objectives*: (i) developing a modelling framework able to reproduce the battery behaviour by encompassing the physical/dynamic processes and degradation mechanisms, and (ii) applying the modelling framework to improve State of Health (SoH) estimation for future implementation in cell-based management systems.

A literature review dedicated to EIS for Li-ion cells aging determination is presented to the readers in Chapter 2, by focusing on battery applications, degradation mechanisms and cell modelling. EIS spectra show clear shifts in different frequency regions depending on the applications (e.g. Depth of Discharge, current rate, etc.). These shifts are attributed to different degradation mechanisms, in particular electrolyte decomposition at high frequency and anode- and cathode-related degradations at mid- and lower frequencies. Different options are used to configure Electric Circuit Models (ECMs) and track the evolution of cell aging. The outcome of Chapter 2 are the links between EIS spectra variations and the underlying degradation mechanisms, and between the same mechanisms and the most accurate ECMs solution to model them. These results are used in Chapter 3 to develop an EIS-based battery model designed to simulate cell dynamics, to estimate State of Charge (SoC) and to account for battery aging.

---

Distribution of Relaxation Times (DRT) is used to deconvolute the impedance spectra and to highlight modelling information that otherwise would have been overlapped in the frequency domain. Chapter 3 shows how to use the peak-based function of DRT to directly configure the ECM and to associate circuital element to the battery physical processes. The modelling framework is applied to large format commercial pouch cells (NMC cathode) validating the obtained ECM over the whole SoC range and wide temperature range (-10°C to 35°C). The several application profiles tested demonstrate the high accuracy of the model in reproducing the cell behaviour. For instance, the RMSE on the battery voltage is lower than 1.50% for driving cycle simulations (based on IEC 62660-1 standard) at variable temperature and SoC.

Chapter 4 lingers on the systematically ageing assessment of Li-ion cells via EIS. The DRT peaks are unambiguously attributed to the degradation mechanisms arising during cell aging. The attribution is validated with invasive characterization techniques. Half-cells are made to discriminate the processes occurring at anode and/or cathode sides. Imaging techniques are used to characterize electrode's surface morphology: digital imaging validates graphite anode degradation (mainly related to lithium plating) and Scanning Electron Microscopy validates the degradation at NMC cathode (mainly related to particle cracking).

The DRT peaks attribution results of Chapter 4 are combined with the modelling framework developed in Chapter 3 to track Li-ion cells aging and estimate SoH. Chapter 5 introduces specific indicators to quantify the degradation mechanisms, which are grouped in the so-called Degradation Modes (DMs). Their correlations are used to derive SoH both for linear and non-linear aging behaviours (also known as "pre-knee" and "after-knee" behaviours). The results show that Loss of Lithium Inventory (LLI) is the main driving factor for the NMC cell under investigation, followed by Loss of Cathode Active Material (LAM<sub>C</sub>). SoH estimation is achievable with a Mean Absolute Error lower than 0.75% for SoH > 85% and lower than 3.70% for SoH < 85% (End of Life).

Chapter 6 summarizes the findings of the different activities and gives an outlook about future research directions to improve the modelling framework both in terms of applicability and replicability.

# Zusammenfassung

Lithium-Ionen-Batterien sind eine wesentliche Technologie zur Beschleunigung des Übergangs zu nachhaltigen Energiesystemen und nachhaltiger Mobilität. Mit dem zunehmenden Einsatz von Lithium-Ionen-Batterien ist es von entscheidender Bedeutung, ihren Betriebszustand genau zu bewerten, um ihre Arbeitsweise zu optimieren, während Zuverlässigkeit und Sicherheit gewährleistet sind.

Das *allgemeine Ziel* dieser Doktorarbeit ist es, das Wissen über den Einsatz der elektrochemischen Impedanzspektroskopie (EIS) für die Untersuchung und das Verständnis der Alterung von Li-ionen-Batterien zu erweitern. EIS ist eine leistungsstarke, nicht-invasive Messtechnik, die es ermöglicht, die Entwicklung von Zellprozessen innerhalb einer kurzen Testzeit zu identifizieren und zu verfolgen. Sie ist ein möglicher Kandidat für die Integration in zukünftige Generation von Batteriemanagementsystemen (BMS). Vor diesem Hintergrund verfolgt diese Arbeit die folgenden *spezifischen Ziele*: (i) Entwicklung eines Modellierungsansatzes, der in der Lage ist, das Verhalten von Batterien durch Einbeziehung der dynamischen physikalischen Prozesse und der Degradationsmechanismen zu reproduzieren, und (ii) Anwendung des Modellierungsansatzes zur Verbesserung der Abschätzung des Alterungszustands (State of Health, SoH) für die künftige Implementierung in zellbasierten Managementsystemen.

In Kapitel 2 wird den Leserinnen und Lesern eine Literaturübersicht über EIS zur Bestimmung der Alterung von Lithium-Ionen-Zellen präsentiert, wobei der Schwerpunkt auf Batterieanwendungen, Degradationsmechanismen und Zellmodellierung liegt. EIS-Spektren zeigen deutliche Verschiebungen in verschiedenen Frequenzbereichen in Abhängigkeit von den Anwendungsparametern (z. B. Entladetiefe, Stromstärke, usw.). Diese Verschiebungen werden auf unterschiedliche Degradationsmechanismen zurückgeführt, wobei insbesondere die Elektrolytzersetzung bei hohen Frequenzen und anoden- und kathodenbedingte Degradationen bei mittleren und niedrigen Frequenzen zu erkennen sind. Es werden verschiedene Optionen verwendet, um elektrische Schaltkreismodelle (ECMs) zu konfigurieren und die Entwicklung der Zellarterung zu

---

verfolgen. Das Ergebnis von Kapitel 2 sind die Zusammenhänge zwischen EIS-Spektren und den zugrundeliegenden Degradationsmechanismen sowie zwischen diesen Mechanismen und der Genauigkeit der ECM-basierten Modellierung. Diese Ergebnisse werden in Kapitel 3 verwendet, um ein EIS-basiertes Batteriemodell zu entwickeln, mit dem die Zelldynamik simuliert, der Ladezustand (State of Charge, SoC) geschätzt und die Batteriealterung berücksichtigt werden kann.

Die Verteilung der Relaxationszeiten (Distribution of Relaxation Times, DRT) wird verwendet, um die Impedanzspektren zu dekonvolutieren und Modellierungsinformationen hervorzuheben, die ansonsten im Frequenzbereich überlagert worden wären. Kapitel 3 zeigt, wie die Peak-basierte Funktion der DRT-Kurve genutzt werden kann, um das ECM direkt zu konfigurieren und Schaltkreiselemente mit den physikalischen Prozessen der Batterie zu verknüpfen. Das Modellierungssystem wird auf großformatige kommerzielle Pouch-Zellen angewandt, um das erhaltene ECM über den gesamten SoC-Bereich und einen breiten Temperaturbereich (-10°C bis 35°C) zu validieren. Die verschiedenen getesteten Anwendungsprofile zeigen die hohe Genauigkeit des Modells bei der Reproduktion des Zellverhaltens. So liegt der RMSE der Batteriespannung bei Fahrzyklus-Simulationen mit variabler Temperatur und SoC unter 1,50 %.

Kapitel 4 widmet sich der systematischen Alterungsanalyse von Li-Ionen-Zellen mittels EIS. Die DRT-Peaks werden eindeutig den Degradationsmechanismen zugeordnet, die während der Zellalterung auftreten. Die Zuordnung wird mit invasiven Charakterisierungstechniken validiert. Halbzellen werden hergestellt, um die an der Anoden- und/oder Kathodenseite ablaufenden Prozesse zu unterscheiden. Bildgebende Verfahren werden eingesetzt, um die Oberflächenmorphologie der Elektroden zu charakterisieren: Hochauflöste digitale Bilder validieren die Graphitdegradation (hauptsächlich im Zusammenhang mit der Lithiumbeschichtung) und die Rasterelektronenmikroskopie validiert die Degradation an der NMC-Kathode (hauptsächlich zurückzuführen auf Partikelrissbildung).

Die Ergebnisse der Zuordnung von DRT Peaks aus Kapitel 4 werden mit dem in Kapitel 3 entwickelten Modellierungssystem kombiniert, um die Alterung von Li-Ionen-Zellen zu überwachen und den SoH zu schätzen. In Kapitel 5 werden spezifische Indikatoren zur

---

Quantifizierung der Degradationsmechanismen eingeführt, die in den so genannten Degradationsmodi (DM) zusammengefasst werden. Ihre Korrelationen werden verwendet, um den SoH sowohl für lineares als auch für nichtlineares Alterungsverhalten abzuleiten. Die Ergebnisse zeigen, dass der Verlust des Lithiuminventars (Loss of Lithium Inventory, LLI) der wichtigste treibende Faktor für die untersuchte NMC-Zelle ist, gefolgt vom Verlust des kathodenaktiven Materials (Loss of Cathode Active Material, LAM<sub>C</sub>). Die SoH-Schätzung ist mit einem mittleren absoluten Fehler von weniger als 0,75 % für den SoH Bereich über 85 % und weniger als 3,70 % für den SoH Bereich unter 85 % (End of Life) möglich.

Kapitel 6 fasst die Ergebnisse der verschiedenen Aktivitäten zusammen und gibt einen Ausblick auf zukünftige Forschungsrichtungen zur Verbesserung des Modellierungssystems im Hinblick auf Anwendbarkeit und Replizierbarkeit.



# Résumé

Les batteries lithium-ion sont une clé de voute technologique d'une transition énergétique vers un modèle renouvelable, tant pour les infrastructures que pour les transports. Au vu de l'augmentation rapide de la diversité d'utilisation et du nombre de batteries utilisées, il est crucial d'offrir une capacité opérationnelle complète quant à la supervision des états internes des batteries pour garantir fiabilité et sécurité à l'utilisateur.

Le *but général* de cette étude doctorale est d'étendre le champ des connaissances relatif à l'utilisation de la spectroscopie électro-chimique (Electrochemical Impedance Spectroscopy, EIS) pour le suivi et l'analyse non-invasive de l'évolution des processus internes se produisant au cours du vieillissement de la batterie. L'unique besoin de l'EIS étant de mettre la batterie au repos pour court laps de temps fait de cette technique un outil de choix pour augmenter la finesse de mesure de la prochaine génération de superviseurs de batteries (Battery Management System, BMS). Dans cette optique, la recherche présentée répond aux *deux objectifs* suivants : (i) la conception d'un outil de modélisation dynamique capable de reproduire le comportement électrique de la batterie. Pour ce faire, le modèle se repose sur les caractéristiques physiques et cinétiques des processus chimiques liés aux dégradations internes de la batterie. (ii) L'utilisation de l'outil de modélisation définit précédemment pour améliorer les algorithmes d'estimation d'état de vieillesse (State of Health, SoH) destinés à être embarqués dans les BMS futurs.

Une étude détaillée de l'état de l'art concernant l'utilisation de l'EIS pour l'étude du vieillissement des batteries est proposée au chapitre 2 de cette thèse, avec un focus particulier sur la modélisation des mécaniques de dégradation et la modélisation de batterie. Il est montré que le spectre de l'EIS présente un décalage fréquentiel local spécifique pour différentes situations (par exemple un abus par sur-décharge et un par sur courant présenteront des déformations du spectre à des fréquences différentes). Ces décalages peuvent être attribués à des mécanismes de dégradation différents. Ainsi, les décompositions de l'électrolyte se reflète dans les hautes fréquences, alors que les phénomènes liés aux dégradations des électrodes présentent une signature se situant des fréquences moyennes et basses du spectre. Il existe des options différentes permettant

---

de configurer des modèles électriques (Electric Circuit Models, ECMs) puis de les utiliser pour surveiller l'évolution du vieillissement des batteries. En conclusion le deuxième chapitre propose un lien entre les variations du spectre obtenu par EIS et les processus de dégradation se produisant dans la cellule d'une part, et entre les mêmes processus et les modèles à base d'ECM les plus précis pour modéliser lesdits processus. Le chapitre 3 présente l'utilisation des modèles se reposant sur l'EIS capables de simuler les caractéristiques dynamiques des batteries, permettant ainsi l'estimation de l'état de charge (SOC) tout en prenant en compte le vieillissement de la batterie.

La distribution de temps de relaxation (DRT) est utilisée pour déconvoluer le spectre de l'EIS et pour mettre en lumière les informations utiles à la modélisation qui seraient autrement restées superposées dans le domaine fréquentiel. Le chapitre 3 démontre la configuration directe d'un ECM depuis l'analyse des pics obtenus par application de la DRT, ainsi que l'attribution des paramètres de l'ECM à des processus physiques se produisant dans la batterie. Cet outil de modélisation est validé avec des batteries « pouch » sur l'intégralité de la plage SOC, et sur une plage de température étendue (-10°C to 35°C). Les résultats démontrent une haute précision du modèle quant à sa capacité à reproduire le comportement dynamique de la batterie ; par exemple la RMSE sur la tension est de moins de 1.50% durant les cycles simulant une conduite de véhicule (norme IEC 62660-1) à température variable.

Le chapitre 4 entérine les hypothèses proposées sur le suivi de vieillissement par EIS. Les pics du profil de la DRT sont attribués sans ambiguïté possible à des processus de dégradation spécifiques. Cette attribution est validée par l'utilisation de mesure invasives et destructives sur des demi-cellules fabriquées pour permettre l'isolation des processus se produisant à l'anode de ceux se produisant à la cathode. Des outils d'imagerie sont également utilisés pour caractériser l'état de surface des électrodes ; de l'imagerie numérique est utilisée pour confirmer les dégradations de l'anode (principalement lié au placage de lithium), and la microscopie électronique à balayage est utilisée pour confirmer les dégradations sur les cathodes NMC (principalement dues au craquelage des électrodes).

Les résultats de l'attribution des pics de la DRT effectuée au chapitre 4 sont combinés avec l'outil de modélisation développé au chapitre 3 servant au suivi du vieillissement et à

---

l'estimation du SoH. Le chapitre 5 introduit des indicateurs permettant de spécifier le mécanisme de dégradation en cours. Ces indicateurs sont regroupés en modes de dégradation (DMs). Ces indicateurs et leurs corrélations sont utilisés pour déterminer les SoH dans les cas de vieillissement linéaires et non linéaires. Les résultats obtenus montrent que la principale cause de dégradation des performances des batteries NMC étudiées est la perte de lithium (Loss of Lithium Inventory, LLI), suivie par la perte de matériau actif à la cathode (Loss of Cathode Active Material, LAMc). L'estimation du SoH est obtenue avec une RMSE inférieure à 0.75% pour des SoH de moins de 85% et inférieure à 3.70% pour des SoH de plus de 85% (fin de vie).

Le chapitre 6 résume les résultats des différentes activités de recherche et propose une vue générale de la direction à prendre pour les activités futures, dans une optique d'amélioration de l'outil de modélisation tant en termes de reproductibilité que d'utilisabilité.



# Sommario

Le batterie agli ioni di litio (in seguito “batterie al litio”, “celle al litio”, o semplicemente “celle”) rappresentano una tecnologia essenziale per accelerare la transizione verso sistemi energetici e mobilità sostenibili. Con l'aumento delle applicazioni delle batterie al litio, è fondamentale valutare accuratamente il loro stato di funzionamento per massimizzare le prestazioni e garantire affidabilità e sicurezza.

*L'obiettivo generale* di questa tesi di dottorato è quello di ampliare le conoscenze sulla spettroscopia di impedenza (in seguito EIS, Electrochemical Impedance Spectroscopy) quando utilizzata per studiare e comprendere l'invecchiamento delle batterie al litio. L'EIS è una misura elettrica non invasiva e di breve durata che permette di identificare e monitorare l'evoluzione dei processi elettrochimici che avvengono all'interno di qualsivoglia cella, ponendosi quindi come una valida candidata per migliorare l'intelligenza dei sistemi a batteria e specialmente i loro sistemi di controllo (Battery Management Systems, BMS). In quest'ottica, la presente tesi di dottorato si pone i seguenti *obiettivi specifici*: (i) sviluppare un framework di modellazione in grado di riprodurre il comportamento della cella includendo i processi fisici/dinamici e i meccanismi di degradazione e (ii) applicare tale framework di modellazione per migliorare la stima dello stato di vita (in seguito SoH, State of Health) e per favorire la sua implementazione nei sistemi a batteria.

Una review della letteratura sull'utilizzo della EIS per determinare l'invecchiamento delle celle al litio è presentata nel Capitolo 2, con focus speciale sui diversi tipi di applicazioni delle batterie, sui meccanismi di degrado e sulla modellazione delle celle. Gli spettri di impedenza mostrano chiare variazioni in diverse regioni di frequenza a seconda delle applicazioni (ad es. profondità di scarica, corrente di carica/scarica, ecc.). Queste variazioni sono attribuibili a diversi meccanismi di degradazione, in particolare alla decomposizione dell'elettrolita alle alte frequenze e alla degradazione dell'anodo e del catodo a frequenze medio-basse. Diverse opzioni sono proposte per configurare correttamente dei modelli di circuito elettrico equivalente (nel seguito ECM, Equivalent

---

Circuit Model) capaci di monitorare l'evoluzione dell'invecchiamento. Il risultato del Capitolo 2 è la creazione di un collegamento tra le variazioni negli spettri di EIS e i sottostanti meccanismi di degrado, e, successivamente, tra gli stessi meccanismi di degrado e la più accurata configurazione ECM per modellarli. Questi risultati sono utilizzati nel Capitolo 3 per sviluppare un modello di cella basato sull'EIS, progettato per simulare la dinamica delle celle, stimare lo Stato di Carica (SoC), tenendo in conto dell'invecchiamento.

Il metodo denominato “Distribution of Relaxation Times” (DRT) permette la deconvoluzione degli spettri di impedenza evidenziando informazioni che altrimenti sarebbero sovrapposte nel dominio di frequenza. Il capitolo 3 mostra come utilizzare i classici picchi risultanti della funzione DRT per configurare l'ECM e associare i processi fisici della batteria agli elementi circuitali. Il framework di modellazione risultante è stato applicato a celle al litio commerciali di grande formato (catodo NMC), validando il modello ottenuto sull'intero intervallo di SoC e su un ampio intervallo di temperatura (da -10°C a 35°C). I diversi profili applicativi testati dimostrano l'elevata precisione del modello nel riprodurre il comportamento della cella. Ad esempio, l'RMSE sulla tensione della batteria è inferiore all'1,50% per simulazioni con profilo automotive (IEC 62660-1) a temperatura e SoC variabili.

Il capitolo 4 si concentra sulla modellazione sistematica dell'invecchiamento delle celle al litio tramite EIS. I picchi della funzione DRT sono attribuiti in modo inequivocabile ai meccanismi di degrado e tale attribuzione viene validata con tecniche di caratterizzazione invasive. Le cosiddette “half-cells” sono state realizzate e sfruttate per discriminare i processi che si verificano all'anodo e al catodo. Diverse tecniche di imaging sono state poi utilizzate per caratterizzare la morfologia superficiale dell'elettrodo: la semplice fotografia digitale per validare il degrado dell'anodo di grafite (principalmente legato al fenomeno di “lithium plating”) e la microscopia elettronica a scansione per validare il degrado del catodo NMC (principalmente legato al fenomeno di “particle cracking”).

I risultati del Capitolo 4 sono combinati con il framework di modellazione sviluppata nel Capitolo 3 per monitorare l'invecchiamento delle celle agli ioni di litio e stimare il SoH. Il Capitolo 5 introduce specifici indicatori per quantificare i meccanismi di degradazione, raggruppati nei cosiddetti “Degradation Modes” (DM). Le loro correlazioni sono utilizzate

---

per ricavare il SoH, sia per comportamenti di invecchiamento lineari (all'inizio del ciclaggio, conosciuti come "pre-knee") che non lineari (dopo un numero rilevante di cicli e/o in condizioni di ciclaggio severe, conosciuti come "after-knee"). I risultati mostrano che la perdita di ioni di litio (Loss of Lithium Inventory, LLI) è il principale fattore determinante la degradazione nelle celle in esame, seguito dalla perdita di materiale attivo del catodo (Loss of Cathode Active Material, LAM<sub>C</sub>). Grazie alla tecnica di modellazione proposta, la stima del SoH è ottenibile con un errore assoluto medio inferiore allo 0,75% per SoH > 85% e inferiore al 3,70% per SoH < 85% (fine vita della cella).



# Preface

This doctoral thesis is the result of collaboration between CSEM, a Research and Technology Organization in Neuchâtel and the Swiss Federal Institute of Technology (ETH) in Zürich, Switzerland.

I would like to thank my supervisor at ETH, Prof. Vanessa Wood. She welcomed me into the Materials and Device Engineering Group (MaDE) and she gave me support, constructive inputs and feedback over the years. I am grateful to Dr. Claudio Brivio, my supervisor at CSEM. He ignited the passion for battery research and he always believed in my capabilities. He gave me constant support and he thought me so much, even before the start of this journey, when I arrived at CSEM as an intern. I would also like to thank Prof. Francesco Ciucci and Prof. Mario Paolone for agreeing to be part of the doctoral committee.

It was a unique opportunity to carry out my work in an interdisciplinary environment, not only being involved in two groups with different competences, but also being part of industrial and EU projects that gave me the opportunity to meet new people, exchange ideas and opinions. I grew both scientifically and personally.

I would like to thank my colleagues at the Institute of Electronics. Even though I spent most of the time in Neuchâtel, I have always been involved in meetings, seminars and even group outings. I am thankful to all the members of the battery group, discussing science and posing challenging questions. A special thank goes to Peter and Ramesh who introduced me to the chemical laboratories in BRNC and supported my activities at the beginning of my journey.

A big thank goes to my colleagues at CSEM and in particular to the battery team (Claudio, Nelson, Guillaume, Enrico, Shubham and, formerly, Emil), Rafael and Leonardo. We shared the offices, the laboratories and so many occasions to discuss about science and anything else. I am thankful to my group leader, Andreas Hutter, who welcomed me at CSEM and gave the possibility to start the doctoral research. A special thank goes to Leonardo, who shared its competences and supported me for post-mortem analyses giving the access to

---

the battery material laboratory. Finally, I also acknowledge my students, Luigi and Chiara: it was a great joy to work with such motivated students on different topics that were not directly related to this work.

Finally, my deepest gratitude goes to my family, my girlfriend Elena and my friends for the continuous moral support, dedication and example. The weekends back home in Italy, an aperitif every so often, hiking trips or travelling around the world: all these moments helped keeping high my motivation and bringing this journey to an end. Thank you all!

# Contents

Abstract .....	V
Zusammenfassung .....	VII
Résumé .....	XI
Sommario .....	XV
Preface .....	XIX
Contents .....	XXI
Chapter 1 Introduction.....	1
1.1. Background .....	1
1.2. Research drivers .....	3
1.3. Research objectives.....	5
1.4. Layout of the work .....	7
Chapter 2 Background analysis: on the use of EIS to characterize and model Li-ion cells aging .....	11
2.1. Context.....	12
2.2. Methodology and outline .....	14
2.3. How the application impacts on the EIS spectra .....	17
2.4. How EIS spectra are linked to degradation .....	29
2.5. How EIS spectra are modelled trough ECMs.....	38
2.6. Critical assessment.....	46
2.7. Final remarks .....	56
Chapter 3 EIS2MOD: DRT-based Modelling framework for Li-ion Cells.....	59
3.1. Context.....	60
3.2. Methodology .....	63

---

3.2.1. DRT calculation .....	64
3.2.2. DRT analysis: ECM configuration .....	67
3.2.3. Parameters extraction and fitting.....	70
3.3. Proposed ECM for Li-ion NMC cells.....	71
3.4. Validation results.....	78
3.4.1. Dynamic profile.....	78
3.4.2. Full discharge profile.....	78
3.4.3. Driving profile.....	81
3.5. Final remarks .....	83
Chapter 4 Detection of Li-ion cells degradation with DRT .....	85
4.1. Context.....	86
4.2. Material and methods .....	89
4.2.1. Cell testing and disassembly .....	90
4.2.2. Analysis of DRT profiles.....	93
4.2.3. Validation of DRT results.....	94
4.3. Results and discussion.....	95
4.3.1. Analysis of DRT profiles.....	96
4.3.2. Validation through imaging .....	103
4.4. Final remarks .....	110
Chapter 5 Physics-based SoH estimation.....	113
5.1. Context.....	114
5.2. Materials and Methods .....	117
5.2.1. Inputs: experimental dataset and DRT characterization .....	117
5.2.2. Methodology.....	121
5.3. Results.....	126
5.3.1. Degradation indicators .....	127

---

5.3.2. SoH estimation .....	130
5.4. Discussion.....	133
5.5. Final remarks .....	137
Chapter 6 Conclusions .....	139
Future works.....	143
Appendix A     Support material to Chapter 3 .....	145
A.1   Kramers-Kronig criterium .....	145
A.2   Inductive behaviour correction .....	147
A.3   Regularization coefficient determination .....	148
A.4   Averaged impedance spectra.....	149
Appendix B     Application of EIS2MOD to commercial cylindrical cells .....	151
B.1   Proposed ECM.....	151
B.2   Validation results at BoL .....	154
B.3   Validation results after 400 Equivalent Cycles .....	156
B.4   Remarks .....	158
Appendix C     Support material to Chapter 4 .....	159
C.1   Cell disassembling procedure.....	159
C.2   Electrode samples preparation.....	161
C.3   Coin cells assembly.....	163
C.4   Sample preparation for imaging techniques .....	164
C.4.1   Digital imaging .....	164
C.4.2   Optical microscopy and Scanning Electron Microscopy.....	165
C.5   OCV balancing of half-cells.....	167
Appendix D     Datasheets of the investigated Li-ion cells.....	169
List of Figures.....	171
List of Tables .....	175

---

Glossary (nomenclature and acronyms) .....	177
Nomenclature .....	177
Acronyms .....	178
References .....	181
Publications .....	207
Scientific Journals.....	207
Other publications not related to doctoral research.....	207
Conference Contributions.....	208

# Chapter 1

## Introduction

### 1.1. Background

This doctoral research is focused on non-invasive characterization of Li-ion battery cells. It is centred on the use of Electrochemical Impedance Spectroscopy (EIS) to identify and quantify cell aging. Non-invasive characterization is essential to develop controlling algorithms that can be deployed into commercial battery systems to improve their performances and safety.

This doctoral research builds upon the expertise of CSEM's battery system research group and the ETHZ's Material and Device Engineering group. On one side, the doctoral research benefits from the testing, modelling and system knowledge available at CSEM, which has the primary objective to develop sensors and algorithms for the optimal management of Li-ion batteries. On the other side, it also benefits from the knowledge on advanced characterization techniques, from the atomistic- to macro-scale, to determine how structures influence material and end-device performances. The combination of the two approaches, bridging systemic analyses with deeper electrochemical and material science analyses, allows to develop physics-based models and algorithms that will improve the capabilities of future Battery Management Systems (BMSs).

Therefore, this doctoral thesis gains particular importance given the spread of battery applications and the forecasted market sales in the next years. Furthermore, upcoming regulations, especially at European level, require drastic reduction of emissions. In this context, Li-ion batteries represent an essential technology to fulfil the ambitions of the European Green Deal and the European Climate Law, including the GHG emission reduction target of 55% with respect to 1990 by 2030 and a zero net GHG emission target by 2050 [1]. The two main industrial sectors were Li-ion technology will give their

## 1. Introduction

---

contribution are power systems (stationary storage) and mobility (automotive as well as passenger and goods transportation).

Renewable Energy Sources (RESs) have a fundamental role in the energy sector. After the target of 20% in 2020, the Renewable Energy Directive proposed a new binding target to at least 32% of renewables in the EU energy mix production in 2030, with possible upwards review by 2023. The large expansion of RESs in the form of scattered distributed generators represent a challenge for grid operators [2]. Their integration into existing grids affects the optimum power flow computation and brings about problems of congestion, safety and reliability, power quality, voltage and frequency control, events unpredictability and system economics [3]–[5]. In this context, the use of Battery Energy Storage Systems could be a solution to increase the flexibility of the grid, maximizing local consumption and to providing grid services [2], [6], [7]. This is confirmed by the increasing number of stationary installations worldwide, with an exponential increase in the last decade [8].

As regards the transportation sector, the main challenges will be related to vehicle emissions: the European Commission proposed the ambitious target of reducing car emissions by 55% and truck emissions by 50% within 2030 by boosting zero-emission vehicles and strengthening the railway infrastructures. In June 2022, all climate ministers of the EU member states agreed to the EU commission proposal of a reduction of 100% of emissions for new sales of cars and vans as of 2035 [9], [10]. Therefore, hybridization and electrification of vehicles become the only viable roads for the future of mobility. In this perspective, Li-ion batteries present high gravimetric and volumetric energy density overcoming space and weight limitations [11].

Energy transition and electromobility are market drivers for Li-ion cells. For instance, in 2021 these two sectors accounted for 83% of annual battery sales [12]. The total market shifted from 24 GWh in 2010, to 250 GWh in 2020 and will grow of another order of magnitude by 2030 with 2260 GWh. The exponential market annual growth rate was of 29% from 2010 to 2021 [12]–[14]. Analysing the passenger vehicles market, Plug-in Hybrid Electric Vehicles (PHEVs) and Electric Vehicle (EVs) sales represented 10.1% of the European market in 2020 and are expected to grow up to 39% in 2025 and to 59% in 2030 [13]. With those volumes and thanks to economy of scale, batteries became more

accessible with almost 80% drop of prices with respect to 2013 for cell production and almost 90% with respect to 2010 for battery pack production. A temporary rise of prices has been recorded for 2022 and is forecasted for 2023 due to the international situation causing shortage of raw materials [13].

In order to fulfil the battery market needs in both stationary and mobility sectors, the EU Commission launched several initiatives to promote in-house production and supporting the battery industry throughout the value chain. The most famous initiative is the European Battery Alliance (EBA), launched in 2017. Since the EBA launch, a European Strategic Action Plan on Batteries was defined to set the direction for the development of a competitive battery industry in Europe [15]. Two main fundings mechanisms were set and are still exploited: (i) the H2020 and Horizon Europe programme and the (ii) Important Projects of Common European Interests (IPCEIs) [16]–[18]. Thanks to these frameworks, the European Commission enables and finances research activities distributed on the whole battery value chain, from material development, cell, modules battery system development and repurposing to recycling and refining of used materials [19]–[21].

## 1.2. Research drivers

The exponential Li-ion battery market numbers presented in the previous section rise sustainability questions of the whole battery industry, from mining to recycling. Already in 2025, around 5 billion of used electrochemical cells will have to disposed. Looking at the passenger vehicle market described above, nearly 95 GWh/year of used batteries will come out from cars already in 2025, increasing to 750 GWh/y in 2030 [22]. The 10<sup>th</sup> December 2020, the EU commission proposes to modernize EU legislation on batteries to be more sustainable throughout the lifecycle in order to achieve the goals of the European Green Deal [23]. Specific guidelines have been also published in 2020 about the “*New circular economy action plan*”, stating that end of life of vehicles will be regulated promoting more circular business models linking design issues with end of life treatment [24], [25]. Overall, these problems are all related to life management of batteries. The EU commission identified the circular economy principles as the right pillars on which to build a sustainable battery industry. Circular economy can be seen as an industrial system

## 1. Introduction

---

that is restorative or regenerative by intention and design, and that requires a radical transformation of business models to avoid the impacts of the current linear system based on the “take, make and dispose” paradigm [26], [27]. Although uncertain, it is forecasted that 27% of disposed batteries could be re-used in other less energy-intensive applications (i.e. second-life applications) such as BESSs, before being recycled [28]. However, a barrier to second-life adoption of batteries is the lack of traceability and standardization in battery packs, together with insufficient, inaccessible or unstandardized information on usage history/battery status from BMSs [29]. Therefore, solutions to unleash the full potential of circular economy in the battery industry are needed on the market. Fine tracking of battery states during its first life to promote maintenance, improved traceability of battery cells, design for disassembly approaches, reliable and fast grading tests to assess whether a battery cell should be reused or recycled, are some of the possible technical solutions to ease reuse and remanufacturing of batteries, as requested by EU commission [1], [30], [31]. Looking at tracking of battery states, it becomes necessary to fully understand the electrochemical processes occurring during operations, without considering the battery systems as “black boxes”. In this way, agile and reliable algorithms will allow for optimized state estimation, including State of Charge (SoC), State of Safety (SoS) and State of Health (SoH) to prevent hazardous failures. Those algorithms should represent the best compromise between accuracy and complexity in order to be used on future generation of BMSs. Consequently, relevant non-invasive characterization techniques should be adopted to obtain as much information as possible complying with required level of accuracy. Moreover, laboratory testing campaign and investigations should be performed on commercial size or market available batteries to meet the requests of industry and regulations.

In this optic, laboratory research becomes a pillar to investigate non-invasive techniques and to validate the obtained results with more accurate analyses, including on-purpose cell making and invasive characterization techniques to deeply analyse the cell components and understand the causes of degradation and failure. Then, those analyses will enable to reliably use only non-invasive techniques in the field.

Among the non-invasive techniques, a solution to guarantee proper battery management is the use of Electrochemical Impedance Spectroscopy (EIS). EIS allows to obtain a fingerprint of the processes occurring inside the cells over different measured

frequencies. Specific hardware is required to obtain this measurement; however, it is promising given the amount of information that can be recorded in a relatively short time. This technique has been already widely applied in literature but with different interpretations and methodologies. So that, even though it could be a game changer for precise state estimation, it is difficult to apply it with a simple univocal procedure and exploit the full potential of the obtained results.

### 1.3. Research objectives

This doctoral research project explores the use of Electrochemical Impedance Spectroscopy (EIS) to investigate and understand Li-ion battery aging. The work is organized in three main research objectives: (i) background analysis, (ii) modelling framework and (iii) application of developed algorithms. The schematic representation of these objectives is given in Figure 1.1.

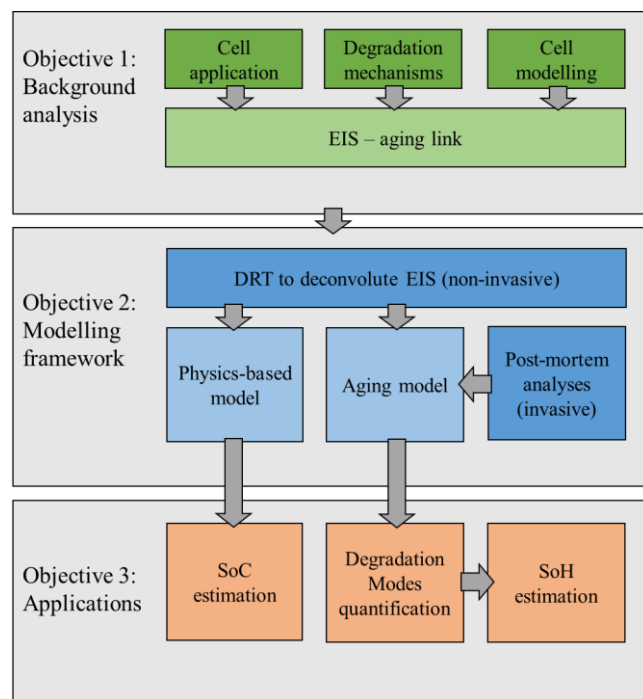


**Figure 1.1. Schematic representation of the objectives of the thesis.** 1) Background analysis, assessing state of the art on the use of EIS measurements to characterize and model Li-ion cells aging; 2) Modelling framework, applying EIS deconvolution to develop physics-based cell model and aging model (validated through post-mortem analyses) and 3) Application of the developed algorithm to perform SoC estimation, quantification of cell degradation and ultimately SoH estimation.

## 1. Introduction

---

*Background analysis:* the first objective is to assess the existing works that applied EIS to characterize and model Li-ion cells degradation. The analysis is performed by looking at (i) the link between EIS spectra variations and cell application (i.e. temperature, Depth of Discharge, C-rate, etc.); (ii) the link between EIS spectra variations and degradation mechanisms and (iii) the available options to develop Electric Circuit Models (ECMs) of aged cells. The expected result is a panoramic view to the readers on the use of EIS characterization with aged Li-ion cells including a critical review to discuss existing links between degradation mechanisms and most reliable solutions to model them with ECMs.

*Modelling framework:* the second objective is to exploit the information obtained by the background analysis to develop specific algorithms modelling Li-ion cells behaviour with EIS measurements. Distribution of Relaxation Times (DRT) is used to deconvolute the impedance spectra and to highlight modelling information that otherwise would have been overlapped in the frequency domain. The expected result is firstly the development of a physics-based model and secondly the development of an aging model. The aim of the first is to define ECMs where each element is attributed to different physical processes without having to make a-priori assumptions on the number of circuital elements. The aim of the second is to deeply analyse how Li-ion cells age to understand which degradation mechanisms are taking place and to attribute the underlying processes to DRT peaks variations. The impedance measurements will be also validated by invasive characterization, including half-cells making and imaging techniques to investigate aged electrodes morphology.

*Applications:* the third objective of this work is to apply the developed models to improve cell state assessment. On the one side, the physics-based cell model is employed to accurately simulate the cell's voltage profile for given input current profiles and to improve SoC estimation accuracy by leveraging existing CSEM's estimation algorithms [32]. On the other side, the aging model is employed to obtain specific indicators to quantify and track the so-called Degradation Modes (DMs), enabling a "degradation aware" monitoring of Li-ion cells. In turn, those indicators are exploited to obtain SoH estimation both in linear and in more severe aging conditions. Therefore, the expected result of the applications is to obtain accurate and degradation-aware SoC and SoH estimation for Li-ion commercial cells.

Overall, the ambition of this work is to bridge the gap between battery engineers, who analyse batteries from a systemic point of view by exploiting non-invasive characterization techniques such as EIS, and material scientists, who analyse batteries from a material perspective by making use of advanced characterization methods, mainly invasive. The expected result of the doctoral thesis is the development and validation of algorithms that, after dedicated tuning and optimisation, can be deployed in embedded systems but also effectively used in research laboratories. On the one side, the target is to strengthen the battery algorithms competences of CSEM, where hardware and software solutions are under development to prototype smart sensing Cell Management Systems (CMS) with embedded EIS measurements capabilities. On the other side, the DRT-based modelling framework can be exploited as practical non-invasive tool or as complementary method to accelerate investigations at material, component or cell level in battery research labs.

### 1.4. Layout of the work

This doctoral thesis includes theoretical, experimental and numerical analyses. As anticipated in the previous Section, this thesis includes an accurate analysis of the state of the art about the use of EIS with Li-ion cells degradation. The mirroring between the research objectives and the thesis chapter is showed in Figure 1.2.

Chapter 2 presents the background analysis with state-of-the-art articles, including a critical assessment of the reviewed works enabling the reader to replicate the described experiments or to apply the same methodology for their own experiments.

The following chapters, presents the methodology developed in this doctoral research. To better introduce the reader to the specific topics and activities, each chapter includes a referenced analysis with respect to the state of the art.

Chapter 3 introduces a modelling framework to develop a physics-based model from EIS and OCV measurements for Li-ion cells. DRT has been applied to deconvolve EIS spectra as an efficient technique to distinguish electrochemical phenomena which are difficult to interpret directly from EIS. The chapter includes all the algorithmic steps to obtain DRT profiles and derive the ECM of the Li-ion cell under investigation. Together with the

## 1. Introduction

---

additional material in Appendix A, the methodology description allows the readers to apply the modelling framework and obtain the ECM. As explanatory example, the methodology is applied to large format commercial pouch cells and the obtained ECM is validated with different current profiles and at different temperatures. SoC estimation is presented with driving profile simulation performed with a variable temperature profile. Moreover, the same methodology is preliminary applied to commercial cylindrical cells during aging in Appendix B.

Chapter 4 presents a deep analysis of DRT profiles during Li-ion cells degradation. An exhaustive methodology that systematically analyse DRT profiles is introduced and, by means of a validation process, DRT peaks are unambiguously attributed to the degradation mechanisms arising during cell aging. Commercial cylindrical cells are cycled in different testing conditions to embrace different degradation mechanisms. Half-cells are built at beginning and end of life to link the electrochemical and aging processes occurring at anode and/or the cathode sides. Moreover, lab-made full-cells are exploited to verify the reproducibility when compared to cylindrical cell. Imaging techniques with different accuracy, complexity and duration are exploited to characterize surface morphology of the electrodes and to validate the above attributions between DRT peaks and degradation mechanisms. As in the previous chapter, the methodology description and the additional material in Appendix C give the readers the tools to replicate the experiments.

Chapter 5 applies the results of DRT peaks attribution analysis of Chapter 4 to track Li-ion cells degradation and estimate SoH. A methodology to develop degradation indicators and to set up SoH estimation is presented and applied to cylindrical commercial cells (already exploited in Chapter 4). The chapter presents the main results of methodology application and specific guidelines addressed to the readers to perform online degradation tracking and SoH estimation in BMSs.

Finally, Chapter 6 summarizes the findings of the different activities giving final remarks and considerations for future works.

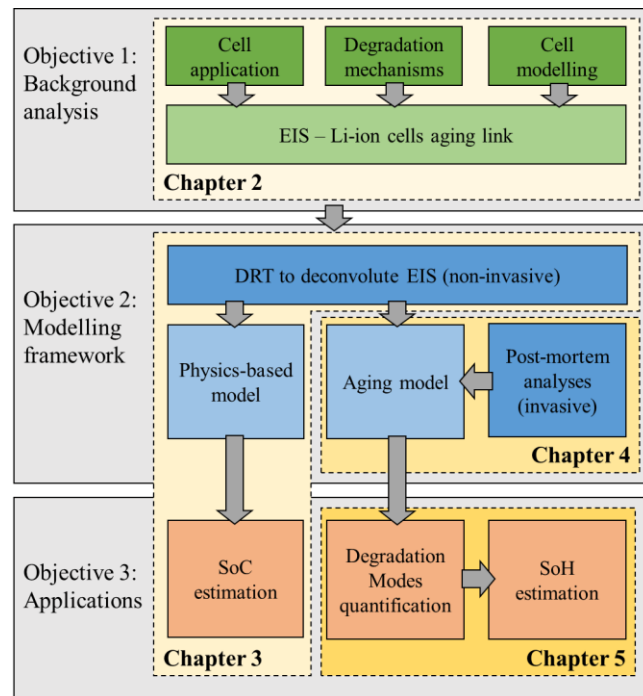


**Figure 1.2. Thesis layout.** Schematic representation of the research objectives highlighting the layout of the thesis with the different chapters.



# Chapter 2

## Background analysis: on the use of EIS to characterize and model Li-ion cells aging

Electrochemical Impedance Spectroscopy (EIS) is a powerful non-invasive technique used to characterize Lithium-ion cells. Its application allows to identify and track the evolutions of cell degradation processes within a short testing time. This chapter presents a review of all the available works which have used EIS spectra either to characterize Li-ion cell degradation or to develop Electric Circuit Models (ECMs). The objectives of this chapter are: (i) to highlight the influence of different aging test conditions on the EIS spectra; (ii) to find the correlations between EIS spectra variations and the underlying degradation mechanisms and (iii) to list the available options to formulate ECMs from EIS spectra of aged cells. After an exhaustive analysis of the state-of-the-art, a critical review is presented to discuss the existing links between degradation mechanisms and the most reliable solutions to model them.

The content of this chapter has been published in the Journal of Power Sources under the title “On the use of electrochemical impedance spectroscopy to characterize and model the aging phenomena of lithium-ion batteries: a critical review” [33].

## 2.1. Context

As discussed in Chapter 1, Li-ion batteries represent a pivotal technology to fulfil the ambitions of the European Green Deal [1]. They will contribute to the specific objectives of ensuring the supply of clean energy and accelerating the shift to sustainable mobility. On one side, Li-ion stationary solutions allow indeed the large-scale utilization of intermittent renewable energy sources; on the other side, their high gravimetric and volumetric energy density allow the electrification and hybridization of vehicles overcoming space and weight limitations [11]. However, degradation and improper operation of Li-ion batteries can significantly affect performances. Battery leakage, insulation damage and partial short circuit problems lead to unsafe operation and, in the worst case, to accidents [34]. So that, Li-ion batteries require the BMS to ensure safe and reliable operations during their lifetime, to guarantee a more efficient use and possibly reuse in second-life applications [35]. The detection of battery aging is challenging due to the interdependency of the various degradation mechanisms that manifest themselves by capacity and power fade and can have chemical and mechanical origins [11]. State of Health (SoH) is the indicator used to evaluate the status (i.e. health) of the battery, accounting the ability to convey a specific performance compared with a new battery [36]. Several different estimation methods have been developed to calculate the SoH, depending on the battery chemistry, computational complexity, battery model and data processing mode. The simplest solutions are to track the decrease of cell capacity and the increase of internal resistance [37]. A comprehensive review of the models and method developed in the last years and nowadays used is given by Ungurean et al. in [38]. All these methods are based on measurements done on the full cell and they can be categorized as non-invasive characterization technique.

Another class of characterization technique is given by physico-chemical post-mortem analyses. By opening the cell and harvesting the materials, these techniques provide valuable and detailed information on the chemical composition and eventual degradation of the elements inside the cell (i.e. electrodes, residual electrolyte and separator) [39], [40]. The effects occurring at the electrodes can be separated by making experimental half-cells that contain li-metal as counter-electrode or by including a reference electrode in the cell (three-electrodes configuration) [11], [44], [30], [36], [45]. The chemical

structure and surface morphology of the electrodes harvested from dismantled cells can be investigated with several different techniques. The most used ones can be classified in three categories:

- X-ray based techniques: such as X-Ray Diffraction (XRD) [39], [41], [45]–[51]; Energy Dispersive Spectroscopy (EDS) [39], [43], [47], [50], [52], X-ray Absorption Spectroscopy (XAS) [48], [40], and X-ray Photoelectron Technique (XPS) [53], [54], [55], [56].
- Electron and Scanning probe microscopy: such as Scanning Electron Microscopy (SEM) [41], [46], [57] Transmission Electron Microscopy (TEM) [41], [46], [39], [57], [53], Electron Probe Microscopic Analysis (EPMA) [58] and Focused Ion Beam (FIB) technique [53].
- Spectroscopic techniques: such as Fourier Transform InfraRed spectrometry (FTIR) [49], Raman spectroscopy [40] and Prompt Gamma Activation Analysis (PGAA) [45].

Even if all these invasive techniques allow a more precise understanding of the degradation mechanisms, their application in a BMS is clearly unfeasible [59]. The BMS monitors simple variables, such as voltage, current and temperature and combines them with variable complexity depending on the available algorithm and computational power: degradation monitoring in real-time condition could be an issue [59]. In the last years, efforts have been made to determine battery states like temperature, State of Charge (SoC) and SoH by means of EIS coupled with an Electric Circuit Model (ECM) [60]. EIS characterizes the impedance of an electrochemical system using low amplitude sinusoidal current or voltage signals excitations over a range of frequencies [61]. Being based on voltage and current measurements acquisition, EIS has been proposed as a fast, non-invasive and reliable technique, able to identify the actual origin of cell degradation processes [62], [63]. So that, the impedance rise and the processes occurring inside the cell can be directly tracked with the ECM parameters evolution [64].

Here, we collect the available articles where EIS has been exploited to analyse Li-ion cell degradation and to model it by means of ECMs. This review is addressed to both scientists and industrial representatives who aim to approach degradation modelling of Li-ion cells via EIS characterization. The readers will be able to replicate the described experiments or to apply the same methodology for their own experiments.

## 2.2. Methodology and outline

The reviewed papers are listed in Table 2.1, where the main author, year of publication, cathode chemistry type (i.e. Li-ion cells with graphite-based anode), the testing type and information about the use of invasive characterization techniques are given for each specific article. Since Li-ion cells show different characteristics (i.e. energy density, open circuit voltage and degradation phenomena) depending on the chemical composition of the cathode, four main chemistries have been taken into account in the review: Lithium Cobalt Oxide (LCO) cells [39], [41], [44], [46], [57], [58], [65]–[70]; Lithium Iron Phosphate (LFP) [47]–[49], [71]–[77], Lithium Nickel Manganese Cobalt Oxide (NMC) cells [40], [42], [43], [45], [50], [52], [54], [78]–[92] and Lithium Nickel Cobalt Aluminium Oxide (NCA) cells [51], [55], [56], [63], [93]–[96]. Minor influence and also smaller number of publication have been found for Li-ion Polymer (LiPO) [97] and Lithium Manganese Oxide (LMO) cells [98], [53]. It is remarkable that, even if two cells have the same cathode chemistry type, they can have slightly different behaviour due to chemistry (e.g. different fractions of each element with respect the total mass of the electrode or presence of additives) and due to physical variables (e.g. thickness of the electrode). Looking at the year of publication and cathode chemistry type, it results that the oldest studies done in the first decade of 2000 are mostly related to LCO and LMO, while the studies published in the second decade of 2000 are related to LFP, NMC and NCA. This trend follows the development of Li-ion cells cathode materials with respect to the main technologies that have been commercialized along the years [99]. Two main testing types are normally exploited to study battery degradation: cycling and calendar aging tests. The first class consists in charging and discharging the cells with a predefined set of parameters: current rate, Depth of Discharge (DoD - voltage window used to run the test) and temperature. These parameters could be fixed differently for charging and discharging phase; symmetric cycling is defined when the current rate is fixed to the same value for both charge and discharge. The second class of tests consists in storing the cells for a predefined period at a specific temperature and SoC. Further details on the parameters used in the aging tests will be given in Section 2.3. To verify the existence of a link between EIS results and physical processes occurring inside the cell, it is possible to exploit invasive characterization techniques. This type of validation, combining EIS and

other optical, chemical and electrochemical analyses is very often applied [100]. The last column of Table 2.1 lists the techniques exploited in the works under review. The description on the use of these techniques to detect specific processes or degradation mechanisms that occurred in the cell will be given in the next sections, where the findings of the reviewed articles are presented.

**Table 2.1. Overview of the reviewed articles with additional information:** author, year of publication, cathode chemistry type, type of experimental test (cycling or calendar test) and specifications on invasive techniques (if any). The reference numbers (Ref) correspond to the ones given at the end of the work, in the References section.

Ref	Author	Available online	Cathode chemistry type	Testing type (calendar /cycling)	Invasive Techniques
[65]	H. De Vries	2015	LCO	cycling	Not used
[41]	J. Li	2010	LCO	calendar	XRD, SEM, half cells
[66]	T. Osaka	2003	LCO	calendar, cycling	Not used
[67]	U. Tröltzsch	2005	LCO	cycling	Not used
[68]	K. Kato	2003	LCO	cycling	Not used
[44]	M. -S. Wu	2004	LCO	cycling	Three electrodes
[69]	D. Mukoyama	2012	LCO	cycling	Not used
[46]	J. Li	2001	LCO	cycling	SEM, TEM, XRD
[58]	D. Zhang	2000	LCO	cycling	Half cells, EPMA
[39]	J. Zhou	2007	LCO	cycling	EDS, XRD, half cells, TEM
[57]	G. Ning	2003	LCO	cycling	Half cells, SEM
[70]	C. Lyu	2019	LCO	cycling	Not used
[98]	H. Popp	2012	LMO	cycling	Not used
[53]	T. Yoshida	2006	LMO	calendar	FIB, SEM, XPS
[97]	M. Galeotti	2016	LiPO	cycling	Not used
[71]	S. Schindler	2017	LFP	cycling	Not used
[72]	M. Petzl	2014	LFP	cycling	Half cells
[47]	E. Sarasketa-Zabala	2014	LFP	cycling	SEM, EDS, XRD
[73]	Y. Zhang	2010	LFP	cycling	Not used
[48]	D. Wong	2015	LFP	cycling	XRD, SEM, XAS
[74]	M. A. Monem	2015	LFP	cycling	Not used
[75]	D.-I. Stroe	2017	LFP	calendar	Not used
[49]	M. Kassem	2013	LFP	calendar	FTIR, XRD, SEM, half cells
[76]	T. G. Zavalis	2013	LFP	calendar, cycling	Three electrodes, SEM
[77]	X. Wang	2019	LFP	cycling	Not used
[42]	B. Stiaszny	2013	NMC	cycling	Half cells, SEM, light microscopy
[78]	Y. Leng	2017	NMC	cycling	Three electrodes
[52]	A. Maheshwari	2018	NMC	cycling	SEM, EDS
[79]	S. F. Schuster	2015	NMC	cycling	SEM
[80]	X. Zhou	2019	NMC	cycling	Not used
[81]	U. Westerhoff	2016	NMC	cycling	Not used

## 2. Background analysis: on the use of EIS to characterize and model Li-ion cells aging

---

Ref	Author	Available online	Cathode chemistry type	Testing type (calendar /cycling)	Invasive Techniques
[43]	X. Li	2019	NMC	cycling	Half cells, SEM, EDS
[50]	K. Jalkanen	2015	NMC	cycling	XRD, SEM, EDS
[82]	Q. Yang	2020	NMC	cycling	Not used
[83]	P. Aurora	2013	NMC	cycling	Not used
[84]	M. Klett	2016	NMC	cycling	Three electrodes
[85]	T. P. Heins	2019	NMC	cycling	Three electrodes
[86]	T. P. Heins	2020	NMC	cycling	Not used
[87]	R. Xiong	2017	NMC	cycling	Not used
[45]	I. Buchberger	2015	NMC	cycling	XRD, PGAA, Three-electrodes
[40]	Y. Li	2013	NMC	cycling	Three electrodes, SEM, XRD, XAS, Raman Spectroscopy
[54]	T. Joshi	2014	NMC	cycling	SEM, XPS
[88]	B. Stiaszny	2014	NMC	calendar	Half cells, SEM, light microscopy
[89]	J. Schmitt	2017	NMC	calendar	Not used
[90]	P. S. Sabet	2020	NMC	calendar, cycling	Not used
[91]	M. Ecker	2012	NMC	calendar, cycling	Not used
[92]	W. Waag	2013	NMC	calendar, cycling	Not used
[51]	Y. Zhang	2009	NCA	cycling	Three electrodes
[63]	C. P. Fernàndez	2017	NCA	cycling	Not used
[96]	P. S. Sabet	2020	NCA	cycling	Half cells
[55]	X. Zhang	2020	NCA	cycling	XRD, XPS, SEM
[93]	D. Wong	2015	NCA	cycling	Not used
[94]	R. G. Jungst	2003	NCA	calendar	Not used
[56]	D. P. Abraham	2005	NCA	calendar	Half-cells, XPS
[95]	H. Sun	2021	NCA	cycling	Not used
[101]	A. Eddahech	2011	n.d.	cycling	Not used

All the works listed in Table 2.1 have been used to understand how the EIS curve is related to the cell application, to the cell degradation and to the ECM solutions applied to model the cell behaviour. These connections are showed by the chart in Figure 2.1 and they represent how this chapter is organised (4 sections). In Section 2.32.3., the relationship between the cell application (i.e. the test characteristics) and the variations in the impedance curve are analysed in the reviewed papers. In Section 2.4, the relationship between the registered impedance curve variations and the associated degradation mechanisms is highlighted. In Section 2.5, the proposed ECMs are analysed with specific attention on how the EIS variations are modelled. Finally, in Section 2.6, a critical review will be made on all the works included in this article and on any link between Sections 2.4.

and 2.52.5., that is between the degradation mechanism occurring in the cell and the ECM specificity to model them. The final remarks and conclusions are given in Section 2.7.

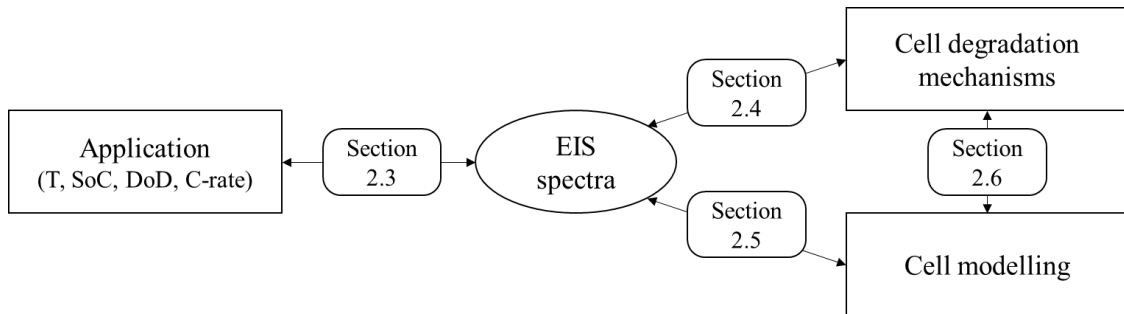


**Figure 2.1. Graphical representation of the structure of the review.** Section 2.3: link between cell application and EIS spectra; Section 2.4: link between EIS spectra and cell degradation; Section 2.5: link between EIS spectra and ECMs solutions; Section 2.6: link between the degradation mechanisms and the circuital elements.

## 2.3. How the application impacts on the EIS spectra

The slower or faster degradation of a Li-ion cell depends on how the cell is used during its lifetime. On top of the calendar and cycling aging difference, specific testing-types are a combination of the so-called extrinsic factors [59]: time, temperature, SoC level (or voltage level), current rate (C-rate), DoD (or voltage interval) and mechanical stress. Their magnitude and variation affect the impedance of the cell and consequently the EIS curve.

Table 2.2 and Table 2.3 describe respectively calendar aging and cycling aging experiments with the parameters chosen for the different experiments in the reviewed articles and the effects on the impedance curve. The first and second column of the two tables give information about the article reference and the cathode chemistry type. A specific notation is introduced to define different regions of the impedance curve and to follow their changes with aging (i.e. impedance rise). This notation has been already used in other works, such as in [81] and [102], and it is shown in Figure 2.2. The high frequency inductive behaviour of the cell does not provide useful information about the cell behaviour and is neglected in this work. EIS spectrum could be divided in 3 regions:

- Ohmic region (frequency higher than 1000 Hz): it represents the internal resistance of the cell measured where the cell impedance switch from an inductive to capacitive behaviour [29]. The value of the internal resistance could be use as indicator of the state of health of the battery [64].

## 2. Background analysis: on the use of EIS to characterize and model Li-ion cells aging

---

- Mid-frequency region (frequency interval between 1000 Hz and 0.1 Hz): it represents the charge-transfer processes, both from electrolyte to electrodes surface and from electrodes surface into the bulk active material of the electrodes. It has always the shape of depressed semi-circular arches. It is usually composed by a singular semicircle or by two semicircles, depending on the cell chemistries and/or the specific ongoing aging mechanism [64], [81].
- Low-frequency region (frequency lower than 0.1 Hz): it represents the diffusion processes at the two electrodes [29]. This region is often neglected [42], [88], [91] or even not measured [68]: the reasons could be traced in the longer time required to measure impedance at lower frequencies.

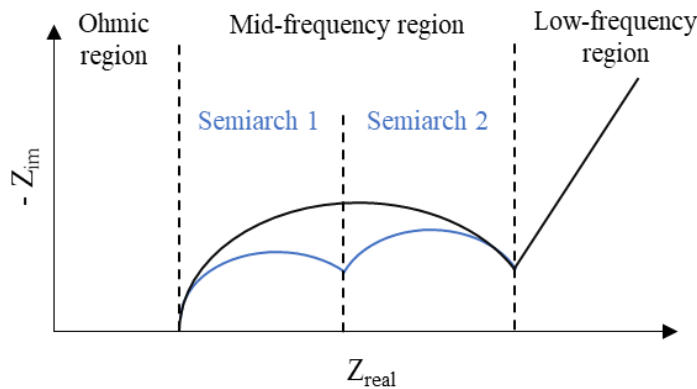


**Figure 2.2. Representation of the frequency regions on a Nyquist plot.** The typical EIS spectrum of a Li-ion cell could be composed of a unique semicircle or two semicircles in the Mid-frequency region.

When a specific part of the EIS curve is affected by the testing conditions, a X symbol is marked into the corresponding cell of Table 2.2 and Table 2.3. This symbol is followed by a qualitative indicator of its magnitude:

- the single sign “-“ means a decrease of the impedance, that in the Nyquist plot corresponds to a shift of the curve on the left side or a decrease of the size of the Mid-frequency semicircle;
- the sign “+“ means an impedance rise, that in the Nyquist plot corresponds to a shift of the curve on the right side or an increase of the size of the Mid-frequency semicircle.

When a double sign is used (e.g. “++”) it means that the effect is stronger than in the other regions where only a single sign is present.

Looking at calendar aging experiments, from Table 2.2 it emerges that the impedance growth affects the different regions depending on the cathode chemistry type. In detail, the tests done on LCO cells in [41] and [66] show that at high temperature there is no effect on Ohmic region but only in the Mid-frequency region. It is remarkable the different duration of the tests: in [66], the experiments done by Osaka et al. lasted only 20 days and show an impedance increase only in the 2<sup>nd</sup> semiarch of Mid-frequency region; in [41] the experiments lasted 5 times more (100 days) and show an increase in both the semiarches. Looking at the SoC level, when it is high (up to 100% SoC), an impedance rise is also visible in the Low-frequency region [41]. A similar behaviour is described by Jungst et al. in [94] and by Abraham et al. in [56] for NCA cells: the tests were performed at 55°C for about 140 days with SoC respectively of 100% and 80%. A general impedance rise was observed in the Mid-frequency region for both the papers and a rise in the Low-frequency region was also observed in [56]. Looking at the other cathode chemistry types, i.e. at LMO, LFP and NMC cells, the effects of calendar aging have been also observed in the Ohmic region. In the first case, i.e. LMO cells, Yoshida et al. stored cells at 40°C and 50% SoC for 400 days [53]. The evolution of EIS spectrum shows a homogeneous impedance rise with a shift of the curve on the right side and a growth of the semiarch in the Mid-frequency region. Looking at LFP cells, no common results are highlighted between the articles under review. The effects of calendar aging appear only in one region per each different article. In [75] Stroe et al. observed a large increase of ohmic resistance, storing the cells for a duration up to 24 months, at high temperature and at three SoC levels (10%, 50% and 90%). Also Zavalis et al. observed the effects of calendar aging in the Ohmic region, but in this case with a decrease of ohmic resistance: the tests were performed at ambient temperature and 60% SoC; the test duration is not specified in days but the calendar tests lasted until the cells under cycling aging reached End of Life (EoL) [76]. The EoL condition is reached when the residual capacity of a Li-ion cell is 80% of the nominal capacity given in the datasheet by the manufacturer (SoH=80%). In [49] instead, Kassem et al. stored the cells for 8 months at 60°C and 100% SoC observing only a rise in the size of Mid-frequency semiarch. As regards NMC cathode chemistry type, Schmitt et al. observed an homogeneous impedance rise within the Ohmic and Mid-frequency regions, storing the cells at 45°C and 100% SoC for about 12 months [89]. Similar results have been collected by Sabet et al. in [90]: they observed a marked impedance rise in the Ohmic

## 2. Background analysis: on the use of EIS to characterize and model Li-ion cells aging

region and in both the two semiarches of Mid-frequency region storing the cells at 100% SoC and at 35°C for about 23 months. The authors also performed calendar aging tests storing cells at 80% SoC at two different temperatures: 35°C and 45°C. The article does not include the evolution of EIS spectra in these two cases but includes the discussion about the specific impedance rise related to SEI layer (i.e. 1<sup>st</sup> semiarch of Mid-frequency region). With respect to the case at 100% SoC and 35°C, at 80% SoC the calendar aging is less severe at 35°C and more severe at 45°C. In the remaining cases the impedance rise is stronger in the Mid-frequency region than in the Ohmic one. Stiasnzy et al. observed a large impedance rise in the 2<sup>nd</sup> semiarch of Mid-frequency region storing the cells at 100% SoC level and high temperature (60°C) for about 10 months [88]. In [92] Wang et al. combined calendar and cycling aging experiments to simulate the application in an electric vehicle. They stored the cells at various SoC levels and at different temperatures between 25°C and 50°C and they observed a negligible impedance rise in the Ohmic region compared to Mid-frequency one. Finally, Ecker et al. observed a doubled impedance value with respect to initial one in the Mid-frequency region, storing the cell for 420 days at three levels of temperature (35°C, 50°C and 65°C) and at 50% SoC in [91].

Having analysed the articles listed in Table 2.2, the effects of the different parameters involved in calendar aging experiments onto the EIS spectra can be now analysed. A graphical representation of the EIS spectrum evolution during calendar aging experiments is given in the Nyquist plot of Figure 2.3. The Mid-frequency region is represented with a singular semiarch. The black arrows show the expected EIS shifts during aging: a homogeneous impedance rise in the Ohmic region (i.e. a shift from the left to the right) together with an enlargement of the semiarch. When the application of the cell implies high temperatures and/or storage at high or low SoC, the calendar aging becomes stronger. The effects are shown by the dotted arrows in Figure 2.3: a larger shift on the X-axis and a larger expansion of the Mid-frequency semiarch, which implies a greater shift of the diffusive tail to the right side. Across the different chemistry types, LCO and NCA cells showed an impedance rise only in the Mid- and Low-frequency regions [41], [66], [94], [56]; LFP, LMO and NMC showed an impedance rise in the Ohmic and Mid-frequency regions [49], [53], [75], [76], [88], [90], [91], [92]. Moreover, NMC cells exhibited the largest EIS spectra shifts with respect to the other cathode chemistries [88],

[90], [91], [92]. Further details and a critical assessment about the reviewed works on calendar aging will be given in Section 2.6.

**Table 2.2. Calendar aging tests characteristics and correspondent effect on the impedance curve of the Li-ion cell.** The impedance rise is marked with symbol X and its intensity is given by: (+) increase; (++) increase higher compared to the others. Abbreviation: EOL = End Of Life.

Ref	Cathode chemistry type	Time of storage	Temp-erature	SoC	Ohmic region	Mid-frequency region		Low-frequency region
						Semiarch 1	Semiarch 2	
[41]	LCO	100 days	55°C	0%, 50%	-	X (+)	X (+)	-
[41]	LCO	100 days	55°C	100%	-	X (+)	X (+)	X (+)
[66]	LCO	20 days	50°C	-	-	-	X (+)	-
[53]	LMO	400 days	40°C	50%	X (+)	X (+)		-
[75]	LFP	12-24 months	40°C - 55°C	10%, 50%, 90%	X (+)	-	-	-
[49]	LFP	240 days	60°C	100%	-	X (+)		-
[76]	LFP	Up to EOL of cycling test	22°C	60%	X (-)	-	-	-
[88]	NMC	300 days	60°C	100%	X (+)	X (+)	X (++)	-
[89]	NMC	375 days	45°C	100%	X (+)	X (+)		-
[90]	NMC	700 days	35°C	100%	X (+)	X (+)	X (+)	-
[91]	NMC	420 days	35°C, 50°C, 65°C	50%	X (+)	X (++)		-
[92]	NMC	18 months	50°C to 25°C	-	X (+)	X (++)		-
[94]	NCA	140 days	55°C	100%	-	X (+)		-
[56]	NCA	142 days	55°C	>50%	-	X (+)		X (+)

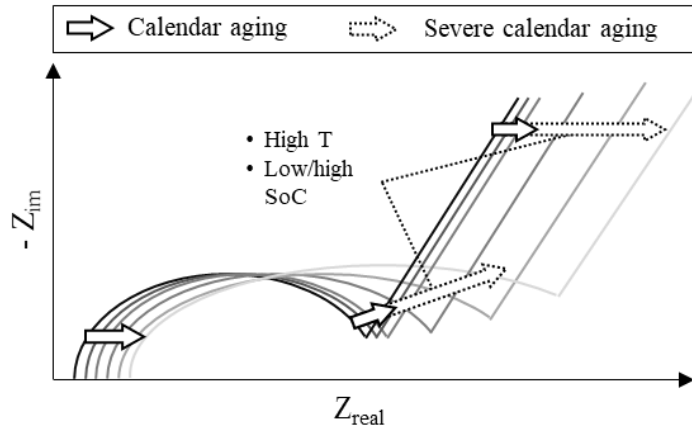


**Figure 2.3. Representation of the EIS spectrum evolution of a cell subjected to calendar aging experiments.** Depending on the cell application, the impedance rise could be smaller (black arrows) or larger (dotted arrows). Large impedance rise is mainly due to high temperature and low or high SoC at which the cell is stored.

Looking at the cycling aging experiments in Table 2.3, it emerges that the effect of degradation is observable both in the Ohmic and in the Mid-frequency regions for all the different cathode chemistry types. For an effective analysis of the experimental results, the SoH values of the cells have been reported with the number of cycles. When this variable was not available in the article under review, it has been calculated as fraction of the measured capacity after cycling over the nominal capacity. Almost the totality of the works reviewed exploited the full capacity of the cells: only in four cases the DoD is lower than 100% [68], [73], [52], [90]. As regards the current rate, most of the articles used high rates (equal or higher than 1C) obtaining EIS spectra that could be categorized depending on their evolution: (i) impedance rise only in one frequency region; (ii) homogeneous impedance rise in different frequency regions and (iii) generalized impedance rise with larger increase in one or more areas of the whole EIS spectrum. Looking at the first category, a further distinction could be based on the cathode chemistry. LFP cells showed only an increase of ohmic resistance with 1C cycling at -22°C and at 30°C respectively in [72] and in [47]. At very low temperature (-22°C) the cells under testing reached 74% SoH after 300 cycles while at higher temperature (30°C) the cells reached 80% SoH after 3200 cycles. The same EIS spectrum evolution has been observed by Zavalis et al. in [76] simulating the Hybrid Electric Vehicle (HEV) application until the cells reached 80% SoH. For LCO and NMC cathode chemistry types the impedance changes have been observed in the Mid-frequency region. LCO cells showed an impedance rise in both the two semiarches

of Mid-frequency region in [57] and in [58] with respectively 3C and 0.8C symmetric cycling reaching 83% SoH (300 cycles) and 68% SoH (800 cycles). A peculiar behaviour is observed by Osaka et al. cycling LCO cells at 2C in [66]: after 20 cycles the cell reached 78% SoH and showed an impedance reduction in the 1<sup>st</sup> semiarch and an augmentation in the 2<sup>nd</sup> semiarch. In the case of NMC cells, the impedance rise in the Mid-frequency region (both the semiarches) has been observed by Leng et al. in [78] with 1C charge-2C discharge cycling; by Heins et al. in [85] with 1.5C symmetric cycling and by Buchberger et al. in [45] with 1C symmetric cycling conditions. The same behaviour has also been detected by Li et al. in [43] with lower current rate (0.5C). In other works testing NMC cells, the impedance rise was detected only in the first semiarch of the Mid-frequency region [86], [87], [54]. In [86] the authors applied 1C symmetric cycling, reaching 85% SoH after 450 cycles at 20°C; in [87] Xiong et al. applied a constant charging rate of 1C and different discharging rates (1C, 2C and 3C) at 10°C and they reached 70% SoH after 650 cycles; in [54] Joshi et al. made laboratory cells and applied a lower rate cycling (0.5C) reaching 96% SoH after 50 cycles. As regards the second category (homogeneous impedance rise in different frequency regions) similar results have been observed for different cathode chemistry types with impedance rise both in the Ohmic and Mid-frequency regions: applying 1C symmetric cycling to LCO cells [69] [46], to LiPO cells [97] and to NMC cells [79]; applying C/3 charge and 1C discharge cycling to NMC cells in [90] and applying 0.5C charge and 1C discharge cycling to NCA cells in [63]. The same result has been also obtained by Sabet et al. for NCA cells in [96] and by Wang et al. for LFP cells in [77]. In the first case, Sabet et al. applied very severe testing conditions: the cells reached 70% SoH after 400 cycles down to -10°C and with a current rate up to 3C. In the second case, Wang et al. performed 800 cycles at 45°C with high current rate (2C) reaching 80% SoH. The third category includes all the works where a generalized impedance rise with larger increase in one or more areas of the whole EIS spectrum was observed. As regards NMC cells, 1C symmetric cycling was performed in [42], [81], [50] and [83] reaching respectively 5%, 86%, 80% and 97% of SoH. In the first case, Stiaszny et al. performed 800 cycles at ambient temperature and observed a large increase of ohmic resistance, coupled with a small decrease and a small increase of impedance respectively in the first and second semiarches of Mid-frequency region [42]. In the second case, Westerhoff et al. tested the cells in a temperature range between 20°C and

50°C observing a strong impedance rise in the 2<sup>nd</sup> semiarch of the Mid-frequency region [81]. In the latter cases, Jalkanen et al. performed long term cycling tests (1500 cycles) at high temperature (45°C during charging phase and 65°C during discharging phase) while Aurora et al. performed a short test campaign (50 cycles) obtaining similar results: an increase of ohmic resistance and an augmentation of the 2<sup>nd</sup> semiarch with a small or negligible impedance rise in the 1<sup>st</sup> semiarch of Mid-frequency region [50], [83]. Looking at other experimental conditions, Maheshwari et al. performed 500 cycles at 1C in charging phase and 2C in discharging phase with 50% DoD in [52]. After cycling they reached 55% SoH and the EIS spectrum evolution showed a large increase of ohmic resistance coupled with a small impedance rise in the 1<sup>st</sup> semiarch of Mid-frequency region. In [92] instead, Waag et al. applied a specific current profile to simulate EV use: they reached 90% SoH with 1900 cycles. As already mentioned, they coupled cycling and calendar aging tests and they observed a larger impedance rise in the Mid-frequency region than in the Ohmic one. As regards NCA cells, a strong impedance rise was observed in the 2<sup>nd</sup> semiarch of Mid-frequency region by Zhang et al. performing symmetric cycles at high current rate and temperature (5C and 40°C) reaching 82% SoH with 5250 cycles [51]. The same impedance evolution behaviour has been observed by Wong et al. in [93]. They studied the impact of high pulsed rate discharge with current peak of 83C; the charging phase was fixed to 1C to neglect its effect on the impedance curve with respect to the discharging phase. The cells under testing reached 80% SoH after 400 cycles. A different result was observed by Zhang et al. in [55]: they cycled different cells at different symmetric cycling conditions obtaining a strong increase of Ohmic resistance and a small augmentation of the Mid-frequency semiarch. Testing the cells at 1C, 2C and 3C, they reached respectively 75%, 72% and 64% SoH after 400 cycles. As regards LFP cathode chemistry, Zhang et al. simulated Plug-in Hybrid Electric Vehicle (PHEV) application applying a pulsed profile defined by the United States Environmental Protection Agency (US EPA) and named Urban Dynamometer Driving Schedule (UDDS) [73]. A general impedance rise is observed, with an increase of three times of the size of the Mid-frequency semiarch with respect to the value before cycling.

**Table 2.3. Cycling aging tests characteristics and correspondent effect on the impedance curve of the Li-ion cell.** When not available in the article, the SoH has been calculated with the given measurements of initial and EoL capacity. The impedance rise is marked with letter X and its intensity is given by: (+) increase; (++) increase higher compared to the others. Abbreviations: d = discharge; c = charge; Tamb = ambient temperature, HDC = Hybrid Drive Cycle.

Ref	Cathode chem. type	# of cycles	SoH [%]	Temperature	DoD [%]	C-rate	Ohmic region	Mid-frequency region		Low-frequency region
								Semiarch 1	Semiarch 2	
[65]	LCO	890	80%	T <sub>amb</sub>	100%	C/2 d; 1C c	-	X (++)	X (+)	-
[66]	LCO	20	78%	T <sub>amb</sub>	100%	2C	-	X (-)	X (+)	-
[67]	LCO	230	86%	19°C	100%	C/2 d; 1C c	X (+)	-	X (+)	X (+)
[68]	LCO	1980 0	68%	25°C	10%	0.1 / 0.3C	X (+)	-	X (++)	-
[44]	LCO	200	94%	-	100%	0.2C	X (+)	X (+)	X (+)	-
[69]	LCO	550	<23%	T <sub>amb</sub>	100%	1C	X (+)	X (+)	X (+)	-
[46]	LCO	286	70%	T <sub>amb</sub>	100%	1C	X (-)	X (+)	X (+)	-
[58]	LCO	800	68%	-	100%	0.8C	-	X (+)	X (+)	-
[39]	LCO	500	87%	-	100%	0.5C	-	X (+)	X (++)	-
[57]	LCO	300	83%	T <sub>amb</sub>	100%	3C	-	X (+)	X (+)	-
[70]	LCO	400	-	25°C	100%	1C	X (+)	X (+)	appears X	-
[70]	LCO	360	-	25°C	100%	2C	X (+)	X (+)	appears and X(++)	-
[98]	LMO	1400	67%	23°C	100%	2C	X (+)	X (+)	appears X	X (+)
[97]	LiPO	315	60%	25°C	100%	1C	X (+)	X (+)	X (+)	-
[101]	n.d.	3.8*1 0^5	81%	25°C	100%	Pulses 1C up to 7C	X (+)	-	appears and X(++)	-
[71]	LFP	100	80%	-22°C	100%	2C	X (+)	X (+)		X (+)
[72]	LFP	300	74%	-22°C	100%	1C	X (+)	-	-	-
[47]	LFP	3200	80%	30°C	100%	1C	X (+)	-	-	-
[73]	LFP	600	86%	45°C	50%	US EPA UDDS	X (+)	X (++)		X (+)
[48]	LFP	40	0%	-	100%	Pulses $\leq 15C$	X (+)	-	appears and X (+)	-
[74]	LFP	500	95%	T <sub>amb</sub>	100%	Pulses $\leq 1C c;$ 5C d	X (+)	-	X (+)	X (+)
[76]	LFP	n.d.	80%	22°C	100 %	HDC	X (+)	-	-	-
[77]	LFP	800	80%	45°C	100%	2C	X (+)	X (+)	X (+)	-
[42]	NMC	800	5%	T <sub>amb</sub>	100%	1C	X (++)	X (-)	X (+)	-

## 2. Background analysis: on the use of EIS to characterize and model Li-ion cells aging

Ref	Cathode chem. type	# of cycles	SoH [%]	Temperature	DoD [%]	C-rate	Ohmic region	Mid-frequency region		Low-frequency region
								Semiarch 1	Semiarch 2	
[78]	NMC	1500	75%	25°C	100%	1C c; 2C d	-	X (+)	X (+)	-
[52]	NMC	500	55%	20°C	50%	1C c; 2C d	X (++)	X (+)	-	-
[79]	NMC	977	50%	35°C	100%	1C	X (+)	X (+)		-
[80]	NMC	n.d.	71%	45°C	100%	≥1C	X (+)	X (+)	X (+)	X (+)
[81]	NMC	n.d.	86%	Range 50 to -20°C	100%	1C	X (+)	X (+)	X (++)	-
[43]	NMC	250	84%	T <sub>amb</sub>	100%	0.5C	-	X (+)	X (-)	-
[50]	NMC	2500	80%	T <sub>amb</sub>	100%	1C	X (+)	X (+)	X (+)	-
[50]	NMC	1500	80%	45°C c; 65°C d	100%	1C	X (++)	X (+)	X (++)	-
[82]	NMC	550	82%	T <sub>amb</sub>	100%	C/3	X (+)	X (+)	X (++)	-
[83]	NMC	50	97%	-	100%	1C	X (+)	-	X (+)	-
[84]	NMC	50	95%	30°C	100%	C/3	X (+)	X (+)	-	X (+)
[85]	NMC	1000	95%	-	100%	1.5 C	-	X (+)		-
[86]	NMC	450	85%	20°C	100%	1C	-	X (+)	-	-
[87]	NMC	650	70%	10°C	100%	1C c; 1C, 2C, 3C d	-	X (+)	-	-
[45]	NMC	300	60%	25°C, 60°C	100%	1C	-	X (+)	X (+)	-
[40]	NMC	1500	43%	30°C	100%	0.5C	-	X (++)	X (+)	-
[54]	NMC	50	96%	T <sub>amb</sub>	100%	0.5C	-	X (+)	-	-
[90]	NMC	3000	92%, 85%	25°C	80%, 100%	C/3 c; 1C d	X (+)	X (+)	X (+)	-
[92]	NMC	200, 1900	94%, 90%	40°C to -10°C	100%	EV profile	X (+)	X (++)		-
[51]	NCA	5250	82%	40°C	100%	5C	X (+)	X (+)	X (++)	-
[63]	NCA	500	84%	25°C	100%	C/2 c; 1C d	X (+)	X (+)	X (+)	-
[96]	NCA	120	70%	≥ -10°C	100%	≤ 3C	X (+)	X (+)	X (+)	-
[55]	NCA	400	75%, 72%, 64%	25°C	100%	1C, 2C, 3C	X (++)	X (+)		-
[93]	NCA	400	80%	T <sub>amb</sub>	100%	Pulses ≤ 83C	X (+)	X (+)	X (++)	-
[95]	NCA	250	-	25°C	100%	1C	X(++)	X(+)	X(+)	X(+)
[95]	NCA	250	-	45°C	100%	1C	X(+)	X(+)	X(+)	X(+)

Looking at the other works where high rate cycling experiments were performed (Table 2.3), a peculiar behaviour is observed in [70], [98], [101] and [48] where the 2<sup>nd</sup> semiarch of Mid-frequency region appeared and grew due to cycling. In [70] Lyu et al. performed 1C and 2C symmetric cycling tests on LCO cells at 25°C. In the first case the authors observed an impedance rise in the Ohmic region and in the 1<sup>st</sup> semiarch, with the rise of the 2<sup>nd</sup> semiarch. With higher rate, they observed a similar behaviour with a more pronounced impedance rise in the 2<sup>nd</sup> semiarch. In [98] Popp et al. cycled LMO cells with a symmetric rate of 2C and reached 67% SoH after 1400 cycles. The EIS spectrum evolution showed a general impedance rise for the whole curve and the appearance and large growth of a 2<sup>nd</sup> semiarch in the Mid-frequency region. In [101] Eddahech et al. monitored aging of Li-ion cells during power cycling tests: they reached 81% SoH performing  $3.8 \cdot 10^5$  micro-cycles with current pulses from 1C to 7C. They observed the appearance and growth of 2<sup>nd</sup> semiarch in the Mid-frequency region and a small shift to the right of the EIS curve due to grow of the ohmic resistance. The same behaviour was observed by Wong et al in [48]. They tested LFP cells with pulsed current up to 15C: after 40 full cycles the ions intercalation was completely inhibited leading to no available capacity for cycling (i.e. SoH=0%). In a smaller number of cases, a large impedance rise in the 1<sup>st</sup> or 2<sup>nd</sup> semiarch of Mid-frequency region is observed when cycling tests were performed at reduced current rate (i.e. lower than 1C). This is the case in [68], where Kato et al. tested LCO cells with a protocol composed by repetition of 200 symmetric cycles at 0.3C with 10% DoD and one full cycle (i.e. 100% DoD) at 0.1C. After 19800 cycles, the cells reached 68% of SoH showing a large augmentation of the 2<sup>nd</sup> semiarch. The same result was obtained by Zhou et al. for LCO cells in [39] and by Yang et al. for NMC cells in [82]. In [39] the authors performed 0.5C symmetric cycling tests and they reached 87% SoH after 500 cycles; in [82] the authors applied C/3 symmetric cycling protocol and they reached 82% SoH after 550 cycles. Another example is given by Li et al. in [40], where they reached a very low residual capacity (43% SoH) with 1500 cycles at 0.5C. Among all the works listed in Table 2.3, only few cases present impedance variations in the Low-frequency region: these variations are always coupled with impedance rise in the Ohmic and in the Mid-frequency regions, as in the work on LMO cells of Popp et al. already presented [98]. In [67] Tröltzscher et al. performed cycling tests on LCO cells with high rate charging phase (1C) and 0.5C discharging phase. They observed the impedance rise in the Ohmic region,

## 2. Background analysis: on the use of EIS to characterize and model Li-ion cells aging

in the 2<sup>nd</sup> semiarch of Mid-frequency and in the Low-frequency region. As regards LFP cells, the impedance rise in the Low-frequency region was observed with high current rate testing at different temperatures in [71], [73] and [74]. In the first case, Schindler et al. performed 100 cycles at -22°C reaching 80% SoH; they applied 2C symmetric cycling protocol and they observed an homogeneous impedance growth among the different frequency regions [71]. In the second case, Zhang et al. simulated PHEV application at 45°C (the cycling tests have been already presented) [73]. In the third case, Monem et al. evaluated different pulsed charging protocols [74]. Exploiting a constant current-constant voltage with negative pulse (maximum 1C) protocols and constant discharge at 5C at ambient temperature, the authors reached 95% SoH after 500 cycles. Looking at NMC cells, the impedance rise in the Low-frequency region was observed in [80] and in [84]. In the first case, Zhou et al. performed cycling tests at 45°C with two different cycling rates: 1C symmetric rate and more severe conditions not specified. In the worst case the cell reached 72% SoH [80]. In the second case, Klett et al. performed a short test campaign, composed by 50 symmetric cycles at 30°C. They reached 95% SoH with a current rate of C/3. Finally, concerning NCA cells, Sun et al. performed 1C symmetric cycling at two different temperatures: 25°C and 45°C [95]. In both the cases the impedance rise was generalized overall the EIS spectra. However, at 25°C a larger increase of Ohmic resistance was observed compared to the other part of EIS spectrum. At 45°C instead, the impedance rise was larger than at 25°C but it was homogeneous overall the different frequency regions.

Having analysed the articles listed in Table 2.3, the effects of the different parameters involved in cycling aging experiments onto the EIS spectra can be now analysed. The graphical representation in the Nyquist plot is given in Figure 2.4, where only one semiarch is represented in the Mid-frequency region. In general, as the number of cycles increases (i.e. the cycled energy increases), the EIS spectrum is shifted on the right side (increase of ohmic resistance) together with a specific impact on the Mid- and Low-frequency regions.

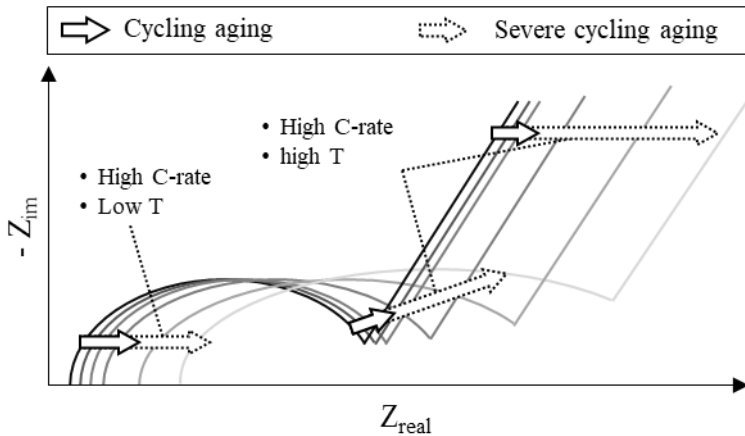


**Figure 2.4.** Representation of the EIS spectrum evolution of a cell subjected to cycling aging experiments. Depending on the cell application, the impedance rise could be smaller (black arrows) or larger (dotted arrows). Large impedance rise is mainly due to low temperature (in the Ohmic region), high temperature (in the Mid-frequency region) and high C-rate.

A stronger impedance rise, marked by the dotted arrows in Figure 2.4, is caused by severe temperatures. On the one side, low temperatures mainly impact on the ohmic resistance of the cell, leading to large shift of the EIS spectrum on the right side of the Nyquist plot [72]. On the other side, high temperatures impact mainly on the Mid-frequency region, leading to an enlargement of the semiarch (or of the two semiarches if present) [50], [73], [92]. High current rates also have their impacts onto the EIS spectra and mainly on the 2<sup>nd</sup> semiarch, when it is present [46], [81], [101], [51], [93]. The combination of severe conditions, e.g. low temperature and high C-rate clearly shows an even more severe effect on the cycled cell [71], [92], [96]. On the contrary, a parameter that usually reduces the severity of cycling is DoD. At reduced DoD the impedance rise is slowed if compared to higher DoD [90]. Further comments and the critical assessment of the impact of the cycling aging application on the EIS spectra will be given in Section 2.6.

## 2.4. How EIS spectra are linked to degradation

Degradation in Li-ion cells is caused by many physical and chemical mechanisms, which affect the different elements inside a cell: the electrodes, the electrolyte, the separator and the current collectors [62], [103], [104]. The most common reported degradation mechanisms in Li-ion cells will be mentioned in this review; the list is given in the left side of Figure 2.5 (first column). These degradation mechanisms do not leave a unique

## 2. Background analysis: on the use of EIS to characterize and model Li-ion cells aging

fingerprint in the cell's OCV and impedance curve, but they can be clustered into the so-called degradation modes, as shown in Figure 2.5. The three commonly reported modes, with the respective degradation mechanisms, are [63], [105]–[107]:

1. Loss of Lithium Inventory (LLI): lithium ions are consumed by processes such as parasitic reactions, decomposition reactions (SEI layer decomposition, electrolyte decomposition), SEI layer growth, lithium plating and they are no longer available for cycling between anode and cathode. So that, the available capacity of the cell decreases leading to capacity fade.
2. Loss of Anode Active Material (LAM<sub>A</sub>): active material of the anode is no longer available due to structural disordering, particle cracking, graphite exfoliation, loss of electrical contact or blocking of the active sites by passivation surface layers. Consequently, the effects can be accounted both in capacity and power fade.
3. Loss of Cathode Active Material (LAM<sub>C</sub>): this mode is similar to the previous one but it concerns the cathode. Active material is no longer available due to structural disordering, particle cracking, loss of electrical contact or Cathode Electrolyte Interface (CEI) formation. This degradation mode leads both to capacity and power fades.

A more specific description of the degradation mechanisms is out of the objective of this work. However, the readers interested in more details are addressed to the work of Vetter et al. [62] and to the review article of Agubra et al. [104].

The relationship between Li-ion cell degradation and impedance curve variations is shown in **Table 2.4**: the four main row-sections of the table represent the three distinctive regions of EIS curve with the specific distinction of Mid-frequency region semiarches. These row-sections are divided in 5 rows representing the different cell chemistries. On the other side, each column represents a different degradation mechanism. For a more effective analysis of the literature, the degradation mechanisms (graphite exfoliation, structural disordering and particle cracking) related to the anode have been grouped in the “loss of anode active material” degradation mode. When a correspondence between EIS region and degradation mechanism is found, the article reference number is used to mark the link in the correspondent cell.

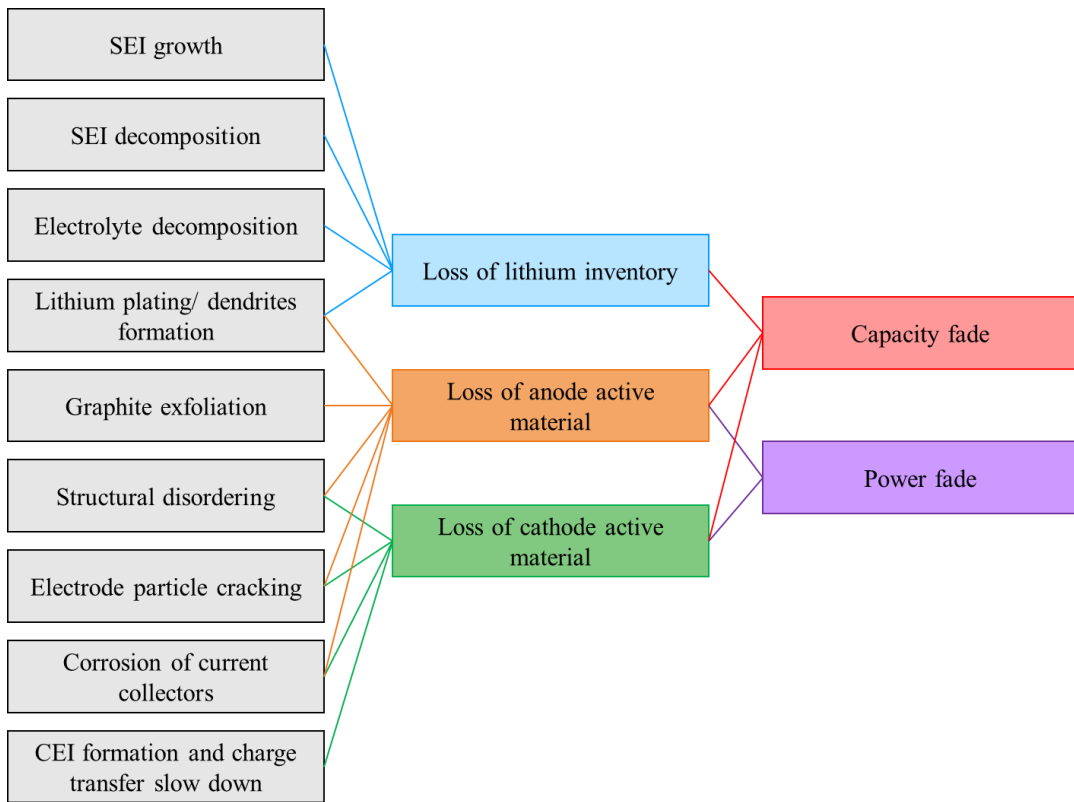


**Figure 2.5.** List of the commonly reported degradation mechanisms in Li-ion cells, associated degradation modes and related fade caused on the cell. Adapted from [107].

As will emerge in the discussion below, most of the degradation mechanisms are not uniquely assigned to a specific region of the impedance curve. When available from the reviewed paper, the validation of EIS observation via more detailed characterization has been included in the analyses to deepen the investigation.

As regards of LCO chemistry, in [65] De Vries et al. studied the cell lifetime depending on the DoD in cycling. In the results, they showed the impedance spectra of a cell aged with 100% DoD. They observed a pronounced impedance rise in the Mid-frequency region, assigning this variation to SEI layer growth, in agreement to previous investigations. Similarly, Mukoyama et al. observed variations along the whole impedance spectra in [69]: they assigned SEI layer growth to semiarch 1 and disconnection/cracking of cathode particles to semiarch 2. In [66] Osaka et al. observed an increase of interfacial resistance of the cathode during cycling and nearly a constant value for the anode. They explained this observation with the formation of stable SEI layer on anode surface during formation and a growing CEI layer on the cathode surface due to the strong oxidizing power of cobalt

ions. This effect is assigned to the Mid-frequency region of impedance spectra. The same degradation mechanism has also been addressed in the Mid-frequency region by the analyses of Li et al. in [46] and of Zhang et al. in [58]. In the first case, the authors validated their results by detecting the formation of defect on the cathode and the growth of passivation layer by means of SEM, TEM and XRD [46]; in the latter case the authors made half-cells to analyse the EIS spectra of the two electrodes separately [58]. Differently, Tröltzsch et al. measured an increase of the ohmic resistance and an impedance rise in the Mid- and Low-frequency regions in [67]. They assigned the variations in the Ohmic region to electrolyte decomposition and the variations in the Mid- and Low-frequency regions to cathode charge transfer slow down. Analogous result was obtained by Lyu et al. in [70]: however, in this case, the 1<sup>st</sup> semiarch of Mid-frequency region was not assigned to cathode related degradation but it was assigned to SEI growth. In [39] Zhou et al. used half-cells for the characterization of the electrodes. They found out that the variations in anode impedance are negligible and they focussed on the cathode: the EIS spectra showed variations in the Ohmic and in the Mid-frequency regions (2<sup>nd</sup> semiarch).

These variations have been respectively assigned to CEI layer formation and growth and to cracks and defects in the cathode structure (validation with TEM imaging). A similar analysis has been performed by Ning et al. in [57], using half-cells and SEM imaging to validate the results. They observed degradation and charge transfer slow down on the cathode side in the second semiarch of Mid-frequency region. Differently from the previous work, the anode impedance rise was not negligible and SEI layer growth has been addressed in the 1<sup>st</sup> semiarch of Mid-frequency region.

As regards of LMO chemistry, in [98] Popp et al. addressed the changes in the impedance curve of the cell to lithium plating and to electrolyte decomposition. These mechanisms have been identified by a huge shift of the impedance curve to the right-hand side of the Nyquist plot and by a growth of the size of the semiarches related to Mid-frequency region. So that the degradation has been assigned to all the three regions of the impedance spectra. Different results have been presented by Yoshida et al. in [53]. They exploited FIB, XPS and SEM imaging to characterize the electrodes after aging and to measure the thickness of the SEI layer. They concluded that both the electrodes contribute to the cell degradation: increase of ohmic resistance is due to SEI layer growth and the impedance rise in the Mid-frequency region is due to cathode charge transfer slow down.

**Table 2.4. Correlation between impedance curve variations and degradation mechanisms.** The cathode chemistry types are specified per each different EIS region. The region interested by a specific degradation mechanism is marked with the reference number of the related article. Specific notation is given for: \* = the Mid-frequency region is described only with a singular semiarch; for half-cells or three-electrodes configuration: <sup>c</sup> measurement related to the cathode side; <sup>a</sup> measurement related to the anode side.

EIS region	Cathode chemistry type	Degradation mechanism						
		SEI growth	SEI decomposition	Li plating / dendrites formation	Loss of anode active material	Electrolyte decomposition	Structural disordering / particle cracking	CEI formation and charge transfer slow
Ohmic region	LCO				[67], [70]		[39] <sup>c</sup>	
	LiPO – LMO – n.d.	[53], [97]		[98]		[98]		
	LFP	[72], [47], [48]		[72]		[71], [72], [47], [73]		[71]
	NMC	[42], [81], [79], [90]		[79]	[84] <sup>a</sup>	[50], [91], [42], [88], [89], [52], [81], [84] <sup>c</sup>		[91]
	NCA	[96], [55]			[96], [55]			[63]
Mid-frequency region [semiarch 1]	LCO	[65]*, [69], [57], [70]					[46]*, [66], [58]	
	LiPO – LMO – n.d.			[98]		[98]	[53]*	
	LFP	[73]*, [71]*, [77]	[71]*, [49] <sup>a*</sup>				[73]*, [49] <sup>c*</sup>	
	NMC	[91]*, [88], [50], [81], [79], [90], [89]*, [43] <sup>a</sup> , [52], [87], [54]	[91]*	[50], [79], [84] <sup>a</sup> , [85]*, [86]	[81], [43] <sup>c</sup> , [84] <sup>c</sup> , [45]	[89]*, [86], [45], [40]	[78], [89]*, [43] <sup>c</sup>	
	NCA	[51], [63], [96], [55]*, [93], [95]	[63], [95]	[63], [96]		[55]*, [56]* <sup>c</sup>	[96], [56] <sup>c*</sup> , [93], [56] <sup>c*</sup> , [94]*	
Mid-frequency region [semiarch 2]	LCO						[69], [39] <sup>1</sup>	[67], [65], [58], [57], [70]
	LiPO – LMO – n.d.	[101]	[101]	[98]		[98]		[53]*
	LFP							[48], [77]
	NMC	[81], [79]		[79]	[43] <sup>a</sup> , [45]	[81], [43] <sup>c</sup> , [50], [90], [45], [40]	[42], [88], [43] <sup>c</sup> , [90]	
	NCA	[55]*, [63]	[63], [93]	[63]		[55]*		[51], [93], [95]
Low-frequency region	LCO							[67]
	LiPO – LMO – n.d.			[98]		[98]		
	LFP						[71]	
	NMC					[84] <sup>c</sup>		
	NCA						[63], [95]	

## 2. Background analysis: on the use of EIS to characterize and model Li-ion cells aging

As regards of LFP chemistry, in [71] Schindler et al. assigned the increase of ohmic resistance to corrosion of current collector and electrolyte decomposition. Observing the EIS spectra variations in the Mid- and Low-frequency regions, they addressed the impedance rise respectively to SEI layer processes (growth and decomposition) and particle cracking of the cathode. In [72] Petzl et al. assigned the increase of ohmic resistance to electrolyte decomposition caused by surface film formation on plated lithium and to SEI layer growth; these investigations have been validated by material characterization of the anode. Also Zhang et al. highlighted the relationship between the electrolyte decomposition and passivation film formation on the negative electrode in [73]. The first mechanism has been assigned to the Ohmic region and the second one to the Mid-frequency region, coupled with formation of a passivation layer on the positive electrode (CEI). All the remaining works on LFP cells exploited invasive characterization techniques to validate the EIS characterization results: in [47] Sarasketa-Zabala et al. exploited SEM, EDS and XRD and they observed an increase of the ohmic resistance due to SEI layer growing and non-uniform electrolyte decomposition; in [49] Kassem et al. exploited half-cells attributing the cathode impedance rise to formation of CEI layer and the anode impedance rise to decomposition of SEI layer. They demonstrated that the cell degradation is mainly due to loss of lithium inventory (by means of XRD and residual capacity measurements) and that there is no loss of active material (by means of capacity measurements on separate electrodes). Similar conclusions have been presented by Wong et al, in [48]. They showed that the rapid impedance rise in the Mid-frequency region, with the appearance of the 2<sup>nd</sup> semiarch, is mainly due to the formation of CEI layer; minor influence is due to SEI layer growth. In this case, the authors validated their results exploiting SEM and X-ray techniques (XRD and XAS). In [77] Wang et al. performed cycling tests to develop a model for SoH estimation. Analysing the EIS spectra evolution, they assigned the impedance rise of the Mid-frequency region to SEI layer growth (1<sup>st</sup> semiarch) and to charge transfer slow down (2<sup>nd</sup> semiarch).

As regards of NMC chemistry, many studies are available in literature. The results of the characterizations lead to clustering the works in two groups: the ones addressing the degradation only to loss of lithium inventory related processes and the ones addressing the degradation also to loss of active material at positive, negative or both the electrodes. Looking at the first group, in [52] Maheshwari et al. addressed the ohmic resistance rise

to electrolyte decomposition and the impedance rise in the Mid-frequency region to SEI layer growth; they validated the results with electrochemical measurements and material analyses (SEM and EDS). In [87] Xiong et al. confirmed that the impedance rise in the Mid-frequency region is due to SEI layer growth and they indicated this phenomenon as the most sensitive one to describe cell degradation. Also Joshi et al. assigned the Mid-frequency region impedance rise to SEI layer growth in [54]. The authors demonstrated that the addition of transition metal species in the electrolyte facilitate the growth of SEI layer. The EIS measurement were coupled with SEM and XPS experiments to analyse the SEI layer and measure its thickness. In [79] and [81] the degradation mechanisms have been attributed indistinctly to the impedance rise in Ohmic and Mid-frequency regions. In the first case, Schuster et al. studied the nonlinear aging characteristic of NMC cells: until 80% SoH the impedance rise is mainly due to SEI layer growth (linear aging behaviour); afterwards, the cell capacity drops with a nonlinear behaviour and the impedance rise is faster. This degradation has been attributed to SEI layer growth and lithium plating (validation with SEM experiments) [79]. In the second case, Westerhoff et al. attributed the impedance rise to SEI layer growth and to electrolyte decomposition. In [91] Ecker et al. analysed the EIS spectra of a cell stored at high temperature: the impedance rise is larger in the Mid-frequency region than in the Ohmic region. This huge rise has been addressed to SEI layer growth and decomposition. The minor rise of the Ohmic region has been addressed to electrolyte decomposition and corrosion of current collector. Looking at the second group of works, i.e. the ones considering both loss of lithium inventory and loss of active material related processes, in [85] Heins et al. applied Distribution of Relaxation Times (DRT) to EIS, observing an impedance rise in the Mid-frequency region due to loss of anode active material. DRT is a mathematical operation that allows to find the time constants of the different processes and to track their changes to understand how the behaviour of the cell evolves [108]; this method is effective to extract useful information by the EIS spectra that are not so evident only analysing the EIS curve in the Nyquist plot. DRT has been also applied in the same research group by Heins et al. in [86] to evaluate the impact of erroneous cell assembly on aging of NMC cells. They discovered a faster degradation of the cathode due to incomplete coverage: in this case the impedance rise was assigned to anode active material loss and to structural disordering of the cathode. In [90] Sabet et al. assigned the impedance rise in the Ohmic region and in the

## 2. Background analysis: on the use of EIS to characterize and model Li-ion cells aging

first semiarch of Mid-frequency to SEI layer growth and the impedance rise in the second part of Mid-frequency region to CEI formation. In [50] Jalkanen et al. performed cycling aging on NMC cells, characterizing them by means of EIS, SEM imaging, XRD and EDS. Disassembling the cell, they found almost dry electrodes, meaning the electrolyte was consumed during testing: they assigned the increase of ohmic resistance to electrolyte decomposition. As regards the impedance rise in the Mid-frequency region, they assigned it to SEI layer growth and lithium plating for the 1<sup>st</sup> semiarch and to mechanical cracking and loss of contact of the cathode active material for the 2<sup>nd</sup> semiarch. In [42] and in [88] Stiaszny et al. performed electrochemical characterization and post-mortem analyses of cells subjected respectively to cycling and calendar aging experiments. They exploited half-cells and imaging techniques (light microscopy and SEM) to separate the effects at the two electrodes and to validate their results of EIS characterization. They found that the increase in ohmic resistance is caused by the growth of the SEI layer and by electrolyte decomposition while the impedance rise in the Mid-frequency region is caused by CEI layer formation. Analogous results have been found by Schmitt et al. in [89], exploiting only EIS characterization and adding also structural disordering to the causes of Mid-frequency region impedance rise. In [84] Klett et al. exploited a three-electrodes configuration to address separately the phenomena occurring at the two electrodes: for the cathode EIS curve, they attributed the general impedance rise to electrolyte decomposition; for the anode EIS curve they assigned loss of anode active material to the Ohmic and Mid-frequency regions. Analogous results have been presented by Li et al. in [43] using half-cells and validating the measurements by means of SEM and EDS. The Mid-frequency region impedance rise was attributed to electrolyte decomposition and to CEI formation for the cathode half-cell and to SEI layer growth (1<sup>st</sup> semiarch) and loss of anode active material (2<sup>nd</sup> semiarch) for the anode half-cell. Interesting results are showed by Buchberger et al. in [45] performing cycling aging tests at different temperatures. At ambient temperature the pronounced impedance rise has been observed in the Mid-frequency region and it has been assigned to electrolyte decomposition and dissolution of transition metal from NMC cathode. At 60°C instead the impedance spectrum showed negligible variations with respect to the reference one: this effect has been attributed to partial SEI dissolution, that is a decrease of SEI layer resistance that compensate the resistance increase at cathode side. The authors validated their results by means of XRD

and PGAA [45]. As observed in the EIS spectra evolution by Buchberger et al., also in [78] and in [40] the cell degradation caused an impedance rise only in the Mid-frequency region. In [78] Leng et al. introduced a novel methodology to perform three electrodes measurements without dismantling the cell. Analysing the EIS spectra of the two electrodes they stated the cathode has the highest influence on the full cell EIS spectrum and the impedance rise is due to CEI formation. In [40] Li et al. applied several material characterization techniques to validate the results obtained with EIS measurements on a three electrodes cell. Comparing the EIS spectrum of the full cell with the ones of the two electrodes, they found the cathode is the main responsible of the impedance rise of the full cell. This impedance rise is concentrated in the 2<sup>nd</sup> semicircle, with almost no variations in the 1<sup>st</sup> semicircle and it has been attributed to cathode's structural disordering and particle cracking.

As regards of NCA chemistry, in [51] Zhang et al. exploited a three-electrodes configuration to study the impedance variations of NCA cells. The impedance rise is observed in the Mid-frequency region: the variation of the 1<sup>st</sup> semicircle is assigned to SEI layer growth and the variation of the 2<sup>nd</sup> semicircle is assigned to cathode charge transfer slow down. Similar results have been presented by Sabet et al. in [96], exploiting half-cells and DRT analysis. They identified electrolyte decomposition and in the Ohmic region, lithium plating and cathode structural disordering in the Mid-frequency region and SEI layer growth in both the two mentioned regions. In [55] Zhang et al. exploited XRD, XPS and SEM to characterize the SEI layer during cell degradation and to validate the results of EIS. They assigned the impedance rise in the Ohmic and Mid-frequency regions to SEI layer growth and to electrolyte decomposition. A more detailed attribution of EIS spectra variations has been carried out by Pastor-Fernández et al. in [63]. They assigned corrosion of current collector to the Ohmic region, lithium plating and SEI layer processes (growth and decomposition) to the Mid-frequency region and cathode particle cracking to the Low-frequency region. In this case no material characterization or separation of electrodes contributions was directly applied: the EIS spectra characterization was based on an exhaustive review of previous works [63]. As in the previous work, Sun et al. assigned the impedance rise in the Low-frequency region to particle cracking [95]. The two semicircles of the Mid-frequency region instead, were assigned respectively to SEI layer growth and decomposition and to charge transfer slow down at the cathode side. In

[93] Wong et al. studied the impact of high rate discharge on aging of NCA cells. The characterization results showed an impedance rise in the Mid-frequency region: SEI layer growth and small structural damage of the cathode were attributed to the 1<sup>st</sup> semiarch and SEI layer decomposition and CEI formation on the cathode side were attributed to the 2<sup>nd</sup> semiarch. In [94] instead, Jungst et al. performed accelerated calendar aging tests. The experimental results showed a large variation in the Mid-frequency region semiarch after 20 weeks. This impedance rise has been attributed to CEI formation and charge transfer slow down exploiting three-electrodes measurements of a previous work [109]. Similarly, calendar aging tests have been carried out by Abraham et al. in [56]. The authors analysed the EIS spectra of half-cells and exploited XPS for material characterization. They observed that the EIS variations of the full cell could be almost entirely attributed to the positive electrode. The impedance rise in the Mid-frequency region is due to cathode's particle cracking and to CEI formation, with consequent consumption of the electrolyte. So that, they stated that during cell degradation, the CEI formation process enable and speed up the electrolyte decomposition.

## 2.5. How EIS spectra are modelled through ECMs

The most common approach used to evaluate impedance spectra of Li-ion cells is to choose an ECM according to the shape of the impedance curve on the Nyquist plot and a subsequent Complex Nonlinear Least Square (CNLS) fitting [100]. The choice of the elements constituting the circuit depends on the complexity of the impedance curve. In general, the model includes a resistor for the Ohmic region and an inductance or a parallel circuit of inductance and resistor when the inductive tail is present. This scheme is shown in Figure 2.6. The Mid- and Low-frequency regions are represented with a general impedance because they can be modelled with several different elements. These elements are:

- RC element: parallel circuit of resistor and capacitor. In electrochemistry, this element is usually applied for the description of interface loss processes, for instance a charge transfer process between electrode and electrolyte. The resistor represents the limited exchange rate and the capacitor describes the double layer capacity [100].

- Constant Phase Element (CPE): the CPE is an empirical element without a direct physical meaning; it is used to describe the dispersion effect and its behaviour deviates from the capacitance [110]. When its exponent is equal to 1 it behaves as capacitor and when its exponent is equal to 0 it corresponds to a resistor [100], [111].
- Zarc element: parallel circuit of resistor and CPE. This element is used to increase the accuracy when fitting the impedance curve of Li-ion cell [112]. The CPE leads to fit semiarches that does not have constant radius.
- HN element: it is a generalized Zarc element. This element has been developed by Havriliak and Negami. They introduced empirical equations to describe relaxation processes in polymer. These HN-equations were applied to describe dielectric relaxation in Li-ion conducting polymer electrolytes [113].
- Warburg (W) element: it is used to describe the diffusion mechanism in the low frequency region. Several different models of Warburg element are available in literature, depending on the dimensions considered in the problem and on boundary conditions [114], [115], [116]. One dimensional elements are the mostly used in ECM of Li-ion cells [100].
- Transmission Line Model (TLM): it defines a complex ECM design to take the impact of the electrode structure on its loss mechanisms into account. In detail, a TLM is designed to describe a porous electrode structure comprising an electron and an ion conducting path and an interface between them [100].

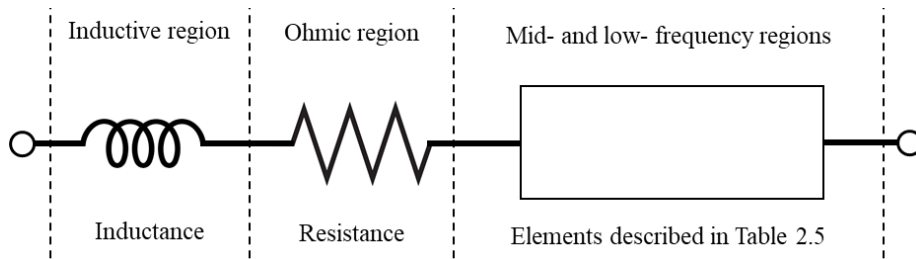


**Figure 2.6. Representation of ECM model of a Li-ion cell.** Inductance and resistance are used to model the high frequency region (inductive and Ohmic regions). The specifications about Mid- and Low-frequency regions are given in Table 2.5.

Table 2.5 shows how these elements have been combined in literature to model the Mid- and Low- frequency regions of impedance curve. Each column includes an element or series of elements that are intended to be in series with the elements given in the other

## 2. Background analysis: on the use of EIS to characterize and model Li-ion cells aging

columns on the same circuit. The first and second columns include respectively the reference of the article and the cathode chemistry type, while the last column includes information about the presence of a voltage source in series to simulate the SoC of the cell. The description of the work listed in Table 2.5 will be given by analysing the similarities of ECMs across the different cathode chemistry types. In most of the cases the circuit configuration is independent by the cathode chemistry type and it presents different layouts depending on how the elements are combined. Several publications use RC elements to characterize the Mid-frequency region of the impedance: in [65], [66], [67], [68], [39], [57] and [70] for LCO cells; in [74] for LFP cells; in [85], [86], [87], [92] for NMC cells; in [51] and [93] for NCA cells. As shown in Table 2.5, most of these cases present RC elements in series and an element to describe the Low-frequency region. However, in specific cases, the RC elements are modified with additional elements on the two different branches. This is the case in [66], where the authors use an RC with additional Warburg element on the resistive branch to describe the anode processes and a capacitance in parallel to two series of a resistor and a Warburg element to describe the cathode. This choice has been made with the presumption that the electrode is constituted of two different particle sizes.

Looking at low level of model complexity, in [68] the authors used 4 RC elements in series: 3 for the 1<sup>st</sup> semicircle and the latter for the 2<sup>nd</sup> semicircle. They explained that the elements do not completely correspond to separated physical processes but all together they describe the double layer capacity, reaction resistance and possible SEI at anode and cathode. An analogous choice has been made by Ning et al. in [57] exploiting 3 RC elements to represent: (i) the SEI layer; (ii) charge transfer resistance and double layer capacitance and (iii) the electric conductivity of the bulk of electrode material. This model has been derived by studies of [117]. Looking at NMC cathode cells, a similar solution has been adopted by Heins et al. in [85] and [86]: 4 RC elements are used to model the Mid-frequency region. However, in this case the number of elements is defined by the number of peaks identified applying the DRT transformation to the impedance curve. In this way, each element is related to a physical process occurring at a specific time constant [118].

**Table 2.5. List of the ECMs used in the works under review.** When half cells have been used, the label is added to the reference of the article with the name of the electrode used vs lithium. The model structure is given by using symbols and abbreviations: - = series connection; // = parallel connection; R = resistance; C = capacitance; CPE = constant phase element; W = Warburg element; Zarc = parallel circuit of resistance and constant phase element; RC = parallel circuit of resistance and capacitance; TLM = Transmission Line Model; HN = Havriliak and Negami element (generalized Zarc).

Reference	Cathode chemistry	Mid-frequency region [ 0.1 Hz < f < 1000 Hz]		Low frequency region [ f < 0.1 Hz]	Voltage source
		Semiarch 1	Semiarch 2		
[65]	LCO	RC	C // (R - CPE)		N
[41] anode half cell	LCO	Zarc	Zarc	CPE	N
[41] cathode half cell	LCO	Zarc	C // (R - W)		N
[66]	LCO	C // (R - W)	C // (R - W) // (R - W)		N
[67]	LCO	RC	Z_composite_electrode		N
[68]	LCO	RC-RC-RC	C // (R - W)	[Not measured]	N
[69]	LCO	Zarc	CPE // (R - W) - CPE // (R - W) // (R - W)		N
[46]	LCO	Zarc		Zarc	N
[39] cathode half cell	LCO	RC	RC	C // W	N
[57]	LCO	RC - RC - RC		W - C	N
[70]	LCO	C // (RC-R)	RC	[Not in the model]	N
[97]	LiPO	Zarc	Zarc	CPE	N
[101]	n.d.	Zarc	Zarc	CPE	Y
[74]	LFP	(R - W) // C			Y
[75]	LFP	Zarc		Zarc	N
[77]	LFP	Zarc	Zarc	W	N
[42] anode half cell	NMC	Zarc	Zarc - Zarc	[Not in the model]	N
[42] cathode half cell	NMC	Zarc	TLM	[Not in the model]	N
[78]	NMC	Zarc	Zarc	[Not in the model]	N
[52]	NMC	Zarc	Zarc	CPE	N
[43] anode half cell	NMC	Zarc	Zarc	W	N
[43] cathode half cell	NMC	Zarc	Zarc - CPE // (R - CPE)		N
[82]	NMC	Zarc	Zarc		N
[83]	NMC	Zarc	CPE // (R - W) - CPE // (R - W)		N
[85], [86]	NMC	RC - RC	RC - RC	W	N
[87]	NMC	Zarc	Zarc	W	Y
[87]	NMC	RC	RC	[Not in the model]	N
[88]	NMC	Zarc - Zarc	TLM	[Not in the model]	N
[89]	NMC	Zarc	CPE	[Not in the model]	N
[90]	NMC	HN	HN	W	N
[91]	NMC	Zarc	Zarc	[Not in the model]	N
[92]	NMC	RC		[Not in the model]	Y
[51] positive electr.	NCA	RC	C // (R - W)		N
[63]	NCA	Zarc	CPE // (R - W)		Y
[96]	NCA	HN	HN	W	N
[93]	NCA	RC	Zarc	CPE	N
[95]	NCA	Zarc	CPE // (R - W)		N

## 2. Background analysis: on the use of EIS to characterize and model Li-ion cells aging

A different approach, with the same objective of modelling the physical processes, is presented in [67] for LCO cells. For an accurate modelling of the EIS paired with an easily handling model, Tröltzsch et al. combined an RC element with a composite electrode model to represent the cell behaviour in Mid- and Low- frequency regions. This model gives a clear idea of the processes occurring at the cathode. With 8 parameters, the authors claimed a simple estimation process able to represent the porous structure of the electrode, the electrolyte and their interactions. A simpler solution is given in [65] for LCO cells: the 1<sup>st</sup> semiarch is modelled with a RC element and the 2<sup>nd</sup> semiarch with a modified RC that includes a CPE to describe the diffusive behaviour of the cell and also fit the low frequency tail of the impedance curve. In [70] instead, the authors exploited a simple RC element to model the 2<sup>nd</sup> semiarch, representing the cathode, and a more sophisticated element to model the anode and its passivation layer: a capacitance in parallel to a series connection of an RC element and a resistor. The resistor and the capacitance are used to describe the SEI layer and the RC element for the anode.

To increase the robustness of the model and to reinforce the connection with the physical processes occurring inside the cell, it is possible to exploit the results of invasive characterization to build the ECMs. So that the model is not anymore only based on fitting of EIS spectra and experience gained by previous works dealing with the same topic. Half-cells, three-electrodes configuration and material characterization can be used to validate the results of EIS and to distinguish the contribution of anode and cathode in the Nyquist plot. This is the case in [41] where half-cells have been exploited to make cathode- and anode-ECMs. Both the two models include a Zarc element for semiarch 1, respectively to describe SEI layer for anode-cell and the CEI layer for the cathode-cell. Then, they show two different structures: the anode ECM includes a Zarc element to describe charge transfer and double layer and a CPE for the diffusion processes of Low-frequency region; the cathode ECM instead includes a modified RC element with a Warburg element in the capacitive branch. This choice allowed to a better description of the cathode EIS spectrum. A similar solution, exploiting half cells, has been applied by Li et al. in [43] for NMC cells. The anode-cell model includes two Zarc elements (as in [41]) and a Warburg element to describe the diffusive tail; the cathode-cell model presents an identical configuration to [41], using CPE elements instead of Warburg to describe the diffusive behaviour. In [39] Zhou et al. stated that the positive electrode contributes almost solely to the increase of

the total battery impedance in LCO cells. So that, they introduced an ECM to evaluate the impedance variation only of the cathode half-cell. This circuit is a modified Randles model: an RC element is used to model surface layer process; a second RC element is used to model charge transfer and double layer effects and a Warburg element in parallel to a capacitance is used to model the low frequency tail. A similar result is presented by Zhang et al. in [51], where the tests have been done on NCA cells in a three-electrodes configuration. The EIS spectra evolution of the negative electrode did not show a rising trend during aging. The authors built the ECM for the positive electrode including a RC element to describe the 1<sup>st</sup> semicircle of Mid-frequency region and a modified RC element with a Warburg element on the resistive branch to describe the 2<sup>nd</sup> semicircle of Mid-frequency region and the diffusive tail. The impedance rise is tracked with the two resistors that represent respectively the CEI layer and the charge transfer resistance. Finally, Stiaszny et al. exploited half cells to study NMC cells in [42]. In their models they only considered the Mid-frequency region. As regards the 1<sup>st</sup> semicircle, the two models are identical, exploiting a Zarc element to describe the particle-current collector resistance. As regards the 2<sup>nd</sup> semicircle, the two models are different: for the anode ECM two Zarc elements are used to describe SEI layer and charge transfer; for the cathode ECM the charge transfer process is described by a TLM. As already mentioned, the TLM is used to account the impact of the electrode structure on the cell degradation [100].

In the other works under review, material characterization has been used to build a unique ECM for the full cell. In [78] Leng et al. exploited a three-electrodes configuration and modelled the Mid-frequency region with two Zarc elements. The first element describes the migration of ions through the surface film on the positive electrode and the electronic transport in the positive electrode; the second element represents the charge transfer phenomena at positive and negative electrodes. In [52] Maheshwary et al. applied EIS and characterize the electrodes with SEM and EDS. They developed an ECM with two Zarc elements for the Mid-frequency region (one per each semicircle) and a CPE for the Low-frequency region. The three elements represent respectively the SEI layer related processes, the cathode related processes and the solid state mass diffusion effects. In [88], Stiaszny et al. created a model based on the DRT analysis of the impedance spectra. The DRT showed three main peaks corresponding to three different processes: SEI layer, modelled with Zarc element; anode charge transfer, modelled with a Zarc element and

## 2. Background analysis: on the use of EIS to characterize and model Li-ion cells aging

cathode charge transfer modelled with a TLM. A solution similar to TLM is applied by Xiong et al. in [87]: the authors identified the ECM considering the inner structure and general behaviour of Li-ion cells. The model consists in two Zarc elements to describe the Mid-frequency region (the first one corresponding to the SEI layer of the anode and the second one accounting for the charge transfer processes) in series with a Warburg element to model the diffusion processes. However, to achieve the objective of online identification, Xiong et al. decided to simplify their model by substituting the Zarc elements with RC elements and by neglecting the Low-frequency region. Furthermore, an ideal voltage source has been added to describe open circuit voltage. This simplified model is the so called “dual polarization model” [119].

Looking at Table 2.5, there are modelling solutions that have not been clustered in any of the groups already discussed. These models can be classified in three categories. The first one, where the ECM is made only of two Zarc elements, as in [46], [75], [82], [91]. In the first two cases, one element is assigned to the Mid-frequency region and the other one to the Low-frequency region for LCO [46] and for LFP cells [75]. In [82] instead, Yang et al. applied the same model to NMC cells, exploiting one element to describe the 1<sup>st</sup> semiarch and the other one for the 2<sup>nd</sup> semiarch and the Low-frequency region. Also in [91] Ecker et al. exploited the same structure for NMC cells ECM but describing only the two semiarches of the Mid-frequency region. The second category includes the solutions where Zarc elements are modified or coupled with other elements to model and describe the diffusive tail. Galeotti et al. in [97] and Eddahech et al. in [101] applied the same ECM, with two Zarc elements describing the Mid-frequency region and a CPE describing the Low-frequency region. The same choice was taken by Lyu et al. in [77], exploiting a Warburg element instead of a CPE to describe the Low-frequency region. A similar configuration with only two elements was adopted by Schmitt et al. in [89], with a Zarc element to describe the 1<sup>st</sup> semiarch (capacitive effects and polarization resistance) and a CPE to describe the 2<sup>nd</sup> semiarch of Mid-frequency region (solid state mass diffusion). In [63] Fernàndez et al. tested NCA cells and adopted a solution with a Zarc element to model the 1<sup>st</sup> semiarch and a modified Zarc element with a Warburg element on the resistive branch to model the remaining part of the EIS spectrum and to describe cathode related processes and diffusion processes. The same configuration was also adopted for NCA cells by Sun et al. in [95]. For NMC cells instead, Aurora et al. modified the

configuration used by the two previous works placing an additional modified Zarc element [83]. An additional level of complexity, with respect to the previous work, has been presented by Mukoyama et al. in [69] for LCO cells. To model the 2<sup>nd</sup> semiarcs and the Low-frequency region the authors exploited a modified Zarc elements (with Warburg element on the resistive branch) and an element made of a CPE in parallel to two series connections of a resistor with a Warburg element. This modelling choice has been taken to represent respectively the anode and the cathode with two different particle size components [69]. The third category includes two articles of the same research group where the same ECM has been adopted for NMC [90] and NCA cells [96]. The authors exploited HN elements to model the Mid-frequency region; they adopted an ECM that was developed by Witzenhausen in [120]. As mentioned before, HN elements are generalized Zarc elements; in the EIS fitting process they could represent better than Zarc elements the depressed semiarcs [113].

Several different model options have been found in literature, but no predominant model architecture per each different cathode chemistry type. In some cases, as for LFP cells, the few publications cannot motivate any conclusion. In other cases, such as LCO, NCA and NMC cells, the larger number of publications clearly allow for a comparison. Figure 2.7 shows the main ECMs emerged from the reviewed works listed in Table 2.5. LCO cells are commonly modelled by exploiting RC elements for the Mid-frequency region and Warburg element for the Low-frequency region. Two main ECM options are found for this chemistry: (a) the Warburg element is placed in series with respect to the other circuital elements, (b) the Warburg element is placed on the resistive branch of the 2<sup>nd</sup> RC element. NMC and NCA cells are usually modelled similarly (i.e. they have similar performances). The model, showed in Figure 2.7-c, includes two Zarc elements to describe the two semiarcs of the Mid-frequency region and an in-series connected Warburg element to describe the diffusive tail. In all chemistry types, a resistor is used to account for the Ohmic resistance changes. Further analyses and the critical assessment of the reviewed works will be given in Section 2.6.

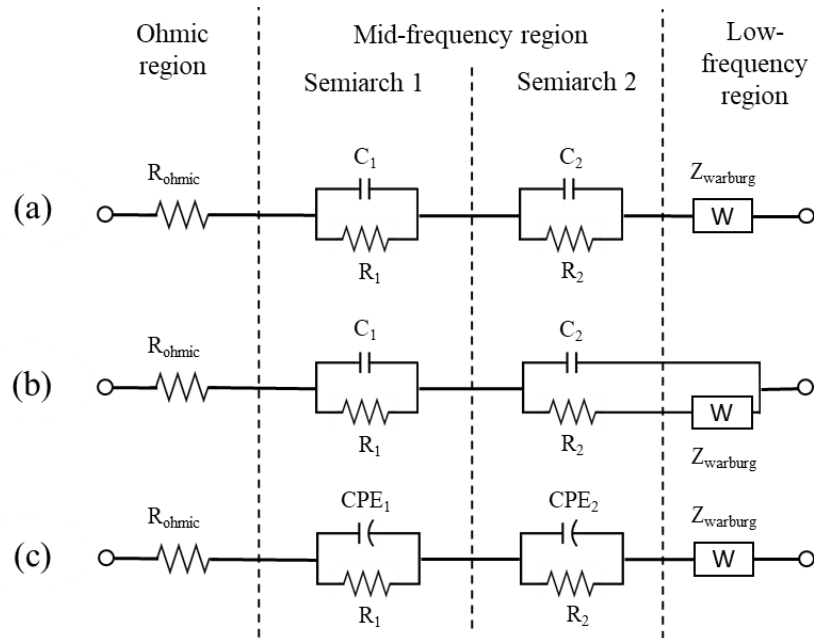


**Figure 2.7. ECMs developed by the review of the articles listed in Table 2.5.** (a) Model developed for LCO cells with Warburg element in series to RC elements; (b) model developed for LCO cells with Warburg element on the resistive branch of the 2<sup>nd</sup> RC element; (c) model developed for NMC and NCA cells with two Zarc elements and a Warburg element in series. The Ohmic region is always modelled with a resistor.

## 2.6. Critical assessment

After having detailed the impact of cell application on EIS spectra in Section 2.3, the connections among EIS spectra and degradation mechanisms in Section 2.4 and the multiple options to build ECM from EIS in Section 2.5, a critical assessment of the reviewed papers (Table 2.1) is proposed in this section aiming at investigating the link between degradation mechanisms and the most correct option to model them.

Figure 2.8 analyses the findings of Section 2.3.3. by showing the impact of different types of aging tests on the EIS. The analysis has been done by clustering the publications with similar testing conditions (e.g. calendar aging tests with SoC lower than 20%) and counting the cases in which a specific EIS region was impacted; the results are normalized on the total number of publications per each different set of parameters.

- **Calendar aging tests:** Figure 2.8-a shows how the EIS spectrum is similarly impacted both in the Ohmic and in the Mid-frequency regions; almost the totality of the tests have been performed at temperature higher than 30°C. The different SoC levels at

which the cells have been stored did not show different behaviours across the EIS regions; however an impedance rise in the Low-frequency region was only detected with SoC  $\geq$  80% [41], [56]. Among the different cathode chemistries, the experimental results of LCO and NCA cells showed an impedance rise concentrated in the Mid- and Low-frequency regions while the tests on NMC, LFP and LMO cells showed EIS variations in the Ohmic and Mid-frequency regions.

- Cycling aging tests: Figure 2.8-b shows how the different tests conditions impact on the EIS regions, accounting all the experiments at 100% DoD. Here the impedance rise is stronger than in calendar aging tests. Specifically:
  1. For medium temperature ( $10^{\circ}\text{C} < T < 25^{\circ}\text{C}$ ) and high current rate (equal or larger than 1C) experiments, the EIS curve is mainly impacted in the Mid-frequency region, specifically in the 2<sup>nd</sup> semiarch.
  2. For medium temperature and low current rate (lower than 1C) experiments, the behaviour is similar, impacting mainly Mid-frequency region. However, the EIS variations are smoother than in the previous case and are concentrated in the area of 1<sup>st</sup> semiarch.
  3. For low temperature ( $T < 10^{\circ}\text{C}$ ) and high current rate experiments, the rise of ohmic resistance is stronger and the impact on EIS is equivalent both in the Ohmic and Mid-frequency regions (mainly in the 1<sup>st</sup> semiarch).
  4. For high temperature ( $T > 25^{\circ}\text{C}$ ) and high current rate experiments, the impact is relevant in the ohmic region but mostly concentrated in the Mid-frequency region.
- In a small number of the reviewed publications a reduced DoD is applied. The impact is generally observable in the Ohmic region and in the 1<sup>st</sup> semiarch of Mid-frequency region. In contrast to the reviewed articles on calendar aging tests, it is not possible to clearly describe different behaviours depending on the cathode chemistry type for the works related to cycling aging tests. The impedance rise is mostly impacted by the experimental parameters described above.

## 2. Background analysis: on the use of EIS to characterize and model Li-ion cells aging

---

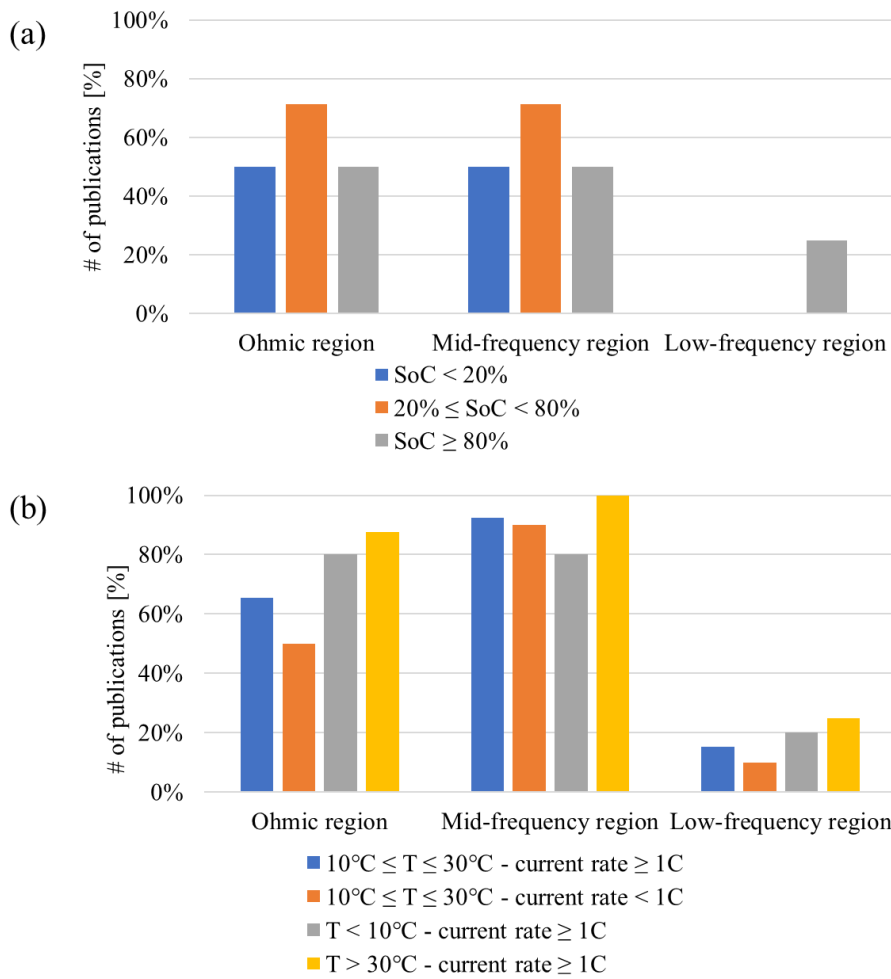


**Figure 2.8. Critical assessment of the impact of aging tests procedures on EIS spectra given in Section 2.3. .** The analysis has been done by clustering the publications with similar testing conditions and counting the cases in which a specific EIS region was impacted; the results are normalized on the total number of publications per each different set of parameters. (a) Impact of calendar aging tests at temperature higher than 30°C and at different SoC levels on the EIS curve; (b) impact of cycling aging tests at 100% DoD, different temperature levels and current rate on the EIS curve.

Figure 2.9-a analyses the findings of Section 2.4 by showing how the different degradation mechanisms have been assigned to the different EIS regions for all the cathode chemistries under review.

- The resistance rise in the Ohmic region is mainly attributed to electrolyte decomposition, as shown in 49% of the cases and to SEI layer growth (29% of the cases). Among the other mechanisms assigned to this region, corrosion of current collector is the only one that is univocally attributed to ohmic resistance rise. However, it has been reported only in three of the articles under review: by Schindler

et al. in [71] for LFP cells, by Ecker et al. in [91] for NMC cells and by Pastor-Fernàndez et al. in [63] for NCA cells.

- The Mid-frequency region has been attributed mainly to two different classes of degradation:
  1. LLI processes: SEI layer growth and decomposition are mentioned in 40% of the studies, while electrolyte decomposition and lithium plating are mentioned in 14% of the cases.
  2. LAM<sub>C</sub>: The degradation is attributed to structural disordering/particle cracking in 14% of the studies and CEI formation in 28% of the studies. Minor influence is given to loss of anode active material mentioned in less than 5% of the cases.

When two separated semiarches are highlighted in the study, a clearer separation of processes occurs and these processes are often assigned to the two different electrodes (Figure 2.9-a – details about Mid-frequency region). The 1<sup>st</sup> semiarch is attributed to SEI layer growth and decomposition in 49% of the cases, to lithium plating and electrolyte decomposition in 24% of the cases and to loss of anode active material in 5% of the cases. This leads to a value of 78% of the cases where semiarch 1 is related to the anode, its passivation layer and loss of lithium ions. The remaining 22% of cases is referred to the cathode side. However, the cathode is the main actor of the 2<sup>nd</sup> semiarch, representing 61% of the cases with respectively 18% of the cases addressing particle cracking and 42% of the cases addressing CEI formation.

- The Low-frequency region is considered only by 7 reviewed works: in 4 cases the impedance rise is attributed to structural disordering of the cathode and to CEI formation while in the other 3 cases is attributed more in general to loss of lithium inventory processes. The predominant attribution to cathode-related processes can be justified knowing that in this region it is possible to track the intercalation process. This process describes the accumulation and depletion of lithium ions within the cathode. So that, the capacity fade related processes observed in this region could be directly pointed to the cathode degradation. In fact, in some studies the authors coupled the variations of the Low-frequency region to the ones occurring in correspondence of the second semiarch of the Mid-frequency region (i.e. to the degradation of the positive electrode) [41], [67], [69], [43], [82], [83], [51], [63]. Other

## 2. Background analysis: on the use of EIS to characterize and model Li-ion cells aging

works instead, truncated the EIS measurement at 0.1 Hz [68], [42], [78], [87], [88], [89], [91], [92].

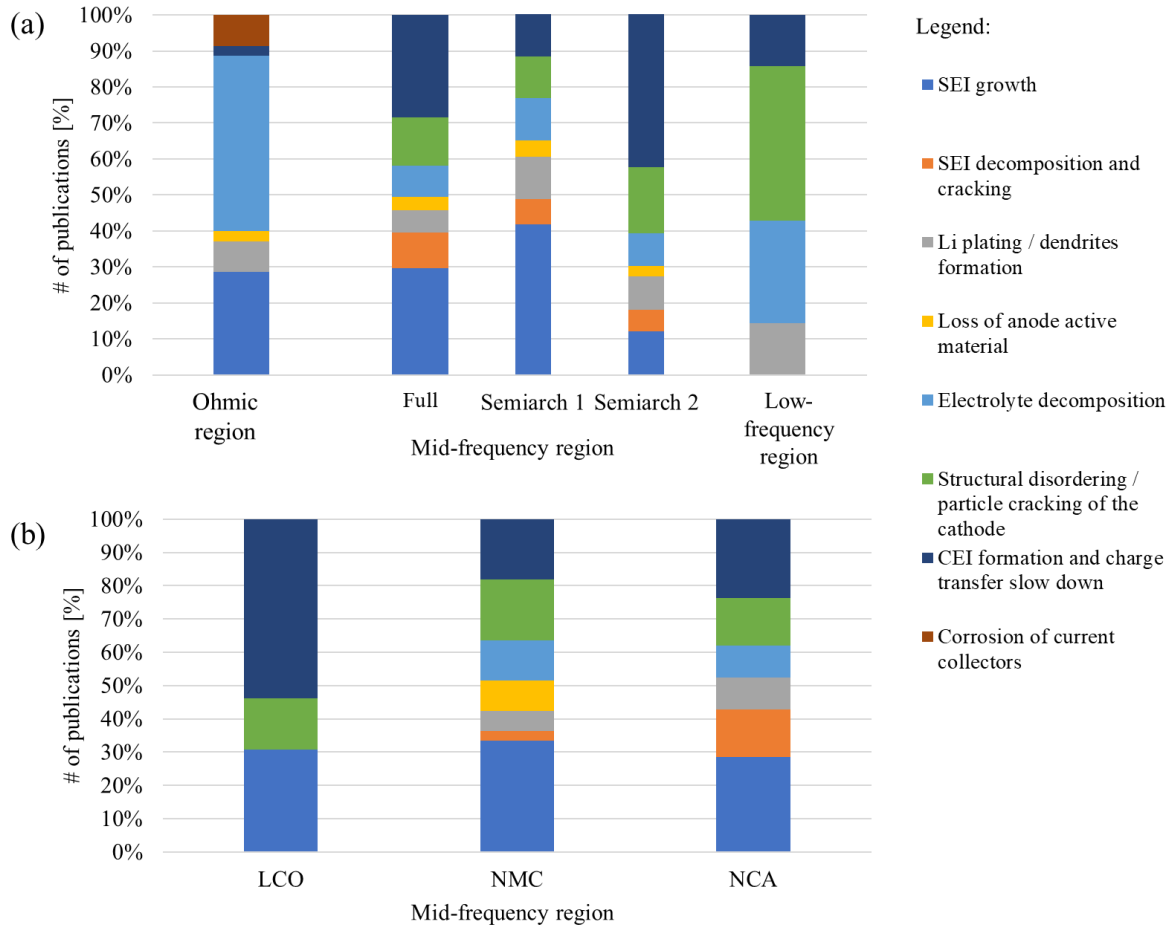


**Figure 2.9. Critical assessment of the connections among EIS spectra and degradation mechanisms given in Section 2.4. . (a) Distribution of the degradation mechanisms in the three regions of the impedance curve; the Mid-frequency region includes the details on the different contributions of the two semiarches. (b) Distribution of the degradation mechanisms in the Mid-frequency region for LCO, NMC and NCA cathode cells. The results are normalized on the total number of cases per each region given in Table 2.4.**

If one would like to separately analyse the main findings for the different chemistry, Figure 2.9-b presents the distribution of degradation mechanisms for LCO, NMC and NCA cells in the Mid-frequency region (the remaining cathode chemistries have been neglected due to few available publications).

- In LCO cells, the impedance rise is mainly addressed to the degradation of the cathode, with the formation of CEI and structural degradation/cracking. In a smaller number of cases the impedance rise is attributed to the anode passivation layer growth.

- In NMC cells, the distribution of degradation mechanisms is very similar to the general distribution showed in Figure 2.9-a. Lithium plating, electrolyte decomposition, SEI layer growth and decomposition account for 64% of the cases; the remaining share is attributed to loss of active material in the anode and in the cathode. The separation of contribution between the first and the second semiarch shows respectively prevalence of SEI and anode related degradation in the first area and cathode related degradation in the second area.
- NCA cells show similar results with respect to NMC cells. However, it is peculiar the observation of SEI layer decomposition, not present in the other cases.

Finally, Figure 2.10 analyses the findings of Section 2.5 by showing how different circuital elements have been assigned to the different EIS characteristic regions to build ECMs. These elements have been analysed in the Mid- and Low-frequency regions; the Ohmic region is always modelled with a resistor.

- The resistive-capacitive behaviour observable in the Mid-frequency region of the impedance curve have been mainly described with 2 elements:
  1. RC element: it is the simplest element that can be used in this region, describing a perfect semicircle; it has been chosen in 31% of the cases under review.
  2. Zarc element: it has the advantage to reproduce the depression of the semicircles and it has been chosen in 51% of the cases. Its disadvantage is the absence of Laplace transformation that make its use in time domain models problematic [121].
- These two elements are used without big distinctions in both the two semiarches. It is remarkable the exploitation of other elements to describe the 2<sup>nd</sup> semiarch region, mostly assigned to cathode-related processes. Specifically:
  1. HN element has been used in 6% of the cases, allowing to a similar description of depressed semicircle as the Zarc element.
  2. CPE has been used in 6% of the cases to specifically describe the diffusion processes that are usually attributed to Low-frequency region.
  3. TLM and composite electrode models have been exploited in 9%; the choice is justified assuming that the impedance curve is related to the cathode in that specific area [67], [42], [88].

## 2. Background analysis: on the use of EIS to characterize and model Li-ion cells aging

- The diffusion processes observable in the Low-frequency region have been mainly described with two elements. However, these elements present different placement in the ECM. Specifically:
  1. CPE is used in 26% of the cases. It has mainly been placed in series to the other elements, such as in [41], [97], [52], [93], and [101]. Another solution has been to place it on the resistive branch of RC or of Zarc elements, such as in [65] and [43].
  2. Warburg element is applied in 59% of the cases. As described in Section 2.5., this is a more complex solution to describe the diffusive processes, with different structure depending on the boundary condition chosen for the specific problem [114]. This element has been placed on the resistive branch of RC and Zarc, such as in [41], [51] and [63]. More complex configurations have been exploited in [66], [69] and [83].
- A smaller number of publications exploited the Zarc element to describe the diffusive processes (7% of the cases). A specific mention is needed to the small number of works (another 7% of the cases) that exploited a capacitor in this region: this element is used to describe the intercalation process, that, has already mentioned, represents the accumulation and depletion of lithium ions within the cathode. So that, in passive electrical model the charge stored in this capacitor is assumed to be the charge stored in the battery [122], [123].

If one would like to separately analyse the main findings for the different chemistry, Figure 2.10-b presents the distribution of circuital elements used to describe the Mid-frequency region for LCO, NMC and NCA cells (as before, the remaining cathode chemistries have been neglected due to few available publications).

- In LCO cells the most used element is RC (57% of the cases); it is used singularly to describe a semiarch or in a series chain up to 3 elements. Increasing the number of RC elements in series is a way of improving the quality of the approximation [81].
- In NMC cells the most used element is Zarc (60% of the cases). It is dominant in the first semiarch area and less used in the second semiarch, where other solutions have been applied. A specific mention is needed for CPE, used in 10% of the reviewed articles. This element is not used to model the electrodes but for the diffusion

processes occurring at low frequency. This is the case in [89], where the Low-frequency region is not measured and the EIS is truncated at 0.1 Hz.

- NCA cells shows a prevalence of the elements able to describe depressed semicircles: Zarc element and HN element exploited respectively in 50% and 17% of the cases. In the remaining cases, RC elements have been chosen.

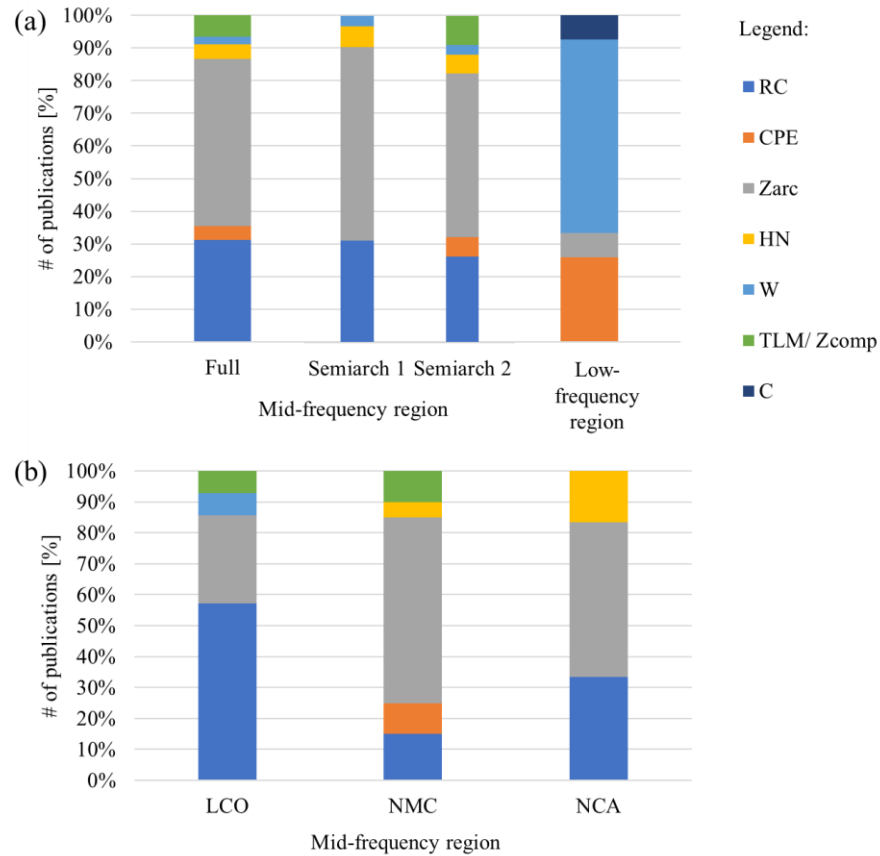


**Figure 2.10. Critical assessment of the connections among EIS spectra and circuital elements given in Section 2.5..** (a) Use of ECM elements to model the different regions of the impedance curve. The ohmic region is neglected because it is always modelled with a simple resistance; the Mid-frequency region includes the details on the different contributions of the two semiarches. (b) Use of specific ECM elements to model the impedance curve in the Mid-frequency region for LCO, NMC and NCA cathode chemistry cells. The results are normalized on the total number of cases recorded for each region given in Table 2.5.

By cross-referencing the information collected in Figure 2.9 and in Figure 2.10, one can now infer which is the most occurring degradation mode in each specific region of the EIS spectrum and which is the most used circuital element to model it. The results are showed in Table 2.6.

## 2. Background analysis: on the use of EIS to characterize and model Li-ion cells aging

---

**Table 2.6. Assessment of the review works.** Outcomes of the analysis of Section 2.4. and Section 2.5. by cross-referencing the information collected in Figure 2.9 and in Figure 2.10. The table shows the most occurring degradation modes and the most used circuital elements for each region of the EIS spectrum.

EIS region	Ohmic region	Mid-frequency region		Low-frequency region
<b>Degradation mode</b>	Loss of lithium inventory: 78%	Loss of lithium inventory: 54% Loss of cathode active material: 42%		Loss of cathode active material: 57%
		<b>Semiarch 1</b>	<b>Semiarch 2</b>	
		Loss of Lithium inventory + loss of anode active material: 78%	Loss of cathode active material: 61%	
<b>Circuital element for ECM</b>	Resistor: 100%	Zarc element: 50%		Warburg element: 59%
		<b>Semiarch 1</b>	<b>Semiarch 2</b>	
		Zarc element: 59%	Zarc element: 50%	

Specifically:

- Ohmic region: degradation is caused by Loss of Lithium Inventory (78% of the reviewed cases); the most occurring degradation mechanism is electrolyte decomposition. The effect is an increase of ohmic resistance and it is modelled in all the reviewed publications by a simple resistor.
- Mid-frequency region: the impedance rise is mainly caused by Loss of Lithium Inventory and Loss of Cathode Active Material, respectively in 54% and 42% of the cases. Looking at the two separated semiarches, the first one is related to loss of lithium ions (mainly SEI growth and SEI layer decomposition mechanisms) and Loss of Anode Active Material degradation modes in 78% of the cases. The second semiarch is related to Loss of Cathode Active Material in 61% of the cases, mainly due to CEI formation and electrode particle cracking. The most effective way to model the resistive-capacitive behaviour and the shape variations of the semiarches is using the Zarc element. It is applied in 51% of the reviewed articles and more specifically in 59% of the cases to describe the first semiarch and in 50% of the cases to describe the second semiarch. However, simple RC elements are more suitable when dealing with time domain models, thanks to their Laplace transformation.
- Low-frequency region: the impedance rise is caused by Loss of Cathode Active Material in 57% of the cases, mainly addressed to structural changes of the electrode

and charge transfer slow down. The attribution of this region to the cathode is strengthened by the presence of the intercalation process. The most effective way to model the diffusive tail is to use the Warburg element, exploited in the 59% of the reviewed publications.

Finally, Figure 2.11 summarises the main findings of this critical assessment. The typical EIS spectrum of a Li-ion cell is represented at the top, specifying the different frequency regions. For each of these regions, the most occurring degradation mechanisms (described in the previous paragraphs) are shown at the middle of the figure, grouped in the corresponding degradation modes. At the bottom of the figure, the most used ECM option is presented; the model includes a resistor for the Ohmic region, two Zarc elements for the Mid-frequency region (one element per each semiarc) and a Warburg element for the Low-frequency region.

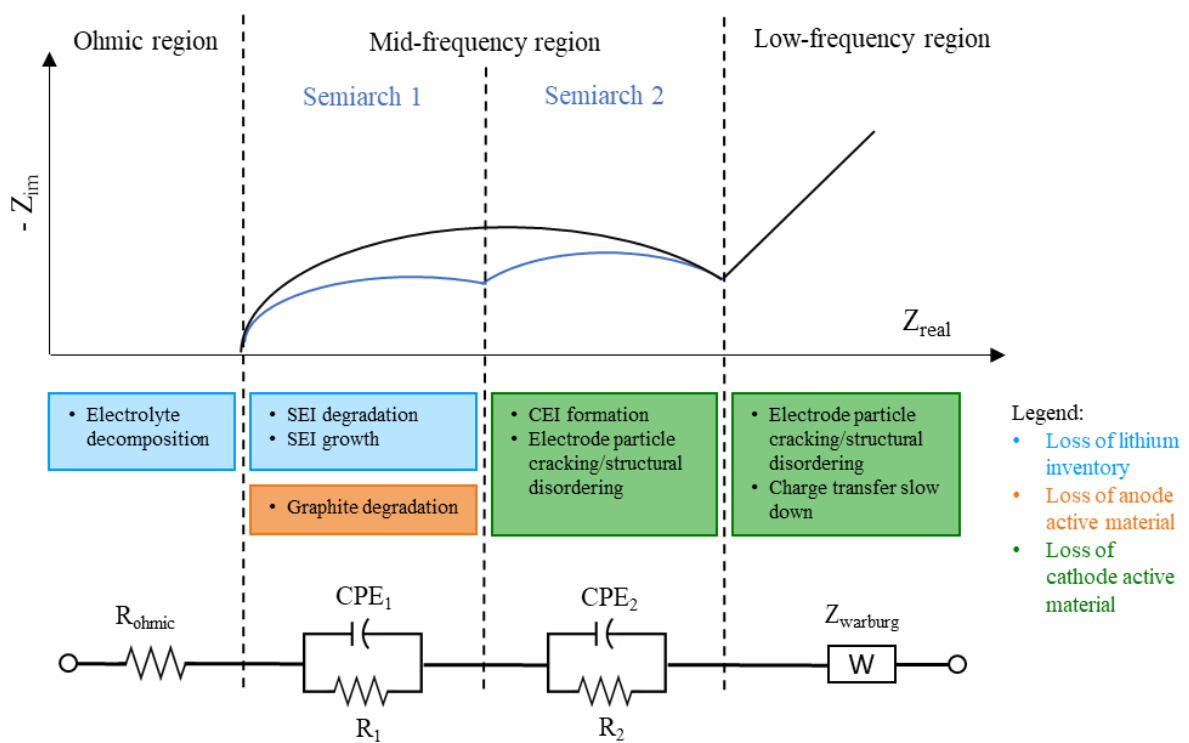


**Figure 2.11. Outcome of the critical review.** Representation of the typical EIS spectrum of a Li-ion cell specifying the most occurring degradation mechanisms and the related circuital element used to describe and model each region of the curve.

## 2.7. Final remarks

This Chapter presented a comprehensive review on the use of Electrochemical Impedance Spectroscopy (EIS) to characterize Li-ion battery degradation phenomena and to model them through Electric Circuit Models (ECMs). The review process allowed to highlight three main aspects: (i) the existence of links between the cell application (i.e. experimental parameters) and their impacts on the EIS spectra, presented in Section 2.3; (ii) the existence of links between the EIS spectra variations and the underlying degradation mechanisms, presented in Section 2.4 and (iii) the existence of many options to build ECMs from EIS spectra, presented in Section 2.5. Finally, the critical assessment given in Section 2.6 allowed to formulate links between the degradation mechanisms and the most reliable options to model them.

As regards of point (i) – cell application, the EIS spectra showed clear impedance shifts in different frequency regions depending on the magnitude of the chosen parameters (T, DoD, C-rate, etc.). The EIS variations were more pronounced for cycling aged cells than calendar aged cells. The use of heavy calendar or cycling aging conditions (e.g. high temperature, high current rate) led to accelerated degradation which can be easily sensed via EIS.

As regards of point (ii) – cell characterization, the observed EIS variations have been attributed to specific degradation mechanisms for each characteristic frequency region. Specifically, electrolyte decomposition was associated to Ohmic region shift; anode degradation and SEI layer growth to shifts in the first semiarch of Mid-frequency region; CEI layer formation and cathode particle cracking to shifts in the second semiarch of Mid-frequency region and cathode structural disordering to shifts in the Low-frequency region. Minor differences have been found among the different cathode chemistries. Many studies used invasive techniques to properly attribute degradation mechanisms and validate EIS interpretation. Alternatively, an effective solution to improve the EIS interpretation is the application of DRT transformation. DRT allowed to understand how the behaviour of the cell evolves by tracking the time constants of the different processes.

As regards of point (iii) – cell modelling, many ECM options have been reviewed which were not strictly related to the cathode chemistry type. Specifically, in-series resistor is

usually used for the Ohmic region; one or two Zarc elements for the Mid-frequency region and Warburg element for the Low-frequency region. Most of the works used ECMs to fit the EIS measurements and to track the evolution of the degradation phenomena through the associated model's parameters. Few cases showed that the same modelling approaches can be implemented into BMS to improve the estimation of main battery indicators (i.e. SoC, SoH, etc.) or to enhance battery lifetime prediction.

In short, the results of this review work motivate the exploitation of EIS as a fast, non-invasive, and reliable characterisation tool which help in building cell's models able to track the main degradation phenomena. However, further studies and analyses are needed to reinforce the strength and reliability of this characterization method: an important role is played by the validation process via half-cell tests, three-electrodes tests and material characterization. The next Chapters will present the application of EIS to develop ECM of Li-ion cells (Chapter 3) and to investigate degradation mechanisms including a detailed validation process with half-cells and material characterization with imaging techniques (Chapter 4).



# Chapter 3

## EIS2MOD: DRT-based Modelling framework for Li-ion Cells

The correct assessment of battery states is essential to maximize battery pack performances while ensuring reliable and safe operation. This chapter introduces EIS2MOD, a novel modelling framework for Li-ion cells based on Distribution of Relaxation Times (DRT). A physically based Electric Circuit Model (ECM) is developed starting from Electrochemical Impedance Spectroscopy (EIS) and Open Circuit Voltage (OCV) measurements. DRT is applied to deconvolve the electrochemical phenomena from the EIS. The presented methodology is based on: i) DRT calculation from EIS, ii) DRT analysis for ECM configuration and iii) Model parameters extraction and fitting. The proposed framework is applied to large format Li-ion pouch cells, which are tested over the whole State of Charge (SoC) range and a wide temperature range (-10°C to 35°C). Different current profiles have been tested to validate the model, showing its high accuracy in reproducing the battery cell behaviour (e.g. RMSE on the battery terminals voltage lower than 1.50% for driving cycle simulations at variable temperature and SoC). An additional advantage of EIS2MOD is its light computational load thus offering an attractive framework for battery management system implementation.

The content of this chapter has been published in the IEEE Transactions on Industry Applications under the title “EIS2MOD: A DRT-Based Modeling Framework for Li-Ion Cells” [124].

### 3.1. Context

The correct assessment of Li-ion battery cell states is essential to maximize battery pack performances while ensuring reliable and safe operation [35]. For this purpose, voltage and current signals are sensed by the Battery Management System (BMS) and combined to estimate indicators such as the State of Charge (SoC), i.e. the fraction of cell's available capacity and the State of Health (SoH), i.e. the remaining capacity with respect to original one. The practical implementations adopted in BMS can be classified in three main groups [34], [38], [125], [126]: (i) *Coulomb Counting methods*, in which a simplified analytical representation of the battery (i.e. current integration) is used to compute the SoC and to update the SoH by referring to manufacturer's datasheets; (ii) *model-based estimation methods* in which battery cell models are used to infer about the SoC/SoH and online estimators or adaptive filters are used to account for measurements errors and correct deviations on the estimation; and (iii) *data-driven based methods* in which an input-output approach (i.e. black-box models) is used to develop estimators; typical examples of this approach are fuzzy controllers, neural networks and support vector machines.

The above solutions differentiates when it comes to evaluate the trade-off between accuracy and computational effort. For instance, coulomb counting methods are well suited when looking for low computational effort, but their simplicity comes at the expense of low accuracy. On the other side, data-driven based methods could give very accurate results but they require intensive computing and offline learning processes based on specific and high quality data in large quantity [127]. Between these two solutions, model-based approaches are mostly used in literature due to the interpretability of the models [127], and their capability to reflect the electrochemical characteristics of the cell [128], [129]. Among all possibilities, Electric Circuit Models (ECMs) show a good balance between accuracy and model complexity [128].

In ECMs the response of the battery at the two terminals is represented by a combination of circuit elements [130]. Model's configurations ranges from simple ones, where a voltage source and a resistor are used to simulate the Open Circuit Voltage (OCV) and total internal resistance of the cell, to more complex ones, where a chain of resistors and capacities is used to simulate the full dynamic behaviour of the cell [128]. In all cases, the model's parameters must be identified based on dedicated measurements.

Electrochemical Impedance Spectroscopy (EIS) is widely used for this purpose [33], [131]–[133]. As already highlighted in Chapter 2, EIS is a non-invasive technique that characterize the electrical properties of different material and their interfaces by means of low amplitude sinusoidal voltage or current excitation over a range of frequencies [114]. The most common approach to derive the ECM is to choose the series connection of elements according to the shape of the impedance curve and followed by a Nonlinear Least Square parameter fitting [100]. Therefore, the model derived by EIS is based on a-priori assumption about the circuit configuration: expertise on electrochemical processes is required to determine the type and number of elements necessary to simulate the cell behaviour [128], [134]. However, it is often difficult to interpret the impedance spectra: the overlapping of different processes in the same frequency range makes difficult the choice of adequate circuit elements [118]. Moreover, the model validation with respect to experimental measurements could lead to unnecessary over-parameterization [131], [135]. In ECMs the response of the battery at the two terminals is represented by a combination of circuit elements [130]. Model's configurations ranges from simple ones, where a voltage source and a resistor are used to simulate the Open Circuit Voltage (OCV) and total internal resistance of the cell, to more complex ones, where a chain of resistors and capacities is used to simulate the full dynamic behaviour of the cell [128]. In all cases, the model's parameters must be identified based on dedicated measurements. Electrochemical Impedance Spectroscopy (EIS) is widely used for this purpose [33], [131]–[133]. As already highlighted in Chapter 2, EIS is a non-invasive technique that characterize the electrical properties of different material and their interfaces by means of low amplitude sinusoidal voltage or current excitation over a range of frequencies [114]. The most common approach to derive the ECM is to choose the series connection of elements according to the shape of the impedance curve and followed by a Nonlinear Least Square parameter fitting [100]. Therefore, the model derived by EIS is based on a-priori assumption about the circuit configuration: expertise on electrochemical processes is required to determine the type and number of elements necessary to simulate the cell behaviour [128], [134]. However, it is often difficult to interpret the impedance spectra: the overlapping of different processes in the same frequency range makes difficult the choice of adequate circuit elements [118]. Moreover, the model validation with respect to

experimental measurements could lead to unnecessary over-parameterization [131], [135].

A way to overcome these issues is to apply the Distribution of Relaxation Times (DRT) method. DRT is a mathematical transformation that allows to find the time constants of the physical processes occurring inside an electrochemical system [135]. The EIS spectra are deconvoluted in the time domain making possible to distinguish major and minor polarization effects that are normally overlapped in the frequency domain. These effects are represented by peaks with different magnitude and time constants. Those peaks allow to a better visualization of the individual processes occurring in the system under investigation and provide direct access to their kinetic parameters [136]. In this way, DRT representation provides higher resolution than classical impedance representations such as Nyquist or Bode plot. This technique has been widely applied in literature. For instance, Sabet et al. investigated the DRT profiles of pristine and aged Lithium Nickel Cobalt Aluminum Oxide (NCA) and Lithium Nickel Manganese Cobalt Oxide (NMC) cells, respectively in [96] and in [137]. In both the cases, the authors were able to define the main processes occurring in the cells and to track the cell degradation by analysing the peaks variation of DRT profiles. The variation in position and magnitude of the DRT peaks has been also analysed in [85] and [80]. In both the two cases the authors computed DRT profiles from EIS at different temperatures for new and aged cells. As in the previous case, the analysis of DRT profiles has been used to detect degradation processes occurring in the cell. However, the same results were not used to develop a model of the cell under investigation. In [100], Illig developed a very detailed physically based model of Lithium Iron Phosphate (LFP) cells exploiting DRT profiles derived by EIS and time domain measurements. The model was based on dedicated lab-scale cells to identify separately the electrochemical loss processes of the anode and of the cathode and it was used to analyse and improve the electrodes' performances. Another approach related to modelling, is presented by Schmidt et al. in [138]. The authors introduce a procedure to develop ECMs of Li-ion cells from DRT derived by combination of EIS and pulsed test. The model validation is performed through simulation in the time domain at constant temperature. The number of circuit elements is defined by the user: the higher the number of elements, the higher the accuracy but also the computational effort. Thus, there

is no connection between the physical processes occurring in the cell and the circuit elements used to simulate its behaviour.

This chapter presents EIS2MOD, an extension of the work presented in [32]. EIS2MOD is a novel modelling framework based on DRT that goes automatically from EIS and OCV measurements to a complete battery model. DRT is applied to commercial Li-ion cells (and not only to lab-scale formats as in [100]) as an insightful tool to: (i) identify the physical processes occurring inside an electrochemical cell, and (ii) to model the detected processes by means of a physically-based ECM. By doing so, each circuit element has a clear physical meaning related to different processes, differently from the solution proposed in [138]. Moreover, as stated in Chapter 1, this modelling framework is an attractive option for BMS implementation since it offers a high model accuracy while keeping a low computational load and a simple implementation.

The chapter is structured as follows. Section 3.2 introduces the different steps of the novel methodology, from DRT calculation to ECM configuration, to parameters extraction and fitting. Section 3.3 details the description of the experimental tests on large format pouch cells and the model developed applying the novel methodology. The cell characterization has been performed over the whole SoC range at four different temperatures: -10°C, 5°C, 20°C and 35°C. Finally, Section 3.4 presents the results of the model validation with different current profiles at constant and variable temperature.

## 3.2. Methodology

The schematic representation of the methodology presented in this work is shown in Figure 3.1. It is divided in two main blocks: model development and model validation. The first block is the EIS2MOD modelling framework and includes three main steps: A) DRT calculation, B) DRT analysis for ECM configuration and, C) parameters extraction and fitting. The second block, i.e. the validation process, is necessary to benchmark the model and assess its performance compared to real cells' measurements. Three current profiles have been used to perform the model validation: full discharge at constant current rate, charging and discharging steps at different current rates and driving profile simulation derived by the dynamic discharge profiles for Battery Electrical Vehicles (BEV) from the international standard on performance testing of Li-ion cells for electric vehicles use

[139]. More details on the validation process and on the testing protocols will be given in Section 3.4.. In the following we detail the main steps of the model development block.

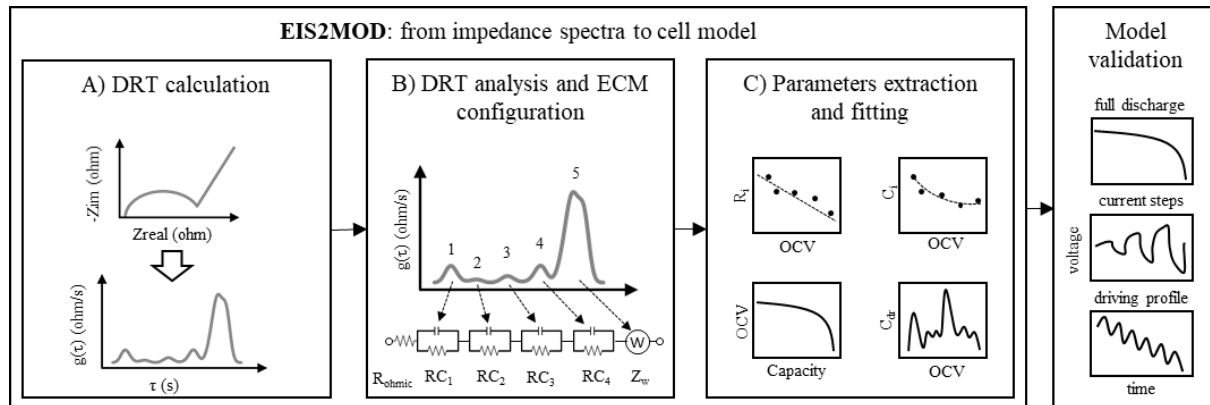


**Figure 3.1. Schematic representation of the methodology presented in this chapter.** The EIS2MOD modelling framework is based on three steps: A) the calculation of DRT profile from EIS spectrum; B) the analysis of DRT profile, attributing physical processes to different peaks and making the configuration of the ECM; C) the extraction and fitting (linear or quadratic) of parameters from DRT peaks and calculation of intercalation capacitance from the OCV curve. The model validation is performed with three different profiles: full discharge at constant rate, current steps at different rate and driving profile simulation derived by IEC 62660-1 [23].

#### 3.2.1. DRT calculation

The DRT method allows the deconvolution of EIS measurements into the multiple polarization processes occurring in an electrochemical system. The DRT function is normally depicted as  $g(\tau)$  and is plotted against the time constants axis (as shown in Figure 3.1) resulting in a profile with variable number of peaks that describe the properties of the studied system. The area below  $g(\tau)$  peaks represents the polarization resistance of the system under investigation. High quality measurement and time invariance are required to correctly apply the DRT method. A suitable tool to check the validity of the impedance spectra is to apply the Kramers-Kronig (KK) criterium [140]. DRT calculation can be performed when the residuals between measured and Kramers-Kronig reconstructed spectrum are below 1% [141], [142]. More insights on KK test are given in Appendix A.

Once linearity and time invariance are fulfilled, it is possible to represent the impedance as an infinite number of RC-elements in series with a resistor:

$$Z(j\omega) = R_{ohmic} + \int_0^{\infty} \frac{g(\tau)}{1+j\omega\tau} d\tau, \quad (3.1)$$

where  $R_{ohmic}$  represents the ohmic resistance and  $g(\tau)$  is the function that represents the time relaxation characteristics of the electrochemical system under evaluation and that satisfies the conditions of non-negativity (total and partial polarization resistances are positive for most of the electrochemical systems) [143]. The integral in (3.1) is often normalized, leading to:

$$Z(j\omega) = R_{ohmic} + R_{pol} \cdot \int_0^{\infty} \frac{\gamma(\tau)}{1+j\omega\tau} d\tau, \quad (3.2)$$

where  $R_{pol}$  represents the total polarization resistance and the term  $\gamma(\tau)/(1+j\omega\tau)$  represents the relative differential contribution of a single ohmic-capacitive element [142].

In practice, the integral equation in (3.2) is computed numerically as a finite sum of  $n$  RC-elements:

$$Z(j\omega) = R_{ohmic} + R_{pol} \cdot \sum_{k=1}^n \frac{\gamma(\tau_k)}{1+j\omega\tau_k}. \quad (3.3)$$

The discretization process brings to an intrinsic approximation error that is unavoidable but that can be reduced as much as possible by properly choosing the discretization basis [118], [144]. In [145] Wan et al. studied the effect of discretization methods on DRT calculation, applying piecewise linear functions and radial basis functions (RBFs). They demonstrated that RBFs have more advantages, such as faster convergence and validity overall the time constants domain, including the extension to non-measured points. The main findings of Wan et al. have been exploited in this work to apply RBFs for the problem discretization. The readers are referred to [145] for further details in the mathematical formulation.

Once discretization is applied, the DRT function can be estimated from the impedance measurement by posing a linear inverse problem and solving the following optimization problem:

$$\min_x \|Ax - b\|_2^2, \quad (3.4)$$

where  $\|\cdot\|_2^2$  denotes the Euclidean (L2) norm for vectors,  $x$  is an  $n$ -dimensional vector representing the unknown DRT function, evaluated at the set  $\{\tau_k\}_{k=1}^n$  of target time constants,  $b$  is an  $m$ -dimensional vector consisting of the measured impedance points at the frequency set  $\{\omega_i\}_{i=1}^m$ , and,  $A$  is an  $m \times n$  matrix whose  $A_{ik}$  elements represent the normalized RC elements for the measured frequency  $\omega_i$  and the target time constant  $\tau_k$  convolved with the RBFs (see [145]).

However, this inverse problem is intrinsically ill-posed [145]. A way to obtain a solution is to apply a numerical regularization. The most used method when applying DRT to Li-ion cells is Tikhonov regularization [108], [142], [143], [145].

The regularization is used to avoid false peaks and oscillations in the solution. The problem in (3.4) can be rewritten adding a regularization term:

$$\min_x \|Ax - b\|_2^2 + \lambda \cdot x^T M x, \quad (3.5)$$

where  $\lambda$  is the regularization coefficient and  $M$  is the regularization matrix. The regularization coefficient  $\lambda$  allows to have the best compromise between exactness of the solution and its stability. The choice of this parameter highly influences the final results; in literature three main criteria have been defined to find its optimal value: the real-imaginary part discrepancy test, the real-imaginary cross validation test and the L-curve criterion [146], [147]. The regularization matrix  $M$  is used to further improve the problem solution; in the simplest case it is defined as identity matrix. More details on the optimization problem and regularization matrix are given in [146], [148]. For the methodology presented in this work, the L-curve criterion has been chosen for the determination of  $\lambda$  (more details in Appendix A) and a term proportional to the second derivative of the  $\gamma(\tau)$  function has been chosen for the penalty term  $x^T M x$ .

As stated before, the DRT method works well with ohmic-capacitive electrochemical system. However the inductive behaviour at high frequencies and diffusive behaviour at low frequencies of Li-ion cells could bring to artefacts in DRT calculation [142]. In both cases, the simplest solution is to truncate the measurement analysing only the pure ohmic-capacitive part of the spectrum. However, this method leads to lose of valuable information [149]. A second way to proceed is to subtract the inductive contribution from the measurement and to extend the vector of time constants used in DRT calculation. The

inductance correction is performed fitting the high frequency part of EIS spectrum with an inductor or with a parallel connection of inductor and resistor [149]. A practical example with the EIS measurements of the cell under investigation is given in Appendix A. Regarding the diverging tail of the spectrum at low frequency, a used practice is to extend the vector of time constants beyond the minimum and maximum values that corresponds to the minimum and maximum measured frequency points. With this approach there is no extrapolation of EIS points beyond the measured frequency range and the optimization process brings to a stable solution [142].

### 3.2.2. DRT analysis: ECM configuration

For a full mapping of the cell behaviour, the DRT calculation must be applied to EIS measurements at different SoC (i.e. different OCVs). Once the DRT profiles have been obtained, it is possible to configure the ECM. The configuration is done by analysing the different peaks of the function  $g(\tau)$  that can be associated to the physical processes occurring inside the Li-ion cell. In literature, several works analysed the time constants range and DRT profiles, allocating four main types of processes [80], [90], [142], [150]–[152]:

- Time constant lower than  $10^{-3}$ s: particle-particle or particle-current collector interfaces contact resistance. The peculiarity of the peak in this region is its invariance with respect to the SoC of the cell and a small variation due to temperature changes.
- Time constant in the range  $10^{-3}$ - $10^{-2}$ s: the peak represents the transport of Li ions through the SEI layer. There is no a specific variation of the peak linked to the SoC of the cell. However, this peak is sensitive to temperature changes, showing a shift to the right side and an increase in magnitude for low temperatures.
- Time constant in the range  $10^{-2}$ - $10^1$ s: charge transfer in the two electrodes: usually two or more peaks are present. In general, the peaks related to the cathode have higher impact (i.e. larger peak) at low SoC, while the ones related to the anode have higher impact at high SoC. At low temperatures charge transfer processes are slowed down due to lower ionic conductivity of the electrolyte and the DRT peaks increase their magnitude. The distinction and position of the peaks within the time constant range depends mainly on the cathode chemistry.

- Time constant higher than  $10^1$ s: diffusive processes. As in the previous case, the peak related to diffusive processes is highly impacted by SoC, depending on the concentration of solid active particles. At low temperatures the diffusivity of ions within the electrodes is reduced and the impedance is higher, implying higher magnitude of the DRT peak.

The allocation of the physical processes and the total number of peaks give a hint on the number of circuit elements that should be adopted in the ECM. For instance, the 5 peaks represented in the DRT profile of Figure 3.1 lead to a model including 5 elements. The model can be developed adopting RC branches, given the capacitive-resistive nature of the processes described by the DRT. The main advantages using these simple elements are that the parameters can be calculated from the DRT profile and the direct applicability of the developed model in time-domain simulations. However, in the case of diffusive processes, i.e. at high time constant, the use of a simple RC branch leads to high residuals between the measured and the estimated impedance spectrum. One possible solution to overcome this limitation is to introduce a Warburg element in the model. In the literature, Boukamp et al. demonstrated how the DRT of finite length Warburg element can be derived [153]. This element is represented by a large peak with a high time constant and a series of smaller peaks for decreasing values of time constants that present a defined spacing. This derivation has been exploited in [147], [149] to characterize the peaks related to diffusive processes of the cells under investigation. The authors proved that the time constants of the peaks related to diffusion were compliant with relationship derived in the [153]. In this work a different approach has been chosen. In the frequency domain, the Warburg element with reflective boundary condition can be written as function of the limiting factors  $R_{D,R}$  and  $C_{D,R}$  [128]:

$$Z_W(j\omega) = \frac{3 \cdot R_{D,R} \cdot \coth \sqrt{3 \cdot j\omega \cdot R_{D,R} \cdot C_{D,R}}}{\sqrt{3 \cdot j\omega \cdot R_{D,R} \cdot C_{D,R}}} \quad (3.6)$$

The resistance value  $R_{D,R}$  is obtained from the DRT profile, in the region where the time constant is higher than  $10^1$ s. The value of the capacitor  $C_{D,R}$  instead, is obtained by differentiation of the OCV curve, as shown in the following equation:

$$C_{D,R} (OCV) = dQ/dV. \quad (3.7)$$

This parameter, known as the intercalation capacitance, represents the equivalent capacitance of the cell at a specific OCV value. The correspondence between the value of  $C_{D,R}$  obtained by OCV differentiation and from EIS measurements at very low frequency have been verified by Brivio et al. in [128]. In this way, the characterization of the cell becomes shorter, avoiding too long impedance measurements or time domain measurements. Another advantage is also on the testing side: it is not necessary to have sophisticated and expensive testing equipment that reach ultra-low frequency values.

Given the objective of developing a time domain model, it is possible to anti-transform the expression in (3.6) and approximate the Warburg element as a series connection of a capacitor  $C_{D,R}$  and an infinite number of RC elements with parameters [154]:

$$C_{n,R} = C_{D,R}/2 \quad \text{and} \quad R_{n,R} = 6 \cdot R_{D,R}/(n^2 \cdot \pi^2), \quad (3.8)$$

where  $n$  represents the  $n$ -th element.

The infinite series of RC branches can be limited to a finite number with a negligible effect on the model performances and accuracy [155]. Exploiting the experimental results of [128], in this work we adopted 5 RC branches to describe the Warburg element.

Summarizing all the considerations above, the ECM model for a cell showing  $n$  peaks in the DRT profile includes:

- A resistor for the ohmic resistance.
- $n - 1$  RC branches to model contact resistance, SEI layer, charge transfer and double layer effects.
- Series connection of a capacitor and 5 RC elements to approximate the Warburg element exploited to model the diffusion phenomena.

The voltage drop across the capacitor  $C_{D,R}$  is used to estimate the OCV value of the model and no voltage generator is needed (i.e. passive electrical model). In turn, the OCV value is used to estimate the SoC of the cell, through the OCV-SoC relationship. This relationship is derived from the OCV curve, computing the SoC as fraction of the whole discharged capacity.

The model can be implemented as a linear system with time-varying parameters that are function of the OCV/SoC [32]. These parameters account for the non-linearities related to

the battery dynamic and allow for a simple model implementation. The state space representation of the model is:

$$\begin{aligned} x(k) &= A_k x(k-1) + B_k u(k), \\ y(k) &= C_k x(k) + D_k u(k), \end{aligned} \quad (3.9)$$

where the state vector  $x(k)$  is defined as:

$$x(k) = \begin{bmatrix} V_{oc}(k) \\ V_1(k) \\ \vdots \\ V_n(k) \end{bmatrix}, \quad (3.10)$$

with  $V_{oc}$  denoting the OCV and  $V_i$  the voltage of the  $i$ -th RC element. The input  $u(k)$  is the current and the observation  $y(k)$  is the voltage at the battery terminals at discrete time  $k$ . The state transition matrix at time  $k$  is defined as:

$$A_k = \begin{bmatrix} 1 & 0 & \cdots & 0 \\ 0 & e^{-\frac{T_s}{R_1(k)C_1(k)}} & 0 & 0 \\ \vdots & 0 & \ddots & \vdots \\ 0 & 0 & \cdots & e^{-\frac{T_s}{R_n(k)C_n(k)}} \end{bmatrix} \quad (3.11)$$

and the input matrix is defined as:

$$B_k = \begin{bmatrix} \frac{T_s}{C_d(k)} \\ R_1(k) \left[ 1 - e^{-\frac{T_s}{R_1(k)C_1(k)}} \right] \\ \vdots \\ R_n(k) \left[ 1 - e^{-\frac{T_s}{R_n(k)C_n(k)}} \right] \end{bmatrix}. \quad (3.12)$$

The output matrix  $C_k$  is a vector of ones and the feedforward matrix  $D_k$  is the ohmic resistance.

### 3.2.3. Parameters extraction and fitting

The parameters needed for the ECM presented in Section 3.2.2 are extracted from the EIS measurement, the DRT profile and the OCV curve.

The ohmic resistance is directly extracted from the EIS curve, looking at the zero-crossing value of the impedance with respect to the real axis in the Nyquist plot. As regard the RC elements, as already mentioned the parameters are extracted by the DRT profile. For the  $i^{th}$  peak, the position of its maximum gives the value of the time constant  $\tau_i$  and its area gives the value of resistance  $R_i$ . The value of capacitance is simply computed as:

$$C_i = \tau_i / R_i \quad (3.13)$$

A specific algorithm has been developed to improve the estimation of the parameters extracted by the DRT. The algorithm identifies the number of peaks which are present in the DRT profile and performs a fitting with a variable number of gaussian distributions. This number mainly depends on the number of peaks. The main advantage of the algorithm is the ability to distinguish processes also when the peaks are partially overlapped. However, a cross check between the algorithm outcome and the physical processes described in the previous paragraph is always required to ensure that the correct number of peaks is considered. This topic will be addressed in Chapter 4.

Once all the parameters are extracted at different SoC values (i.e. OCV values), it is possible to fit them to obtain the parameters trends. An example for  $R_i$  and  $C_i$  is showed in step C of Figure 3.1, respectively with linear and quadratic fitting. The functions obtained are then used by the model during simulations. The only exception is the intercalation capacitance. Its trend is extracted by exploiting (3.7) as shown in the lower part of step C of Figure 3.1. Given the high non-linearity of this parameter, a look-up table is used by the model.

To extend the model validity to different environmental conditions, it is possible to characterize the cell at different temperatures. In this way, the model will include different sets of parameters at given temperatures. When simulating profiles at variable temperature, linear fitting allows to estimate the model parameters over a continuous temperature range between the tested values.

### 3.3. Proposed ECM for Li-ion NMC cells

The methodology presented in Section 3.23.2. has been applied to large format NMC pouch cells [156]. The nominal capacity is 55Ah, the nominal voltage is 3.7V and the

voltage range is between 3V and 4.2V. Cell's datasheet is available in Appendix D. To develop a generalized model of the battery model under investigation, the characterization tests have been performed on three identical cells. Then, the collected results have been used to calculate the averaged impedance spectra and OCV curves that have been exploited for the model development.

The characterization tests have been performed at the CSEM Sustainable Energy Center, located in Neuchâtel, Switzerland, using the following equipment:

- Cell cycler BioLogic BCS815 [157]: battery tester equipped with 32 parallel, 9V-15A channels.  $\pm 0.01\%$  FSD accuracy on the voltage and  $\pm 0.015\%$  FSD accuracy on current, for each available range. EIS capability from 10kHz to 10mHz.
- Thermostatic chamber (ATT-DM1200T [158]) with -45°C/180°C temperature range and a volume of 1200 L.

Experiments run at different ambient temperatures: -10°C, 5°C, 20°C and 35°C. A resting phase of 10h has been fixed before the start of the characterization to stabilize the cell temperature. Then, a two steps procedure has been applied:

- Full charge-discharge cycle at C/10 to obtain the OCV curve;
- EIS spectra acquisition at 0%, 25%, 50%, 75% and 100% SoC in the 10mHz-10kHz frequency range (1h rest between the SoC adjustment and the spectrum acquisition).

The OCV protocol has been chosen as an optimal trade-off to reduce the testing time at minimum when compared with longer protocols such as GITT. The OCV curve has been then used to determine the voltage levels corresponding to the chosen SoCs at which the EIS measurements have been run. Looking at test duration, the two steps characterization procedure lasted 44h. The full characterization of the cells at four temperatures has been performed within 10 days.

The data analyses have been performed with dedicated Python scripts, as well as the different steps of the methodology showed in Figure 3.1 and described in Section 3.2.; all the scripts are available in a specific repository [159]. All the EIS measurements have been pre-processed to correct the inductive behaviour with a parallel circuit of a resistor and an inductor. The L-curve criteria has been applied to define the regularization parameter that has been fixed to  $10^{-5}$  (Figure A.3in Appendix A).

The DRT calculation results are shown in Figure 3.2: on the left side the DRT profiles at 20°C and different SoC are presented; on the right side the profiles at 50% SoC and different temperature are presented. The numbering under the peaks helps the reader to check the correspondence between the two charts. As stated in Section 3.2., it is possible to link the peaks to the processes occurring in the cell. Peak 1 has negligible variations with respect to the SoC and show a small increase in magnitude decreasing the temperature; it is attributed to particle-particle and particle-current collector contact resistances. All the other peaks instead, show large variations with temperature, with a rise of polarization resistance at low temperatures. This effect is due to the slower reaction rates and diffusion rates. Peak 2 is attributed to the transport of ions through the SEI layer, with small variations varying the SoC. Peak 6 shows large variations at low SoC and it is attributed to the slower diffusion of ions within the electrodes. The remaining three peaks (i.e. number 3,4 and 5) show a large rise at low SoC: this is due to the slower rate of charge transfer processes of the two electrodes. Peak 4 shows the largest variations among the three peaks and at low SoC. For this reason, this peak is attributed to the cathodic charge transfer [80]. More precise information about the attribution of peaks 3 and 5 could be given by measuring EIS spectra of three-electrodes cells or half cells [90], [137]. DRT peak attribution and validation will be presented in Chapter 4.

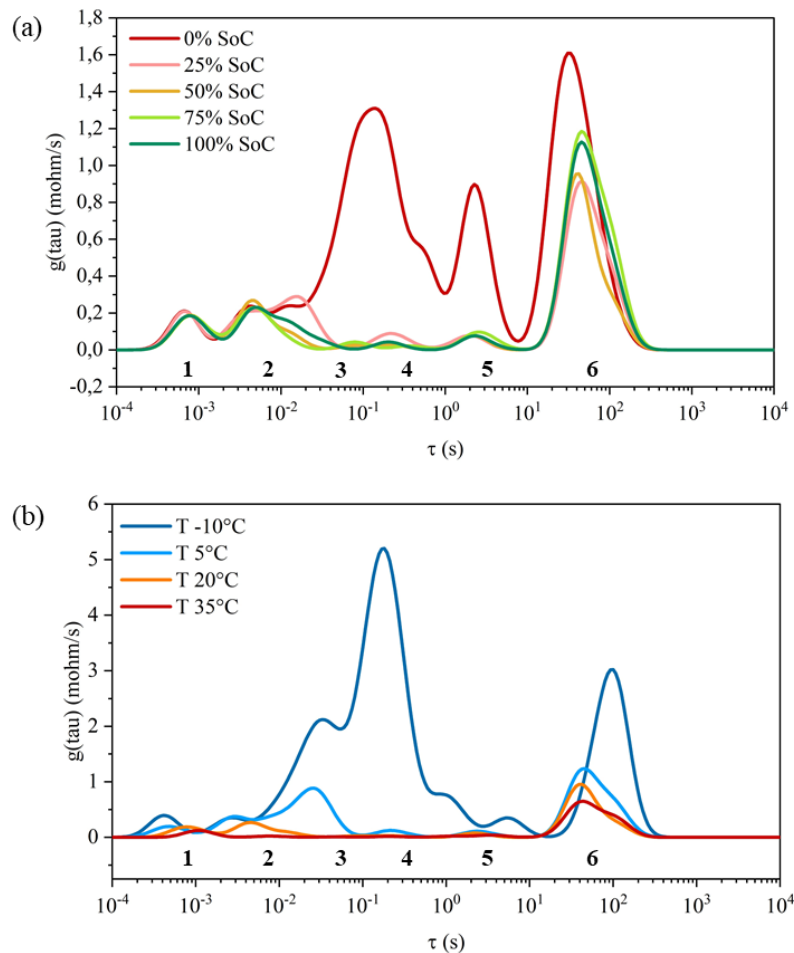


**Figure 3.2. DRT profiles of the large format pouch NMC cell under investigation.** a) DRT profiles at 20°C and different SoC levels; b) DRT profiles at 50% SoC and different SoC levels. At different SoCs and temperatures the cell shows 6 peaks corresponding to: 1) particle-particle, particle-current collector interface; 2) SEI layer; 3-4-5) charge transfer processes; 6) diffusive processes.

Once the peak attribution has been performed, it is possible to proceed with the ECM configuration. The model developed for the cell under investigation is showed in Figure 3.3 and it includes 12 elements with a total number of 13 independent parameters:

- A resistor to model the ohmic resistance;
- 1 RC element to represent the particle-particle, particle-current collector interface (peak 1);
- 1 RC element to represent the SEI layer (peak 2);
- 3 RC elements to represent the charge transfer processes (peaks 3, 4, 5);

- 5 RC elements in series with a capacitor ( $C_{D,R}$ ) to approximate the Warburg element representing the diffusive processes (peak 6).

As anticipated in Section 3.2., the voltage drop across the capacitor  $C_{D,R}$  is used to estimate the OCV value and in turn the SoC. The OCV of the cell is initialized by the user with a fixed value (the actual SoC of the cell or an estimate of it) and then it is updated at each step of simulation calculating the state vector  $x(k)$  defined in (10). The OCV curve (i.e. OCV-SoC relationship) and  $C_{D,R}$  profiles at different temperatures are showed in Figure 3.4. The SoC has been calculated as fraction of the discharged capacity at C/10 per each different temperature. Analysing the OCV curves (Figure 3.4-a), given a SoC value the corresponding voltage is higher for lower temperatures.

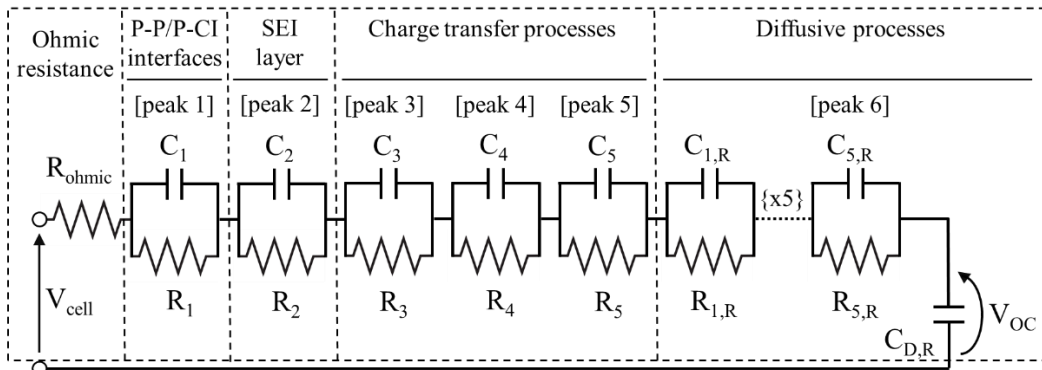


**Figure 3.3. ECM developed for the large format pouch NMC cell under investigation.** The different elements are referred to the modelled physical process and to the related DRT peaks in Figure 3.2.

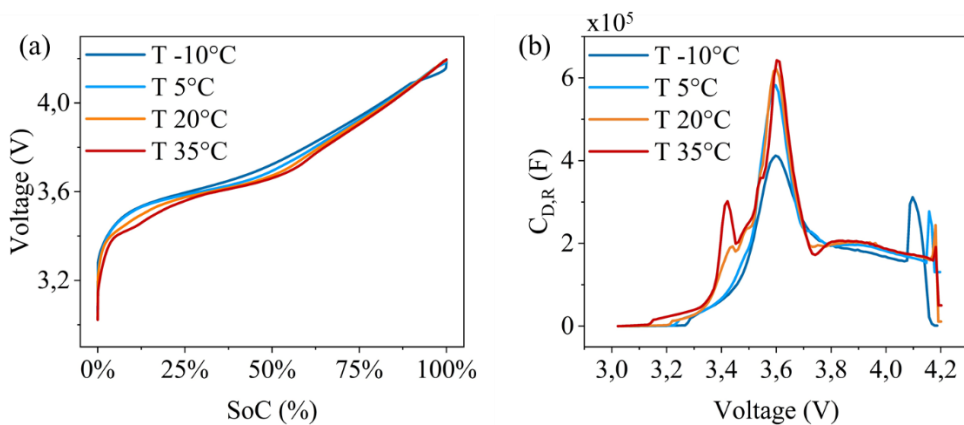


**Figure 3.4. Voltage-based parameters.** a) OCV curves of the averaged cell at different temperatures. b) Intercalation capacitance  $C_{D,R}$  as function of the voltage obtained from the OCV curves in a) at different temperatures.

This effect is due to the slower cell kinetic at low temperature, and it results in steep voltage variation for SoC lower than 10%. Consequently, the discharged capacity is lower than at ambient conditions. On the contrary, the OCV curve at 35°C presents an additional small plateau region around 10% SoC allowing for a slightly higher value of discharge capacity. The differences between OCV curves reflect also in Figure 3.4-b, where the  $C_{D,R}$  parameter is investigated. At voltages below 3.4V, the curves at 20°C and 35°C present a peak that is absent in the curves at lower temperatures. At voltages above 4.1V instead, there is a peak with larger magnitude only at lower temperature. Figure 3.4-b is also a practical tool to visualize the capacity variation of the due to temperature: the smaller the area under the  $C_{D,R}$  curve, the lower the available capacity of the cell. The ohmic resistance from EIS and the parameters extracted by analysing the DRT profiles in Figure 3.2 are presented in Figure 3.5. With lower or higher spread depending on the temperature level, the three tested cells show similar behaviours for all the resistive parameters but slightly different magnitudes. Overall, there is a resistance rise with decreasing temperatures. The ohmic resistance shows a linear trend over the tested OCV range. The spread of measurements around the depicted trend is mainly attributed to the contact between the cell tabs and the holder connected to the cycler. This difference is not affecting all the other parameters given that the ohmic resistance is not part of the  $g(\tau)$ . The parameter  $R_1$  represents the contact resistance and it is characterized by negligible variations over the tested OCV range.  $R_2$  is related to the SEI layer and shows well distinct trends at 35°C and 20°C. At lower temperature instead, there is a less clear pattern. The parameters  $R_3$ ,  $R_4$  and  $R_5$  are related to charge transfer and show a large increase in resistance at low OCV for all temperatures. Moreover,  $R_3$  and  $R_4$  show similar values at mid- and high temperatures and much higher values at low and very low temperatures. As regards the diffusive processes,  $R_6$  shows similar quadratic behaviour at different temperatures, with higher magnitude at low and high voltages and a minimum around 3.9V.

The parameters' trends shown in Figure 3.5 have been given as inputs for the model simulations. As mentioned in Section 3.2.3, when dealing with variable temperature simulations, the parameters' estimation over a continuous temperature range is performed with linear fitting between the two closest characterized values.

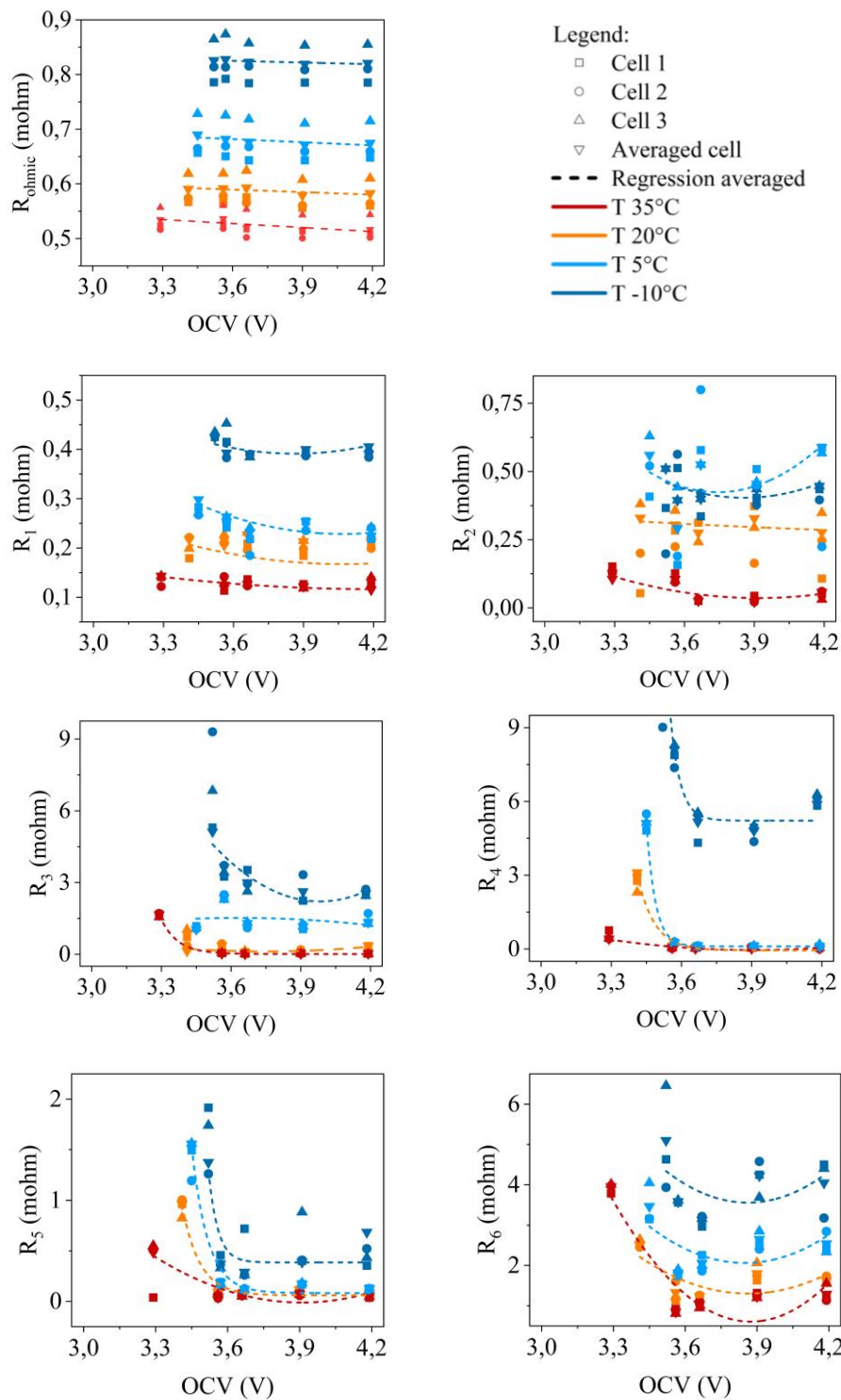


**Figure 3.5. Resistance parameters of the cell under investigation.** Resistance parameters extracted by the DRT and ohmic resistance as function of the OCV of the three cells under testing and of the averaged cell representing them. The four temperatures are represented by the different colours. The dashed lines represent the linear or quadratic fitting used to describe the trend.

### 3.4. Validation results

The model developed in Section 3.3 has been validated with time domain simulations. Three types of current profiles have been tested: dynamic profile (i.e. current steps), full discharge and driving profile. These profiles have been applied at the four temperature levels chosen for cell characterization (i.e. -10°C, 5°C, 20°C and 35°C). Moreover, the driving profile has been also applied under variable temperature conditions to simulate different seasons. The details about the testing protocols and the tests results will be given in the next paragraphs.

#### 3.4.1. Dynamic profile

The dynamic testing profile has been performed with a repetition of 4 steps sequence including rest, discharging, rest and charging phases. The duration of each step has been fixed to 5 minutes. Four C-rates have been applied: C/10, C/5, C/2 and 1C. The obtained current profile is showed in Figure 3.6-a. The measured and simulated voltage profiles at 35°C, 20°C, 5°C and -10°C are showed respectively in Figure 3.6-b, c, d and e. The profile at -10°C has been performed only up to C/2 as indicated in the cell datasheet [156]. In general, the model is able to simulate the cell dynamics in the full range of currents and temperatures. It shows a good level of accuracy at 20°C and 35°C: the absolute RMSE values are lower than 10mV at 50% and 75% SoC (Table 3.1). At lower SoC, the maximum error is 17 mV at 20°C. Considering lower temperatures, additional non-linearities occur in the cell behaviour due to slower dynamic, impacting the model accuracy. At -10°C and 25% SoC, the dynamic profile simulation showed 64.26mV of absolute error (5.35% with respect to the voltage interval). This is the maximum error registered over the 12 run simulations.

#### 3.4.2. Full discharge profile

The full discharge tests have been performed at the four defined temperatures with a constant rate of C/10. In addition, higher current rates have been analysed at 20°C: C/5, C/2 and 1C.

**Table 3.1.** Averaged RMSE errors of the dynamic and driving profiles at different SoCs and of the full discharge at 0.1C. The RMSE values are given as absolute value (mV) and as percentage of the voltage interval exploited by the cell (3-4.2V) at the four tested temperatures. At -10 ° C the dynamic profiles include only 3 current steps: C/10, C/5 and C/2 (depicted with \*).

Temp- erature	RMSE	Dynamic profile			Driving profile			Full discharge
		75% SoC	50% SoC	25% SoC	75% SoC	50% SoC	25% SoC	
35°C	absolute (mV)	6.46	6.07	14.35	2.70	1.47	3.64	9.84
	% of voltage interval	0.54%	0.51%	1.20%	0.22%	0.12%	0.30%	0.82%
20°C	absolute (mV)	5.99	8.86	16.56	2.72	2.44	6.03	17.54
	% of voltage interval	0.50%	0.74%	1.38%	0.23%	0.20%	0.50%	1.46%
5°C	absolute (mV)	12.93	20.26	35.05	5.20	7.00	22.56	38.23
	% of voltage interval	1.08%	1.69%	2.92%	0.43%	0.58%	1.88%	3.19%
-10°C	absolute (mV)	19.83*	41.07*	64.26*	32.26	41.31	19.18	35.21
	% of voltage interval	1.65%	3.42%	5.35%	2.69%	3.44%	1.60%	2.93%

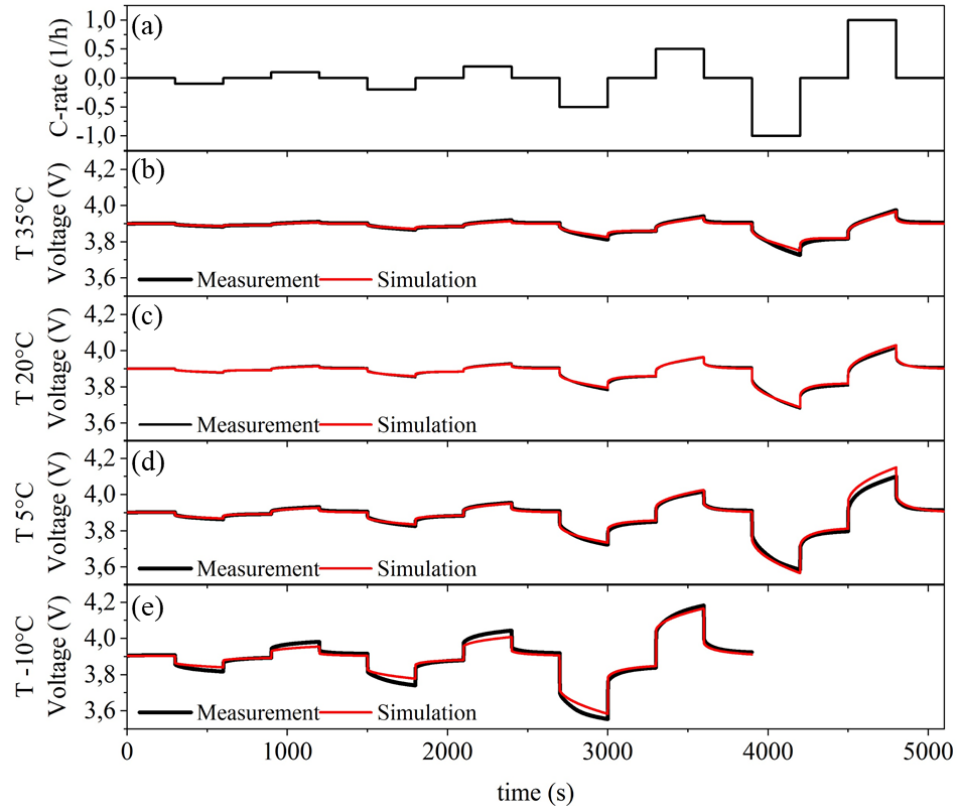


**Figure 3.6.** Dynamic test at four C-rates (C/10, C/5, C/2 and 1C) with 5 minutes steps of charge and discharge spaced by resting phase. a) Current profile. Measured and simulated voltage profiles at: b) 35°C; c) 20°C; d) 5°C and e) -10°C.

Looking at the results at C/10, the measured and simulated voltage profiles are shown in Figure 3.7. The main difference between the four temperatures is the duration of the test: the lower the temperature, the lower the test duration due to less available capacity. The model well approximates the cell behaviour over the whole voltage range, with the highest discordances at low voltage. The absolute RMSE shows its minimum at 35°C (9.84mV) and its maximum at 5°C (38.23mV).

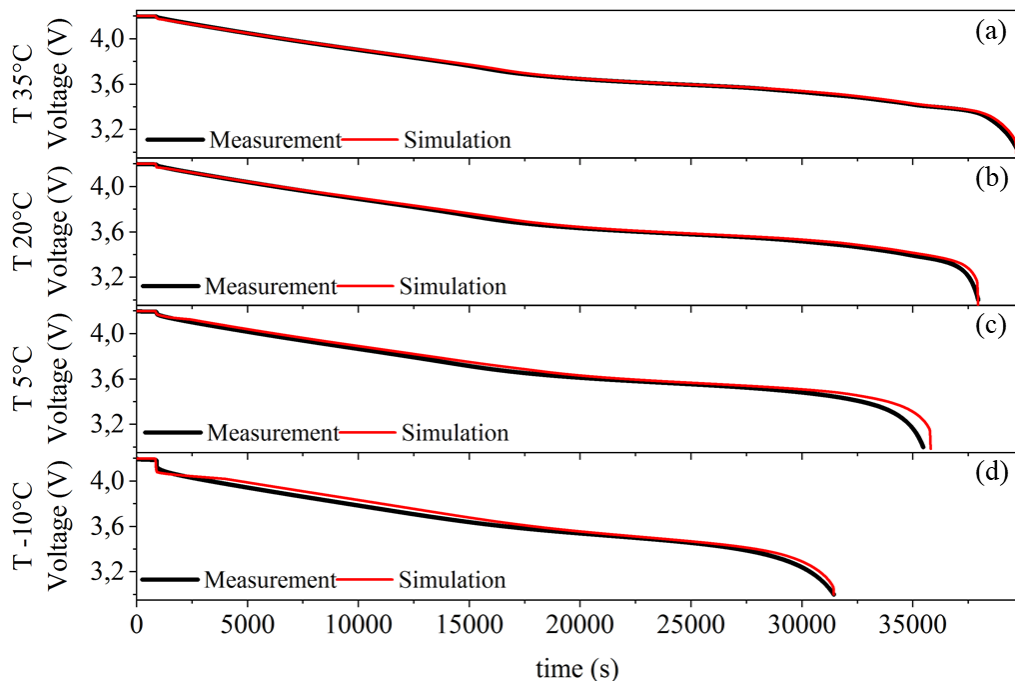


**Figure 3.7.** Full discharge tests at constant current rate of C/10. Measured and simulated voltage profiles at: a) 35°C; b) 20°C; c) 5°C and d) -10°C.

The validation results at 20°C and different rates are compared in Figure 3.8. The model shows good performances following the voltage trend of the real cell. The RMSE values are listed in Table 3.2: the error is lower than 3% (i.e. 36mV) up to C/2 and shows its maximum at 1C (61.68mV).

**Table 3.2.** Averaged RMSE errors of the discharge profile at 20°C and different current rates.

RMSE	Current rate			
	C/10	C/5	C/2	1C
absolute (mV)	17.54	28.07	34.62	61.68
% of voltage interval	1.46%	2.34%	2.88%	5.14%

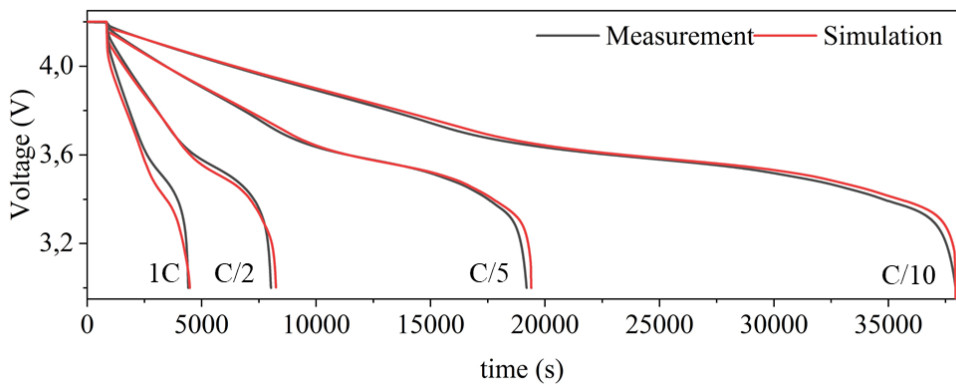


**Figure 3.8. Full discharge tests at various current rates.** Measured and simulated voltage profiles of full discharge tests at 20°C and different current rates: 1C, C/2, C/5 and C/10.

### 3.4.3. Driving profile

The driving profile has been derived combining the dynamic discharge profile A and B for BEV specified in the IEC 62660-1 standards about performance testing of Li-ion cells for propulsion of electric vehicles [139]. The maximum power output defined in these two profiles depends on the parameter  $N$ , that represents the fraction of capacity that can be used with respect to the maximum capacity of the cell. Two groups of experiments have been performed to validate the cell model at constant and at variable temperature.

In the first case, the testing protocol has been developed with series repetition of profile A and B assuming  $N=1/3$  and  $N=1$ . The current and voltage profiles at different temperatures are shown in Figure 3.9. As in the previous cases the model shows higher accuracy at 20°C and 35°C than at 5°C and -10°C. When considering the simulation at SoC higher than 25% and temperature between 5°C and 35°C, the maximum RMSE is 7mV (less than 0.6% of the voltage range).

In the second case, i.e. at variable temperature, the testing protocol has been developed as follows:

- Repetition of Profile A ( $N=1/3$ ) until the cell reaches 50% SoC;
- Resting phase 5 minutes;
- Profile B ( $N=1/3$ )
- Repetition of Profile A ( $N=1/3$ ) until the cell reaches 20% SoC.

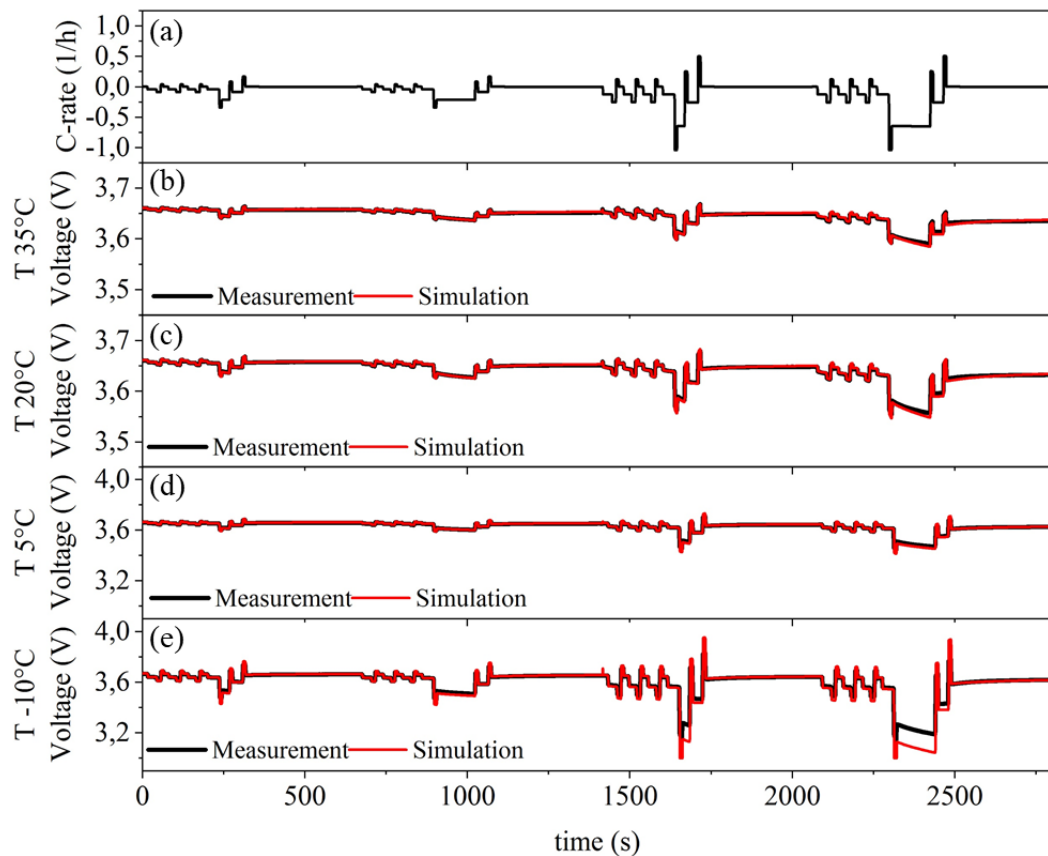


**Figure 3.9. Driving simulation test.** a) Current profile derived by IEC 62-660-1 regulation with repetition of profile A and B at different maximum rates. Measured and simulated voltage profiles at: b) 35°C; c) 20°C; d) 5°C and e) -10°C.

The temperature profiles have been developed with symmetrical heating and cooling ramps (2°C/h) and repeated over three different temperature ranges to simulate summer (15°C-35°C), spring/fall (5°C-25°C) and winter (-5°C-15°C) scenarios. RMSE results are given in **Table 3.3**. The model shows high accuracy in all the three different conditions, with a maximum error of 18mV, corresponding to 1.5% of the voltage range.

**Table 3.3. Averaged RMSE errors of the driving simulation profiles performed at variable temperature.**

RMSE	T range [15°C,35°C] (summer)	T range [5°C,25°C] (spring/ fall)	T range [-5°C,15°C] (winter)
absolute (mV)	11.18	18.01	14.47
% of voltage interval	0.93%	1.50%	1.21%

The measured and simulated voltage profiles are given in Figure 3.10-a. Moreover, given the long duration of the simulation also the SoC estimation is reported for this case (Figure 3.10-b). SoC is directly derived from the model by exploiting the SoC-OCV relationship.

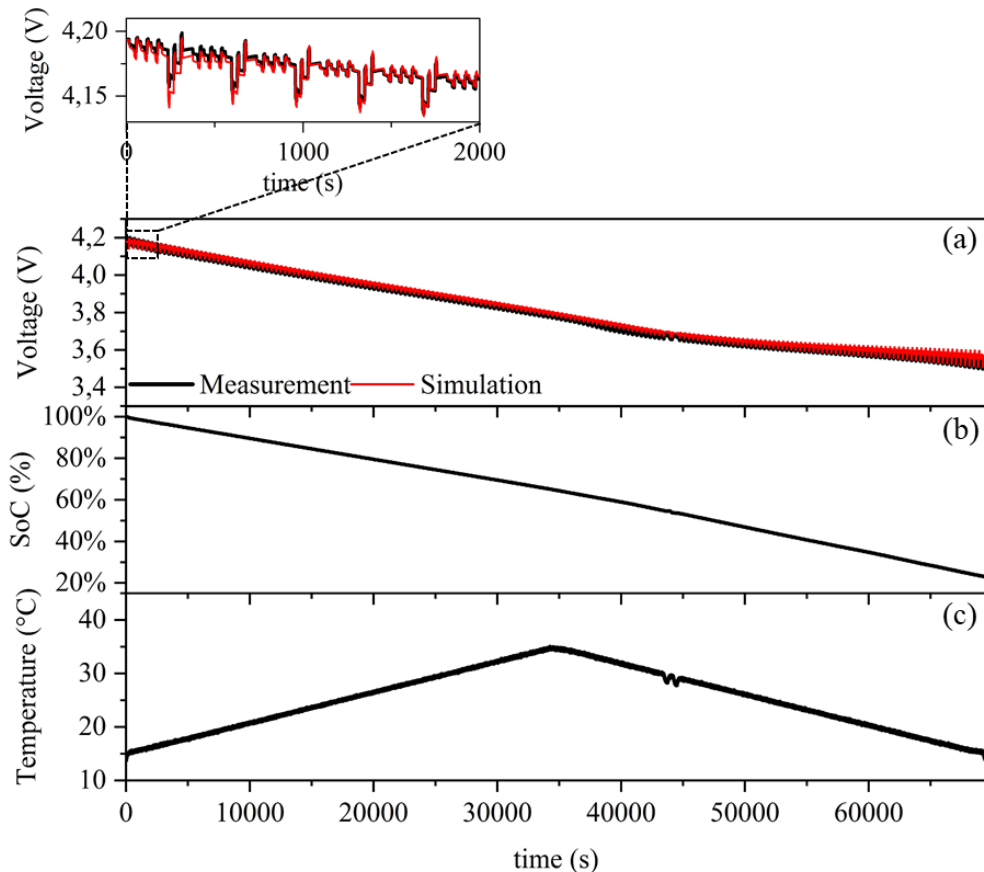


**Figure 3.10. Driving simulation test at variable temperature.** a) Measured and simulated voltage profiles; b) SoC estimated by the model; c) temperature profile measured on the cell surface in the summer condition simulation (temperature between 15°C and 35°C).

### 3.5. Final remarks

This chapter introduced EIS2MOD, a modelling framework to develop a physics-based model from EIS and OCV measurements for Li-ion cells. DRT has been applied to deconvolve EIS spectra as an efficient technique to distinguish electrochemical phenomena which are difficult to interpret directly from EIS.

The analysis of DRT deconvolutions at different SoCs and temperatures allowed to define an ECM in which each circuit element is assigned to a physical phenomenon. Moreover, the model parameter determination is a direct consequence of the DRT post-processing, thus avoiding any fitting process of the EIS and simplifying the model implementation for

simulation purposes. The model developed for large format NMC pouch cells constitutes of five blocks to represent the different phenomena with a total number of 13 independent parameters. These parameters are function of the OCV (i.e. SoC) and the temperature. The model validation has been performed with different current profiles at constant and variable temperature. In the first case, simulations at 20°C and 35°C showed RMSE from 0.2% to 1.5% for dynamic profiles (at different SoCs) and maximum RMSE of 5.1% for full discharge at 1C. At lower temperatures the high non-linearities in battery dynamic influenced the model behaviour and a maximum RMSE of 5.4% was obtained for dynamic simulation at -10°C. In the second case, driving profile simulations at variable temperature showed a maximum RMSE of 1.5%.

The methodology presented in this chapter could be extended to analyse Li-ion cell degradation and eventually perform SoH estimation. Next chapter will present the analysis of DRT profiles during cycling aging and the attribution of the different peaks to the related degradation mechanisms. Then, Chapter 5 will introduce degradation quantification and SoH estimation. Shifts and changes in magnitude of the peaks could be exploited to adjust the ECM parameters over lifetime and to allow for an accurate SoC estimation.

An example of application of EIS2MOD to another cell type and a preliminary application during cell aging is presented in Appendix B for commercial cylindrical cells.

# Chapter 4

## Detection of Li-ion cells degradation with DRT

This chapter introduces a methodology to investigate aging of commercial cylindrical Li-ion cells. Distribution of Relaxation Times (DRT) method is applied to deconvolute Electrochemical Impedance Spectroscopy (EIS) measurements and to separate those polarization effects that are usually overlapped in the frequency domain by means of a peak-based representation. Half-cells are built at beginning and end of life to link the electrochemical and aging processes occurring at anode and/or the cathode sides. Moreover, lab-made full-cells are exploited to verify the reproducibility when compared to cylindrical cell. The results of an extensive analysis of around 500 EIS spectra returns an unambiguous attribution of different electrochemical processes to different time constants, and ultimately to different DRT peaks. Digital imaging validates graphite degradation, mainly related to lithium plating. Scanning Electron Microscopy validates the degradation at NMC cathode, mainly attributed to particle cracking. It is concluded that DRT peaks allows to characterize cell aging and their tracking can help to develop more reliable State of Health (SoH) estimators.

The content of this chapter has been published in the Journal Energy Technology under the title “Detection of Lithium-Ion Cells’ Degradation through Deconvolution of Electrochemical Impedance Spectroscopy with Distribution of Relaxation Time” [160].

## 4.1. Context

As already discussed in Chapter 2, battery aging is still a big uncertainty being caused by complex physical and chemical degradation mechanisms which affect the different components inside the cell[62], [161]. These mechanisms do not leave a unique fingerprint on the cell characteristics but they can be clustered into the so-called degradation modes: (i) Loss of Lithium Inventory (LLI), which entails consumption of lithium ions for decomposition reactions, Solid Electrolyte Interface (SEI) layer growth or lithium plating; (ii) Loss of Anode Active Material (LAM<sub>A</sub>) and (iii) Loss of Cathode Active Material (LAM<sub>C</sub>), which both encompass electrode structural disordering, particle cracking and loss of electric contact[107]. Therefore battery cell measurements should be comprehensive, to embrace the complex interactions between the degradation modes, and non-invasive, to be implemented in Battery Management Systems (BMSs) and ultimately provide a correct estimation of the State of Health (SoH) [32], [60], [90].

Electrochemical Impedance Spectroscopy (EIS) is an example of a comprehensive measurement widely used to characterize Li-ion cells [63], [128], [141], [162]. In literature, several works applied EIS to investigate and track Li-ion cells aging: a summary of those applications and of best metrological practice are given in our previous work and in the works of W. Choi et al. and N. Meddings et al. [33], [64], [131]. In general, the impedance spectrum of a cell is analysed and fitted with an Electric Circuit Model (ECM) to extract the parameters related to the single electrochemical processes occurring inside the cell [52], [63], [78]. However, given the complexity to separate these processes in the EIS spectra, the Distribution of Relaxation Times (DRT) is often used to deconvolute the impedance curves in the time domain and to distinguish polarization effects that are normally overlapped in the frequency domain[118], [124]. These polarization effects are characterized by peaks with different magnitudes and time constants that can be attributed to the underlying physical processes [135]. For instance, M. Yi et al. applied DRT to investigate aging of cells in different conditions [163]. The authors developed a support vector machine classifier to analyse the DRT peaks variations caused by lithium plating with respect to cell Beginning of Life (BoL). A similar work is presented by X. Zhou et al., characterizing NMC pouch cells under high temperature cycling [80]. The authors decoupled the degradation mechanisms of the anode from the ones on the cathode by

focusing on different DRT peaks. However, they concluded that a further step was required to confirm the assumptions made. Including a reference electrode in the cell or manufacturing half-cells with the same material of the full-cells and lithium metal as counter-electrode are the solutions normally adopted in literature [42], [43]. In this way, electrochemical characterization (i.e. EIS measurements), are done separately on anode half-cell and cathode half-cell and reconciled with the full-cells for validation purposes. L. Wildfeuer et al. made half-cells from commercial NCA cylindrical cells and performed DRT characterization on them at different temperatures and State of Charges (SoCs) [164]. They concluded that charge transfer processes on the full-cell are dominated by the cathode at low SoC and by the anode at high SoC. Moreover, they found that a transition process between charge transfer and solid-state diffusion might be attributed to the anode. S. Sabet et al. characterized both NCA cylindrical and NMC pouch cells [96], [137]. They attributed the two main DRT peaks to SEI layer and cathode charge transfer for both the cell chemistries. These insights were also exploited in a following publication, to investigate accelerated aging of NMC cells [90]. The authors attributed the two DRT peaks variations (i) to SEI growth and (ii) to cathode particle cracking, Cathode Electrolyte Interface (CEI) growth and cathode dissolution. These conclusions were validated by means of post-mortem analyses, which is the most widely used process to validate electrochemical findings. Post-mortem analyses allow to investigate the chemical structure and surface morphology of the electrodes, providing valuable and detailed information about the chemical composition and degradation (look at Section 2.1) [39], [40]. For an exhaustive summary of all the available techniques, their advantages and limits, the readers are addressed to the review article of Waldmann et al. [165]. A simple implementation of imaging techniques combined to half-cells DRT analysis, is given by X. Chen et al. who studied lithium plating of LCO pouch cells [150]. The authors built symmetrical lithium metal cells to address the influence of the reference electrode on the DRT profiles of half-cells. They over-discharged anode half-cells to simulate the existence of different amounts of lithium plating and to highlight its effect on the DRT profile. Then, they analysed the results of cycling aging tests of cylindrical cells at 0°C. Based on their measurements, the authors attributed the variations of DRT peaks during aging mainly to the anode electrode. Similar conclusions, on the importance of anode in cells aging, were drawn by Heins et al. who studied large format NMC pouch cells at different temperatures

#### 4. Detection of Li-ion cells degradation with DRT

---

[85]. The authors exploited a three-electrodes configuration to deconvolute the effects of the two electrodes but did not perform further analyses to assess the degradation mechanisms.

Overall, EIS is a comprehensive measurement and DRT is a promising post-processing method to analyse cell aging and to detect the influence of different degradation mechanisms. However, there are two main limitations found in the literature: (i) DRT is applied either at BoL, i.e. with no aging, or analysing a specific degradation mechanism, neglecting other effects [150], [163], [164]; (ii) DRT peaks attribution is not performed univocally, either based on existing literature or validating the result with half-cells and post-mortem analyses only for the most relevant peaks and not for the full time constants range [80], [85], [96].

Therefore, the objective of this Chapter is to overcome those limits with an exhaustive methodology that systematically analyse DRT profiles and, by means of a validation process, unambiguously attribute DRT peaks to the degradation mechanisms arising during cell aging. Commercial cylindrical cells are cycled in different testing conditions to embrace different degradation mechanisms; EIS measurements are taken from cylindrical cells and from Lab-made full-cells and half-cells containing the material harvested from the cylindrical cells. The obtained DRT profiles are analysed at BoL, to link physical processes to specific peaks, and at EoL, to link aging effects to the same peaks. Imaging techniques with different accuracy, complexity and duration are exploited to characterize surface morphology of the electrodes and to validate the above attributions between DRT peaks and degradation mechanisms. Three techniques have been selected: digital imaging, optical microscopy and Scanning Electron Microscopy (SEM).

The chapter is structured as follows: Section 4.2 presents the developed methodology, which includes all the steps necessary to fully investigate Li-ion cells with EIS measurements and DRT post-processing; Section 4.3 presents the main findings derived from the performed aging tests, which includes the attribution of DRT peaks to electrochemical processes at BoL, the attribution of ageing phenomena at EoL and their validation through imaging techniques; finally Section 4.4 summarizes the main take-aways.

## 4.2. Material and methods

The findings of this work have been based on testing cylindrical commercial Li-ion cells: LG chem INR21700-M50 with lithium Nickel Manganese Cobalt oxide cathode (NMC 811) and graphite with silica particles anode (graphite-SiO<sub>x</sub>) [166], [167]. Cell's datasheet is available in Appendix D. Firstly, all the cells have been checked in their capacity and impedance values to ensure the reproducibility of the results. Secondly, all the cells have been subjected to the same testing campaign following the methodology shown in Figure 4.1: (i-a) the cells are cycled with different testing protocols from Beginning of Life (BoL) till End of Life (EoL), which is defined for SoH lower than 80% or End of Test (EoT), which is fixed to 1000 equivalent cycles (EqC)<sup>1</sup>; EIS measurements are done at regular interval to update the impedance; (i-b) the cells are discharged and disassembled to extract the electrodes material, which is used to assemble coin cells and to run imaging for post-mortem analyses; (ii) the EIS/DRT measurements from both commercial and half-cells, pristine and aged, are analysed to attribute electrochemical processes and to assign degradation mechanisms to the anode or the cathode; (iii) imaging is used to validate the correctness of the attribution, specifically digital imaging, optical imaging and SEM. In total 7 cells have been investigated in this work and the performed experiments are presented in Table 4.1. The next paragraphs will provide more information about testing and disassembly, analysis of DRT profiles and validation with imaging techniques.

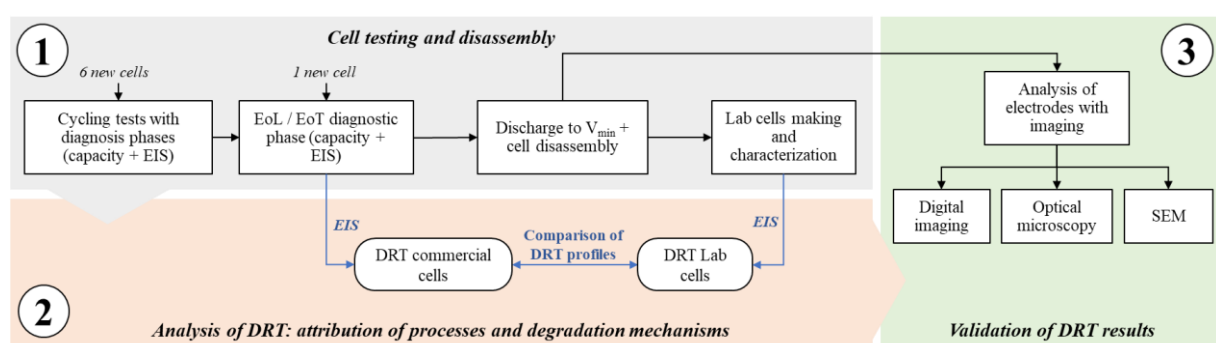


**Figure 4.1. Methodology followed in this chapter.** 1) cell testing and disassembly, 2) DRT analysis and peak attribution, 3) validation with imaging techniques.

<sup>1</sup> Equivalent cycle: it is defined as the ratio between the cumulated cycled capacity of a cell and two times its nominal (or initial) capacity.

### 4.2.1. Cell testing and disassembly

The experiments have been performed at the CSEM's Sustainable Energy Center, Neuchâtel (Switzerland). The first part of the presented methodology is divided in three steps: cycling aging tests, cell disassembly and lab-cells making.

#### *Cycling aging tests*

The testing set-up was composed of: (i) a cell tester Biologic BCS815 equipped with 32 parallel, 9V-15A channels ( $\pm 0.01\%$  FSD accuracy on the voltage and  $\pm 0.015\%$  FSD accuracy on current, for each available range) with EIS spectroscope multiplexed and able to range from 10kHz to 10mHz [157]; and (ii) a thermostatic chamber ATT-DM1200T with -45°C-180°C temperature range [158] (the testing set-up is shown in Figure 5.1 of next chapter). The temperature during the experiments was fixed to 20°C. As anticipated, the 7 cells have been firstly characterized with capacity test and EISs to ensure the reproducibility of the results. Capacity test showed a standard deviation of 0.5% with respect to the cells averaged capacity. EIS spectra showed a standard deviation of 1.0% on the ohmic resistance (i.e. the zero-crossing value on the EIS Nyquist plot) and 3.3% on the polarization resistance (i.e. the full resistivity down to 10mHz) with respect to the averaged values.

Different testing conditions has been set which differ in the Current rates (C-rate) and the Depth of Discharges (DoD) applied during the cycling phase. The testing conditions are listed in Table 4.1, with the corresponding cell ID. The reference cell (ID:REF) follows the cycling conditions as defined by the manufacturer (C/3 both in charge and discharge). Another cell is cycled in reference condition but without CV phase (ID:REF\_w/oCV). The remaining cells are cycled with higher C-rates and/or smaller DoD to explore different aging conditions and to spot different degradation mechanisms.

Regardless from the specific cycling conditions, all experiments alternate cycling phases of 50 EqC and diagnostic phases. The diagnostic phase includes capacity determination (i.e. SoH measurement) in nominal conditions and EIS characterization at five SoC levels: 0%:25%:100%. In this way, the impedance evolution of each cell is tracked during its lifetime and it is possible to compare cells with different cycling conditions. The SoC levels have been fixed to specific voltage value extracted by the cells' Open Circuit Voltage (OCV)

curve at BoL; those values remained unchanged throughout the test duration. The last diagnostic phase is performed at EoL/EoT condition before the cell disassembly.

*Table 4.1. Overview of the cycling protocol applied to the different tested cells. Legend: “✓” test performed; “✗” test not performed; “A” anode; “C” cathode.*

Testing protocols					Post-mortem analyses		Imaging techniques		
Cell ID	DoD	SoC interval	Charging rate	Discharging rate	Cell disassembly	Lab-cells making	Digital imaging	Optical microscopy	SEM
NEW	-	-	-	-	✓	✓	C: ✓ A: ✓	C: ✓ A: ✓	C: ✓ A: ✓
REF	100%	0-100%	C/3 <sup>a)</sup>	C/3	✓	✓	C: ✓ A: ✓	C: ✓ A: ✓	C: ✓ A: ✓
REF_w/o CV	100%	0-100%	C/3	C/3	✓	✓	C: ✓ A: ✓	C: ✗ A: ✓	C: ✗ A: ✗
DOD_20	20%	0-20%	C/3	C/3	✓	✓	C: ✓ A: ✓	C: ✗ A: ✓	C: ✗ A: ✓
FC05	100%	0-100%	C/2 <sup>a)</sup>	C/3	✓	✓	C: ✓ A: ✓	C: ✗ A: ✓	C: ✗ A: ✗
FC1	100%	0-100%	1C <sup>a)</sup>	C/3	✓	✓	C: ✓ A: ✓	C: ✓ A: ✓	C: ✓ A: ✓
FD1	100%	0-100%	C/3 <sup>a)</sup>	1C	✓	✓	C: ✓ A: ✓	C: ✗ A: ✓	C: ✗ A: ✗

<sup>a)</sup> Including Constant Voltage phase with cut-off current at C/50.

### *Cell disassembly*

Cell disassembly procedure has been developed and optimized based on the existing literature (the readers are addressed to Appendix C for more details about cell disassembly and laboratory cell making) [43], [96], [137], [141], [151], [168]–[170]. Firstly, the cell is discharged to the minimum voltage (i.e. 2.5V) at C/3 constant rate and a CV phase with cutoff current of C/100. After that, the cell is transferred inside an argon-filled glovebox. A pipe cutter is used to open the cell on the bottom and on the top sides and the electrodes tabs are cut; the lateral part of the case is removed using pliers. A scalpel is used to cut the tape that close the jellyroll (i.e. electrodes + separator foils) and the cell components are unrolled and separated. References of the inward and outward facing side as well as of the outer and inner roll part of the electrodes are taken to properly reuse the material in the following steps. The electrodes are not washed with DMC to preserve their aged state and to properly perform electrochemical measurements [165], [171]. The electrodes are cut following a precise procedure to guarantee consistency between the different cells analysed: (i) adjacent parts of the outer roll of the electrodes are cut for lab-cells making and for imaging techniques application; (ii) the electrodes are

#### 4. Detection of Li-ion cells degradation with DRT

---

fixed on a hard substrate with adhesive tape; (iii) the coating on one side of the double-coated electrodes is removed using NMP solvent for both the cathode and anode material for practical reason [166], [171]; (iv) the foils are punched in a central area (i.e. equidistant from the edges) to obtain 15mm diameter disk electrodes.

##### *Laboratory cells making*

Lab-cells have been made in 2025 coin format, including two 0.5mm aluminium spacers (at top and bottom) and glass fiber separator Whatman™ GF/C with 19mm diameter. The standard electrolyte is 1M lithium hexafluorophosphate ( $\text{LiPF}_6$ ) in a mixture of ethylene carbonate, dimethyl carbonate and diethyl carbonate produced by Sigma-Aldrich© (EC:DMC:DEC, 1:1:1 w/w/w) with a quantity of 90 $\mu\text{l}$ . Three types of coin cells are made with the electrodes extracted by the cylindrical cells:

- Full-cells: graphite and NMC are coupled to reproduce the standard cylindrical cell and to assess the possible differences due to cell making process or new electrolyte.
- Anode half-cells: graphite is coupled with a disk of lithium metal (reference electrode).
- Cathode half-cells: NMC is coupled with a disk of lithium metal.

Three identical samples are built for each cell type, with a total number of 9 cells, to reduce risks of non-reproducibility due to assembling process. Cell formation is performed with two cycles at C/10 after 12 hours rest to allow the electrolyte to soak the electrodes and the separator [170]. The voltage range is 3V-4.2V for full- and cathode half-cells and 0.01V-1V for anode half-cells. After formation, the cells are characterized with EIS measurements at voltages corresponding to 0%, 50% and 100% SoC of the full-cell SoC. The specific voltage values have been chosen performing the OCV curves balancing of the half-cells and of the full-cell as presented in literature [172] and detailed in Appendix C, Section B.4. EIS measurements have been used to verify cells reproducibility and to discard the cells with abnormal impedance with respect to their twin samples. The standard deviation showed a value of 13.6% for the polarization resistance with respect to its averaged value. However, it reduces to 5.3% when evaluated down to 0.1 Hz only, i.e. in the most interesting portion of the spectra for DRT peaks attribution. It is therefore concluded that the EIS spectra of lab-made cells are of similar quality with respect to the ones of commercial cells, thus confirming the reliability of the assembly process.

### 4.2.2. Analysis of DRT profiles

As performed in Section 3.2.1, all EIS measurements are checked in their quality and time invariance with the Kramers-Kronig (KK) criterium, which returns the residual between the measured spectra and reconstructed Kramers-Kronig spectra [140], [142]. If the criterium is respected, the DRT function can be computed with equation (3.4). The DRT calculation is based on the assumption that an impedance spectrum can be represented as an infinite series of RC elements and the ohmic resistance. The  $g(\tau)$  function is discretized and solved applying regularization methods; details about the mathematical formulation are given in literature by T. Wan et al. [145]. All the algorithmic steps to compute DRT from EIS for Li-ion cells have been presented in the previous chapter (Section 3.2.).  $g(\tau)$  function has a peaks-based representation as shown in Figure 4.2; specific letter and number are used to define the origin and the peak position. The letter used are: "S" for cylindrical cells (i.e. the Standard cells), "F" for laboratory full-cells, "C" for cathode half-cells and "A" for anode half-cells (e.g. Figure 4.2 represents the DRT profile at BoL, 50% SoC for a cylindrical cell). As introduced in Section 0, each peak can be attributed to a different process occurring in the cell. For this reason, high quality and time invariant EIS measurements are required, otherwise the  $g(\tau)$  function will show artefacts and the peak attribution will not be reliable.

Three criteria have been defined to evaluate which specific phenomenon can be attributed to which one of the electrodes, and ultimately to which degradation mechanism. Those criteria are used twofold: (i) to compare DRT measured on lab-made full-cells with lab-made half-cells full-cell and (ii) to compare the same between lab-made full-cells and cylindrical cells. While the first is used to discriminate between the processes happening at the cathode or at the anode sides, the second serves to verify the consistency in the measurements between the cylindrical cells and lab cells. The chosen criteria are:

1. Time constant ( $\tau$ ): depending on the value of the time constant, a specific peak can be attributed to a defined physical process. As discussed in Section 3.2.2, the four main processes that can be allocated are: (i) electric and magnetic effects ( $\tau < \sim 10^{-3}s$ ); (ii) transport of lithium ions through the SEI or CEI layers ( $\sim 10^{-4} < \tau < \sim 10^{-2}s$ ); (iii) electrodes' charge transfer ( $\sim 10^{-2} < \tau < \sim 10^1s$ ); (iv) diffusive processes ( $\tau > \sim 10^1s$ ) [80], [90], [142], [150]–[152].

#### 4. Detection of Li-ion cells degradation with DRT

2. Peak magnitude: the peak magnitude is calculated by measuring the height of the peak, as shown in Figure 4.2. This indicator is mainly used to compare the peaks of lab-cells (full or half-cells).
3. Peak variation w.r.t. SoX: the peak variation is evaluated with respect to SoC (i.e. different OCVs) and to SoH (i.e. different aging stages). In both cases, the indicator allows to understand which electrode is mainly affecting the DRT peaks behaviours.

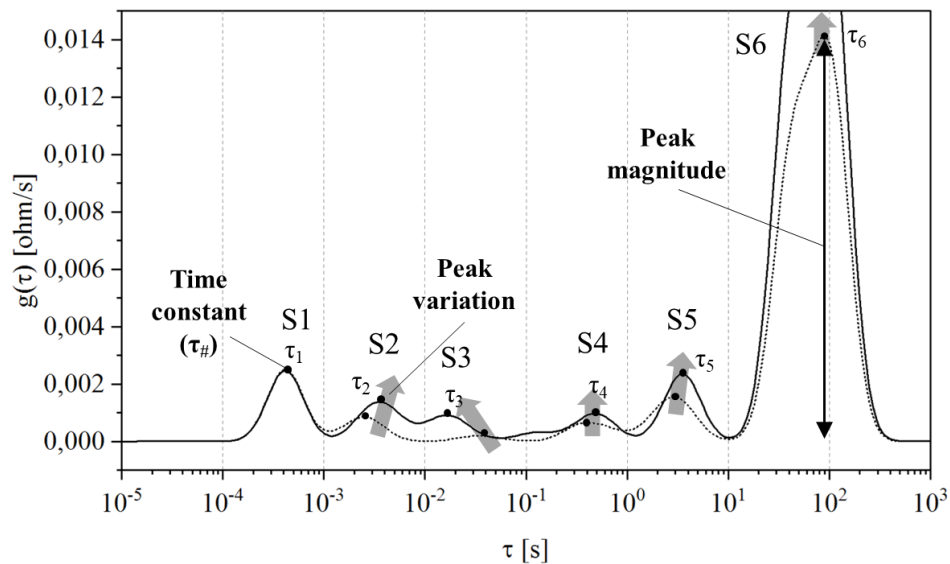


**Figure 4.2. Typical DRT profile of a Li-ion cell and the criteria used to evaluate DRT peaks: time constant, peak magnitude and peak variation.**

##### 4.2.3. Validation of DRT results

The DRT peak attributions defined through the presented criteria are validated via imaging techniques. Three types of imaging with increasing precision, complexity and operation time have been performed: (i) digital imaging by means of a non-professional camera, (ii) optical microscopy by means of an Olympus BX53M and (iii) Scanning Electron Microscopy (SEM) by means of a Thermo Scientific™ Scios™. Digital imaging is performed by taking pictures of the unrolled electrodes, to detect macro-effects on the surface, such as defects, plating or material exfoliation [55], [137]. Optical microscopy is used to detect degradation mechanisms in the  $\mu\text{m}$  range, such as cracks in electrode coating, growth of films on electrode surface, delamination or decomposition of electrodes [165]. Finally, SEM is performed to investigate the surface morphology and the electrodes microstructure, allowing to relate their changes to degradation mechanisms,

such as particles cracking or changes/films formation on particle surface [40], [41], [47], [53]. Both surface (planar samples) and cross-section samples have been analysed.

The validation process is performed by connecting the results obtained by imaging with the results of tentative peak attributions for lab-cells (half- and full-cells) and cylindrical cells. For instance, if cathode imaging reveals particle cracking and the analysis of cathode half-cell reveals a relevant rise of peak C4 w.r.t. BoL value, then this peak is attributed to cathode particle cracking. Similar conclusions are done if anode imaging reveals lithium plating and anode half-cell DRT analysis shows a large rise of peak A2. The validation of full-cells and cylindrical cells is performed combining the results obtained from anode and cathode analyses. However, given the different detection capabilities of the presented imaging techniques, the validation process could be limited by the precision of the available equipment in the testing facility where measurements are performed.

### 4.3. Results and discussion

The cells have been cycled with different testing protocols as already presented in Table 4.1. Overall, the testing results are presented in Figure 4.3, with the SoH progression and EqC for the 6 cycled cells (cell ID:NEW was disassembled at BoL, i.e. SoH=100%). The cell cycled in reference condition (ID:REF) reached the EoT (testing limit of 1000 EqC) at SoH=86%. Increasing the C-rate is detrimental for the battery performances. Higher charging rates are more severe than higher discharging rate: cell FC1 and cell FC05 reach their EoL (SoH = 80%) after 92 and 798 EqC, while cell FD1 reached SoH=81% at the EoT. Reduction of the DoD (i.e. of the voltage range available for cycling) brought to less severe cell aging: SoH = 94% at EoT for cell DOD20. Finally, the cell REF\_w/oCV shows an unexpected trend: only 500 cycles at EoL but with a cycling protocol lighter than cell REF. This is most probably due to an early stage slope change (the so called “knee”) which can be attributed to film formation on electrode surface such as early lithium plating deposition caused by production defects (electrode surface defects or electrolyte quantity) and not detectable at BoL [79].

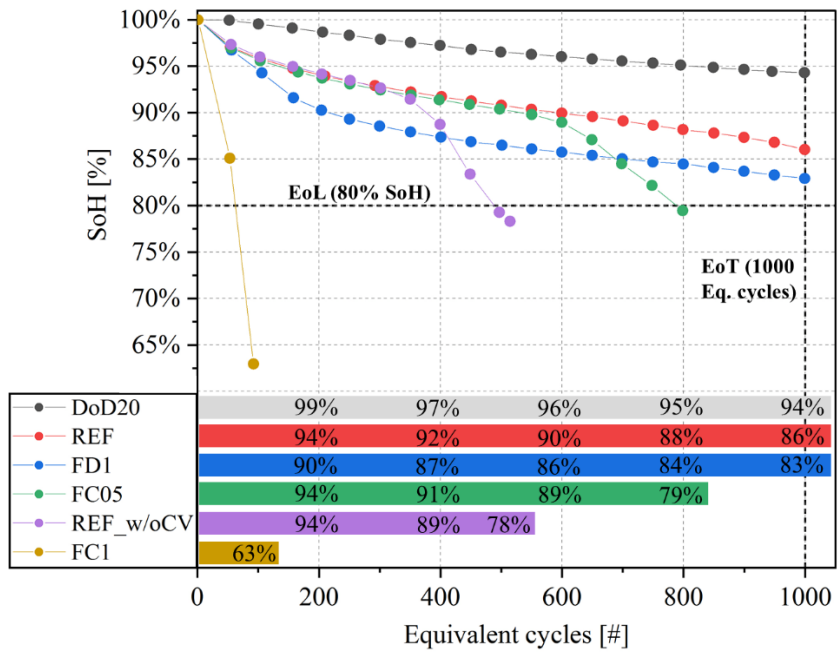


**Figure 4.3. SoH versus EqC for the six cycled cells.** Tests have been stopped once EoL (SoH = 80%) or EoT (equivalent cycles = 1000) conditions were met.

#### 4.3.1. Analysis of DRT profiles

The DRT profiles of cylindrical cells have been derived from the EIS performed every 50 EqC. On average for the tested cells, the maximum residuals between the measurement and KK reconstruction were lower than 1.1% at BoL and lower than 1.0% at EoL/EoT, allowing for a reliable DRT calculation. Figure 4.4 shows an example of DRT profiles evolution at SoC=50% (the peak S6 has been omitted to better appreciate the changes on the smaller peaks). In most of the cases, peaks S2, S3 and S4 show the most relevant trend at increasing cycle number with a clear link to the SoH decrease: for instance, the steepest the capacity fade, the highest the growth of peak S2.

In the following paragraphs the criteria explained in Section 4.2.2 (time constant, peak magnitude, peak variation) will be applied to lab-cells and cylindrical cells DRT profiles at both BoL and EoL/EoT. The first serves to discuss which electrochemical process should be associated to which DRT peak, the second serves to identify which peak should be tracked to identify which degradation mechanism.

It is worth to mention that for half-cells the presence of the reference electrode (i.e. lithium metal) influences the impedance response and consequently the DRT profile of

the cells [150]. Symmetric lithium metal cells have been produced to verify that DRT profiles show one main peak with time constant around  $6 \times 10^{-4}$ s.

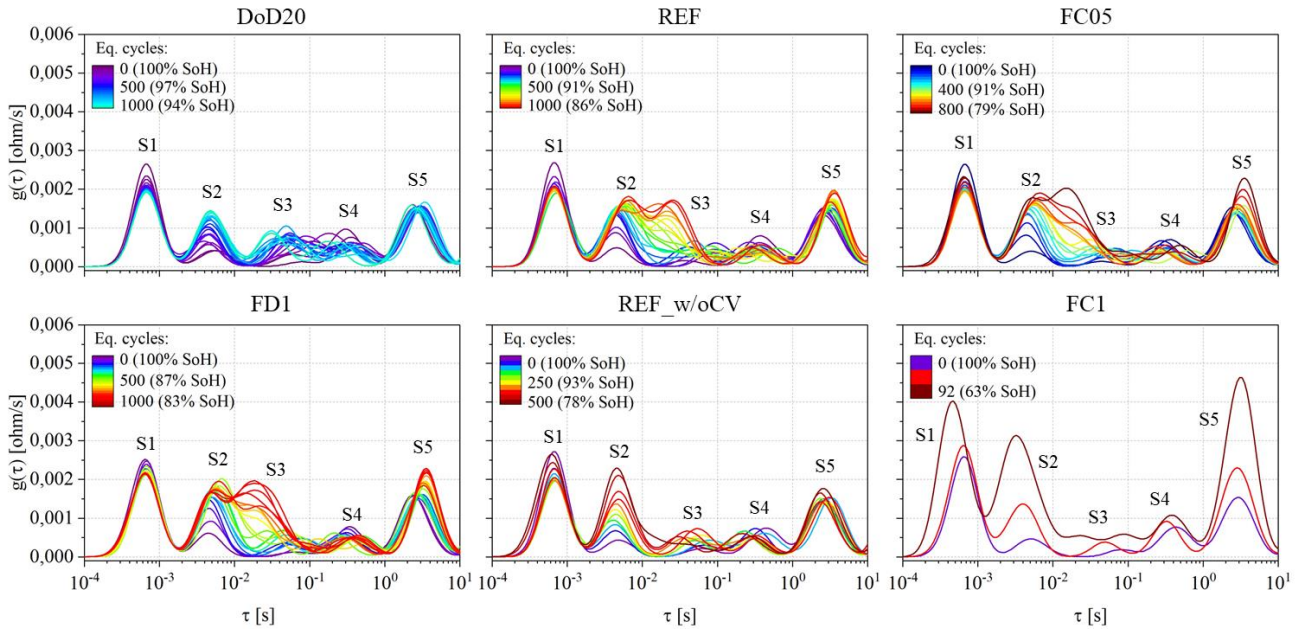


**Figure 4.4. 50% SoC DRT profiles trends during cycling of the six tested cells.** The color scale is based on the SoH (violet = 100% SoH; brown  $\leq$  80% SoH).

#### Assessment at Beginning of Life

The first cell that has been disassembled is the ID:NEW (SoH = 100%). Figure 4.5 shows the DRT profiles at different SoCs including the results of lab-cells (anode, cathode half-cells and full-cells). The slight time constants shift at values lower than  $10^{-2}$ s between cylindrical cell and lab-cells are mainly given by differences in fabrication procedure due to cell format and cell components. As regards cell format, coin cells are free from inductive behaviour, so that the first peak time constant is shifted to lower values with respect to cylindrical cells, around  $10^{-4}$ s [150], [164]. As regards cell components, lab-made cells will be always slightly different from the original dismantled cells due to the different separator and electrolyte additives [151].

The criteria defined in Section 4.2.2 have been applied: (i) to compare the DRT profiles of anode half-cell (Figure 4.5-a) and cathode half-cell (Figure 4.5-b) with respect to the full-cell ones (Figure 4.5-c) and (ii) to compare the DRT profiles of the full-cell with respect to the cylindrical cell ones (Figure 4.5-d).

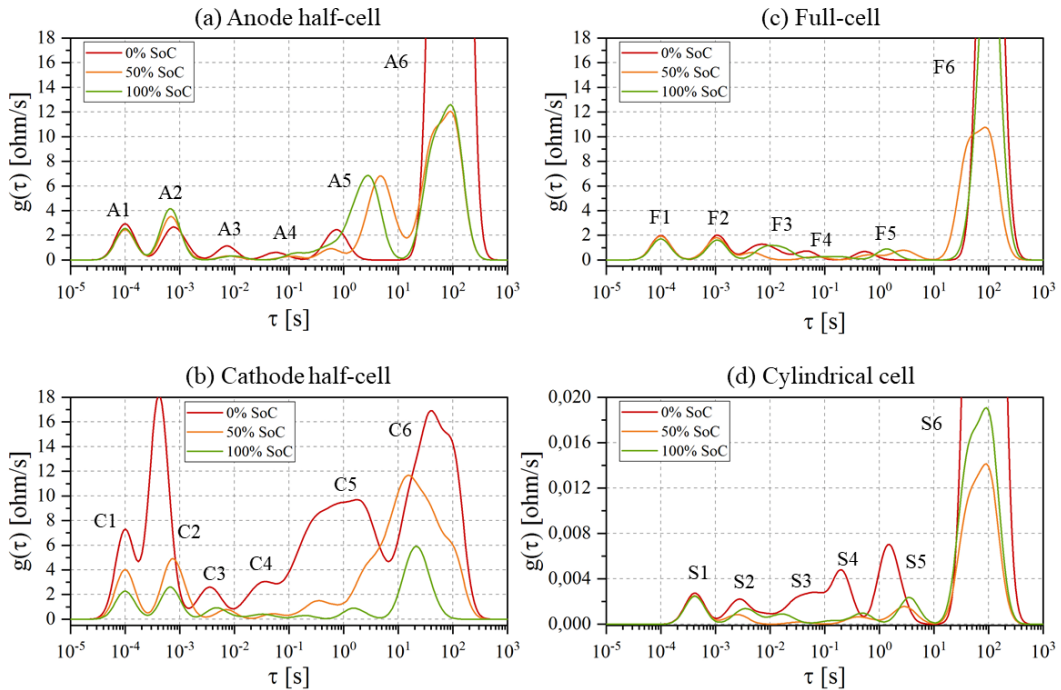


**Figure 4.5. DRT profiles at 0%, 50% and 100% SoC of cell NEW (BoL).** a) Anode half-cell; b) Cathode half-cell; c) Full-cell (coin format); d) Cylindrical cell.

The analysis is performed peak by peak, from 1 to 6, by referring to the nomenclature previously introduced: “S” for cylindrical cells (i.e. the Standard cells), “F” for laboratory full-cells, “C” for cathode half-cells and “A” for anode half-cells:

- Peak 1: half-cells (A1, C1) and full-cell (F1) have the same time constant ( $\tau = 10^{-4}\text{s}$ ) but slightly different behaviour with respect to SoC: peaks A1 and F1 have similar magnitude and are invariant across SoCs; peak C1 instead, shows an increasing magnitude for lower SoC. The behaviour of C1 could be influenced by the large magnitude of peak C2, especially at 0% SoC. In literature, electric and magnetic effects due to particle-particle and particle-current collector interactions are usually attributed in this time constant range [80], [142], [150]. Therefore, peaks A1, C1 and F1 are also linked to these effects. The same phenomenon is also observed in the cylindrical cell with S1 but at slightly lower time constant.
- Peak 2: half-cells A2 and C2 have similar time constants values ( $\sim 7 \times 10^{-4}\text{s}$ ) while F2 has a slightly bigger one ( $10^{-3}\text{s}$ ). The DRT peaks are influenced by the presence of the lithium metal reference electrode in the half-cells: this phenomenon is especially observed in the cathode one where a large magnitude variations at low SoC is registered [150]. Peak A2 instead shows smaller variations with respect to SoC and,

given its time constant, is also influenced by the transport of ions in graphite's SEI layer, as described in literature [80], [150]. Therefore, by comparison of peak magnitudes and knowing that lithium metal is not included in full-cells, peak F2 is tentatively attributed to graphite's SEI layer. Analogously, peak S2 (cylindrical cell) is attributed to the same phenomena.

- Peak 3: at the cathode side, peak C3 shows the lowest magnitude and the smallest change with SoCs if compared to all other peaks. The time constants is between  $3 \times 10^{-3}$ s and  $7 \times 10^{-3}$ s at which CEI formation is typically attributed in literature [96], [137]. At the anode side, half-cell peak A3 has a time constant close to  $10^{-2}$ s, in a region where interface and charge transfer effects could be overlapped [137], [142], [149], [150]. By looking at the peak magnitude variations with respect to SoC, A3 shows a behaviour typically depicted for charge transfer process and similar to peak A4 rather than peaks A2 or C2 that are related to SEI layer and lithium metal reference electrode respectively [142]. Therefore, peak A3 is attributed to graphite charge transfer. When comparing half-cells with the full-cell, F3 is tentatively attributed to the cathode, due to its larger magnitude both at SoC = 0% and SoC = 100%, which is typically related to the cathode [150], [164]. When analysing the cylindrical cell, S3 shows differences (e.g. SoC trend) if compared to F3 but similarities if compared to C4. Therefore, S3 is tentatively attributed to the cathode.
- Peak 4: at the anode side, peak A4 shows a very similar behaviour to A3 but time constant around  $10^{-1}$ s; therefore it is attributed to graphite charge transfer processes. At the cathode side, charge transfer processes are usually marked by peaks with broad magnitude variations with respect to SoC, in the time constant interval  $10^{-2}$ - $10^1$ s [137], [164]. Given the match found on the cathode half-cell, C4 is attributed to NMC charge transfer reactions. When analysing the full-cell, peak F4 cannot be clearly attributed to the anode nor the cathode. Moving then to the cylindrical cell, S4 shows large magnitude variations with SoC, as observed for NMC charge transfer. Peak S4 is therefore tentatively attributed to NMC charge transfer.
- Peak 5: at the anode side, peak A5 shows small magnitude and time constant ( $8 \times 10^{-1}$ s) at SoC = 0% followed by a magnitude growth and a time constant shift to larger values at SoC = 50% and SoC = 100%. This peak is attributed to charge transfer processes, as found in literature [142], [164]. At the cathode side, peak C5 is

#### 4. Detection of Li-ion cells degradation with DRT

---

characterized by a wide SoC variation and therefore attributed to NMC charge transfer, similarly to peak C4. Moreover, peak C4 and C5 are partially overlapped at SoC = 0% SoC. Same behaviour is also found in the full-cell and cylindrical cells with peaks F3/F4 and S3/S4, respectively. If peak F4 is tentatively attributed to NMC charge transfer, peak F5, which shows the same time constant shift and SoC variations as in peak A5, is instead attributed to graphite charge transfer. Same conclusion applies for the 5<sup>th</sup> peak in the cylindrical cell (S5).

- Peak 6: this peak shows the largest magnitude and variations with respect to SoC both for lab-cells and the cylindrical cell. Given the time constant higher than 10s, this peak is attributed to diffusive processes [142]. When comparing the behaviour of peaks A6/C6 with respect to F6, it is hard to define which electrode is having the biggest impact on the full-cell. Consequently, peak F6 and analogously S6 are attributed to the diffusive processes occurring at both electrodes.

The summary of DRT analysis at BoL for half-cells, full-cell and cylindrical cell is given in Table 4.2 with the tentative attribution of physical processes to each DRT peak. The analysis at EoL/EoT and imaging techniques will be used to refine and unambiguously validate these results.

**Table 4.2. Tentative DRT peaks attribution at BoL.**

Cell type	electric and magnetic effects	SEI film	Li metal reference electrode	CEI	Cathode Charge Transfer	Anode Charge Transfer	Diffusion processes
Anode half-cell	A1	A2	A2	-	-	A3, A4, A5	A6
Cathode half-cell	C1	-	C2	C3	C4, C5	-	C6
Full-cell	F1	F2	-	-	F3, F4	F5	F6
Cylindrical cell	S1	S2	-	-	S3, S4	S5	S6

#### *Assessment at End of Life/ End of Test*

The assessment at EoL/EoT is done by comparing the DRT profiles of cells that performed cycling tests with the pristine ones (ID:NEW) presented in the previous paragraph. Figure 4.6 shows the results at 50% SoC for half-cells, full-cells and cylindrical cells for different

SoH values. As in the previous paragraph, the peak analysis is performed from peak 1 to peak 6:

- Peak 1: this peak has not a clear trend with respect to cells' SoH both in lab-made cells and cylindrical cells. In the first case, the small variability on the magnitudes is attributed to the cells assembling process. In the second case, the larger magnitude is observed for cell ID:FC1 that was severely aged (63% SoH). However, no clear behaviour linked to cycling is found and the attribution to electric and magnetic effects is confirmed with no specific link to any degradation.
- Peak 2: anode and cathode half-cells show similar magnitudes (peak heights) for peaks A2 and C2, but not related to SoH levels. More in details, C2 shows a significant higher magnitude for cells ID:NEW (100% SoH) and ID:DOD20 (94% SoH) than for all the other cells. This trend is unrelated to material degradation and is referred to impurities of lithium metal electrode surface. In the case of A2, the peak variability can be addressed to differences among the cells in the SEI layer. It is worthwhile to mention that larger variations were expected for this peak since related to SEI growth/decomposition and surface film formation (lithium plating). However, for consistency in the post-mortem procedure, the disk electrode for coin cells were always cut in the same area on the outer side of graphite that, in most the cases, was not severely aged as the inner part. If compared to the half-cells, peaks F2 show lower magnitude but increasing trend at decreasing SoH. Knowing that C2 is mostly influenced by lithium metal electrode, F2 is tentatively attributed to the SEI peak (A2), confirming the BoL analysis. This is also true in the cylindrical cell (S2), especially for cells that reached SoH<80% before 800 EqC (ID:FC1, REF\_w/oCV and FC05). Therefore, peaks F2 and S2 are tentatively attributed to SEI layer growth/decomposition. However, given the great variations in S2, this peak is also tentatively linked to lithium plating.
- Peak 3: at the anode side, peak A3 does not show relevant variations with SoH. At the cathode side, peak C3 shows two trends: (i) moderate rise in magnitude with no time constant variations for cells ID:FC1, ID:REF\_w/oCV and ID:DOD20 and (ii) large rise in magnitude and shift towards bigger time constants for cells ID:FC05, ID:FD1 and ID:REF. Therefore, cathode degradation looks more relevant after a certain number of cycles (i.e. 700 EqC) and at certain SoH (e.g. SoH < 94%). Similar peak behaviours are

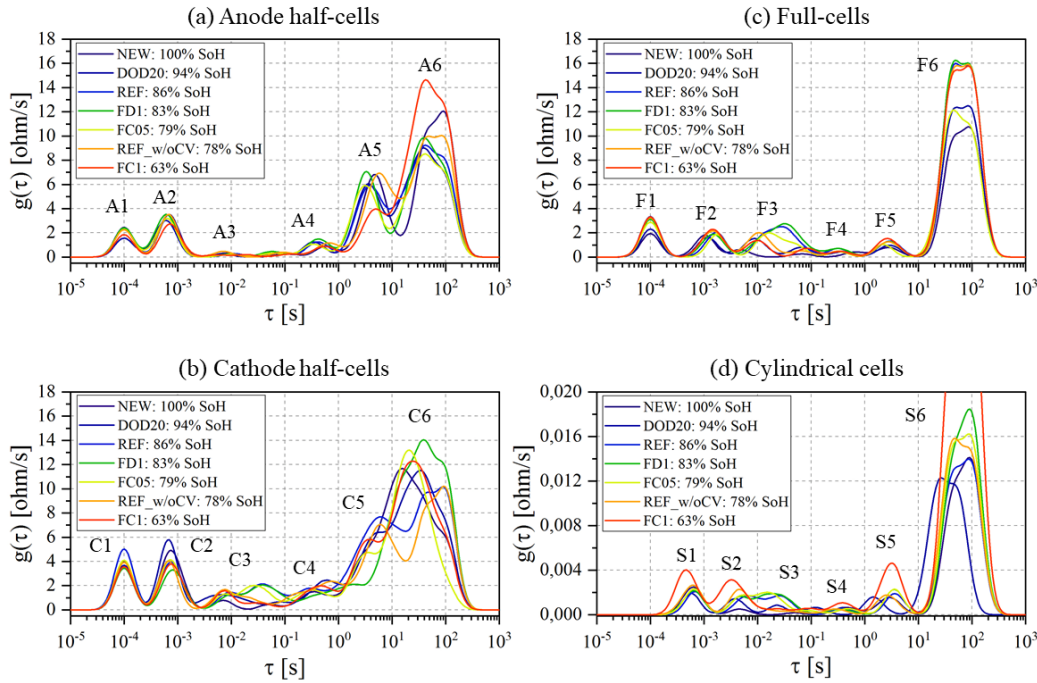


**Figure 4.6. DRT profiles at 50% SoC of a cell NEW (100% SoH) and of the tested cells at EoL/EoT: a) anode half-cells; b) Cathode half-cells; c) full-cells (coin format); d) cylindrical cells.**

found analysing F3 and S3 that confirm the attribution at BoL and that are consequently attributed to NMC degradation mechanisms (such as particle disordering and cracking).

- Peak 4: peaks A4 and C4 show rise in magnitude for cycled cells compared to cell ID:NEW. In both cases, this phenomenon is attributed to electrode degradation which affect charge transfer processes. When analysing F4 and S4, peaks variations are less pronounced but show similar trends. Therefore, and coherently with respect to peak 4 attribution at BoL, peaks F4 and S4 are tentatively attributed to cathode degradation. Imaging techniques applied on electrodes material will be used to validate this result.
- Peak 5: no specific trend with SoH is found at the anode side, nor at the cathode side. However, when analysing the full and cylindrical cells, an increase in magnitude for aged cells is found, specifically at SoH lower than 80% (IDs: FC1, REF\_w/oCV, FC05). Moreover, DRT profiles at SoC = 0% and SoC = 100% of aged cells show similar time constant shift behaviour of peaks F5 and S5 compared to peak A5 of half-cells, as at BoL. Therefore, F5 and S5 attribution at BoL is confirmed (anode charge transfer phenomena) and the rise in magnitude is associated to anode degradation.

- Peak 6: no specific trends allow to attribute peaks F6 and S6 to the anode or the cathode degradation. However, the lower the SoH, the larger the peak magnitude rise. This phenomenon can be related to a general slowdown of the cells kinetic that influences diffusive processes. Consequently, this behaviour confirms the attribution of F6 and S6 at BoL.

The summary of degradation mechanisms attributed to DRT peaks is given in Table 4.3. This analysis allowed to refine most of the attributions done already in Table 4.2 (e.g. the attribution of SEI film to the second DRT peak). The tentative attribution will be validated with the results of imaging techniques that are given in the next paragraph.

**Table 4.3. Tentative DRT peaks attribution at EoL/EoT.**

Cell type	SEI growth/ decomposition	lithium plating	Cathode degradation	Anode degradation	Diffusion process slow down
Anode half-cell	A2	-	-	A4, A5	A6
Cathode half- cell	-	-	C3, C4	-	C6
Full-cell	F2	-	F3, F4	F5	F6
Cylindrical cell	S2	S2	S3, S4	S5	S6

### 4.3.2. Validation through imaging

The DRT peaks attribution performed on lab- and cylindrical cells (Table 4.2 and Table 4.3) has been validated with imaging techniques. The validation objective is twofold: (i) to address the specific degradation mechanisms occurring at anode and cathode sides and (ii) to confirm that specific DRT peaks belong either to the cathode or anode electrodes. As mentioned in Section 4.2.3, three techniques have been exploited: digital imaging, optical microscopy and SEM. The imaging is performed both on the graphite electrode and NMC electrode. Details about samples preparation are given in Appendix C, Section C.4.

#### *Graphite electrode*

After cell disassembling and unrolling, the anode looked fragile and prone to exfoliation on the edges. Digital images have been taken inside the glovebox on both electrode sides. As shown in Figure 4.7 for all the 7 cells (NEW + aged), the most relevant deterioration is concentrated in the inner part of the electrode, i.e. the area close to the positive tab. From

#### 4. Detection of Li-ion cells degradation with DRT

---

left to right, the first two pictures represent the cell ID:NEW (100% SoH) and the cell ID:DOD20 (94% SoH): no differences or deterioration effects are detected. For all the other cells, a grey film formation of variable extent is observed on the graphite surface, which can be associated to lithium plating [173]. These visual findings have been qualitatively compared to the DRT peaks variations of cylindrical cells. Table 4.4 assesses on a 0-5 scale the plating formation over the whole electrode surface assuming 0 for cell ID:NEW and 5 for the most plated electrode (i.e. cell ID:FC1): the larger the plated area the larger the rise in magnitude of peak S2. In fact, deposited lithium leads to a longer path for lithium ions to intercalate into graphite and consequently blocks the contact between electrolyte and SEI layer while reducing the available surface [163]. The all process results in an increase of resistance, which is detected by the S2 peak magnitude rise. Specifically, cell ID:FC1 reached very low SoH (63%) and shows a spotted covering on the whole graphite surface (Figure 4.7-g). Similar effect is found in cell ID:FC05 (Figure 4.7-e). Cell ID:REF\_w/oCV instead, shows a lower extension of plated area but shinier and more homogeneous. All the other cells, i.e. ID:REF and ID:FD1 in Figure 4.7-c and -d show a smaller plated area, corresponding to a smaller rise in magnitude of peak S2. The presence of deposited lithium on these cells suggests that lithium plating is induced by SEI layer growth and decomposition, as found in previous works [107], [174]. These analyses confirm the attribution of peak S2 to SEI layer related phenomena and to lithium plating.

**Table 4.4. Comparison of DRT peaks and anode digital imaging.** Trend of commercial cells DRT peaks at 50% SoC compared with degradation detection made with digital imaging on the anode (graphite). The peak variation is small (↑) or big (↑↑) and evaluated with respect to NEW cell. Lithium plating is ranked on 0-5 scale between NEW and FC1 cells.

Cell	SoH [%]	Commercial cell DRT peaks at 50% SoC						Li plating detection with digital imaging on the anode
		S1	S2	S3	S4	S5	S6	
NEW	100%	-	-	-	-	-	-	□□□□□
DOD20	94%	-	↑	↑	-	-	↑	□□□□□
REF	86%	-	↑	↑↑	↑	↑	↑	■□□□□
FD1	81%	-	↑	↑↑	↑	↑	↑	■■□□□
FC05	79%	-	↑↑	↑↑	-	↑	↑	■■■□□
REF_w/oCV	78%	-	↑↑	-	-	↑	↑	■■■□□
FC1	63%	↑	↑↑	-	-	↑↑	↑↑	■■■■■

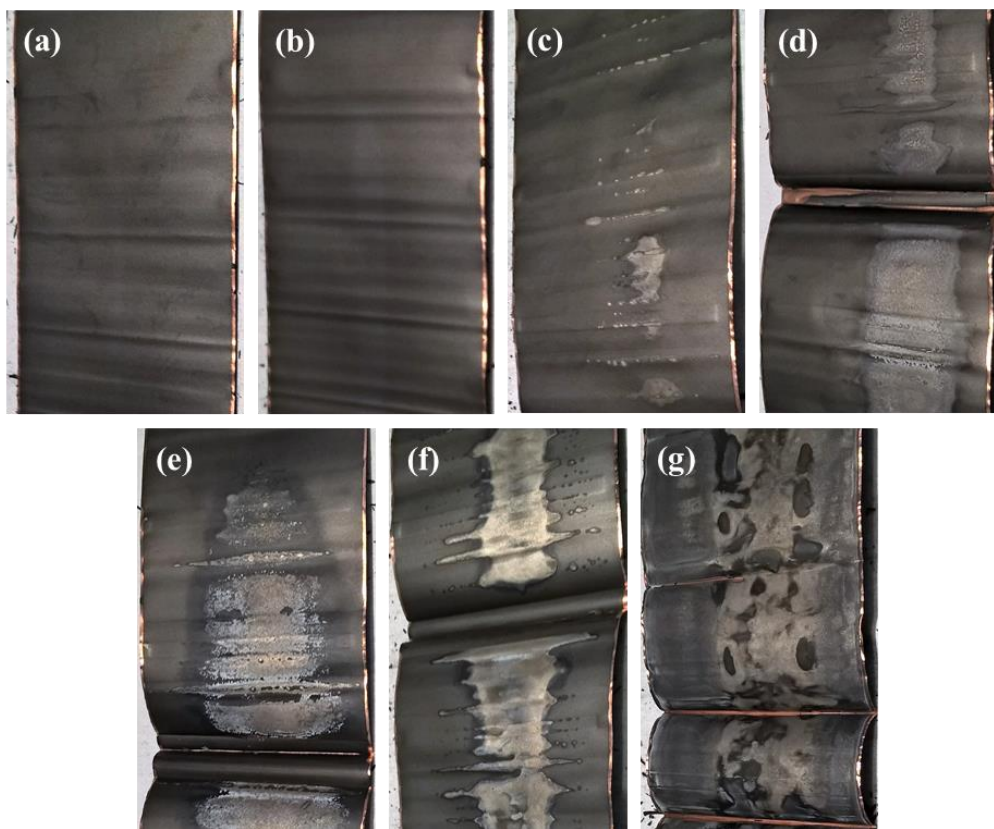


**Figure 4.7. Digital imaging of graphite electrodes:** (a) NEW cell; (b) DOD20 cell; (c) REF cell; (d) FD1 cell; (e) FC05 cell; (f) REF\_w/oCV cell; (g) FC1 cell.

Optical microscopy has been then applied to some graphite samples as listed in Table 4.1 to investigate deeper graphite degradation at the  $\mu\text{m}$  scale. Figure 4.8 shows the results of optical microscopy applied to cell ID:NEW, cell ID:REF and cell ID:FD1 both in a not plated area and plated one. In the first two cases (Figure 4.8-a and -b), the graphite structure is clearly visible over the whole observed area and, despite cell ID:REF reached EoT at 86% SoH, no structural changes or damages are detected if compared to pristine graphite (ID:NEW). In the case of Figure 4.8-c, the graphite structure is visible in the background but a formation on the electrode surface hinders it partially. This formation, not visible in electrode pictures, is associated to SEI layer decomposition which led to lithium plating. When focusing on a fully plated graphite area for the same cell (Figure 4.8-d), the graphite structure is fully covered by a layer of lithium metal with visible cracks. SEM imaging is used to investigate plated and not plated regions when compared to the pristine sample (ID:NEW). Figure 4.9-b shows cell FD1 not plated region: graphite grains are still visible as in cell ID:NEW (Figure 4.9-a) but partially covered with film

#### 4. Detection of Li-ion cells degradation with DRT

formation. This film has cracks and irregular morphology as the one observed on the plated region of cell ID:FD1 (Figure 4.9-c). This confirms that lithium plating, as product of SEI layer growth, is present also when not visible with digital imaging. In general, the partial or full covering of graphite grains could inhibit the ions exchange during cell charging and discharging processes. Consequently, the presence of plating is not only causing consumption of lithium ions but also loss of anode material due to its inhibition; this phenomenon is considered as graphite degradation and, in turn, affect graphite charge transfer reactions. This conclusion validates the attribution of peak S5 both at BoL and EoL/EoT to graphite charge transfer and its degradation (Table 4.4).

Overall, imaging applied to the graphite electrode allowed to validate two DRT peaks: (i) peak S2, which is associated to SEI layer with its growth/decomposition degradation mechanisms and lithium plating, and (ii) peak S5, which is associated to graphite charge transfer reaction and graphite degradation (loss of active material).

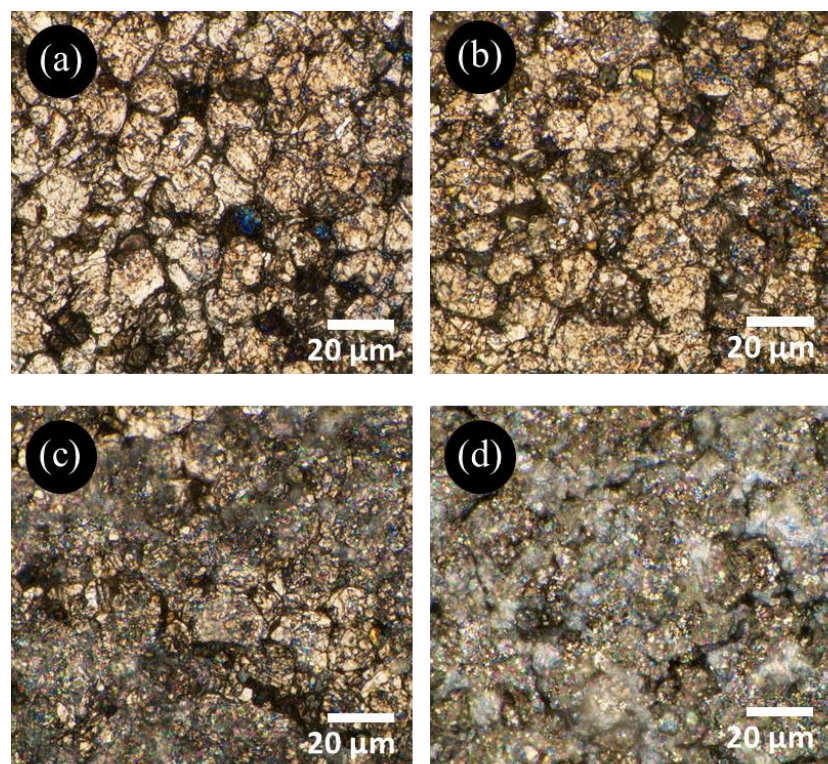


**Figure 4.8. Optical microscope imaging of graphite electrodes:** (a) NEW cell; (b) REF cell; (c) FC1 cell in a not plated area; (d) FC1 cell in a plated area.

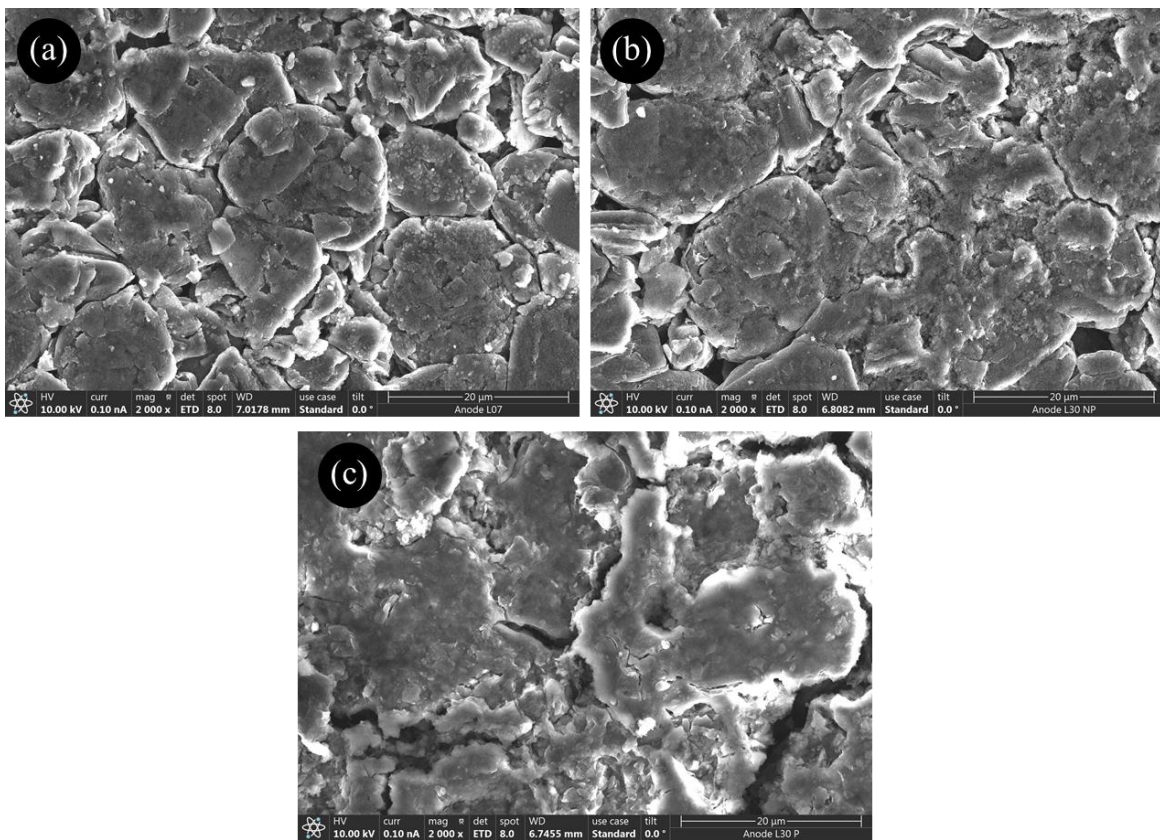


**Figure 4.9. SEM imaging of anode electrodes:** (a) NEW cell; (b) FC1 cell in a plated region; (c) FC1 cell in a not plated region.

#### NMC electrode

Differently from the graphite electrode, NMC electrodes did not show visible degradation during unrolling. The cross-comparison of all pictures taken with the digital camera showed no differences in terms of colours or surface deterioration. Therefore, more accurate investigations were performed with optical microscopy and SEM. If the first only allowed to observe the structure of NMC with its grains, or well-known “secondary particles”, the magnification from SEM provided insights on the degradation mechanisms. Figure 4.10 shows the surface and cross-section SEM images of cell ID:NEW (a-d), cell ID:FC1 (b-e) and cell ID:REF (c-f). In all cases, the cathode structure with secondary particles of variable size is well visible. Cell ID:NEW (100% SoH) and ID:FC1 (63% SoH) are quite similar in term of particles size and materials brightness. Most probably the severe fast charge protocol of cell FC1 (cell brought to EoL in less than 100 EqC) impacted only the graphite electrode, with no impact to cathode. In the case of cell ID:REF, Figure 4.10-c shows small cracks and a general higher shininess, which can be attributed to a

#### 4. Detection of Li-ion cells degradation with DRT

higher amount of non-electronic conductive material in the electrode, i.e. to NMC degradation [175]. Cracking is more evident analysing the cross-section sample in Figure 4.10-f, where several secondary particles are affected by this degradation mechanisms compared to the cross-section samples of cells NEW and FC1 (Figure 4.10-d,-e). The differences in degradation between REF and FC1 can be related to the same difference registered in DRT peaks S3 and S4 for the same cells (Table 4.4).

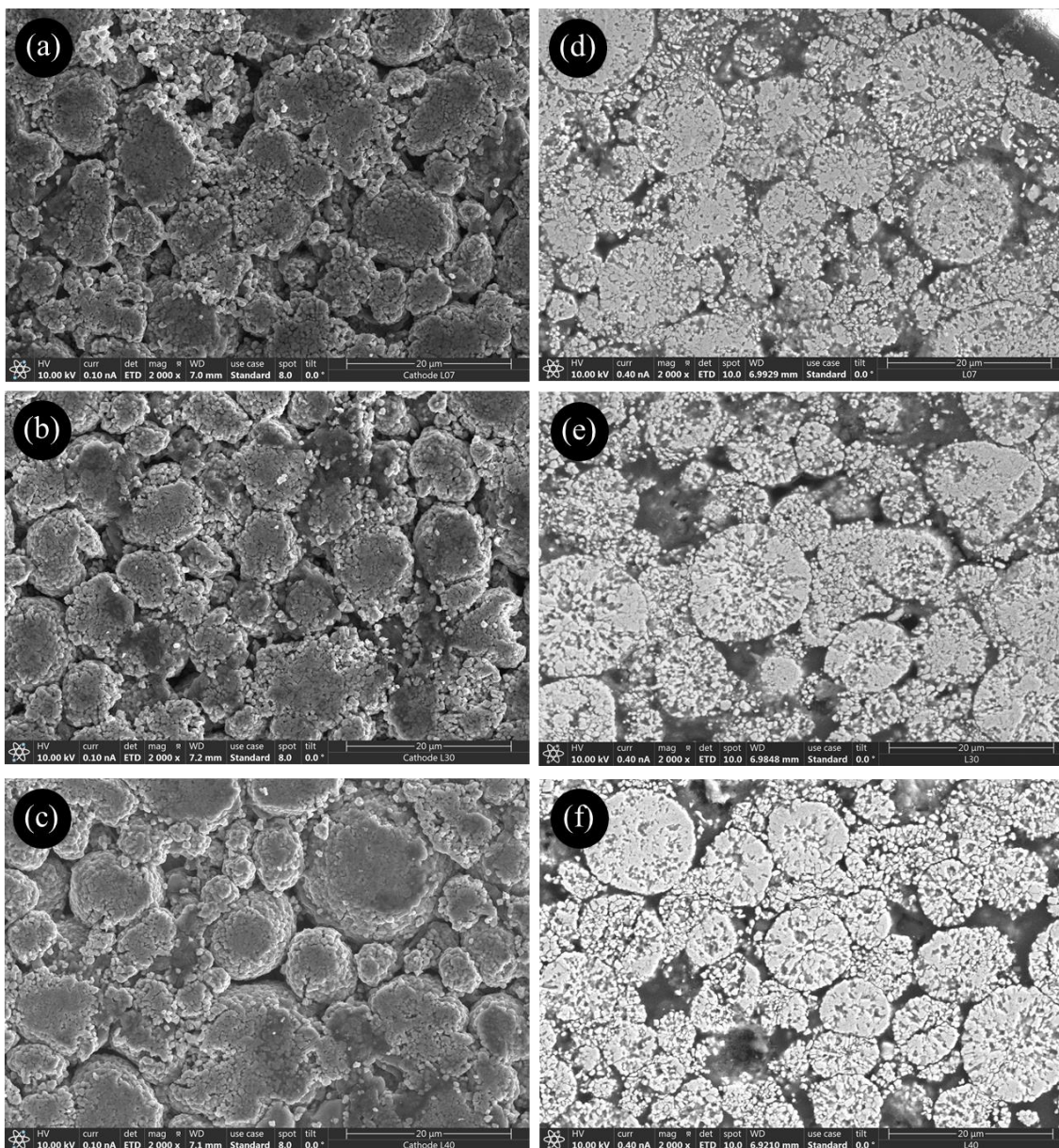


**Figure 4.10. SEM imaging of cathode electrodes.** Planar surface samples: (a) new cell; (b) FC1 cell; (c) REF cell. Cross-section samples: (d) new cell; (e) FC1 cell; (f) REF cell.

While in REF cell there is a rise in magnitude for both peaks, this is not the case for cell ID:FC1. Therefore, it is concluded that peaks S3 and S4 can be used to track cathode degradation, mostly related to particle cracking.

#### *Validation: final remarks*

Imaging techniques allowed to validate the tentative peak attributions made at BoL (Table 4.2) and EoL/EoT (Table 4.3). The summary of physical processes and degradation mechanisms attributed to the DRT peaks of cylindrical cells is reported in Table 4.5, including the time constant range for each peak. On one side, the peaks univocally attributed to the anode are S2, which accounts for SEI layer and its growth/decomposition (including lithium plating), and S5 which accounts for graphite charge transfer and its degradation. On the other side, the peaks univocally attributed to the cathode are S3 and S4, which both account for charge transfer processes and cathode particle cracking degradation. Peak S1 accounts for electric and magnetic effects and it is invariant with respect to cell degradation. Peak S6 accounts for diffusive processes and its behaviour with respect to aging depends mainly by the kinetic caused in turn by the general degradation at the two electrodes.

**Table 4.5. Conclusive DRT peaks attribution: physical processes and degradation mechanisms.**

	DRT peaks cylindrical cell					
	S1	S2	S3	S4	S5	S6
<b>Time constant range [s]</b>	< 10 <sup>-3</sup>	10 <sup>-3</sup> - 10 <sup>-2</sup>	10 <sup>-2</sup> - 10 <sup>-1</sup>	10 <sup>-1</sup> - 10 <sup>0</sup>	10 <sup>0</sup> - 10 <sup>1</sup>	> 10 <sup>1</sup>
<b>Physical process</b>	electric and magnetic effects	SEI	Cathode Charge Transfer / CEI	Cathode Charge Transfer	Anode Charge Transfer	Diffusion processes
<b>Degradation mechanism</b>	-	SEI growth/decomposition; Li plating	Cathode particle cracking		Graphite degradation	kinetic slow down

#### 4.4. Final remarks

EIS and DRT were investigated as a comprehensive measurement and a promising post-processing method to analyse cell aging and to detect the different degradation mechanisms, respectively. DRT is a powerful tool to magnify the polarization effects overlapped in the frequency domain by a peaks-based representation with different peaks (six for the tested cells) characterized by different magnitudes and time constants.

Different cycling protocols have been applied on commercial Li-ion cells to emulate different aging paths, including high charging and discharging rates and reduced DoDs. We analysed DRT profiles at BoL and EoL/EoT and compared them for cylindrical cells and lab-made cells in coin format (full-cells, cathode half-cells and anode half-cells). The objectives were to discriminate between the processes happening at the cathode or the anode sides by analysing the analogies between the lab-made half-cells and full-cells measurements, and to relate them to specific DRT peaks of commercial cells. Imaging techniques (digital imaging, optical microscopy and SEM) on samples extracted from the cylindrical cells were used to assess the degradation mechanisms happening at cathode and/or anode and ultimately to validate their tentative DRT peaks attribution.

The summary of physical processes and degradation mechanisms attributed to the six DRT peaks is as follows: (i) peak S1 is invariant with respect to aging and attributed to electric and magnetic effects; (ii) peak S2 is attributed to ion transport through graphite's SEI layer and it is influenced by SEI growth/decomposition and lithium plating degradation mechanisms; (iii) peaks S3 and S4 are attributed to cathode charge transfer reactions and to NMC degradation due to particle cracking; (iv) peak S5 is attributed to graphite's charge transfer reactions and its related graphite degradation and (v) peak S6 is attributed to diffusive processes and accounts for general kinetic slow down due to general degradation at both electrodes.

The use of imaging techniques validated the different ageing attribution at the graphite and NMC electrodes. In the first case, lithium plating was detected via digital imaging and optical microscopy and its formation from SEI layer growth/decomposition was confirmed with SEM. In the second case, only SEM imaging gave enough accuracy to appreciate particle cracking degradation on the cathode material. Therefore, it is

concluded that digital imaging can be used as a validation tool to spot “macro” degradation effects on the electrode surface; while more complex tools (e.g. optical microscopy, SEM) should be used to differentiate between them and to assess their severity.

Overall, the methodology presented in this chapter included: (i) cell testing with different aging conditions with EIS measurements at regular intervals and cell disassembly for post-mortem analyses (lab-cells making and imaging); (ii) analysis of DRT profiles at BoL and EoL for peaks attribution, comparing lab-made cells (half-cells and full-cells) with cylindrical cells and (iii) validation of the peaks’ attributions through digital imaging, optical microscopy and SEM applied on anode and cathode electrodes. All these steps can be replicated and applied to other Li-ion cells with different format size or cathode chemistry. However, the application of the presented methodology could be limited by two factors: (i) DRT calculation depends on the quality of EIS measurements both for commercial and Lab-made cells, therefore it is necessary to collect reliable measurements; (ii) the validation of  $\mu\text{m}$ -scale degradation mechanisms is only possible with expensive and complex technique (such as SEM).

The next chapter will exploit the results of DRT peaks attribution to develop suitable indicators to quantify cell degradation and to reliably estimate SoH, avoiding long full capacity measurements.



# Chapter 5

## Physics-based SoH estimation

Accurate State of Health (SoH) estimation is crucial to optimize the lifetime of Li-ion cells while ensuring safety during operations. This chapter introduces a methodology to track Li-ion cells degradation and estimate SoH based on Electrochemical Impedance Spectroscopy (EIS) measurements. Distribution of Relaxation Times (DRT) is exploited to derive indicators linked to the so-called Degradation Modes (DMs), which group the different aging mechanisms. The combination of these indicators is used to model the aging progression over the whole lifetime (both in the “pre-knee” and “after-knee” regions) enabling for physics-based SoH estimation. The methodology is applied to commercial cylindrical cells (NMC811|Graphite SiO<sub>x</sub>). The results show that Loss of Lithium Inventory (LLI) is the main driving factor for cell degradation, followed by Loss of Cathode Active Material (LAMc). SoH estimation is achievable with a Mean Absolute Error lower than 0.75% for SoH values higher than 85% and lower than 3.70% SoH values between 85% and 80% (End of Life). The analyses of the results allowed to define guidelines to replicate the presented methodology in order to characterize new Li-ion cell types and perform onboard SoH estimation in Battery Management System (BMS) solutions.

The content of this chapter is under review to be published in Batteries (MDPI) as “Physics-based SoH estimation for Li-ion cells” [176].

## 5.1. Context

Li-ion cells are considered a promising and mature technology to guide the ecological transition to renewable energy sources for mobile devices, transportation sector and also for stationary storage [177]–[179]. This success is based on high energy and power density, long cycle life, relatively high safety and continuously decreasing cost [180]–[182]. Smooth and safe operations of Li-ion cells are ensured by the Battery Management Systems (BMSs). BMSs include several features to monitor the battery cells, to ensure safe operations, and to optimize battery lifetime [35], [183]. As regard the latter point, the tracking of battery health evolution is crucial but challenging because power and capacity fade are caused by various interdependent degradation mechanisms that affect the components inside the cells [107], [161]. As introduced in Chapter 2, those mechanisms can be clustered depending on their main effects into the so-called Degradation Modes (DMs): (i) Loss of Lithium Inventory (*LLI*), which accounts consumption of lithium ions for decomposition reactions, Solid Electrolyte Interface (SEI) layer growth and lithium plating; (ii) Loss of Cathode Active Material (*LAM<sub>C</sub>*), which accounts electrode structural disordering, particle cracking and loss of electric contact and (iii) Loss of Anode Active Material (*LAM<sub>A</sub>*) which accounts the same mechanisms of *LAM<sub>C</sub>* but on the anode side, including also graphite exfoliation and blocking of active sites by passivation surface layers [105]–[107].

Next generation BMSs will exploit non-invasive characterization techniques to provide indication of the occurring DMs and ultimately estimate the State of Health (SoH) [32], [60], [184]. Among the different techniques presented in literature, the most suitable measurements to achieve the objective are: (i) pseudo-Open Circuit Voltage (pOCV), i.e. full charge or discharge profile at low constant current and (ii) Electrochemical Impedance Spectroscopy (EIS), that maps cell's impedance over different galvanostatic or potentiostatic excitation frequencies [59], [185].

pOCV-based techniques allow to identify and quantify DMs with high accuracy but they require low current rate and long test duration to obtain a quasi-equilibrium condition (i.e. no-load condition). However, it is difficult to achieve these conditions during battery operations [185]. pOCV curves of the two electrodes at Beginning of Life (BoL) are directly used in the so called “pOCV methods” to assess degradation in a backward basis [106],

[107], [186]. Even though parametric models have been introduced to estimate *LLI* and *LAM*, the main drawback is that the DMs may not be estimated uniquely [186]. Other pOCV-based methods are the Incremental Capacity (IC) and Differential Voltage (DV) analyses, based on the evaluation of specific features from the OCV profiles. *LAM* and *LLI* indicators are obtained in [63] respectively by IC and DV curves and in [187] by IC curves highlighting the longer incubation time of *LAM* at anode and cathode sides with respect to *LLI*. IC profiles are also exploited for SoH estimation, as shown by Schaltz et al. in [188] and by Lin et al. in [189]. However, the main disadvantage for practical implementation of IC/DV method is the need of smooth and high resolution OCV profiles, which demand for additional computational effort from the BMS hardware in on-board applications [185].

EIS-based techniques allow for a shorter diagnosis and provide valuable information to understand the processes and degradation mechanisms occurring inside the cell [33], [128], [131], [141]. In general, Electric Circuit Models (ECM) are exploited to extract the features of interest and develop degradation indicators. For instance, Pastor-Fernández et al. identified *LLI* from the Mid-frequency region (semiarch) and *LAM* from Low-frequency region (diffusive tail) in [63]. However, the authors explained that the accuracy is highly dependent on measurement quality and the chosen ECM. As mentioned in previous chapters, a way to overcome the model dependency is to apply Distribution of Relaxation Times (DRT), which helps in highlighting the processes that are usually overlapped in the frequency domain (impedance Nyquist plot) [118], [135], [136]. Zhou et al. proposed in [190] and later in [80] a technique to evaluate the growth of resistance related to contact, SEI, charge transfer and diffusion polarization processes. The authors demonstrated the utility in monitoring battery aging and the advantage of using DRT to separate electrolyte- and solid-phase diffusion. However, the analyses were limited to the model parameters and not to the different DMs and SoH estimation. Carthy et al. performed a detailed review about SoH estimation with EIS, showing that ECM fitting methods are widely applied [191]. Those methods showed maximum estimation error between 3.7% and 15% depending on the cell chemistry and on the testing conditions [97], [192]–[194]. However, in most of the cases, even if EIS provide valuable information about the physical processes occurring in the cell, the resulting SoH estimation is not directly related to the physical processes and degradation mechanisms occurring inside

the cell. Zhang et al. instead, proposed a SoH estimation method based on DRT while applying data-driven methods, showing a maximum RMSE of 1.65% [185]. However, the work did not include a specific quantification of DMs but only the evolution of the parameters linked to SoH estimation. For practical implementation of the EIS-based methods described above, different approaches have been presented in literature to perform EIS measurements: use of AC signal generator which can apply current with specific frequency to battery pack [195], [196]; signal processing methods [197] and smart sensing management systems that allows direct measurement of cell impedance [198]. Moreover, there are products already available on the market, such as the evaluation boards and management systems described in [199], [200].

In summary, the main limitations from the literature are twofold: (i) the need of long and complex measurements, as for instance the pOCV and its IC/DV derivation, which make them unexploitable in BMS applications; (ii) the challenge in fitting EIS from ECM, and its utilization for SoH estimation, being aware of the degradation occurring in the cell. The work presented in this chapter aims at overcoming these two limitations by:

1. Defining a suitable EIS-based SoH estimation model which uses degradation indicators directly linked to DMs, allowing principled modelling of the physical phenomena (i.e. physics-based SoH estimation).
2. Defining a simple and robust framework that could be exploited for online-SoH estimation by next generation smart BMSs based on (i) an appropriate testing campaign to initialize the SoH estimation model for a new Li-ion chemistry/model and (ii) the capability to run onboard EIS measurement.

The chapter is organized as in the followings. Section 5.1 presents materials and methods. The inputs of this work (i.e. material) are the results of cycling aging tests, including EIS measurements, and the DRT calculation algorithm with peaks attribution, as presented in Chapter 3 and Chapter 4. This work exploits the findings of the previous ones extending the use of DRT to obtain quantitative information about cell degradation with specific indicators and performing SoH estimation from those indicators. The methodology is applied on the experimental dataset in Section 5.3, where the results about degradation indicators and SoH estimation are showed. Section 5.4 presents the output of this work:

(i) discussion of the obtained results and (ii) the guidelines to perform online degradation tracking and SoH estimation in BMSs. Final remarks are given in Section 5.5.

## 5.2. Materials and Methods

### 5.2.1. Inputs: experimental dataset and DRT characterization

The experimental dataset used in this work includes cycling aging tests performed on the commercial cylindrical cells already exploited in Chapter 4 and presented in Table 5.1 (the full cell's datasheet is available in Appendix D). The testing campaign has been performed at the CSEM's Sustainable Energy Center, Neuchâtel (Switzerland) with testing set-up composed of: (i) a cell tester Biologic BCS815 equipped with 32 parallel, 9V-15A channels ( $\pm 0.01\%$  FSD accuracy on the voltage and  $\pm 0.015\%$  FSD accuracy on current, for each available range) with EIS spectrometer multiplexed and able to range from 10kHz to 10mHz (Figure 5.1-a) [157]; and (ii) a thermostatic chamber ATT-DM1200T with -45°C-180°C temperature range (Figure 5.1-b) [158]. Ten different cycling conditions have been studied and their details together with the corresponding cell's IDs are given in Table 5.2. The tests have been performed in the thermostatic chamber at a constant temperature of 20°C (Figure 5.1-c).

**Table 5.1. Main characteristics of the cylindrical commercial cell under investigation. Current-rate (C-rate) values are calculated with respect to the nominal capacity.**

<b>Cell name</b>	INR21700 M50
<b>Manufacturer</b>	LG Chem
<b>Cathode chemistry</b>	NMC811
<b>Anode chemistry</b>	Graphite-SiO <sub>x</sub>
<b>Nominal capacity [mAh]</b>	5010
<b>Nominal voltage [V]</b>	3.63
<b>Standard charge current [mA]</b>	1455 (C-rate: C/3)
<b>Standard discharge current [mA]</b>	970 (C-rate: C/5)
<b>Standard cycling current [mA]</b>	1455 (C-rate: C/3)
<b>Maximum voltage [V]</b>	4.2
<b>Minimum voltage [V]</b>	2.5
<b>Current cut-off [mA]</b>	50 (C-rate: C/100)
<b>Weight [g]</b>	68.0

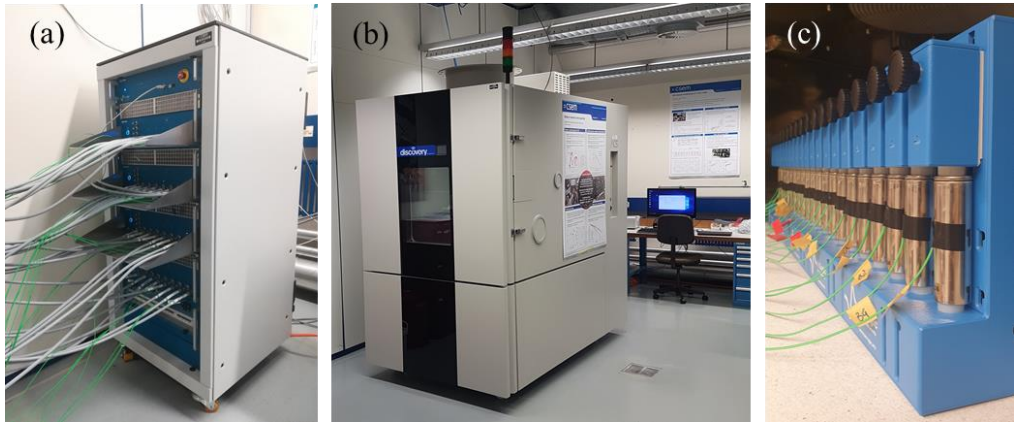


**Figure 5.1. Overview of equipment and cells in Sustainable Energy Center laboratory at CSEM.** (a) Biologic BCS815 Battery tester; (b) ATT-DM1200T Thermostatic chamber and (c) NMC 811 cells under investigation inside the thermostatic chamber.

The reference case (ID:REF) has been set following the details given by the cell manufacturer. Then, in the other cases the Depth of Discharge (DoD), charging rate or discharging rate have been tuned to obtain different degradation paths. The cells have been cycled until End of Life (EoL) or End of Tests (EoT). In the first case, the tests were stopped as soon as they reached SoH = 80%. In the second case, the tests were stopped whenever the cell reached 1000 Equivalent Cycles (EqC) regardless the SoH level, where the EqC is defined as the ratio between the cumulated cycled capacity and two times the initial capacity. At Beginning of Life (BoL) and every 50 EqC a diagnosis phase was run to measure the cell capacity  $C_i$  ( $C_0$  being the one at BoL) and EIS spectra at different SoCs. The capacity measurements have been used to calculate the SoH as the standard ratio  $C_i/C_0$ .

The SoH progressions for the different testing protocol are shown in Figure 5.2. The cells cycled at reduced DoD have been all stopped due to EoT rather than EoL, with SoH higher than 90% in all cases. High discharging rate tests and specifically cells ID:FD05 and FD1 showed a SoH evolution curve similar to cell ID:REF, with SoH higher than 85% at 1000 EqC. Highly fast-charged cells (ID:FC1 and ID:FC2) showed a steep capacity fade, reaching EoL with a number of cycles lower than 100. The remaining cells (ID:REF\_w/oCV and FC05) instead showed the so-called “knee” (inflection-point) where degradation accelerates leading to larger capacity fade. The “knee” can be caused by different pathways (or failure modes) that are driven by a complex combination of parameters,

such as cell geometry, testing condition and degradation status of the cell components [201]. Generally, this inflection-point is attributed to the onset of irreversible lithium plating on the anode surface and it is unrelated to the linear aging behaviour before this point [79], [202]. Therefore, it is relevant to separate those two degradation regions and model them separately: in the following sections, the cells degradation will be described as “pre-knee” or “after-knee” based on the characteristics described above.

**Table 5.2. Overview of cycling aging testing protocols applied to commercial Li-ion cells. The cycling test type is compared to the reference case (1<sup>st</sup> row).**

Cell ID	Cycling test type	DoD [%]	SoC interval [%]	Charging rate	Discharging rate
REF	Reference case (by datasheet)	100	0-100	C/3 <sup>1</sup>	C/3
REF_w/oCV	Reference without CV phase	100	0-100	C/3	C/3
DOD20	Reduced DoD	20	80-100	C/3	C/3
DOD60	Reduced DoD	60	20-80	C/3	C/3
FC05	Faster charging rate	100	0-100	C/2 <sup>1</sup>	C/3
FC1	Faster charging rate	100	0-100	1C <sup>1</sup>	C/3
FC2	Faster charging rate	100	0-100	2C <sup>1</sup>	C/3
FD05	Faster discharging rate	100	0-100	C/3 <sup>1</sup>	C/2
FD1	Faster discharging rate	100	0-100	C/3 <sup>1</sup>	1C
FD2	Faster discharging rate	100	0-100	C/3 <sup>1</sup>	2C

<sup>1</sup> Including Constant Voltage phase with cut-off current at C/50.

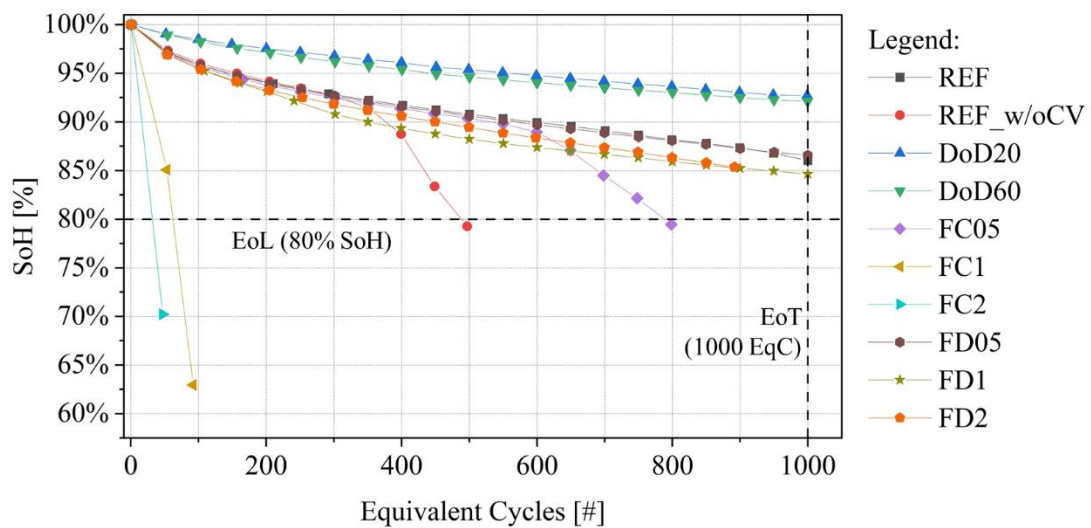


**Figure 5.2. SoH evolution curves over EqC for the cells under investigation.** The details about cycling conditions are given in Table 5.2. Most of the cells reached EoT (i.e. 1000 EqC). High charging rate induced faster degradation than in the other cases reaching EoL reducing cells cyclability.

EIS spectra are validated via Kramers-Kronig (KK) test to verify quality and time invariance and are used to compute DRT profiles (more details in Appendix A) [140], [142]. As presented in Chapter 3, the DRT calculation assumes that an impedance spectrum  $Z(j\omega)$  can be represented as the sum of a resistor that represent ohmic resistance ( $R_{ohmic}$ ) and an infinite series of RC elements, as shown in equation 3.1 in Chapter 3 and for ease of reference here below:

$$Z(j\omega) = R_{ohmic} + \int_0^{\infty} \frac{g(\tau)}{1+j\omega\tau} d\tau, \quad (5.1)$$

where  $g(\tau)$  is the function that represents the time relaxation characteristics of the electrochemical system under evaluation and that satisfies the conditions of non-negativity (total and partial polarization resistances are positive for most of the electrochemical systems). The DRT function, i.e.  $g(\tau)$  is discretized and solved applying Tikhonov regularization method [143], [145]. Details about the mathematical formulation and the algorithm exploited for DRT computation from EIS of Li-ion cells are given in Chapter 3, Section 3.2.1. The peak-based representation of  $g(\tau)$  allows to discriminate between different processes occurring at different time constant values. The contribution of those processes is quantified with the resistance values  $R_i$  which are found by computing the area under the peaks, when knowing the time constant range  $[\tau_{beg}; \tau_{end}]$ :

$$R_i = \int_{\tau_{beg}}^{\tau_{end}} g(\tau) d\tau \quad (5.2)$$

The DRT peaks attribution is crucial to determine which are the main processes and degradation mechanisms occurring in the cells. As mentioned above, this work exploits the peak attribution performed in [160], where previous works, such as the analyses of Wildfeuer et al. in [164] and Zhou et al. in [80], have been analysed and extended with experimental investigations on the same cell type selected in this work. Commercial cells and half-cells DRT profiles were compared to understand the impact of the two electrodes and were validated applying post-mortem analyses with imaging techniques. Those information are used in the next Section to define proxy indicators to track cell degradation.

### 5.2.2. Methodology

Figure 5.3 represents the typical DRT profile of the cells under investigations. The results of DRT peaks attribution have been exploited to define which peaks need to be tracked to quantify which specific DMs:

- Peak 2 is attributed to the growth and decomposition of SEI layer and presence of lithium plating on the anode side; it will be used to account for Loss of Lithium Inventory ( $LLI$ ).
- Peak 3 and peak 4 are attributed to cathode degradation (specifically particle cracking for NMC811) and they are therefore used to account for Loss of Cathode Active Material ( $LAM_C$ ).
- Peak 5 is attributed to graphite degradation and it is hence used to account for Loss of Anode Active Material ( $LAM_A$ ).

The resistance values of the peaks describing the DMs are combined to quantify the total impedance  $R_{DM}$ :

$$R_{DM} = R_{LLI} + R_{LAM_C} + R_{LAM_A} \quad (5.3)$$

where  $R_{LLI}$  is the resistance of peak 2,  $R_{LAM_C}$  the resistance of peaks 3 and 4 and  $R_{LAM_A}$  the resistance of peak 5.  $R_{DM}$  is used as proxy in the following Sections deriving indicators to evaluate cell degradation and to estimate SoH.

#### *Degradation indicators*

Three indicators are defined to track the DMs occurring in Li-ion cells as percentage increase of  $R_k$  at diagnosis step  $i$  with respect to the initial state 0, where  $k = LLI, LAM_C$  and  $LAM_A$ . The generic indicator  $k_i$  is normalized with the initial total impedance  $R_{DM,0}$  and computed as follows:

$$k_i [\%] = \frac{R_{k,i} - R_{k,0}}{R_{DM,0}} \cdot 100, \quad k = LLI, LAM_C, LAM_A \quad (5.4)$$

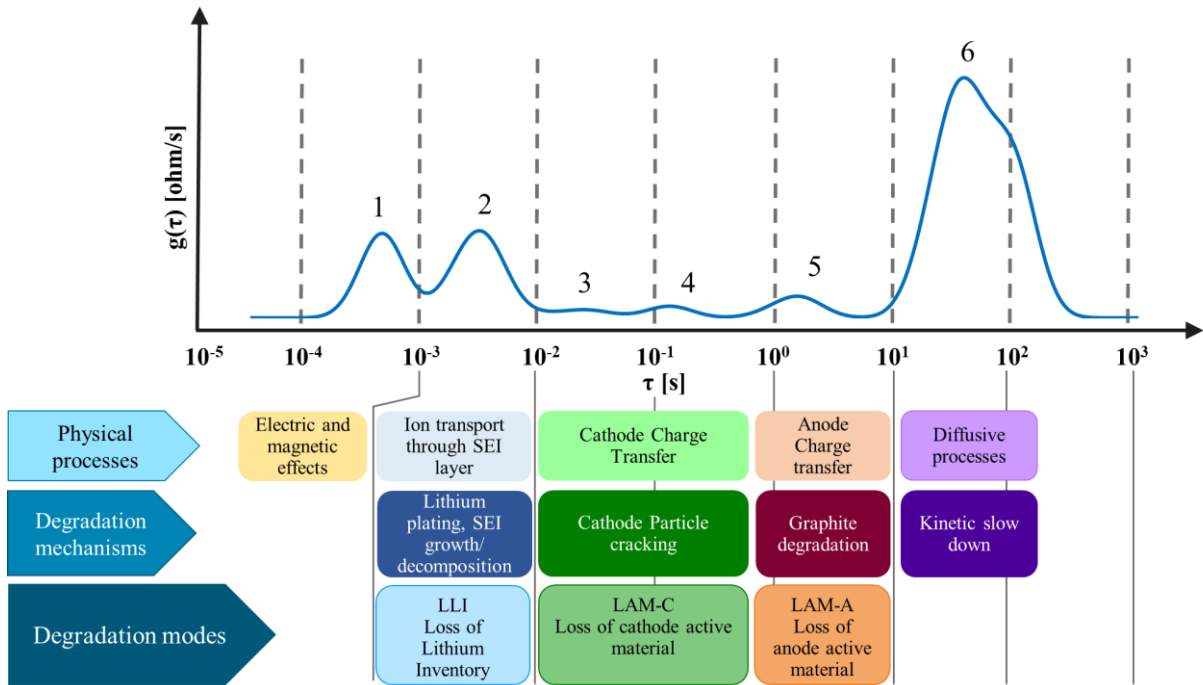


**Figure 5.3. Typical DRT profile of the cylindrical commercial cells under investigation.** Attribution of physical processes, degradation mechanisms and degradation modes. The readers are addressed to Chapter 4 for more details.

The computed values of those indicators could show deviations that are due to the DRT calculation (solving an optimization problem with regularization methods, as presented in Chapter 3, Section 3.2.1) but that could also come from noisy measurements, especially thinking about onboard implementation in BMS [63], [185]. Therefore, a method to filter the indicators is necessary to better appreciate the evolution of DMs and to understand which one is prevailing. The indicators' filtering process is based on a linear fitting model applied on a defined number of prior measured points with a sliding window. The process is composed by 3 steps, as shown in Figure 5.4:

1. A set of prior points is selected based on a sliding window of size  $W$  and is concatenated with the indicator  $k_{i\_calc}$  computed at diagnosis step  $i$ .
2. A linear fitting model is applied to the selected vectors.
3. The resulting corrected value of  $k_i$  computed with the linear model is added in the associated indicator vector for its exploitation.

The sliding window is applied to smooth the indicator small fluctuations and to highlight the large variations due to sudden increase of degradation (e.g. reaching “knee” point).

Knowing the maximum variation of DM indicators, corresponding at EoL condition, it is possible to fix limit thresholds to identify outliers and improve even more the filtering process. When  $k_{i\_calc}$  is considered outlier, the value of  $k_i$  is computed with the linear model obtained only with prior diagnosis points.

Once the degradation indicators are filtered, they are used to compute the Total Degradation Modes parameter  $TDM_i$  as follows:

$$TDM_i[\%] = LLI_i[\%] + LAM_{C,i}[\%] + LAM_{A,i}[\%] \quad (5.5)$$

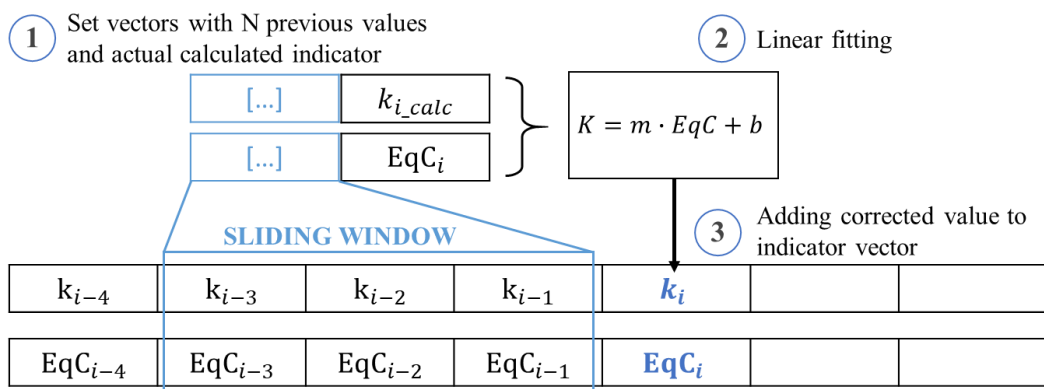


**Figure 5.4. Three-steps procedure to correct the degradation indicators:** 1) set vectors of degradation indicator with  $N$  previous values based on a sliding window; 2) apply a linear fitting model to find corrected value of the indicator and 3) add indicator corrected value in the associated vector.

#### SoH estimation

The parameter  $TDM_i$  is used as indicator to perform SoH estimation. The relationship between SoH and  $TDM_i$  is showed in Figure 5.5-a for the experimental dataset presented in Section 5.2.1: it is possible to distinguish two main regions that are related to the “pre-knee” and the “after-knee” progressions of the SoH trend (Figure 5.2). Having as objective SoH estimation in both the two regions, a piecewise model is adopted to build two SoH functions that represents “pre-knee” and “after-knee” degradations. In this way, the SoH model maintains a simple structure yet robust in the “after-knee” trend, crucial to avoid safety issues related to severely aged Li-ion cells.

Moreover, an additional indicator must be used to distinguish the two regions of Figure 5.5-a. All the parameters extracted by DRT together with the ohmic resistance  $R_{ohmic}$  have

been compared to find the most effective one. The analyses showed that the ohmic resistance variation between two consecutive measurements  $\Delta R_{\Omega,i}$  ( $(R_{ohmic,i} - R_{ohmic,i-1})/R_{ohmic,i-1}$ ) was providing the most accurate results in differentiating between “pre-knee” and “after-knee” behaviour.

Sensitivity analysis was performed to define the threshold value that better discriminate the two regions. A graphical validation of the threshold is obtained checking if the selected value allows to identify all the “after-knee” points on SoH progression curves. For the cells under investigation, the optimal result was found at  $\Delta R_{\Omega,i} = 1\%$ ; the graphical validation is showed in Figure 5.5-b.

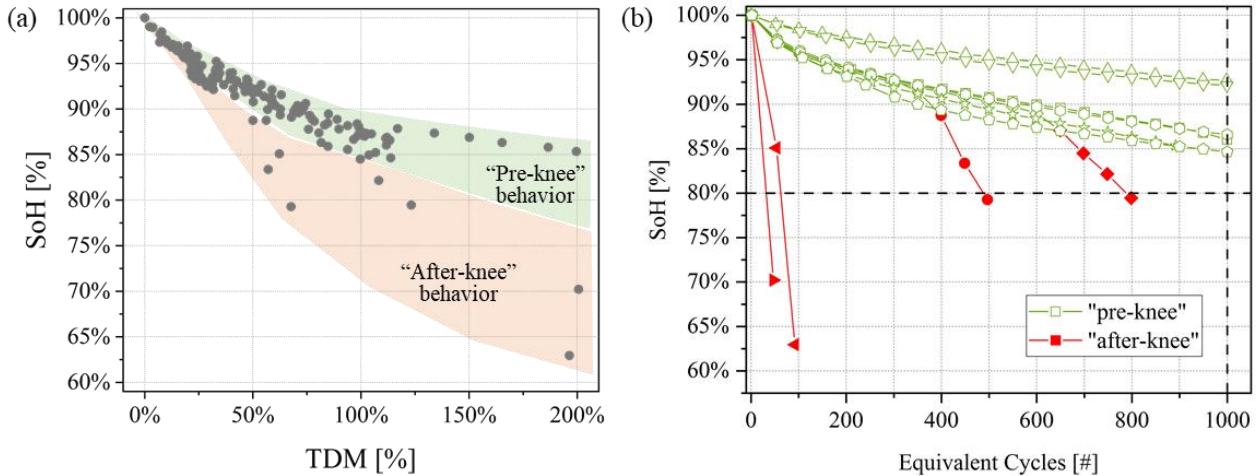


**Figure 5.5. SoH evolution of the cells under investigation.** (a) SoH evolution over  $TDM_i$  [%] values for the cells under investigation. Two regions are depicted, corresponding to “pre-knee” and “after-knee” behaviours. (b) Validation of  $\Delta R_{\Omega,i}$  threshold equal to 1%, identifying all the points with “after-knee” behaviour.

Once  $\Delta R_{\Omega,i}$  threshold is set, SoH can be estimated via logarithmic decay functions. This type of function allows to model the initial steep decay and the consequent slower decay for larger  $TDM_i$  values (Figure 5.5-a). Approaching the inflection point, i.e. the knee, a second function is used to represent the subsequent steep decay. The SoH piecewise model is described as follows:

$$SoH [\%] = \begin{cases} 1 - A_1 \cdot \log (B_1 \cdot TDM_i + 1), & \text{if } \Delta R_{\Omega,i} \leq 1\% \\ SoH_{last} - A_2 \cdot \log (B_2 \cdot (TDM_i - TDM_{last}) + 1), & \text{if } \Delta R_{\Omega,i} > 1\% \end{cases} \quad (5.6)$$

When the cells show “pre-knee” behaviour, i.e.  $\Delta R_{\Omega,i} \leq 1\%$ , the coefficients ( $A_1, B_1$ ) are found by fitting the available measurement of SoH. When the cells show “after-knee” behaviour instead ( $\Delta R_{\Omega,i} > 1\%$ ), the SoH function includes two additional parameters: the value of SoH ( $SoH_{last}$ ) and the value of the total degradation indicator ( $TDM_{last}$ ) before the knee. As described in Section 5.2.1, “after-knee” behaviour shows an acceleration in capacity fade unrelated to the previous aging behaviour. The two additional parameters are introduced to normalize the function because the “knee” does not occur always at the same conditions (i.e. SoH and  $TDM_i$ ) for each cell. Once these parameters are fixed with the last previous point computed in “pre-knee” condition, the coefficients ( $A_2, B_2$ ) are found by fitting the available measurements of SoH.

Finally, a validation flow has been conceived to evaluate the accuracy of the resulting SoH estimation. Training and validation subsets are shown in Figure 5.6. Given a specific number of tested cells  $n$  ( $n = 10$  in this case), the two subsets are defined as follows:

- Training subset:  $n_1$  cells are selected and their EIS measurements are used to compute degradation indicators and ohmic indicator. SoH values are fitted to find the parameters of the model described in equation 5.6.
- Validation subset:  $n_2$  cells (i.e.  $n_2 = 10 - n_1$ ) are used to compute the  $TDM_i$  indicator and the SoH is estimated with the SoH model checking the value of  $\Delta R_\Omega$ . Finally, the estimated value is compared with the one computed by capacity measurement.

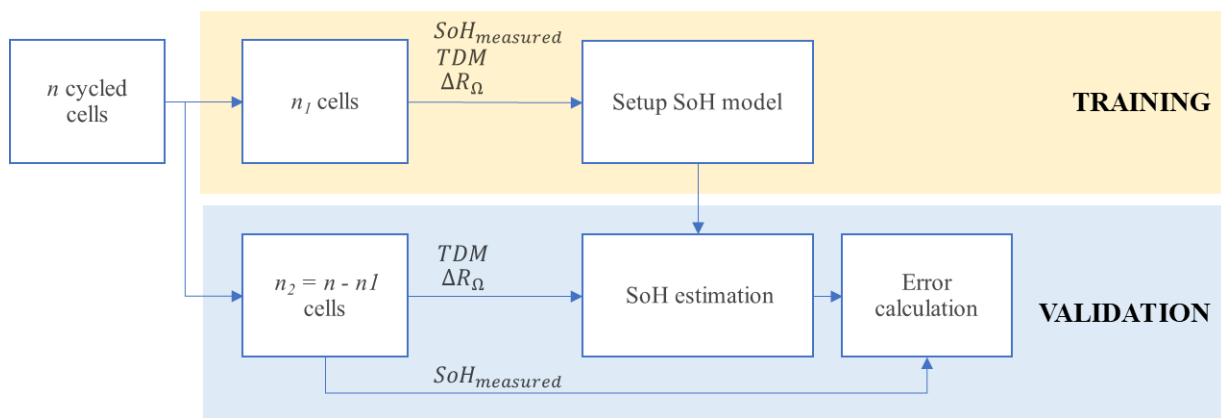


**Figure 5.6. Algorithm to evaluate the developed SoH model.** Training phase, to setup the SoH model and validation phase to perform SoH estimation and evaluate the error.

The error  $E_i[\%]$  between estimated ( $SoH_{estimated,i}$ ) and measured ( $SoH_{measured,i}$ ) SoH is defined as:

$$E_i[\%] = SoH_{estimated,i} - SoH_{measured,i} \quad (5.7)$$

Therefore, a positive error means overestimation and a negative error means underestimation. The estimation error is evaluated for all the measured SoH values (every 50 eqC). Box plots are exploited to interpret the quality of the estimation. Two additional performance indicators are used to quantify reliability on the estimation: the Mean Bias Error (MBE) and the Mean Absolute Error (MAE). The first one captures the average bias in the estimation and is computed as follows:

$$MBE [\%] = \frac{1}{n} \cdot \sum_{i=1}^n E_i \quad (5.8)$$

where  $n$  is the total number of diagnosis points. General underestimation of SoH could be a disadvantage on economic point of view, because the battery could not be exploited in the best way, but it could be an advantage in terms of safety, especially in “after-knee” conditions when the capacity fade is very fast. In this way, it could be possible to avoid cell dangerous conditions. The second performance indicator takes the absolute values of the individual estimation errors and gives more direct information on correctness of the estimation. It is computed as follows (given  $n$  number of points):

$$MAE [\%] = \frac{1}{n} \cdot \sum_{i=1}^n |E_i| \quad (5.9)$$

### 5.3. Results

The results obtained by applying the above methodology on the experimental dataset presented in Section 5.2.1 will be shown in the followings. The algorithms have been developed in python and all the scripts are available in a specific repository [159]. Specifically, Section 5.3.1 will give a quantification to the degradations indicators, and Section 5.3.2 will present the SoH estimation results obtained by using the same.

### 5.3.1. Degradation indicators

The degradation indicators have been computed selecting the EIS spectra measured at 50% SoC on the cells listed in Figure 5.2. On average, the KK test returned maximum residuals lower than 1.1% from BoL to EoL/EoT, which allows for a reliable DRT calculation. The equations presented in Section 2 have been then used to compute the DMs and the degradation indicators. An example of the indicators is given in Figure 5.7-a,b,c for cell ID:REF. The plots show both the calculated values of  $LLI_i$ ,  $LAM_{C,i}$  and  $LAM_{A,i}$  and the filtered values (sliding window size equal to 7 prior points) that are highlighted with dashed lines. The three DMs show different evolutions over the cell lifetime (i.e. at increasing EqC):

- $LLI$  (Figure 5.7-a): a monotonic growth is observed until around 400 EqC when the indicator decreases its growth and starts to oscillate.
- $LAM_C$  (Figure 5.7-c): cell's cathode is not impacted by degradation until 200 EqC; after this point it shows a constant growth up to 60% at 1000 EqC.
- $LAM_A$  (Figure 5.7-b): this DM is not affecting cell performances until about 800 EqC. Moreover, its magnitude is of one order of magnitude lower than the other two indicators.

Those trends suggest that cell aging is mainly driven by SEI-related degradation and lithium plating up to 400 EqC and then by cathode degradation (particle cracking), growing with a faster rate than  $LLI$  related mechanisms until EoT. Graphite degradation is negligible and not influencing battery performances.

The total degradation indicator  $TDM$  is showed in Figure 5.7-d, where the corrected trend (i.e. sum of corrected DMs) shows a more stable evolution compared with the calculated one.

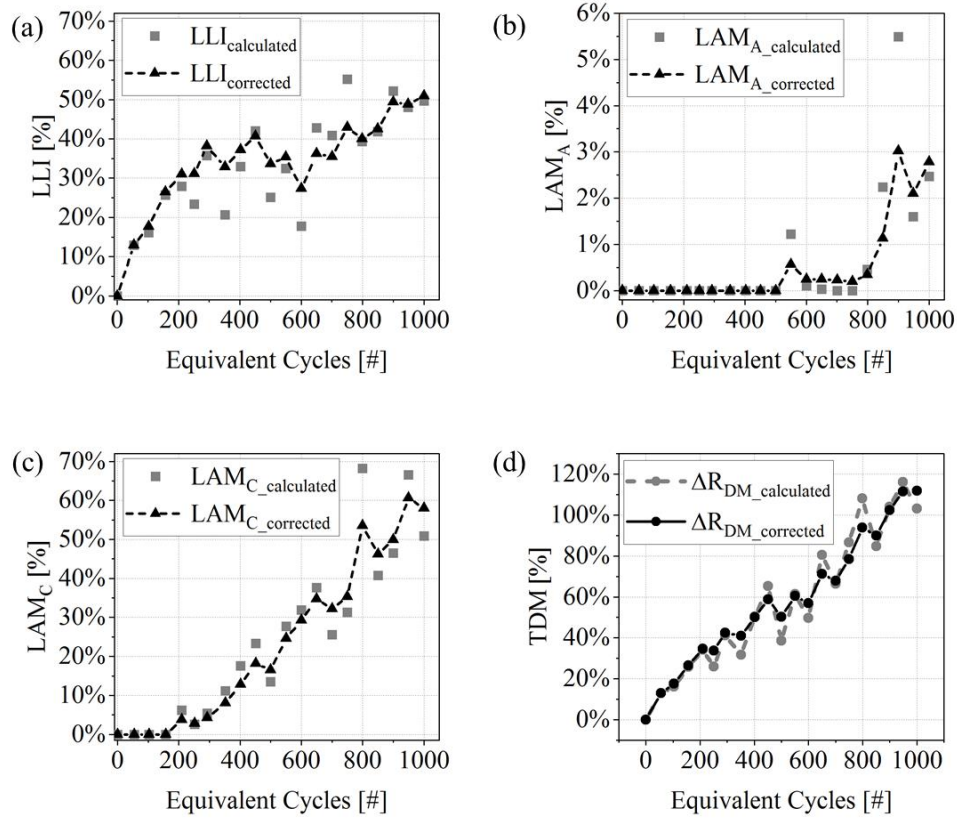


**Figure 5.7. Example of degradation indicators trends.** The indicators have been computed for cell ID:REF (cycling in reference condition, C/3 symmetric with Constant Voltage-phase during charge). The plots show both the not corrected and corrected values of: (a) LLI, (b) LAM<sub>A</sub>, (c) LAM<sub>C</sub> and (d) TDM.

Figure 5.8 presents an overview of all the degradation indicators of all the tested cells (reference to cell IDs in Table 5.2). Each DM is represented with a different color and their cumulated area represents the indicator *TDM* as function of EqC. In general, *LLI* has a big influence on cell degradation and it is the main DM for reduced DoD protocols (Figure 5.8-c,d), but it is also true that the same cells (ID:DOD20, ID:DOD60) recorded the smallest *TDM*, with values lower than 30% at EoT (at 1000 EqC). In other, more stressing conditions, also the other DMs appeared. In cell ID:REF, cell ID:FC05 and the high discharging rate cells, *LAM<sub>C</sub>* has also a large impact on degradation (Figure 5.8-a,e,h-l). In the cases of high discharging rate at 0.5C (cell ID:FD05) and at 2C (cell ID:FD2), *LAM<sub>C</sub>* growth up to 100% and 140%, being the most impacting DM and suggesting that cathode particle cracking is driving cell degradation. High charging rate conditions at 1C and 2C instead brought to large and fast degradation, with an increase of *TDM* up to 200% in less

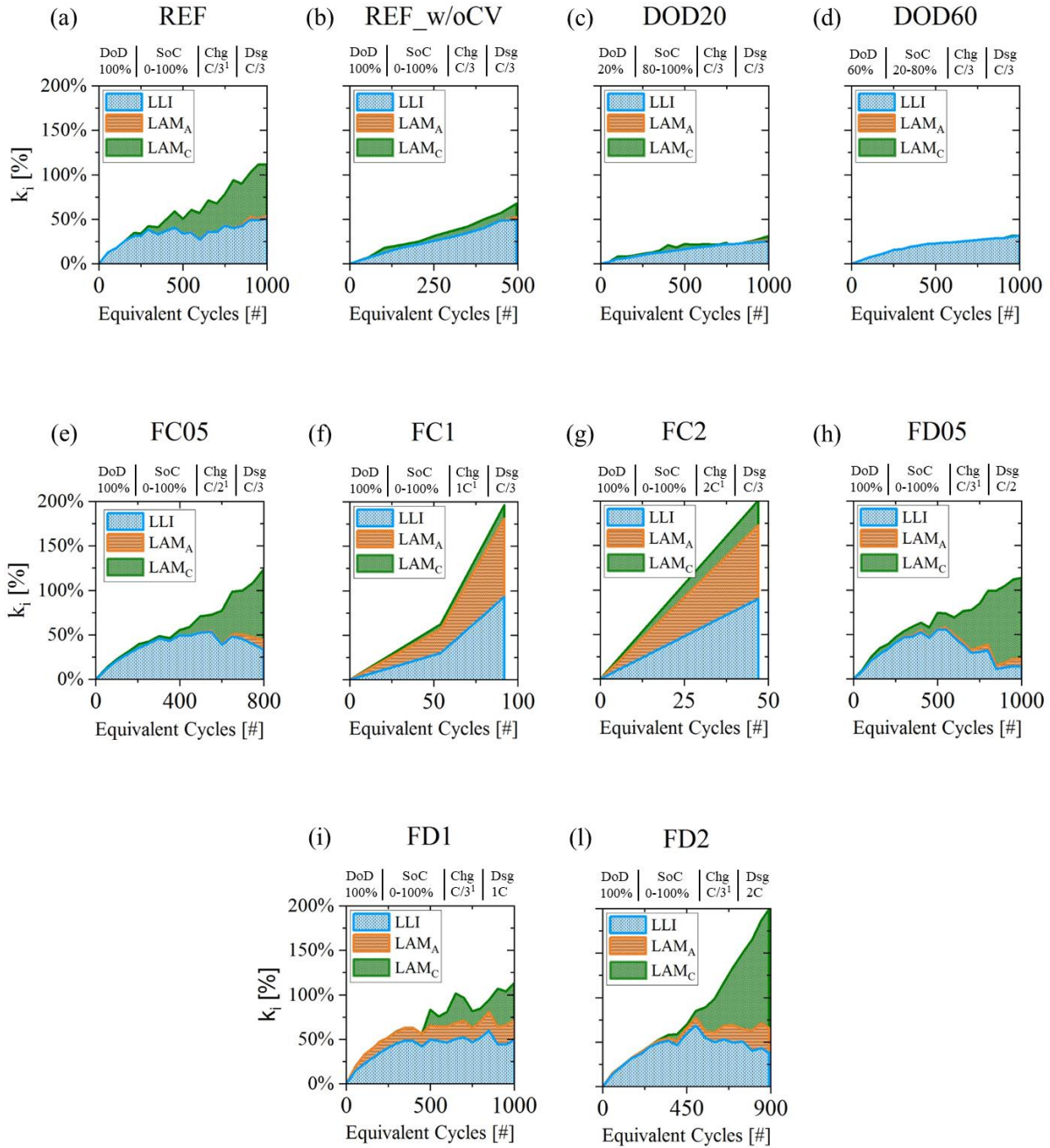


**Figure 5.8. Evolution of the three DMs indicators (LLI,  $LAM_A$  and  $LAM_C$ ) for the cells under investigations.** Details about testing protocols are given in plot titles: (i) DoD: Depth of Discharge; (ii) SoC: SoC interval, (iii) Chg: charging rate (<sup>1</sup>including Constant Voltage phase with cut-off current at C/50); (iv) Dsg: discharging rate.

than 100 EqC (Figure 5.8-f,g). In both cases the degradation is driven by LLI and  $LAM_A$  in similar quantities: the lithium plating generated inside those cells is reducing available surface, therefore inhibiting graphite use [160], [163]. The other two cells that showed

“after-knee” behaviour, i.e. cell ID:REF\_w/oCV and cell ID:FC05 presented a small amount of  $LAM_A$  (5-12%) at late cycles corresponding to the “after-knee” region (Figure 5.8-b,e). In those cases, EoL was reached mainly due to lithium plating without significant inhibition of graphite surface as in high charging rate cells (ID:FC1 and ID:FC2).

### 5.3.2. SoH estimation

The piecewise model presented in Section 5.2.2 has been used to perform SoH estimation on the experimental dataset under investigation. The training subset have been chosen to include different variety of testing conditions: high charging rate, high discharging rate and reduced DoD (Table 5.3). It is paramount to include cells with after-knee SoH behaviour in the training group to properly initialize and set the SoH model. The two found SoH functions are showed in Figure 5.9-a both for “pre-knee” and “after-knee” conditions. The values of fitted coefficients are given in the table of Figure 5.9-b.

**Table 5.3. Training subset for SoH estimation.** The presence of “pre-knee” and “after-knee” SoH behaviour is highlighted in the last two columns. Details about the testing protocols can be found in Table 5.2.

Cell ID	SoH [%] at EoL/EoT	EqC at EoL/EoT	Pre-knee SoH behaviour	After-knee SoH behaviour
DOD20	92.7%	1000	✓	✗
FC05	79.5%	892	✓	✓
FC1	63%	92	✗	✓
FD05	86.6%	1000	✓	✗
FD1	84.6%	1000	✓	✗

The application of the SoH model to the validation subset is shown for each cell in the charts of Figure 5.10-a-e. The list of validation set cells and the results of MBE and MAE are listed in Table 5.4.

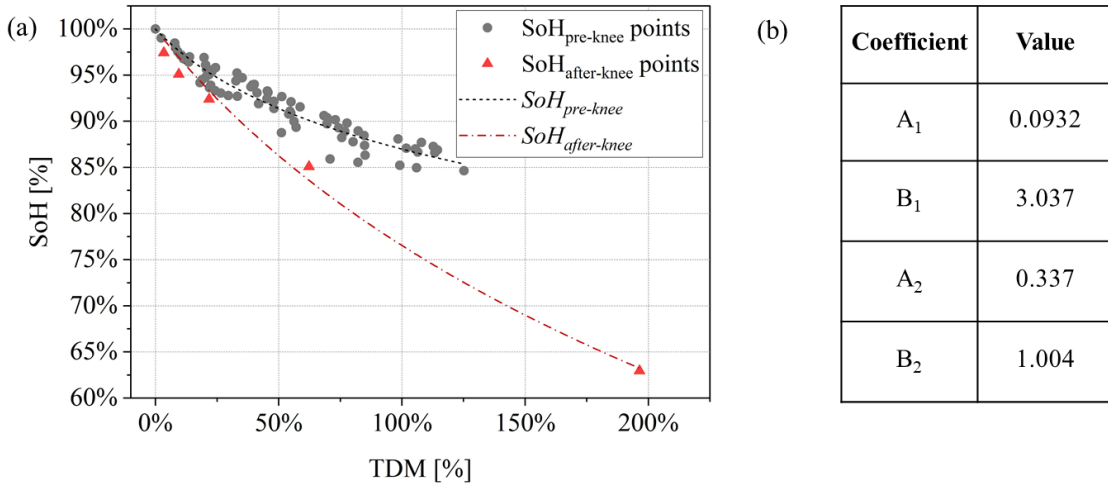


**Figure 5.9. Developed SoH model.** (a) SoH functions found with the training cells in Table 5.3. (b) Fitting coefficients (SoH model described in equation (6)).

Cell ID:REF shows accurate estimation results in Figure 5.10-b, with MAE=0.38% and MBE=-0.11%. Reduced DoD protocol with cell ID:DOD60 shows similar values of MAE and MBE, with a tendency in overestimating SoH when EqC > 400, as shown in Figure 5.10-a. Cell ID:REF\_w/oCV (Figure 5.10-c) shows a good estimation both in the “pre-knee” and “after-knee” regions, even though the SoH tends to be overestimated in the second region, with MAE=1.28% at EoL. In the case of fast discharge at 2C (Cell ID:FD2), the SoH underestimation happens in the range between 400 and 900 EqC, as shown in Figure 5.10-d, accounting for a MAE of 1.56%. Lastly, cell ID:FC2 (Figure 5.10-e) with fast charge at 2C shows the largest MBE and MAE, with same magnitudes (-7.46% and 7.46%). The source of this large error is twofold: on the one side the availability of only one measurement to perform the estimation and (ii) on the other side the deeply aged condition, with measured SoH equal to 70.2%.

**Table 5.4. Validation subset with results of MBE and MAE.** Details about the testing protocols in Table 5.2.

Cell ID	Mean Biased Error [%]	Mean Absolute Error [%]
DOD60	0.69%	0.73%
REF	-0.11%	0.38%
REF_w/oCV	1.27%	1.28%
FD2	-1.54%	1.56%
FC2	-7.46%	7.46%

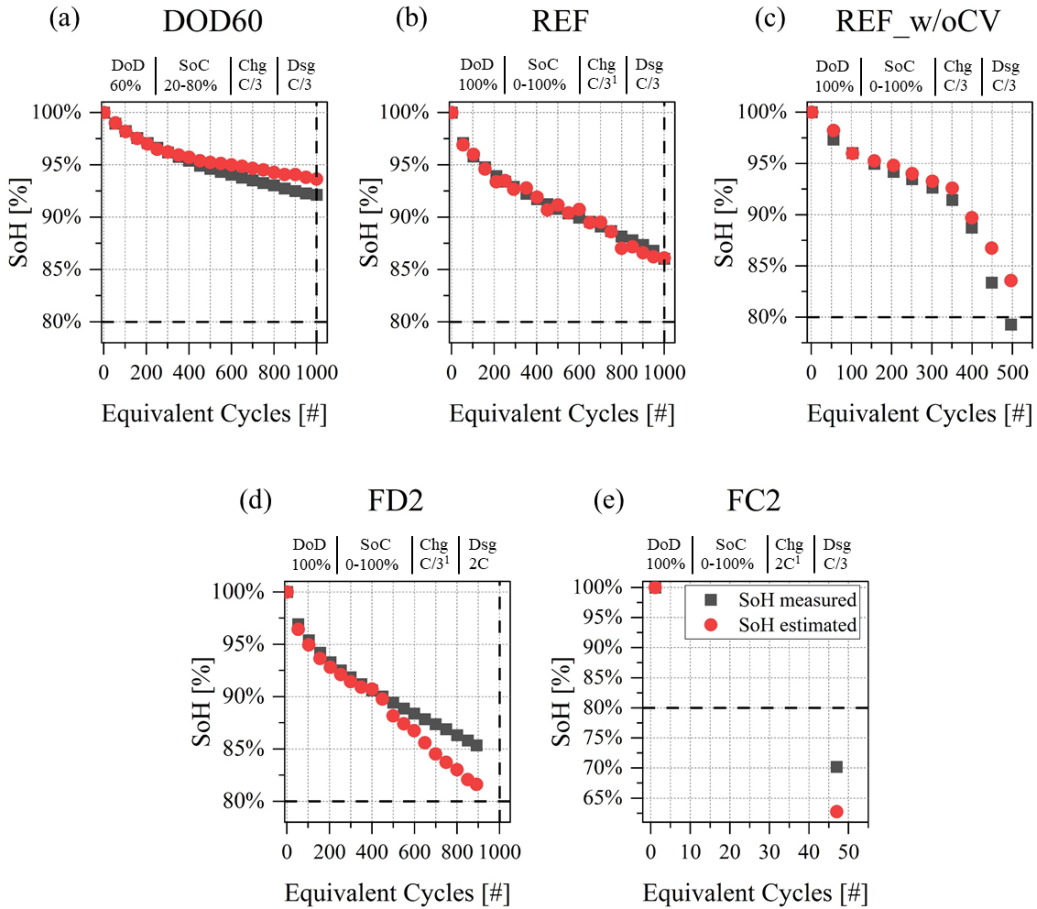


**Figure 5.10. SoH estimation validation applying the SoH model of Figure 5.9.** (a)-(e) Results of application of SoH model to the validation cells of Table 5.4. Details about testing protocols are given in plot titles: (i) DoD: Depth of Discharge; (ii) SoC: SoC interval, (iii) Chg: charging rate (<sup>1</sup>including Constant Voltage phase with cut-off current at C/50); (iv) Dsg: discharging rate.

Additional analyses have been run to understand the error distribution of the SOH estimation in different aging intervals and to understand the stability of the results when testing all the possible combinations of training and validation subsets. The definition of the training group was always based on a key prerequisite: a minimum number of one cell with “after-knee” behaviour has been always included to encompass the highly aged condition. The results are shown in Table 5.5 and in Figure 5.11. Looking at the MBE, the model tends to overestimation for SoH<95%. Looking at the MAE, the error increases as the SoH decreases, particularly with SoH<85%. The result is also influenced by the small quantity of available measured points for SoH<85%: only 8 points are available over more than 150 points for the cells under investigations. This effect is also observed in the box plot of Figure 5.11: both the error and absolute error presents large variations for SoH

ranges under 85% SoH. Moreover, for SoH<80% the distribution of the absolute error is asymmetric, with higher number of points at higher magnitudes.

**Table 5.5. Estimation errors per different SoH ranges.** MBE and MAE in different SoH ranges for all the combinations of 5 training cells and 5 validation cells.

SoH range	Mean Biased Error [%]	Mean Absolute Error [%]
100% > SoH ≥ 95%	-0.05%	0.38%
95% > SoH ≥ 90%	0.01%	0.40%
90% > SoH ≥ 85%	0.43%	0.71%
85% > SoH ≥ 80%	3.57%	3.65%
SoH < 80%	0.65%	6.78%

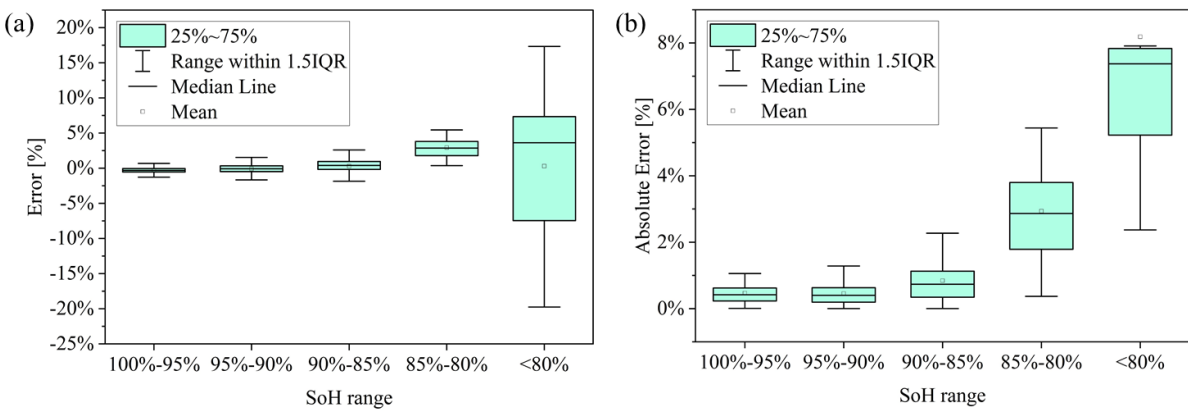


**Figure 5.11.** Box plot representation of the (a) error and the (b) absolute error for the different SoH ranges introduced in Table 5.5 with 5 cells in the training set.

## 5.4. Discussion

The results presented in Section 5.3 and obtained applying the methodology described in Section 5.2 can be analysed and discussed on different levels: validity, replicability and applicability.

Validity: for the selected case study (NMC811|Graphite SiO<sub>x</sub>), the defined proxies allowed to quantify the contributions of different DMs during cells' aging. DMs were distinguished by analyzing the DRT profiles of the cells as explained in Chapter 4, on the same cell type investigated in the present chapter. Indicator filtering (linear and based on a sliding window) was essential to regularize the aging trend and to reduce noise and outliers while preserving information related to steep variations caused by abrupt increase of degradation. The selection of a proper sliding window size was found crucial to

encompass cell degradation in a comprehensive way and it depends not only on the type of data but also on the available number of diagnosis points. In this work, the optimal number of prior points to be used for the sliding window was found equal to 7. Looking at SoH estimation, the piecewise model showed good performances for  $\text{SoH} > 85\%$ , while larger errors for  $\text{SoH} < 85\%$ . These larger errors were mainly linked to the small number of available points (i.e. measurements) all belonging to “after-knee” behaviour. Therefore, for  $\text{SoH} < 85\%$  only accelerated degradation was available. Two possible solutions can be adopted to mitigate the problem: (i) increase the number of diagnosis points when the cells reach a certain capacity (e.g.  $\text{SoH} < 85\%$ ) and (ii) prolong test duration ( $\text{EoT} > 1000 \text{ EqC}$ ) for those cells that ended the testing campaign with  $\text{SoH} > 85\%$  (i.e. with less severe testing conditions).

**Replicability:** the calculation of degradation indicators can be extended to other cell types with the same cell chemistry (e.g. pouch cells), given that it is based on DRT peaks attribution performed for NMC cells. Additional investigations will be needed if one wants to apply this methodology to other cell chemistries, in order to obtain the link between DRT peaks and the DMs. The setup of degradation indicators filtering and of the piecewise model require to follow specific steps, suggesting the need of clear guidelines to replicate the methodology presented in this chapter.

**Applicability:** the methodology presented in Section 5.2.2 allowed to develop a simple piecewise SoH model based on total degradation indicator (*TDM*) with reduced degrees of freedom: 4 fitting coefficients (2 for each SoH function) and 2 parameters (for normalization in “after-knee” function). The model is data-efficient, not requiring large datasets to be trained and its application may be more convenient for on-board applications in BMSs than data-driven approaches, which usually require larger amount of data and more complex hardware [34], [203]. The number of training cells was set choosing 5 different testing conditions that lead to different aging paths. However, the data-efficiency of the SoH model should be checked while varying the number of cells in the training set. All possible combinations of training cells have been simulated in a range between 2 and 8 cells out of the total number of 10 (Table 5.2). As expected, the training with 2 cells brought to very large errors compared to the other cases and it is not represented in Figure 5.12-a (MBE=-2.7% and MAE=3.5%). In all the other cases, the MBE is around 0.1% and the MAE is around 1% (Figure 5.12-a). More in detail, the value of 5

training cells shows the best combination of errors, with MBE=0.11% and MAE=0.94%. This result is also confirmed by the box plot representation given in Figure 5.12-b: increasing the number of training cells, the error rises due to data overfitting. Overall, these results confirm that a reduced but relevant number of tests could be sufficient to train the SoH model.

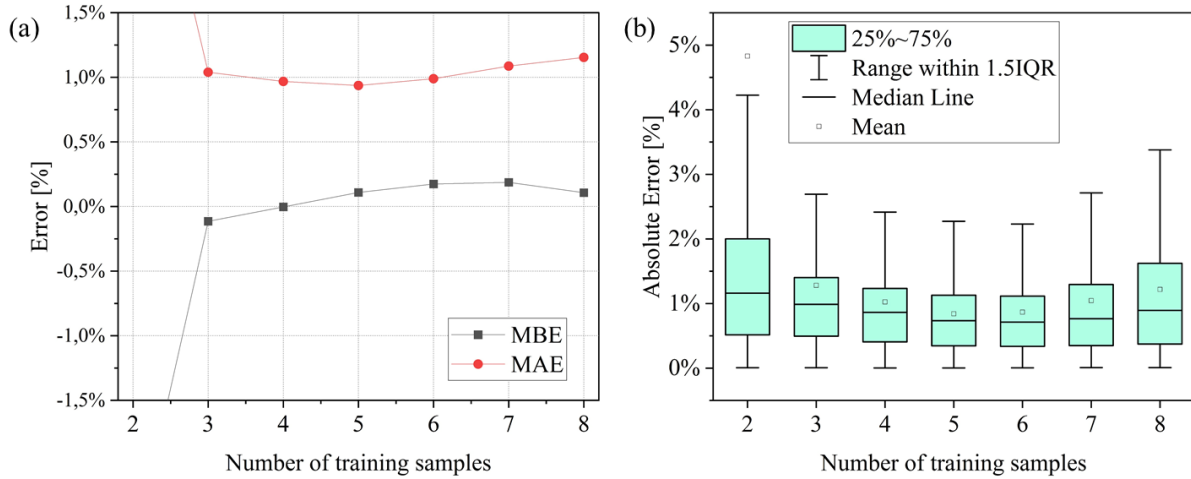


**Figure 5.12. Applicability of developed SoH model.** Analysis of all the possible combinations of training sets with a number of cells between 2 and 8: (a) MBE and MAE results over the whole SoH range; (b) box plot results in the SoH range 90%-85%.

Based on this paper findings, it is possible to define guidelines, which might help in applying the proposed methodology in real use cases.

Guidelines: a two-phases procedure will be required: (i) an offline-phase, mainly in laboratory, to set up the degradation tracking and the SoH model and (ii) an online-phase, mainly onboard in BMS, to perform SoH estimation.

As regards the first phase (offline, in the lab), the main steps to develop the degradation indicators and the SoH model are the following:

- Plan relevant aging tests that cover different aging behaviours and allow to train the SoH model both for “pre-knee” and “after-knee” conditions. The selected protocols should include: (i) reduced DoD condition to appreciate slow degradation ( i.e. capacity fade); (ii) nominal conditions, to verify the specifications from the manufacturer; (iii) moderate charging or discharging conditions that accelerates degradation with respect to nominal conditions and that could guarantee both “pre-

“knee” and “after-knee behaviour” (such as cell ID:FC05) and (iv) high charging or discharging rate that guarantee fast degradation and “after-knee” conditions (such as cell ID:FC2).

- Perform diagnosis phase (capacity+EIS measurements) at fixed number of EqC down to a certain value of SoH (e.g. 85%) and then intensify the number of checks by lowering the number of cycles in each repetition. In this way, more measurements will be available in the region where is mainly occurring the “knee” and accelerated capacity fade, reducing the SoH estimation error.
- Run sensitivity analysis on the ohmic resistance variation parameter  $\Delta R_{\Omega,i}$  to discriminate between “pre-knee” and “after-knee” conditions with a suitable threshold. Validation can be performed graphically on SoH evolution curves as done in Figure 5.5.

As regards the second phase (online, on the BMS) the main requirement is the capability to run EIS measurements and related algorithms on the BMS, as discussed in Section 1 and already available on existing products or prototypes [198]–[200]. Once this is available, the main practical steps for the SoH estimation model are the following:

- Run “diagnosis” based on long-EIS measurements (10kHz – 10mHz). Select an appropriate criterion on when to acquire two consecutive full-EIS measurements. Depending on battery application, this variable could be set based on cycles number, a fixed period of time, or randomly (e.g. exploiting resting periods during application).
- Run “check-up” based on short-EIS measurements only at high frequency (10kHz - 1kHz) to frequently update  $R_{\Omega}$ , which is crucial to activate additional “diagnosis” measurements whenever the “after-knee” behaviour is reached based on the  $\Delta R_{\Omega}$  computation (Section 2.2.2). Additional “diagnosis” can also be activated under a certain estimated value of SoH (e.g. 85%).
- Compute the degradation indicators whenever possible to understand if unexpected behaviours are happening inside the cell. This can be done by updating DMs values and by analysing them over time and/or over cycle number.

## 5.5. Final remarks

This chapter investigated the use of EIS via DRT to track degradation of Li-ion cells and to perform SoH estimation based on physics-based insights.

An experimental dataset of cycling tests in different aging conditions and an already published algorithm to attribute DRT peaks to degradation mechanisms have been used as inputs. The whole methodology is based on defining how to track the overarching degradation modes (DMs), that are  $LLI$ ,  $LAM_A$  and  $LAM_C$ . Relevant indicators were presented in Section 5.2.2, which includes filtering method to discard outlier and reduce noise. A piecewise model has been developed to estimate SoH from degradation indicators, including two logarithmic functions to encompass the “pre-knee” and “after-knee” behaviours of aging cells. In this way, SoH estimation is directly related to the physical processes and degradation mechanisms occurring inside the cell. Finally, a straightforward procedure to train and validate the model has been also presented, which is based on a sensitivity analysis to minimize the dimension of the training subset (i.e. the a-priori knowledge based on testing campaign).

The results showed that  $LLI$  is the main DM affecting cell degradation during the whole lifetime while  $LAM_C$  becomes relevant after 400 EqC. SoH estimation showed MAE lower than 0.75% in the SoH range 100%-85% and lower than 3.70% in the range 85%-80%. At SoH<85% model estimation was negatively influenced by the low number of available measured points with high variability. Tuning the number of training cells in the range 2-8 showed stable error values, proving the data-efficiency of the proposed model, and an optimal training subset of 5 cells (i.e. 5 different testing protocols to comprehensively describe battery degradation).

Finally, user-oriented guidelines have been presented in Section 5.4 to allow both scientists and BMS engineers to replicate the methodology with their own testing and BMS setups. These guidelines are divided into an offline phase (laboratory phase), to set up the degradation tracking and the SoH model, and an online phase (BMS phase), to diagnose degradation and to perform the actual SoH estimation onboard.

Limits of the presented methodology are twofold: (i) the need to generalize the model to deal with EIS measurements done at different SoCs and temperatures; (ii) the need of

precise and accurate EIS measurements embedded into BMS slave boards. If the first can be solved by extending the a-priori offline phase in the laboratory, the second needs a necessary upgrade of current BMS to include more sensing capabilities at cell level.

# Chapter 6

## Conclusions

In a context where battery applications are exponentially growing and regulations demands for batteries to be more sustainable throughout the lifecycle, technical solutions to unleash the full potential of circular economy in the battery industry are strongly required. Among the different viable solutions, fine tracking of battery states during lifetime acquires particular importance to provide valuable information about battery states and battery history for traceability. Therefore, it is crucial to fully understand the electrochemical behaviour during operations, without considering the battery systems as "black boxes".

This doctoral thesis focused on non-invasive characterization of Li-ion cells, investigating the use of Electrochemical Impedance Spectroscopy (EIS) to model and quantify cell aging. Three main objectives were set in the research: (i) background analysis, (ii) modelling framework development and (iii) its application. The schematic representation of these objectives and the main results obtained within this work are shown in Figure 6.1. A wide analysis of the state-of-the-art about the use of EIS for Li-ion cells degradation highlighted existing methodologies and laid the foundations for the development of a modelling framework to characterize the physical processes and degradation mechanisms occurring inside the cells. Distribution of Relaxation Times (DRT) was exploited to deconvolute the impedance spectra in the time domain, making possible to distinguish major and minor polarization effects that are normally overlapped in the frequency domain. The result was a physics-based Electric Circuit Model (ECM) where each element represents a different process occurring in the cell without an a-priori assumptions on the model configuration (as normally done with EIS curve fitting). After that, an aging model was developed that analyse the DRT profiles of aged cells and compare them with laboratory cells (half-cells) to discriminate the effects at anode and cathode sides. Imaging techniques were used to validate the results obtained with DRT.

## 6. Conclusions

The developed models were applied to commercial lithium-ion cells, performing SoC estimation (in the first case) and Degradation Modes (DMs) quantification with SoH estimation (in the second case).

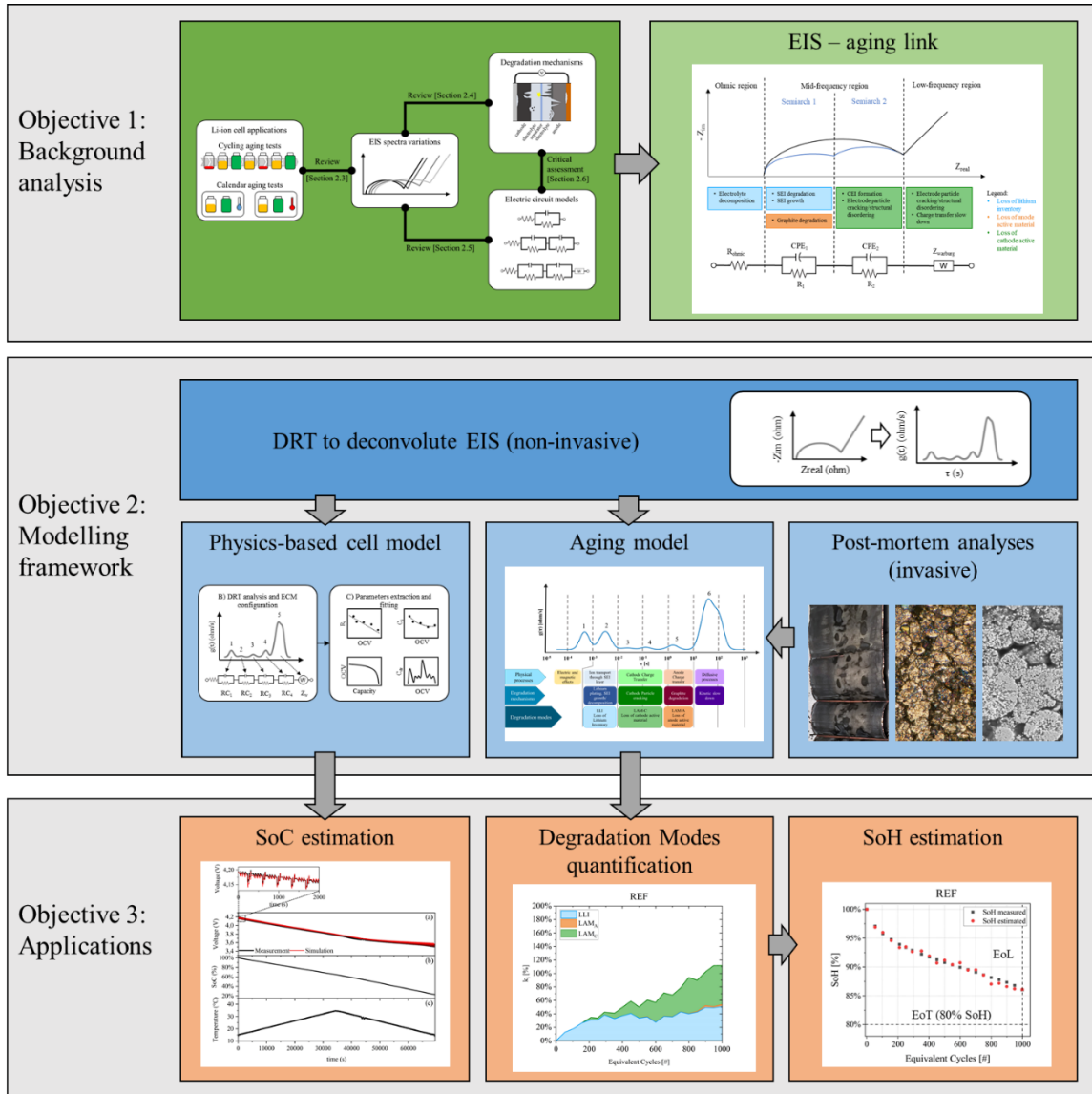


**Figure 6.1. Schematic representation of the research objectives and of the results of the work.** 1) Critical assessment of existing literature analysing the connection between EIS and cell application, degradation mechanisms and the most common ECM configurations. 2) development of a modelling framework exploiting EIS deconvolution through DRT to obtain physics-based cell model and aging model, identifying degradation mechanisms (also validated with post-mortem analyses). 3) application of developed modelling framework to estimate SoC at different temperatures and to quantify Degradation Modes and estimate SoH during cell lifetime.

---

This thesis bridged the gap between the systemic analyses (based on non-invasive characterization techniques) of battery engineers and the advanced material characterization methods (mostly invasive) of material scientists. The resulting algorithms, based on EIS, allows for physics-based and “degradation aware” modelling of the cell enabling improved battery state estimation and accelerated investigations at material, component or cell level in battery research laboratories.

A detailed summary of the thesis contributions in the different chapters is discussed below.

Chapter 2 presented a comprehensive review on the use of EIS to characterize Li-ion battery degradation phenomena and to model them through ECMs. The review process highlighted three main aspects: (i) the link between cell application and EIS spectra variations; (ii) the link between EIS spectra variations and the degradation mechanisms and (iii) the available options to develop ECMs of aged cells. EIS spectra present clear shifts in different frequency regions depending on the applications (Temperature, DoD, C-rate, etc.) and these shifts are attributed to different degradation mechanisms that, in turn, are modelled with different circuital elements. Specifically: (i) the Ohmic region is usually associated to electrolyte decomposition and it is modelled with a resistor; (ii) the Mid-frequency region represents SEI- and cathode-related degradation and is modelled with one or two Zarc elements and (iii) the Low-frequency region also represents cathode degradation and is modelled with a Warburg element. Overall, the results of the review presented in this chapter motivated the exploitation of EIS as a fast, non-invasive, and reliable characterisation tool to develop cell’s models able to track the main degradation phenomena.

Chapter 3 introduced a modelling framework called “EIS2MOD” to develop physics-based models of Li-ion cells from EIS and OCV measurements. DRT deconvolution of EIS spectra was used to distinguish the electrochemical phenomena which are difficult to interpret in the frequency domain. The modelling framework was applied to large format commercial pouch cells validating the obtained ECM over the whole SoC range and over a wide temperature range (-10°C to 35°C). The several application profiles tested demonstrate the high accuracy of the model in reproducing the cell behaviour. For instance, the RMSE on the battery voltage is lower than 1.50% for driving cycle simulations at variable

## 6. Conclusions

---

temperature and SoC. Overall, this chapter presented the advantages of EIS2MOD, with high accuracy and light computational load thus offering an attractive framework for BMS implementation.

Chapter 4 exploited EIS and DRT as a comprehensive measurement and post-processing method to analyse cell aging and to develop an aging model. DRT profiles of commercial Li-ion cells aged in different conditions were analysed at BoL and EoL/EoT and compared to lab-made cells in coin format (full-cells, cathode half-cells and anode half-cells). The comparison was performed to discriminate the processes occurring at anode and cathode sides and to relate them to specific DRT peaks of commercial cells. Imaging techniques were used to assess the degradation mechanisms and ultimately to validate their tentative DRT peaks attribution. The summary of physical processes and degradation mechanisms attributed to the six DRT peaks of the investigated cells is as follows: (i) peak S1 ( $\tau < 10^{-3}$ s) is invariant with respect to aging and attributed to electric and magnetic effects; (ii) peak S2 ( $10^{-3} < \tau < 10^{-2}$ s) is attributed to ion transport through graphite's SEI layer and it is influenced by SEI growth/decomposition and lithium plating degradation mechanisms; (iii) peaks S3 and S4 ( $10^{-2} < \tau < 10^0$ s) are attributed to cathode charge transfer reactions and to NMC degradation due to particle cracking; (iv) peak S5 ( $10^0 < \tau < 10^1$ s) is attributed to graphite's charge transfer reactions and its related graphite degradation and (v) peak S6 ( $\tau > 10^1$ s) is attributed to diffusive processes and accounts for general kinetic slow down due to general electrodes degradation. The attribution process was validated by digital imaging for graphite degradation, mainly related to lithium plating and by Scanning Electron Microscopy for the NMC degradation, mainly related to particle cracking. Overall, the results of this chapter allowed to develop suitable indicators associated to DRT peaks in order to quantify cell degradation, estimate SoH and build more robust battery models.

Chapter 5 exploited the results of Chapter 4 and investigated the modelling framework developed in Chapter 3 to track Li-ion cells aging and estimate SoH. Relevant indicators were introduced to quantify the degradation mechanisms grouped in the so-called Degradation Modes (DMs). A piecewise model has been developed to estimate SoH including two logarithmic functions to encompass the “pre-knee” (linear) and “after-knee” (non-linear) behaviours of aging cells. Finally, a straightforward procedure to train and validate the model has also been presented, which is based on a sensitivity analysis

---

to minimize the dimension of the training subset. The results showed that Loss of Lithium Inventory (LLI) is the main driving factor for the NMC cell under investigation, followed by Loss of Cathode Active Material (LAM<sub>c</sub>). SoH estimation showed Mean Absolute Error lower than 0.75% for SoH values higher than 85% and lower than 3.70% for SoH values lower than 85%. Overall, the analyses of the results presented in this chapter allowed to define guidelines to replicate the presented methodology in order to characterize new Li-ion cell types (laboratory phase) and perform onboard SoH estimation in Battery Management System solutions (BMS phase).

As already mentioned, this work succeeded in bridging the gap between a systemic approach and advanced material characterization methods. EIS and DRT has been proven as valid measurement and post-processing method to model Li-ion cells and to track their State of Charge and State of Health. The description of all the algorithmic steps to calculate and analyse DRT allows the readers to replicate the experiments and the methodology presented. Moreover, the light computational load gives practical possibilities to implement the methodology into prototypes of new generation BMSs with smart functionalities.

## Future works

There are several research directions that can be explored to extend the work presented in this thesis.

From a *theoretical point of view*: the DRT calculation can be improved and to optimized. New algorithms could lead to an easier DRT calculation and a better evaluation of the low-frequency diffusive tail of impedance spectra. The final objective would be to locate all the parameters of the ECM without the need of the OCV measurements. In this way, the application of the model would become easier during battery lifetime, with a regular update of the circuital parameters with EIS measurements only.

From an *experimental point of view*: the whole methodology has been developed for Li-ion cells, where charging and discharging processes are mainly driven by ion intercalation reactions. Therefore, changing cathode would require new testing and re-calibration of the algorithms (e.g. the DRT peaks attribution). As regard other types of chemistry

## 6. Conclusions

---

instead, as Lithium-sulphur or solid-state batteries, the DRT profile analyses will have to be extended to deal with the new specific mechanisms and processes.

From an *application point of view*: the developed modelling toolbox is very promising for dedicated BMS hardware/software solution able to leverage its potentiality. Therefore, the development of additional sensing capabilities at BMS level and the porting of the code would be the natural steps to make this framework functional in prototypal systems. At the same time, the algorithm should be generalized to allow degradation evaluation and SoH estimation when EISs are done at different working temperatures and with DC-offset typical of on-board applications.

# Appendix A

## Support material to Chapter 3

### A.1 Kramers-Kronig criterium

A suitable tool to check high quality and time invariance of the impedance spectra is the Kramers-Kronig criterium [140]. For a linear and time invariant system, the real and imaginary part of the impedance spectrum are interrelated by the following equations [204]:

$$Z_{Re}(\omega) = \frac{2}{\pi} \cdot \int_0^{\infty} \frac{\omega' \cdot Z_{Im}(\omega')}{\omega^2 - \omega'^2} d\omega', \quad (\text{A.1})$$

$$Z_{Im}(\omega) = -\frac{2}{\pi} \cdot \int_0^{\infty} \frac{\omega \cdot Z_{Re}(\omega')}{\omega^2 - \omega'^2} d\omega'. \quad (\text{A.2})$$

By applying these equations respectively to imaginary and real part of measured spectrum, the remaining part can be computed. Then, comparing the measured and calculated part it is possible to judge the quality of the measurement.

KK-criterium has been applied in this work with the Lin-KK test described in [204]. The governing impedance expression is given by:

$$\hat{Z}(\omega) = \hat{R}_{ohmic} + \sum_{k=1}^M \frac{\hat{R}_k}{1 + j\omega\tau_k}. \quad (\text{A.3})$$

The  $M$  time constants are distributed logarithmically spaced over the inverse range of angular frequencies of the impedance spectrum to be analysed.

The function  $J$  to be minimized could penalize errors between the real parts of fitted and measured impedance, the corresponding imaginary parts or both. For instance, to fit the real part, the according function to be minimized is:

$$J = \sum_{k=1}^N \left[ \frac{Z_{Re}(\omega_i) - \hat{Z}_{Re}(\omega_i)}{|Z(\omega_i)|} \right]^2 \quad (\text{A.4})$$

With  $N$  the number of frequency points of the EIS spectrum to be analysed. To obtain better performance with diffusive tail of the EIS spectrum, a capacitor can be included in the calculation (but it has not been exploited in this work).

Finally, the quality and reproducibility of the measurement under investigation is evaluated with the residuals in the following equations, respectively for the real and imaginary parts:

$$\Delta_{Re}(\omega) = \frac{Z_{Re}(\omega) - \hat{Z}_{Re}(\omega)}{|Z(\omega)|} \quad (\text{A.5})$$

$$\Delta_{Im}(\omega) = \frac{Z_{Im}(\omega) - \hat{Z}_{Im}(\omega)}{|Z(\omega)|} \quad (\text{A.6})$$

Those residuals describe the deviation between the measured spectrum and the calculated one. DRT calculation can be performed when those residuals are below 1% [141], [142].

In this work, the function developed in the *impedance.py* python library has been exploited to check all the measured EIS spectra [205]. An example of Lin-KK test application is given in Figure A.1 for the large format pouch cells investigated in Chapter 3. Even though for the singular cells both  $\Delta_{Re}$  and  $\Delta_{Im}$  are higher slightly higher than 1% between 100 and 1000 Hz, the residuals of the averaged cell computed to develop the generalized battery model are always below the threshold. More details about the calculation of the averaged impedance spectra are given in Section A.4.

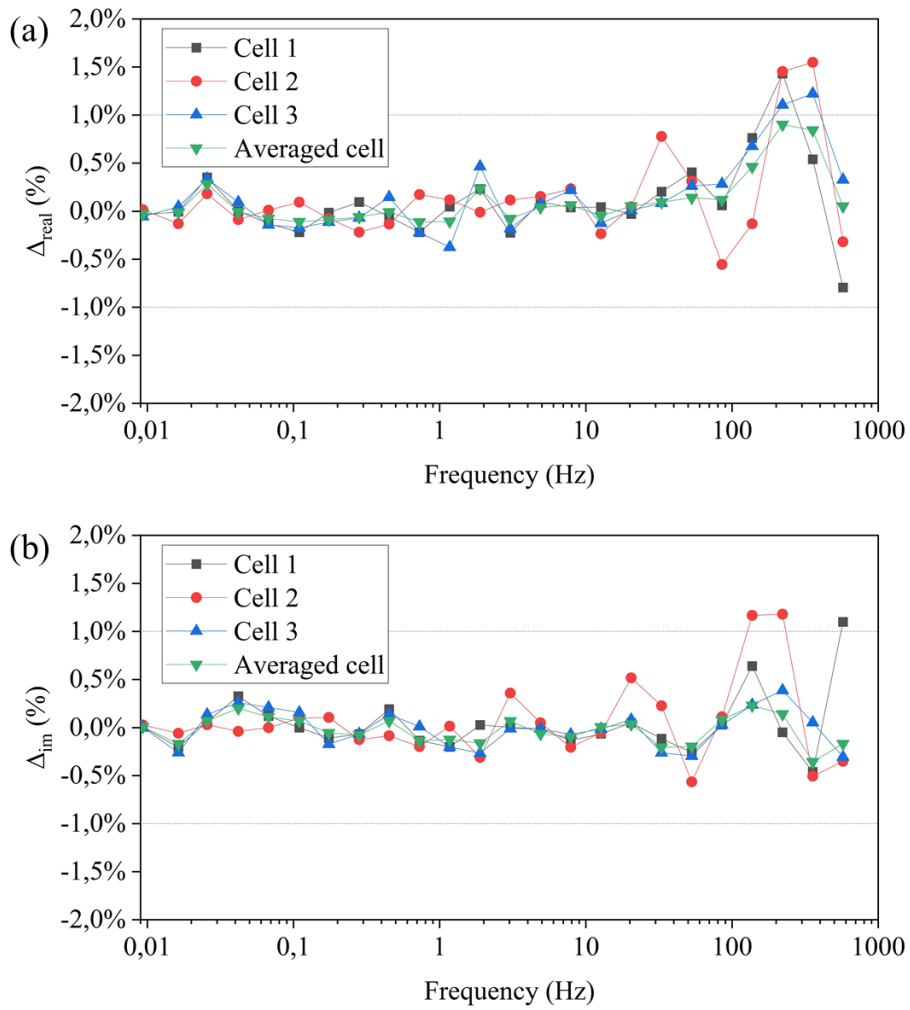


**Figure A.1. Lin-KK test:** application on EIS spectra measured at 50% SoC and 20°C for the cells analysed in Chapter 3. (a) Residuals of the real impedance part; (b) residuals of the imaginary impedance part.

## A.2 Inductive behaviour correction

To properly deconvolve EIS spectra, it is necessary to subtract the inductive behaviour at high frequencies that could bring to artefacts in DRT calculation [142]. In this work, the inductance correction has been performed by fitting the high frequency part of EIS spectrum with a parallel connection of inductor  $L$  and resistor  $R$  described by the following equation:

$$Z_{RL} = \frac{R \cdot j\omega L}{R + j\omega L} \quad (\text{A.7})$$

The parameters  $R$  and  $L$  are found with Complex Nonlinear Least Square (CNLS) fitting and the corrected impedance spectrum is computed as:

$$Z_{corrected} = Z_{measured} - Z_{RL} \quad (\text{A.8})$$

A practical example is shown in Figure A.2, where both the original and the corrected impedance spectra are represented. It is worth to notice that the inductive tail influences the shape of the Mid-frequency semiarch and specifically the zero-crossing impedance value that corresponds to the cell ohmic resistance. The specific python script developed to correct the inductive behaviour is available in *easifier* repository of CSEM battery team [159].

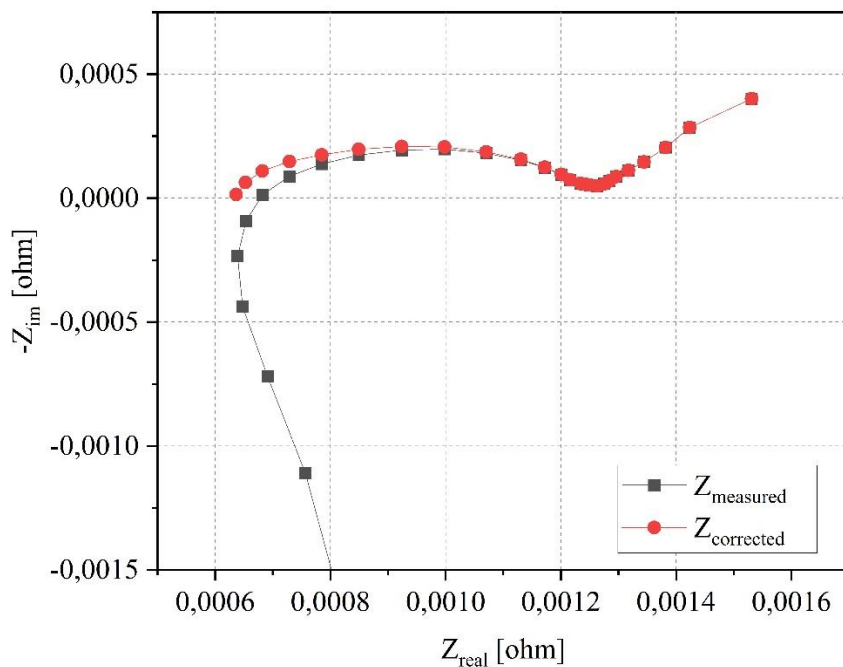


**Figure A.2. Correction of inductive behaviour.** Example with EIS spectrum measured on Cell 1 at 20°C and 50% SoC.

### A.3 Regularization coefficient determination

Tikhonov regularization is used to compute the DRT, as described in Section 3.2.1 [108], [142], [143], [145]. The regularization coefficient  $\lambda$  allows to have the best compromise between exactness of the solution and its stability. In this work, the L-curve criterion has

been chosen for the determination of  $\lambda$ . This method requires graphical representation of the second order norm of the regularized solution  $\|x\|_2$  against the second norm of the corresponding residual  $\|Ax - b\|_2$  for different values of the regularization parameter. A L-shape curve is obtained when plotting these two quantities in a log-log scale. The corner of the curve defines the point for which the solution passes from being dominated by the regularization error to being dominated by the contribution from data errors. The corner represents the trade-off between these two errors. The representation of the L-shape curve for the pouch cells evaluated in Chapter 3 is shown in Figure A.3. The optimal regularization parameter that has been fixed to  $10^{-5}$ .

As in the previous case, the specific python script related to regularization coefficient determination is available in *easier* repository of CSEM battery team [159].

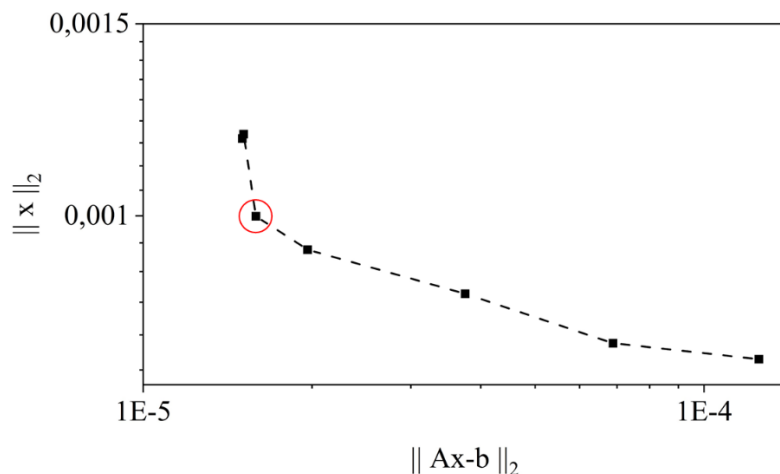


**Figure A.3. L-curve criterion.** L-curve plot for the Li-ion cells investigated in Chapter 3. The optimal regularization parameter value has been found in the highlighted corner of the curve equal to  $10^{-5}$ .

## A.4 Averaged impedance spectra

To develop a generalized model of the large format pouch cell under investigation, the characterization tests presented in Section 3.2.2 have been performed on three identical cells. Then, the collected results have been used to calculate the averaged impedance spectra and OCV curves that have been exploited for the model development.

Figure A.4-a shows an example of the impedance spectra of the three cells at 50% SoC and 20°C compared with the averaged computed profile. The misalignment between the spectra is mainly due to the different values of ohmic resistance. In fact, subtracting the ohmic resistance, the spectra are superimposed, with negligible differences in the Low-frequency region (Figure A.4-b).

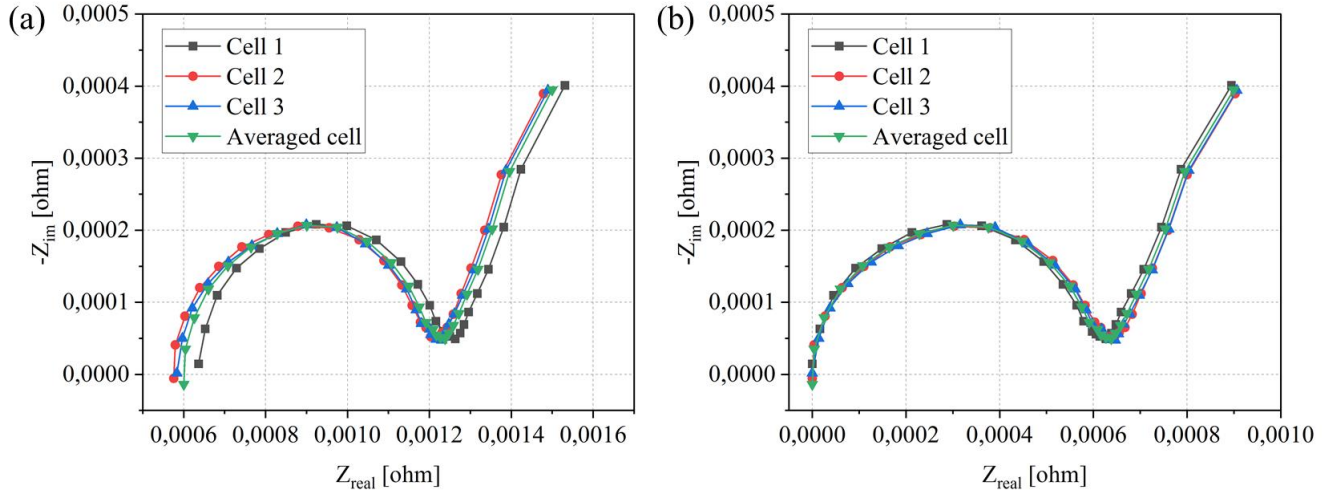


**Figure A.4. Averaged impedance spectra calculation.** (a) EIS spectra of the three tested cells compared with the computed averaged impedance. The measurements have been performed at 20°C and 50% SoC. (b) Representation of the same impedance spectra of (a) subtracting the value of ohmic resistance in each spectrum.

# Appendix B

## Application of EIS2MOD to commercial cylindrical cells

Chapter 3 presented EIS2MOD, a methodology to develop physics-based ECM for Li-ion cells and its application to large format NMC pouch cells [156]. This chapter shows the application of EIS2MOD to the NMC cylindrical cells investigated in Chapter 4 and Chapter 5. The objective was twofold:

- Demonstrate robustness of EIS2MOD applied to a different cell brand and format.
- Demonstrate preliminary application of model parameter update during cell aging to improve simulation accuracy.

### B.1 Proposed ECM

The full modelling procedure (Chapter 3, Section 3.2) has been applied to a cell that performed cycling aging tests with charging phase at C/3 and discharging phase at 1C both at Beginning of Life (BoL) and after 400 Equivalent Cycles (EqC). The cell was cycled and characterized at 20°C.

Analysing the DRT profiles at BoL, the cell presented 6 peaks as in the case of the large format pouch cells of Chapter 3. The attribution of DRT peaks to physical processes (and degradation mechanisms) is shown in Figure 5.3. The corresponding ECM configuration is the same as the one presented in Figure 3.3.

The OCV curve and the intercalation capacitance ( $C_{D,R}$ ) profiles are shown in Figure B.1; the SoC has been calculated as fraction of the discharged capacity at C/20. The OCV curve does not present relevant differences between BoL and 400 EqC when is plotted against the SoC. However, analysing the  $C_{D,R}$  parameter, it is possible to observe the cell capacity fade as reduction of the area under the curve at 400 EqC with respect to BoL.

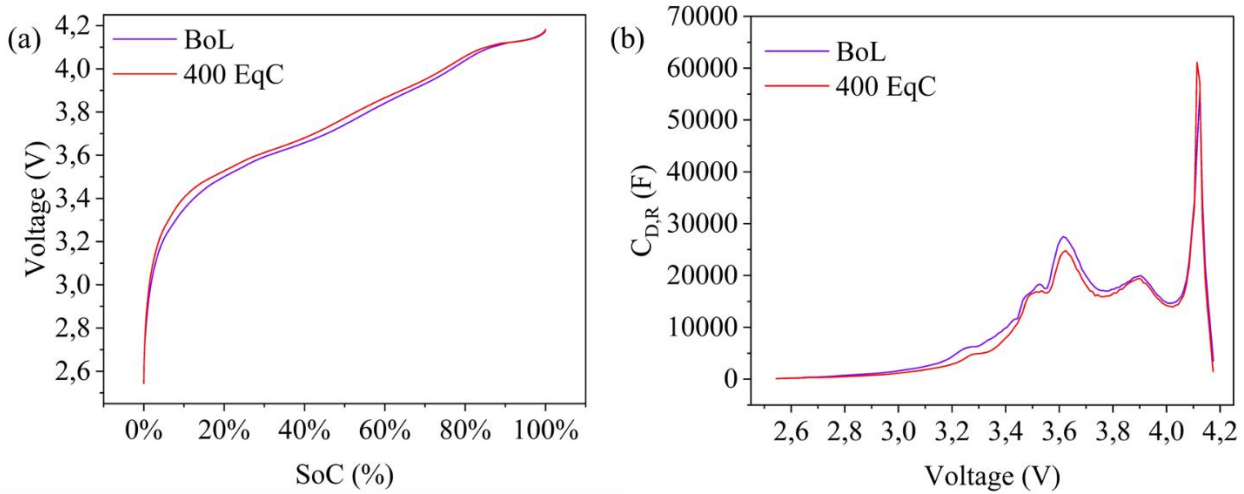


**Figure B.1. Voltage-curve based parameters.** a) OCV curves of the cylindrical cell at BoL and after 400 EqC. b) Intercalation capacitance  $C_{D,R}$  as function of the voltage obtained from the OCV curves in a).

The ohmic resistance obtained by EIS spectra and the parameters extracted by analysing the DRT profiles are given in Figure B.2. The ohmic resistance shows a 2<sup>nd</sup> degree polynomial behaviour with respect to OCV at BoL and a linear behaviour after 400 EqC, with a general shift towards larger magnitude. The parameter  $R_1$  represents the contact resistance and it is characterized by small variations over the tested OCV range. This parameter does not have large influence on cell degradation but it is peculiar the change of behaviour (i.e. curvature) between BoL and 400 EqC.  $R_2$  is related to the SEI layer and shows distinct trends in the two analysed conditions: at BoL, the magnitude is high at low and high OCV values; at later cycling, the magnitude of this parameter growth, especially at mid-OCV values. The large variation during aging of this parameter is driven by Loss of Lithium Inventory mechanisms. The parameters  $R_3$ ,  $R_4$  and  $R_5$  are related to charge transfer and show a large increase in resistance at low OCV values. There is no specific rise of magnitude at 400 EqC. This effect can be explained by the low influence of Loss of Active Material mechanisms at early cycling (Chapter 5). As regards the diffusive processes,  $R_6$  shows similar quadratic behaviour at BoL and 400 EqC.

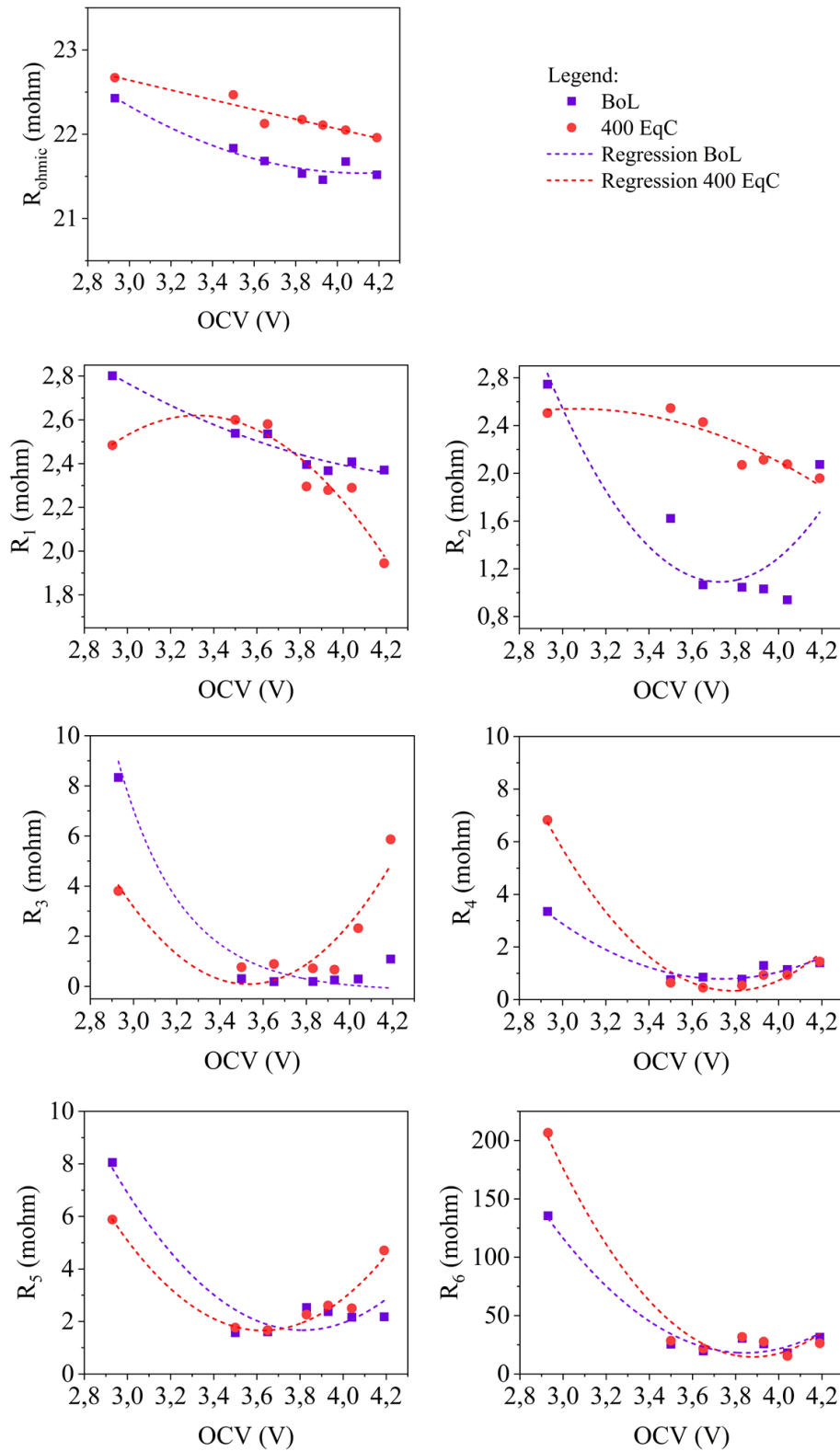


**Figure B.2. EIS based parameters.** Resistance parameters extracted by the DRT and ohmic resistance as function of the OCV of the cell under testing at BoL and after 400 EqC. The dashed lines represent the linear or quadratic fitting used to describe the trend.

The parameters' trends shown in Figure B.2 have been given as inputs for the model validation with time domain simulations. The validation process has been performed firstly to validate the model at BoL and secondly to evaluate the model performances during cell degradation.

The three profiles applied in Chapter 3 has been considered and measured during cell cycling at BoL and after 400 EqC:

- *Full discharge*: performed at C/20 constant rate.
- *Dynamic profile*: repetition of 4 steps sequence including rest, discharging, rest and charging phases. The duration of each step has been fixed to 5 minutes. Four C-rates have been applied: C/10, C/5, C/2 and 1C.
- *Driving profile*: derived combining the dynamic discharge profile A and B for BEV specified in the IEC 62660-1 standards about performance testing of Li-ion cells for propulsion of electric vehicles [139]. The testing protocol has been developed with series repetition of profile A and B assuming the maximum power output  $N=1/3$  and  $N=1$ .

## B.2 Validation results at BoL

The averaged RMSEs of the simulations at BoL are summarized in Table B.1.

Looking at full discharge simulation in Figure B.3, the model well approximates the cell behaviour even if there is a tendency to overestimate the voltage level. The absolute RMSE is 2.36% (40.2 mV).

**Table B.1. Simulations results at BoL.** Averaged RMSE errors of the dynamic and driving profiles at different SoCs and of the full discharge at C/20. The RMSE values are given as absolute value (mV) and as percentage of the voltage interval exploited by the cell (2.5-4.2V).

RMSE	Dynamic profile			Driving profile			Full discharge
	75% SoC	50% SoC	25% SoC	75% SoC	50% SoC	25% SoC	
absolute (mV)	8.6	4.8	15.5	1.3	1.8	4.2	40.2
% of voltage interval	0.51%	0.28%	0.91%	0.08%	0.10%	0.25%	2.36%

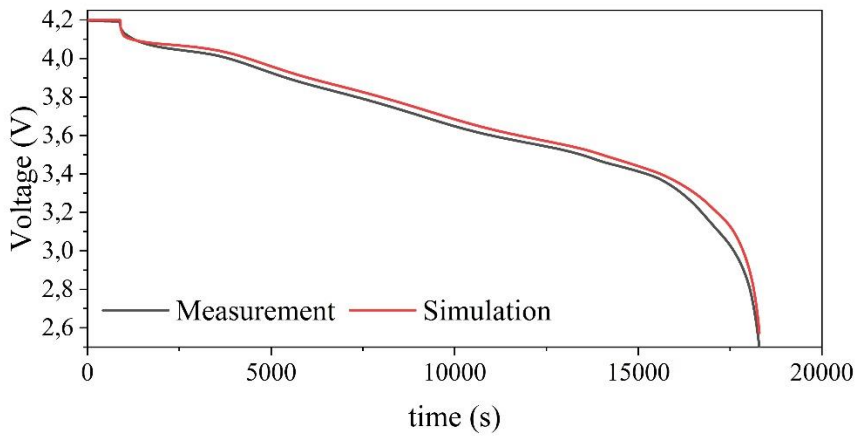


**Figure B.3.** Full discharge simulation at C/20: measured and simulated voltage profiles.

As regard the application of the other two profiles, the model is able to simulate the cell dynamics in the full range of currents applied. Figure B.4 shows the application of the dynamic current profile: increasing the current rate, the model performances decrease but the absolute RMSE is always lower than 1% over the different SoC levels.

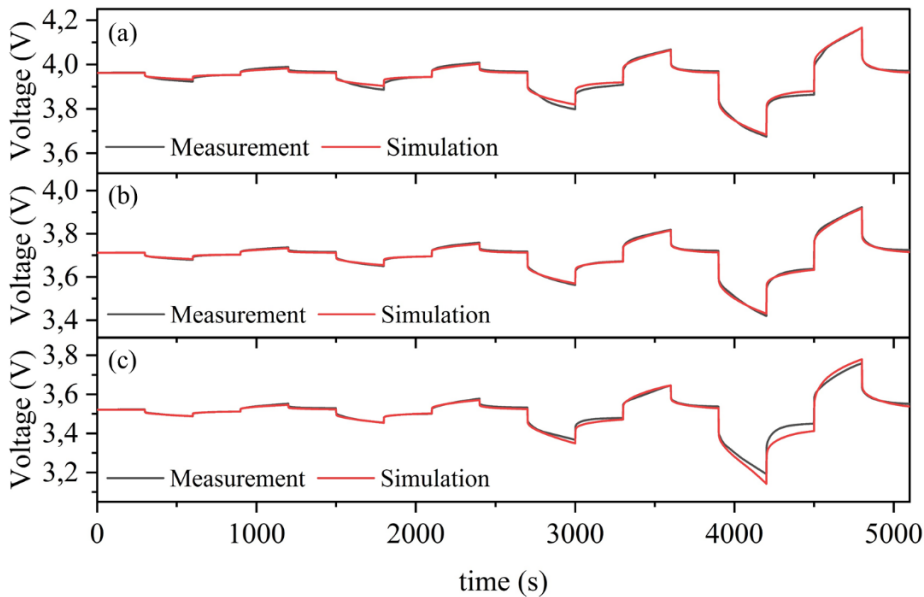


**Figure B.4.** Dynamic test at four C-rates (C/10, C/5, C/2 and 1C). The current profile includes 5 minutes steps of charge and discharge spaced by resting phase (more details in Section 3.4.1). The current profile is given in Section 3.4.1. Measured and simulated voltage profiles at different SoCs: (a) 75% SoC; (b) 50% SoC and (c) 25% SoC.

Also in the case of driving simulation tests, the model is able to follow the cell dynamic and the absolute RMSE do not exceed 0.25% for the three selected SoC levels (Figure B.5).

Therefore, the application of EIS2MOD to a different cell type than the one presented in Chapter 3 has been proven to be valid.

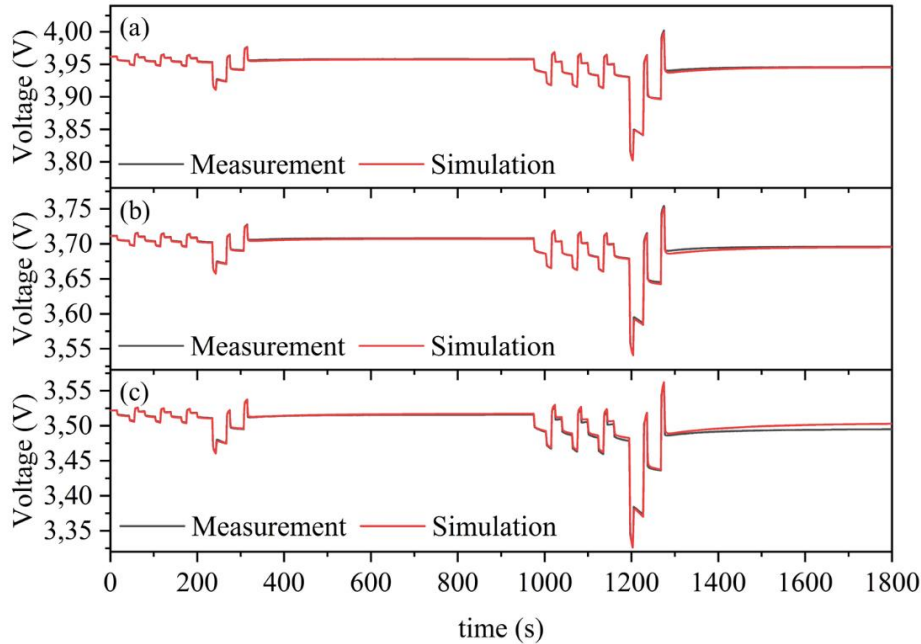


**Figure B.5. Driving simulation test.** The current profile derives by IEC 62-660-1 regulation with repetition of profile A and B at different maximum rates (more details in Section 3.4.3). Measured and simulated voltage profiles at different SoCs: (a) 75% SoC; (b) 50% SoC and (c) 25% SoC.

### B.3 Validation results after 400 Equivalent Cycles

To validate the results during cycling aging, the model has been tested with two configurations:

4. *Standard*: the DRT-based and OCV-based parameters are not updated, i.e. the values obtained at BoL are used.
5. *Updated*: the model parameters are updated exploiting EIS and OCV measurements after 400 EqC.

The averaged RMSEs of the simulations performed with the two configurations are summarized in Table B.2. Looking at dynamic profile application, the updated model shows lower RMSE at 50% SoC, while a larger error than in standard configuration is obtained at 75% and 25% SoC. Also with driving profile simulations the differences are

negligible between the two model configurations. Finally, the full discharge simulation presents a large difference between the two cases: using the standard model, the error is up to 5.53%, while updating the model parameters it is reduced to 1.80%. The voltage profiles of the two simulations are shown in Figure B.6 and compared with the measured voltage after 400 EqC. The standard model is not accounting for the capacity fade and the simulated voltage diverges by the real one especially in the low-voltage region.

**Table B.2. Simulations result after 400 EqC.** Averaged RMSE errors of the dynamic and driving profiles at different SoCs and of the full discharge at C/20 applying the Standard and Updated model configurations. The RMSE values are given percentage of the voltage interval exploited by the cell (2.5-4.2V).

RMSE (% of voltage interval)	Dynamic profile			Driving profile			Full discharge
	75% SoC	50% SoC	25% SoC	75% SoC	50% SoC	25% SoC	
Standard model	0.58%	0.40%	0.73%	0.09%	0.10%	0.2%	5.53%
Updated model	0.62%	0.32%	1.25%	0.11%	0.11%	0.15%	1.80%

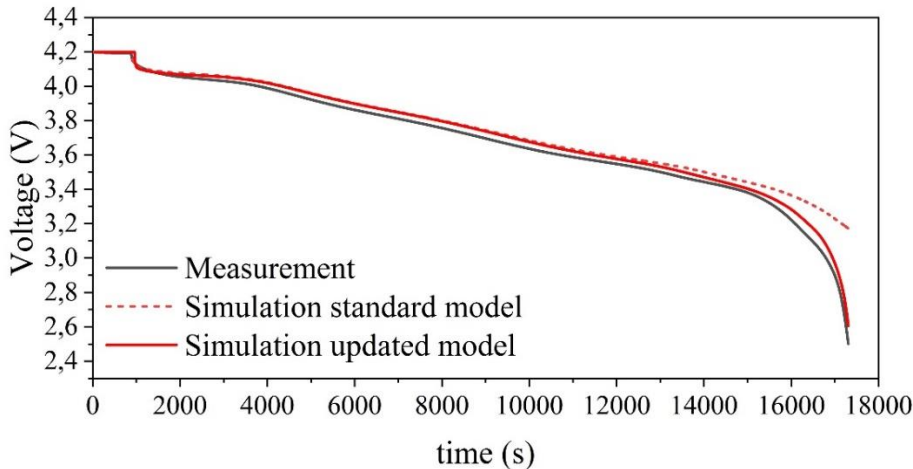


**Figure B.6. Full discharge simulation during cell aging after 400 EqC.** The standard model (obtained at BoL) and the updated model (with EIS and OCV measurements at 400 EqC) voltage profiles are compared with the measured one.

## B.4 Remarks

The robustness of EIS2MOD modelling framework has been proven developing an ECM for a cylindrical commercial cell.

This preliminary activity to understand the potentiality of EIS2MOD applied during cell aging showed that it is possible to obtain better simulation results updating the model parameters. However, the algorithm could be improved, optimizing the DRT calculation and the extraction of the parameters from DRT. In this way, it would be possible to obtain even better simulation results and practically apply the model for optimized SoC estimation.

# Appendix C

## Support material to Chapter 4

### C.1 Cell disassembling procedure

As mentioned in Chapter 4, cell disassembly procedure has been developed and optimized based on the existing literature. Preliminary analyses to perform post-mortem analyses have been made in MaDE group laboratories in Rüschlikon (Zürich). After that, the procedure has been developed in the battery laboratories of CSEM Sustainable Energy Center in Neuchâtel, where all the battery testing phase was also performed. This choice was mainly driven by the travelling and on-site working restrictions we were subjected during the pandemic.

Given the large spread of 18650 cylindrical format cell in the market, most of the existing works are based on this type of cell [43], [96], [137], [141], [151], [168]–[170]. At CSEM Sustainable Energy Center we analysed both 18650 and 21700 cylindrical format cells; the extraction procedure is identical and not influenced by the cell size. However, it must be considered that the bigger format cells normally have higher capacity than the smaller ones and more attention is needed during their handling to avoid short-circuits and accidents. In the following, the procedure is described for the cell type investigated in Chapter 4 and Chapter 5: LG Chem M50 (21700 cylindrical format). The manufacture datasheet of the cell is shown in Table 5.1.

Before cell disassembling, both capacity and impedance measurements are performed to assess the status of the cell. After that, the cell is discharged to the minimum voltage (2.5V in this case) at C/3 constant current rate and a CV phase with current cut-off at C/100. After that, the cell is transferred inside an argon-filled glovebox to avoid oxygen contamination of the cell components during disassembly. The steps of the procedure are shown in Figure C.1 and are explained in the following:

- a. A pipe cutter is used to open the cell on the bottom side, i.e. were the anode is electrically connected to the case. The pipe cutter must be handled carefully, with small increase of the torque to reduce the distance between the sharp disks and to have a deeper cut. As soon as the case is perforated the pipe cutter must be removed to avoid damage and short circuits of the jellyroll. When the bottom disk is detached, it is necessary to cut the anode tab or to electrically insulate it with tape to avoid short-circuits during the following operations.
- b. The pipe cutter is also used to remove the upper part of the case. The cutting must be as close as possible to the thin bending of the case; in this way it is less probable to damage the upper part of the jellyroll.
- c. The remaining side part of the case is removed using pliers and being careful of not damaging the outer part of the jellyroll.
- d. The cell case is completely removed and the tabs to connect electrically the electrodes with the case are secured (cut). Additional separator material is used to kept together the electrodes and is fixed with tape.
- e. A scalpel is used to cut the tape and the cell components can be unrolled and separated.
- f. The jellyroll is unrolled carefully with slow movement to reduce the risk of graphite exfoliation.
- g. Overview of the electrodes unrolling. It is possible to observe the graphite fragments coming off the edges of the anode electrode. During this step, it is important to take reference of the inward and outward facing side as well as of the outer and inner roll part of the electrodes. This information is useful for the characterization of these components.
- h. The electrodes are cut in different sections and stored in plastic bags inside the argon-filled glovebox.

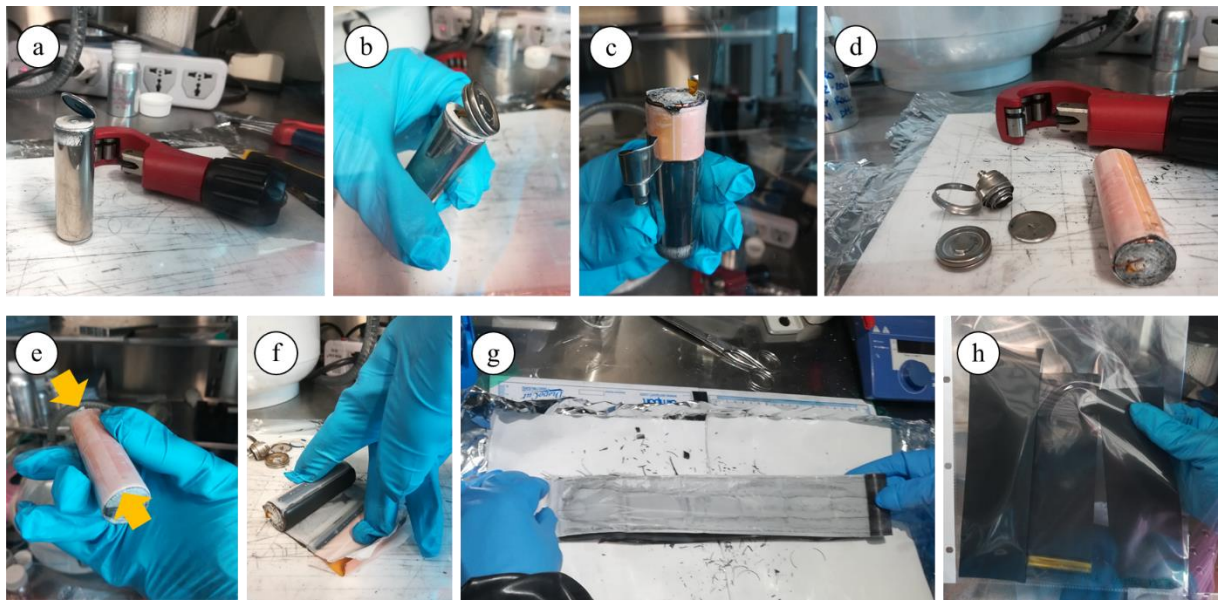


**Figure C.1. Main steps of electrodes extraction from cylindrical cells.** a) Opening on the bottom side with a pipe cutter; b) opening of the upper side as in previous step; c) removing the lateral case with pliers; d) overview of removed case and jellyroll; e) picture of the taped separator that have to be cut with a scalpel to open the jellyroll; f) g) unrolling of the jellyroll. The cathode is positioned within two layers of separator. It is important to take reference of the inward and outward facing parts as well as of inner and outer roll parts of the electrodes. h) Sections of electrode categorized and stored in plastic bag.

## C.2 Electrode samples preparation

After disassembling, the material is ready to be analysed with physico-chemical techniques or to be placed in half-cells for further cell characterization. In the first case, when the objective of the study is to characterize the structure and morphology or the material composition of the electrodes, an additional preparation step is required: washing the electrodes with DMC. This step is necessary to remove all the residues of electrolyte from the electrodes' surfaces [165]. However, this solvent has negative effects on the solid electrolyte interface that was created during cycling on the anode and cathode surfaces [165]. For this reason, the DMC washing was not performed in this work, where the objective was to perform electrochemical testing, such as EIS measurements of half cells.

The schematic representation of disk electrode preparation for half-cells is shown in Figure C.2. The outer part of the electrode is used, discarding the first 5cm that are not used for any other analysis. Moreover, in the case of the anode, also the initial small one-

side coated part is discarded due to higher fragility. The electrode is fixed to a hard plastic or glass substrate with adhesive tape and with the original outward facing side of the electrode now facing the plate, as shown in Figure C.3-a. The electrode coating is removed with a solvent using q-tip and soft brush; mechanical abrasion with spatula is avoided because it causes stress on the current collector foil and on the other side of electrode coating that can be damaged. The cathode material is removed with NMP; this solvent is used because it easily reacts with the PVDF binder. The result on NMC811 cathode is showed in Figure C.3-b. As regard graphite electrode, water-based solvent could be used for the same purpose. However, working inside the glovebox this is not recommended. Therefore, for practical reason, NMP is used also to remove the graphite coating [166], [171].

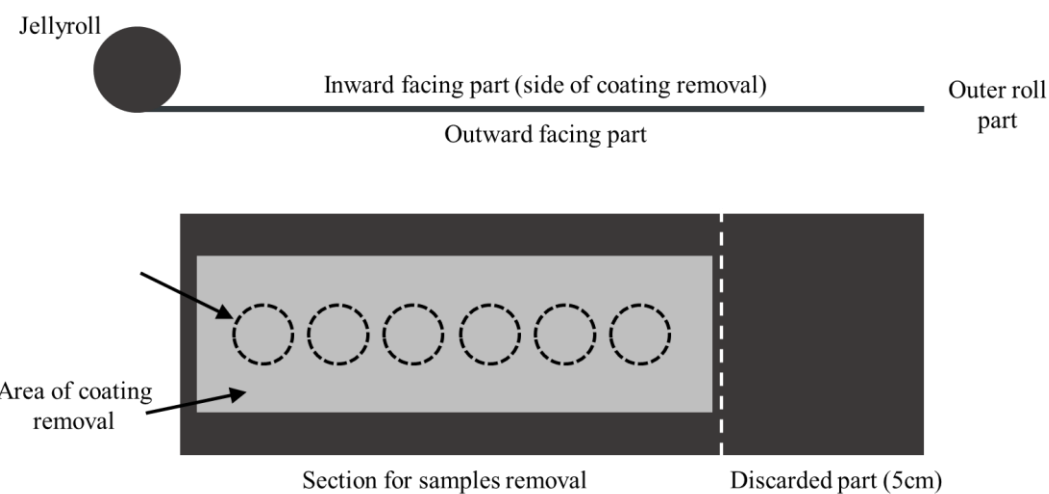


**Figure C.2. Schematic representation of the cathode electrode.** The coating is removed from the Inward facing part. The first outer roll part of the electrode (about 5 cm) is discarded and not used for further analyses. The length of the section for samples removal depends on the number of samples to be collected. The samples for half-cells are extracted from the central part of the electrode.

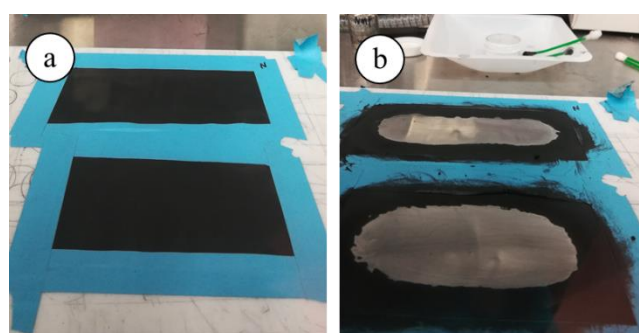


**Figure C.3. Cathode coating removal.** a) Two sections of cathode electrode are fixed to plastic substrate with adhesive tape for coating removal. b) Final result of the coating removal.

### C.3 Coin cells assembly

The 2025 cell format has been chosen to produce half-cells and full cells with the material harvested by commercial cylindrical cells. The cell configuration is showed in Figure C.4 and includes:

- Bottom cap.
- Aluminium spacer of 0.5mm thickness.
- The working electrode: either the cathode or the anode extracted by the commercial cell as 15mm diameter disk.
- A glass fiber separator of 19mm diameter (Whatman<sup>TM</sup> GF/C).
- 90 µl of 1M lithium hexafluorophosphate (LiPF<sub>6</sub>) in a mixture of ethylene carbonate, dimethyl carbonate and diethyl carbonate produced by Sigma-Aldrich© (EC:DMC:DEC, 1:1:1 w/w/w). A small quantity of electrolyte is spilled on the working electrode before inserting the glass fiber separator. This is done to improve the working electrode wetting. The remaining part of electrolyte is spilled on the glass fiber separator.
- A lithium metal disk electrode of 15mm diameter (counter electrode).
- An aluminium spacer of 0.5mm thickness.
- A spring, to keep all the components in the right position.
- Top cap.

Once the stack is completed and closed, a compressed-air crimping machine is used to seal the battery core within the case. The new produced cell is labelled and it can be taken out from the glovebox.

Anode and cathode half-cells are made with lithium metal counter electrode and full-cell are made with the same electrode materials that are present in the disassembled commercial cell (in this work, NMC811 as working electrode and graphite as counter electrode).

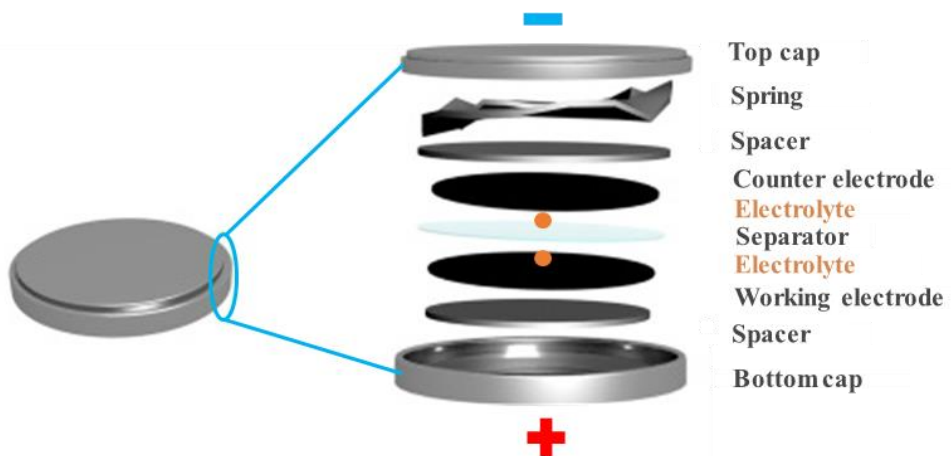


**Figure C.4. Schematic representation of the components of a coin cell.** All the components are listed in the assembly order, starting from the bottom cap. The counter electrode is lithium metal for half-cells configuration and graphite for full-cell configuration.

## C.4 Sample preparation for imaging techniques

The electrodes extracted by the commercial cell as explained in Section C.1, have been also characterized with imaging techniques.

### C.4.1 Digital imaging

After unrolling and sectioning of both graphite and NMC electrodes, a non-professional camera has been used inside the glovebox to avoid the oxygen poisoning of the samples. Both the inward and outward facing parts are analysed and the outer roll part is selected as reference section to compare the electrodes extracted by the different cells. This choice is mainly driven by the difficulty of obtain a flat surface for the inner roll part of the electrode, especially for graphite. An explanatory picture is shown in Figure C.5 for a new cell (cell ID:NEW) and an aged cell (cell ID:FC1). In both cases graphite is prone to exfoliation not allowing proper surface characterization.

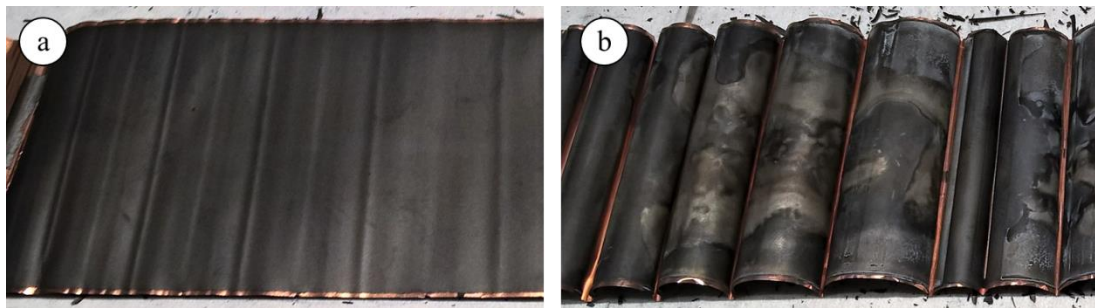


**Figure C.5. Digital imaging of inner roll part of graphite electrodes.** The inner roll part is not suitable for imaging characterization given the high level of exfoliation due to the very small curvature radius at which this portion of electrode was subjected during cell lifetime. Explanatory examples for (a) new cell (ID:NEW) and (b) aged cell (ID:FC1).

#### C.4.2 Optical microscopy and Scanning Electron Microscopy

After digital imaging, as mentioned in Section C.2, the outer roll part of the electrode is used to make disk electrodes for coin cells assembly (Figure C.3). The adjacent part is then used for microscopy characterization. Differently from digital imaging, the samples must be moved outside the glovebox to use the microscopes. Therefore, the samples are kept for about one week inside argon-filled glovebox and then they are moved out for characterization. During this period of time, any residue of electrolyte may evaporate without causing issues during the characterization. The electrode is cut as explained below:

- A portion of about 50mm length and 10mm height is cut for cross-section samples. This portion is taken in the central part of the electrode, as shown in Figure C.6.
- An area of about 5x5mm is cut for planar samples making. This area is taken generally in the central part of the electrode, as shown in Figure C.6, but also in other positions to investigate specific area with peculiar characteristics (e.g. plated surface).

The operation is repeated twice to guarantee reproducibility and store additional material in case the material is damaged in the following steps. Given the distance between the CSEM battery material laboratory and the CSEM microscopy laboratory, sealed bags have been used to transfer the samples. Optical and SEM characterizations were performed thanks to CSEM's group of additive manufacturing and component reliability allowing the use of their infrastructure and collaborating with material science laboratory specialists.

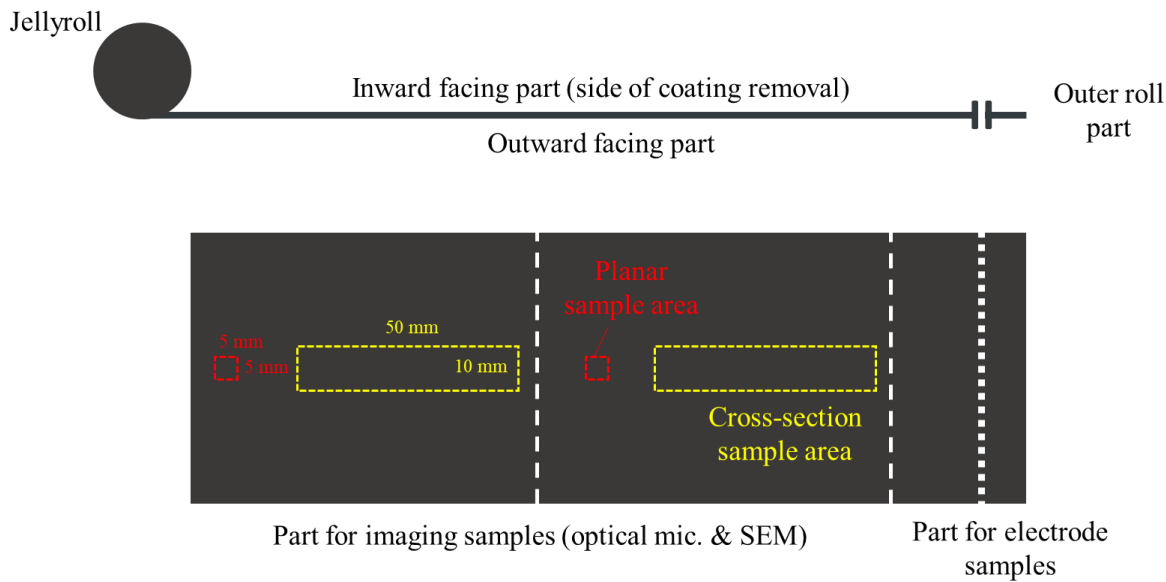


**Figure C.6. Schematic representation for sample preparation.** The samples for optical and scanning electron microscopy are cut by the electrode as shown in the schematic. The cross-section sample area is 50x10mm size and is placed in the central part of the electrode. The planar sample area is 5x5mm size and is placed in the central part of the electrode or in any other relevant position to investigate specific features. The samples are taken twice to ensure reproducibility and store additional material in case of any damage during the following steps.

In order to reduce the oxygen poisoning of the samples, the measurements (or the sample preparation for cross section) are done within 20 minutes from the opening of sealed bags. The preparation for the two sample types is as follows:

- The planar surface samples were placed on SEM sample stubs and a plastic support was employed to fix the stubs under the optical microscope. An example for graphite sample is shown in Figure C.7-a.
- The cross-section samples were prepared by the laboratory specialist, dipping the electrode in epoxy resin and applying mechanical polishing after solidifying. An example of final result for NMC cathode cross-section sample is given in Figure C.7-b. In some cases, electrolyte residues and degradation products reacted with the epoxy resin making the cross-section sample fragile and bringing it to rupture during the mechanical polishing process.

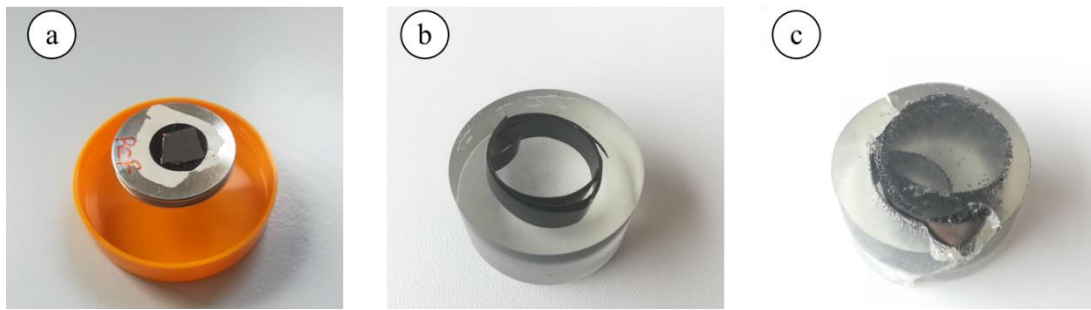


**Figure C.7. Planar surface and cross-section samples.** (a) Planar surface sample of NMC cathode. (b) Cross-section sample of NMC cathode. (c) Failed tentative of cross-section sample of graphite anode: residues of electrolyte reacted with the epoxy resin making the sample fragile and bringing to rupture during mechanical polishing process.

## C.5 OCV balancing of half-cells

To compare impedance spectra of full-cell and half-cells it is necessary to investigate the OCV curves in order to assign the SoC of the full-cell to the one of the half-cells [96]. To perform the balancing, the OCV curves of the half-cells are stretched or compressed and shift on the x-axis to optimally fit the voltage curve of the full cell. This procedure is performed calculating the derivative of the voltage with respect to the capacity  $dV/dQ$  for the half-cells and the full-cell. These parameters are linked by the following relationship:

$$\left(\frac{dV}{dQ}\right)_{full-cell} = \left(\frac{dV}{dQ}\right)_{Cathode} - \left(\frac{dV}{dQ}\right)_{Anode}, \quad (B.1)$$

as consequence of the linear relationship of the full cell OCV with the two electrodes OCVs curves. Plotting together these quantities and adjusting four specific parameters (mass factors and slippage factors), it is possible to overlap peaks and valleys performing the balancing of the electrodes. The mass factors are needed to scale the capacity of the two electrodes to the one of the full-cell; the slippage factors must be applied to match the window of capacity of the two electrodes with the one of the full-cell [164]. The software developed by Dahn et al. and presented in [172] has been used to perform the procedure described above. The result of electrodes balancing is shown in Figure C.7, representing the OCV curves with respect to the SoC of the full cell. Fixing a specific voltage of the full-cell, it is possible to read the related value of SoC and, drawing a vertical line, extract the associated voltage values of cathode and anode when crossing the respective OCV curves.

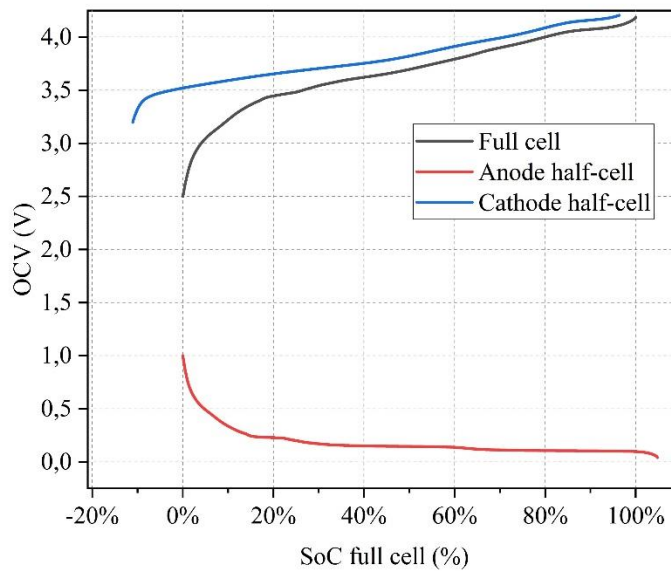


**Figure C.7. OCV balancing of the half-cells and the full-cell.** Anode and Cathode half-cells OCV curves are represented with respect to the SoC of the full cell. Looking at a specific voltage of the full cell, it is possible to find the associated voltage of the cathode and of the anode exploiting the related value of full-cell SoC.

# Appendix D

## Datasheets of the investigated Li-ion cells

This annex details the datasheets of the electrochemical cells which have been tested and modelled in this doctoral thesis.

### Large format NMC pouch cell [156]:

<b>Cell name</b>	GL 55 – 936A03
<b>Manufacturer</b>	Leclanché
<b>Shape format</b>	Pouch
<b>Cell dimension (L-H-W) [mm]</b>	285 x 178.5 x 12
<b>Weight [g]</b>	1140
<b>Cathode chemistry</b>	NMC
<b>Anode chemistry</b>	Graphite
<b>Nominal capacity [Ah]</b>	55
<b>Nominal energy [Wh]</b>	200
<b>Nominal voltage [V]</b>	3.7
<b>Standard charge current [A]</b>	5.5 (C-rate: C/10)
<b>Standard discharge current [A]</b>	5.5 (C-rate: C/10)
<b>Standard cycling current [A]</b>	55 (C-rate: 1C)
<b>Maximum voltage [V]</b>	4.2
<b>Minimum voltage [V]</b>	3.0
<b>Current cut-off [mA]</b>	5.5 (C-rate: C/10)
<b>Maximum charging current [A]</b>	55
<b>Operating temperature (charge) [°C]</b>	0°C to +45°C
<b>Maximum discharging current [A]</b>	165 (C-rate: 3C)
<b>Operating temperature (discharge) [°C]</b>	-20°C to +55°C
<b>Storage temperature [°C]</b>	-20°C to +25°C for up to 1 year

**Cylindrical NMC cell [167]:**

<b>Cell name</b>	INR21700 M50
<b>Manufacturer</b>	LG Chem
<b>Shape format</b>	Cylindrical
<b>Cell dimension (L-H-W) [mm]</b>	Ø 21 x 70
<b>Weight [g]</b>	68.0
<b>Cathode chemistry</b>	NMC811
<b>Anode chemistry</b>	Graphite-SiO <sub>x</sub>
<b>Nominal capacity [mAh]</b>	5010
<b>Nominal energy [Wh]</b>	18.20
<b>Nominal voltage [V]</b>	3.63
<b>Standard charge current [mA]</b>	1455 (C-rate: C/3)
<b>Standard discharge current [mA]</b>	970 (C-rate: C/5)
<b>Standard cycling current [mA]</b>	1455 (C-rate: C/3)
<b>Maximum voltage [V]</b>	4.2
<b>Minimum voltage [V]</b>	2.5
<b>Current cut-off [mA]</b>	50 (C-rate: C/100)
<b>Maximum charging current [mA]</b>	1455 (C-rate: C/3) for 0°C to +25°C
	3395 (C-rate: C/3) for 25°C to +50°C
<b>Maximum discharging current [mA]</b>	970 (C-rate: C/5) for -30°C to -20°C
	1455 (C-rate: C/3) for -20°C to +5°C
	7275 (C-rate: 1.5C) for +5°C to +60°C
<b>Storage temperature [°C]</b>	-20°C to +20°C for up to 1 year

# List of Figures

Figure 1.1. Schematic representation of the objectives of the thesis.....	5
Figure 1.2. Thesis layout.....	9
Figure 2.1. Graphical representation of the structure of the review.....	17
Figure 2.2. Representation of the frequency regions on a Nyquist plot.....	18
Figure 2.3. Representation of the EIS spectrum evolution of a cell subjected to calendar aging experiments.....	22
Figure 2.4. Representation of the EIS spectrum evolution of a cell subjected to cycling aging experiments.....	29
Figure 2.5. List of the commonly reported degradation mechanisms in Li-ion cells, associated degradation modes and related fade caused on the cell.....	31
Figure 2.6. Representation of ECM model of a Li-ion cell.....	39
Figure 2.7. ECMs developed by the review of the articles listed in Table 2.5.....	46
Figure 2.8. Critical assessment of the impact of aging tests procedures on EIS spectra given in Section 2.3.....	48
Figure 2.9. Critical assessment of the connections among EIS spectra and degradation mechanisms given in Section 2.4.....	50
Figure 2.10. Critical assessment of the connections among EIS spectra and circuital elements given in Section 2.5.....	53
Figure 2.11. Outcome of the critical review.....	55
Figure 3.1. Schematic representation of the methodology presented in this chapter....	64
Figure 3.2. DRT profiles of the large format pouch NMC cell under investigation.....	74
Figure 3.3. ECM developed for the large format pouch NMC cell under investigation....	75
Figure 3.4. Voltage-based parameters.....	75
Figure 3.5. Resistance parameters of the cell under investigation.....	77
Figure 3.6. Dynamic test at four C-rates (C/10, C/5, C/2 and 1C).....	79
Figure 3.7. Full discharge tests at constant current rate of C/10.....	80
Figure 3.8. Full discharge tests at various current rates.....	81
Figure 3.9. Driving simulation test.....	82

## List of Figures

---

Figure 3.10. Driving simulation test at variable temperature.....	83
Figure 4.1. Methodology followed in this chapter.....	89
Figure 4.2. Typical DRT profile of a Li-ion cell and the criteria used to evaluate DRT peaks .....	94
Figure 4.3. SoH versus EqC for the six cycled cells.....	96
Figure 4.4. 50% SoC DRT profiles trends during cycling of the six tested cells.....	97
Figure 4.5. DRT profiles at 0%, 50% and 100% SoC of cell NEW (BoL).....	98
Figure 4.6. DRT profiles at 50% SoC of a cell NEW (100% SoH) and of the tested cells at EoL/EoT .....	102
Figure 4.7. Digital imaging of graphite electrodes.....	105
Figure 4.8. Optical microscope imaging of graphite electrodes .....	106
Figure 4.9. SEM imaging of anode electrodes .....	107
Figure 4.10. SEM imaging of cathode electrodes.....	108
Figure 5.1. Overview of equipment and cells in Sustainable Energy Center laboratory at CSEM.....	118
Figure 5.2. SoH evolution curves over EqC for the cells under investigation.....	119
Figure 5.3. Typical DRT profile of the cylindrical commercial cells under investigation. ....	122
Figure 5.4. Three-steps procedure to correct the degradation indicators: .....	123
Figure 5.5. SoH evolution of the cells under investigation.....	124
Figure 5.6. Algorithm to evaluate the developed SoH model.....	125
Figure 5.7. Example of degradation indicators trends.....	128
Figure 5.8. Evolution of the three DMs indicators ( <i>LLI</i> , <i>LAMA</i> and <i>LAMC</i> ) for the cells under investigations.....	129
Figure 5.9. Developed SoH model.....	131
Figure 5.10. SoH estimation validation applying the SoH model of Figure 5.9.....	132
Figure 5.11. ....	133
Figure 5.12. Applicability of developed SoH model.....	135
Figure 6.1. Schematic representation of the research objectives and of the results of the work.....	140
Figure A.1. Lin-KK test.....	147
Figure A.2. Correction of inductive behaviour .....	148
Figure A.3. L-curve criterion .....	149

Figure A.4. Averaged impedance spectra calculation.....	150
Figure B.1. Voltage-curve based parameters.....	152
Figure B.2. EIS based parameters.....	153
Figure B.3. Full discharge simulation at C/20.....	155
Figure B.4. Dynamic test at four C-rates (C/10, C/5, C/2 and 1C).....	155
Figure B.5. Driving simulation test.....	156
Figure B.6. Full discharge simulation during cell aging after 400 EqC.....	157
Figure C.1. Main steps of electrodes extraction from cylindrical cells.....	161
Figure C.2. Schematic representation of the cathode electrode.....	162
Figure C.3. Cathode coating removal.....	162
Figure C.4. Schematic representation of the components of a coin cell.....	164
Figure C.5. Digital imaging of inner roll part of graphite electrodes.....	165
Figure C.6. Schematic representation for sample preparation.....	166
Figure C.7. Planar surface and cross-section samples.....	167
Figure C.7. OCV balancing of the half-cells and the full-cell.....	168



# List of Tables

Table 2.1. Overview of the reviewed articles with additional information .....	15
Table 2.2. Calendar aging tests characteristics and correspondent effect on the impedance curve of the Li-ion cell .....	21
Table 2.3. Cycling aging tests characteristics and correspondent effect on the impedance curve of the Li-ion cell .....	25
Table 2.4. Correlation between impedance curve variations and degradation mechanisms .....	33
Table 2.5. List of the ECMs used in the works under review.....	41
Table 2.6. Assessment of the review works .....	54
Table 3.1. Averaged RMSE errors of the dynamic and driving profiles at different SoCs and of the full discharge at 0.1C.....	79
Table 3.2. Averaged RMSE errors of the discharge profile at 20°C and different current rates.....	80
Table 3.3. Averaged RMSE errors of the driving simulation profiles performed at variable temperature.....	82
Table 4.1. Overview of the cycling protocol applied to the different tested cells.....	91
Table 4.2. Tentative DRT peaks attribution at BoL .....	100
Table 4.3. Tentative DRT peaks attribution at EoL/EoT .....	103
Table 4.4. Comparison of DRT peaks and anode digital imaging.....	104
Table 4.5. Conclusive DRT peaks attribution: physical processes and degradation mechanisms .....	109
Table 5.1. Main characteristics of the cylindrical commercial cell under investigation.	117
Table 5.2. Overview of cycling aging testing protocols applied to commercial Li-ion cells .....	119
Table 5.3. Training subset for SoH estimation .....	130
Table 5.4. Validation subset with results of MBE and MAE .....	131
Table 5.5. Estimation errors per different SoH ranges .....	133
Table B.1. Simulations results at BoL.....	154

List of Tables

---

Table B.2. Simulations result after 400 EqC.....	157
--	-----

# Glossary (nomenclature and acronyms)

## Nomenclature

RC	-	parallel circuit of resistor and capacitor
CPE	-	Constant Phase Element
Zarc	-	Parallel circuit of resistor and CPE
HN	-	Generalized Zarc
W	-	Warburg element
$Z$	<i>ohm</i>	Cell impedance
$R_{ohmic}$	<i>ohm</i>	Ohmic resistance
$R_{pol}$	<i>ohm</i>	Polarization resistance
$\lambda$	-	Regularization parameter
$M$	-	Regularization matrix
$C_{D,R}$	<i>F</i>	Intercalation capacitance
$R_i$	<i>ohm</i>	Resistance of DRT peak $i$
$\tau_i$	<i>s</i>	Time constant of DRT peak $i$
$C_i$	<i>F</i>	Capacitance of DRT peak $i$

## Acronyms

### *Abbreviations*

BMS	Battery Management System
BoL	Beginning of Life
CEI	Cathode Electrode Interface
CNLS	Complex Nonlinear Least Square
CPE	Constant Phase Element
CV	Constant Voltage phase
DEC	Diethyl Carbonate
DMC	Dimethyl Carbonate
DoD	Depth of Discharge
DRT	Distribution of Relaxation Time
EC	Ethylene Carbonate
ECM	Electric Circuit Model
EDS	Energy Dispersive Spectroscopy
EIS	Electrochemical Impedance Spectroscopy
EoL	End of Life
EoT	End of Test
EPMA	Electron Probe Microscopic Analysis
EqC	Equivalent Cycles
EV	Electrical Vehicle
FIB	Focused Ion Beam
FSD	Full Scale Deflection
FTIR	Fourier Transform InfraRed spectrometry
HDC	Hybrid Drive Cycle
KK	Kramers-Kronig
LCO	Lithium Cobalt Oxide
LFP	Lithium Iron Phosphate

---

LiPO	Li-ion Polymer
LMO	Lithium Manganese Oxide
NCA	Lithium Cobalt Aluminum oxide
NMC	Lithium Nickel Manganese Cobalt oxide
NMP	N-Methylpyrrolidone
OCV	Open Circuit Voltage
PGAA	Prompt Gamma Activation Analysis
SEI	Solid Electrolyte Interface
SEM	Scanning Electron Microscopy
SoC	State of Charge
SoH	State of Health
SoX	State of X
TEM	Transmission Electron Microscopy
TLM	Transmission Line Model
UDDS	Urban Dynamometer Driving Schedule
XAS	X-ray Absorption Spectroscopy
XPS	X-ray Photoelectron Technique
XRD	X-ray diffraction

*Tested cells nomenclature*

NEW	Pristine cell - not cycled
REF	Reference cell
REF_w/o CV	Reference cell without CV phase
DOD20	Reference cell cycled with 20% DoD
DOD60	Reference cell cycled with 60% DoD
FC05	Fast Charge at 0.5C
FC1	Fast Charge at 1C
FC2	Fast Charge at 2C

## Glossary

---

FD05	Fast Discharge at 0.5C
FD1	Fast Discharge at 1C
FD2	Fast Discharge at 2C

### *DRT peaks nomenclature*

A#	Anode half-cell peak #
C#	Cathode half-cell peak #
F#	Full cell peak #
S#	Cylindrical cell peak #

# References

- [1] European Commission, 'Communication from the Commission to the european parliament, the european council, the council, the European economic and social committee and the committee of the regions: The European Green Deal'. Dec. 11, 2019. Accessed: Oct. 15, 2020. [Online]. Available: [https://ec.europa.eu/info/sites/info/files/european-green-deal-communication\\_en.pdf](https://ec.europa.eu/info/sites/info/files/european-green-deal-communication_en.pdf)
- [2] J. E. Bistline, 'Economic and technical challenges of flexible operations under large-scale variable renewable deployment', *Energy Econ.*, vol. 64, pp. 363–372, May 2017, doi: 10.1016/j.eneco.2017.04.012.
- [3] K. Guerra, P. Haro, R. E. Gutiérrez, and A. Gómez-Barea, 'Facing the high share of variable renewable energy in the power system: Flexibility and stability requirements', *Appl. Energy*, vol. 310, p. 118561, Mar. 2022, doi: 10.1016/j.apenergy.2022.118561.
- [4] L. Bird *et al.*, 'Wind and solar energy curtailment: A review of international experience', *Renew. Sustain. Energy Rev.*, vol. 65, pp. 577–586, Nov. 2016, doi: 10.1016/j.rser.2016.06.082.
- [5] P. Denholm and M. Hand, 'Grid flexibility and storage required to achieve very high penetration of variable renewable electricity', *Energy Policy*, vol. 39, no. 3, pp. 1817–1830, Mar. 2011, doi: 10.1016/j.enpol.2011.01.019.
- [6] P. Iurilli, C. Brivio, and M. Merlo, 'SoC management strategies in Battery Energy Storage System providing Primary Control Reserve', *Sustain. Energy Grids Netw.*, vol. 19, p. 100230, Sep. 2019, doi: 10.1016/j.segan.2019.100230.
- [7] C. Brivio, S. Mandelli, and M. Merlo, 'Battery energy storage system for primary control reserve and energy arbitrage', *Sustain. Energy Grids Netw.*, vol. 6, pp. 152–165, Jun. 2016, doi: 10.1016/j.segan.2016.03.004.
- [8] Sandia, 'DOE Global Energy Storage Database'. <https://sandia.gov/ess-ssl/gesdb/public/projects.html> (accessed Sep. 30, 2022).

## References

---

- [9] Reuters, 'EU countries reach climate crisis deal after late-night talks', *The Guardian*, Jun. 29, 2022. Accessed: Sep. 29, 2022. [Online]. Available: <https://www.theguardian.com/world/2022/jun/29/eu-countries-reach-climate-crisis-deal-after-late-night-talks>
- [10] 'Fit for 55 package: Council reaches general approaches relating to emissions reductions and their social impacts'. <https://www.consilium.europa.eu/en/press/press-releases/2022/06/29/fit-for-55-council-reaches-general-approaches-relating-to-emissions-reductions-and-removals-and-their-social-impacts/> (accessed Sep. 29, 2022).
- [11] M. M. Kabir and D. E. Demirocak, 'Degradation mechanisms in Li-ion batteries: a state-of-the-art review: Degradation Mechanisms in Li-ion Batteries: A State-of-the-Art Review', *Int. J. Energy Res.*, vol. 41, no. 14, pp. 1963–1986, Nov. 2017, doi: 10.1002/er.3762.
- [12] Avicenne Energy, 'Worldwide Rechargeable Battery Market 2021-2030 2022 edition'. Accessed: Sep. 30, 2022. [Online]. Available: [http://www.avicenne.com/reports\\_energy.php](http://www.avicenne.com/reports_energy.php)
- [13] BloombergNEF, 'EVO 2022'. Accessed: Sep. 30, 2022. [Online]. Available: <https://bnef.turtl.co/story/evo-2022/>
- [14] Wood Mackenzie, 'Global lithium-ion battery supply and demand update: H1 2022', Jul. 2022. Accessed: Sep. 30, 2022. [Online]. Available: <https://www.woodmac.com/reports/power-markets-global-lithium-ion-battery-supply-and-demand-update-h1-2022-150048235>
- [15] European Commission, 'Strategic Action Plan on Batteries', Mar. 2019. Accessed: Sep. 30, 2022. [Online]. Available: <https://www.eesc.europa.eu/en/our-work/opinions-information-reports/opinions/strategic-action-plan-batteries-report>
- [16] 'IPCEI Batteries: Technology Fields'. <https://www.ipcei-batteries.eu/technology-fields> (accessed Sep. 29, 2022).
- [17] European Commission, 'Projects - Batteries Europe'. [https://wayback.archive-it.org/12090/20220912123832/https://energy.ec.europa.eu/topics/research-and-technology/batteries-europe/projects\\_en](https://wayback.archive-it.org/12090/20220912123832/https://energy.ec.europa.eu/topics/research-and-technology/batteries-europe/projects_en) (accessed Sep. 29, 2022).

---

References

- [18] BEPA Office, ‘Horizon Europe Calls – BATT4EU’. <https://bepassociation.eu/funding-opportunities/horizon-europe/> (accessed Oct. 24, 2022).
- [19] ‘SPARTACUS Project’. <https://www.spartacus-battery.eu/> (accessed Jul. 13, 2022).
- [20] ‘HIDDEN Project’. <https://hidden-project.eu/> (accessed Aug. 12, 2022).
- [21] ‘Challenges - Battery 2030+'. <https://battery2030.eu/battery2030/about-us/challenges/> (accessed Mar. 16, 2022).
- [22] H. Engel, P. Hertzke, and G. Siccardo, ‘Second-life EV batteries: The newest value pool in energy storage’, p. 5.
- [23] European Commission, ‘Proposal for a REGULATION OF THE EUROPEAN PARLIAMENT AND OF THE COUNCIL concerning batteries and waste batteries, repealing Directive 2006/66/EC and amending Regulation (EU) No 2019/1020’. 2020. Accessed: Oct. 24, 2022. [Online]. Available: <https://eur-lex.europa.eu/legal-content/EN/TXT/?uri=CELEX%3A52020PC0798>
- [24] European Commission, ‘Circular economy action plan’. [https://environment.ec.europa.eu/strategy/circular-economy-action-plan\\_en](https://environment.ec.europa.eu/strategy/circular-economy-action-plan_en) (accessed Oct. 24, 2022).
- [25] European Parliament, ‘Directive 2006/66/EC of the European Parliament and of the Council of 6 September 2006 on batteries and accumulators and waste batteries and accumulators and repealing Directive 91/157/EEC (Text with EEA relevance)’. <https://eur-lex.europa.eu/eli/dir/2006/66/oj> (accessed Oct. 24, 2022).
- [26] Ellen MacArthur Foundation, ‘Towards the Circular Economy Vol. 1: an economic and business rationale for an accelerated transition’. <https://emf.thirdlight.com/link/x8ay372a3r11-k6775n/@/preview/1?o> (accessed Oct. 24, 2022).
- [27] Y. Kalmykova, M. Sadagopan, and L. Rosado, ‘Circular economy – From review of theories and practices to development of implementation tools’, *Resour. Conserv. Recycl.*, vol. 135, pp. 190–201, Aug. 2018, doi: 10.1016/j.resconrec.2017.10.034.

## References

---

- [28] C. Curry, 'Lithium-ion Battery Costs and Market'. Bloomberg New Energy Finance. Accessed: Oct. 24, 2022. [Online]. Available: <https://data.bloomberglp.com/bnef/sites/14/2017/07/BNEF-Lithium-ion-battery-costs-and-market.pdf>
- [29] N. Hill *et al.*, *Circular economy perspectives for the management of batteries used in electric vehicles*. 2019. Accessed: May 27, 2020. [Online]. Available: [http://publications.europa.eu/publication/manifestation\\_identifier/PUB\\_KJ0319666EN](http://publications.europa.eu/publication/manifestation_identifier/PUB_KJ0319666EN)
- [30] European Parliament, 'A new EU regulatory framework for batteries', p. 1.
- [31] K. Berger, J.-P. Schögl, and R. J. Baumgartner, 'Digital battery passports to enable circular and sustainable value chains: Conceptualization and use cases', *J. Clean. Prod.*, vol. 353, p. 131492, Jun. 2022, doi: 10.1016/j.jclepro.2022.131492.
- [32] C. Brivio, R. E. Carrillo, P.-J. Alet, and A. Hutter, 'Bestimator<sup>TM</sup>: a novel model-based algorithm for robust estimation of battery SoC', in *2020 International Symposium on Power Electronics, Electrical Drives, Automation and Motion (SPEEDAM)*, Sorrento, Italy, Jun. 2020, pp. 184–188. doi: 10.1109/SPEEDAM48782.2020.9161869.
- [33] P. Iurilli, C. Brivio, and V. Wood, 'On the use of electrochemical impedance spectroscopy to characterize and model the aging phenomena of lithium-ion batteries: a critical review', *J. Power Sources*, vol. 505, p. 229860, Sep. 2021, doi: 10.1016/j.jpowsour.2021.229860.
- [34] H. Tian, P. Qin, K. Li, and Z. Zhao, 'A review of the state of health for lithium-ion batteries: Research status and suggestions', *J. Clean. Prod.*, vol. 261, p. 120813, Jul. 2020, doi: 10.1016/j.jclepro.2020.120813.
- [35] Y. Hu, S. Yurkovich, Y. Guezennec, and B. J. Yurkovich, 'Electro-thermal battery model identification for automotive applications', *J. Power Sources*, vol. 196, pp. 449–457, Jan. 2011, doi: 10.1016/J.JPOWSOUR.2010.06.037.
- [36] M. Berecibar, I. Gandiaga, I. Villarreal, N. Omar, J. Van Mierlo, and P. Van den Bossche, 'Critical review of state of health estimation methods of Li-ion batteries for real

- applications', *Renew. Sustain. Energy Rev.*, vol. 56, pp. 572–587, Apr. 2016, doi: 10.1016/j.rser.2015.11.042.
- [37] P. Weicker, *A Systems Approach to Lithium-Ion Battery Management*. Artech House, 2013.
- [38] L. Ungurean, G. Cârstoiu, M. V. Micea, and V. Groza, 'Battery state of health estimation: a structured review of models, methods and commercial devices: Battery State of Health Estimation: a Structured Review', *Int. J. Energy Res.*, vol. 41, no. 2, pp. 151–181, Feb. 2017, doi: 10.1002/er.3598.
- [39] J. Zhou and P. H. L. Notten, 'Studies on the degradation of Li-ion batteries by the use of microreference electrodes', *J. Power Sources*, vol. 177, no. 2, pp. 553–560, Mar. 2008, doi: 10.1016/j.jpowsour.2007.11.032.
- [40] Y. Li, M. Bettge, B. Polzin, Y. Zhu, M. Balasubramanian, and D. P. Abraham, 'Understanding Long-Term Cycling Performance of Li<sub>1.2</sub>Ni<sub>0.15</sub>Mn<sub>0.55</sub>Co<sub>0.102</sub>-Graphite Lithium-Ion Cells', *J. Electrochem. Soc.*, vol. 160, no. 5, p. A3006, Feb. 2013, doi: 10.1149/2.002305jes.
- [41] J. Li, J. Zhang, X. Zhang, C. Yang, N. Xu, and B. Xia, 'Study of the storage performance of a Li-ion cell at elevated temperature', *Electrochimica Acta*, vol. 55, no. 3, pp. 927–934, Jan. 2010, doi: 10.1016/j.electacta.2009.09.077.
- [42] B. Stiaszny, J. C. Ziegler, E. E. Krauß, J. P. Schmidt, and E. Ivers-Tiffée, 'Electrochemical characterization and post-mortem analysis of aged LiMn<sub>2</sub>O<sub>4</sub>-Li(Ni<sub>0.5</sub>Mn<sub>0.3</sub>Co<sub>0.2</sub>)O<sub>2</sub>/graphite lithium ion batteries. Part I: Cycle aging', *J. Power Sources*, vol. 251, pp. 439–450, Apr. 2014, doi: 10.1016/j.jpowsour.2013.11.080.
- [43] X. Li *et al.*, 'Degradation mechanisms of high capacity 18650 cells containing Si-graphite anode and nickel-rich NMC cathode', *Electrochimica Acta*, vol. 297, pp. 1109–1120, Feb. 2019, doi: 10.1016/j.electacta.2018.11.194.
- [44] M.-S. Wu, P.-C. J. Chiang, and J.-C. Lin, 'Electrochemical Investigations on Advanced Lithium-Ion Batteries by Three-Electrode Measurements', *J. Electrochem. Soc.*, vol. 152, no. 1, p. A47, Nov. 2004, doi: 10.1149/1.1825385.

## References

---

- [45] I. Buchberger *et al.*, ‘Aging Analysis of Graphite/LiNi1/3Mn1/3Co1/3O2 Cells Using XRD, PGAA, and AC Impedance’, *J. Electrochem. Soc.*, vol. 162, no. 14, p. A2737, Oct. 2015, doi: 10.1149/2.0721514jes.
- [46] J. Li, E. Murphy, J. Winnick, and P. A. Kohl, ‘Studies on the cycle life of commercial lithium ion batteries during rapid charge–discharge cycling’, *J. Power Sources*, vol. 102, no. 1, pp. 294–301, Dec. 2001, doi: 10.1016/S0378-7753(01)00821-7.
- [47] E. Sarasketa-Zabala, F. Aguesse, I. Villarreal, L. M. Rodriguez-Martinez, C. M. López, and P. Kubiak, ‘Understanding Lithium Inventory Loss and Sudden Performance Fade in Cylindrical Cells during Cycling with Deep-Discharge Steps’, *J. Phys. Chem. C*, vol. 119, no. 2, pp. 896–906, Jan. 2015, doi: 10.1021/jp510071d.
- [48] D. N. Wong, D. A. Wetz, A. M. Mansour, and J. M. Heinzel, ‘The influence of high C rate pulsed discharge on lithium-ion battery cell degradation’, in *2015 IEEE Pulsed Power Conference (PPC)*, May 2015, pp. 1–6. doi: 10.1109/PPC.2015.7297030.
- [49] M. Kassem and C. Delacourt, ‘Postmortem analysis of calendar-aged graphite/LiFePO<sub>4</sub> cells’, *J. Power Sources*, vol. 235, pp. 159–171, Aug. 2013, doi: 10.1016/j.jpowsour.2013.01.147.
- [50] K. Jalkanen, J. Karppinen, L. Skogström, T. Laurila, M. Nisula, and K. Vuorilehto, ‘Cycle aging of commercial NMC/graphite pouch cells at different temperatures’, *Appl. Energy*, vol. 154, pp. 160–172, Sep. 2015, doi: 10.1016/j.apenergy.2015.04.110.
- [51] Y. Zhang and C.-Y. Wang, ‘Cycle-Life Characterization of Automotive Lithium-Ion Batteries with LiNiO<sub>2</sub> Cathode’, *J. Electrochem. Soc.*, vol. 156, no. 7, p. A527, May 2009, doi: 10.1149/1.3126385.
- [52] A. Maheshwari, M. Heck, and M. Santarelli, ‘Cycle aging studies of lithium nickel manganese cobalt oxide-based batteries using electrochemical impedance spectroscopy’, *Electrochimica Acta*, vol. 273, pp. 335–348, May 2018, doi: 10.1016/j.electacta.2018.04.045.
- [53] T. Yoshida *et al.*, ‘Degradation Mechanism and Life Prediction of Lithium-Ion Batteries’, *J. Electrochem. Soc.*, vol. 153, no. 3, p. A576, Feb. 2006, doi: 10.1149/1.2162467.

- [54] T. Joshi, K. Eom, G. Yushin, and T. F. Fuller, 'Effects of Dissolved Transition Metals on the Electrochemical Performance and SEI Growth in Lithium-Ion Batteries', *J. Electrochem. Soc.*, vol. 161, no. 12, p. A1915, Sep. 2014, doi: 10.1149/2.0861412jes.
- [55] X. Zhang *et al.*, 'A novel quantitative electrochemical aging model considering side reactions for lithium-ion batteries', *Electrochimica Acta*, vol. 343, p. 136070, May 2020, doi: 10.1016/j.electacta.2020.136070.
- [56] D. P. Abraham, E. M. Reynolds, E. Sammann, A. N. Jansen, and D. W. Dees, 'Aging characteristics of high-power lithium-ion cells with LiNi<sub>0.8</sub>Co<sub>0.15</sub>Al<sub>0.05</sub>O<sub>2</sub> and Li<sub>4</sub>/3Ti<sub>5</sub>/3O<sub>4</sub> electrodes', *Electrochimica Acta*, vol. 51, no. 3, pp. 502–510, Oct. 2005, doi: 10.1016/j.electacta.2005.05.008.
- [57] G. Ning, B. Haran, and B. N. Popov, 'Capacity fade study of lithium-ion batteries cycled at high discharge rates', *J. Power Sources*, vol. 117, no. 1, pp. 160–169, May 2003, doi: 10.1016/S0378-7753(03)00029-6.
- [58] D. Zhang, B. S. Haran, A. Durairajan, R. E. White, Y. Podrazhansky, and B. N. Popov, 'Studies on capacity fade of lithium-ion batteries', *J. Power Sources*, vol. 91, no. 2, pp. 122–129, Dec. 2000, doi: 10.1016/S0378-7753(00)00469-9.
- [59] C. Pastor-Fernández, T. F. Yu, W. D. Widanage, and J. Marco, 'Critical review of non-invasive diagnosis techniques for quantification of degradation modes in lithium-ion batteries', *Renew. Sustain. Energy Rev.*, vol. 109, pp. 138–159, Jul. 2019, doi: 10.1016/j.rser.2019.03.060.
- [60] W. Waag, C. Fleischer, and D. Sauer, 'Critical review of the methods for monitoring of lithium-ion batteries in electric and hybrid vehicles', *J. Power Sources*, vol. 258, pp. 321–339, Jul. 2014, doi: 10.1016/j.jpowsour.2014.02.064.
- [61] A. Lasia, *Electrochemical Impedance Spectroscopy and its Applications*. New York, NY: Springer New York, 2014. doi: 10.1007/978-1-4614-8933-7.
- [62] J. Vetter *et al.*, 'Ageing mechanisms in lithium-ion batteries', *J. Power Sources*, vol. 147, no. 1–2, pp. 269–281, Sep. 2005, doi: 10.1016/j.jpowsour.2005.01.006.
- [63] C. Pastor-Fernández, K. Uddin, G. H. Chouchelamane, W. D. Widanage, and J. Marco, 'A Comparison between Electrochemical Impedance Spectroscopy and Incremental Capacity-Differential Voltage as Li-ion Diagnostic Techniques to Identify and Quantify the

## References

---

- Effects of Degradation Modes within Battery Management Systems', *J. Power Sources*, vol. 360, pp. 301–318, Aug. 2017, doi: 10.1016/j.jpowsour.2017.03.042.
- [64] W. Choi, H.-C. Shin, J. M. Kim, J.-Y. Choi, and W.-S. Yoon, 'Modeling and Applications of Electrochemical Impedance Spectroscopy (EIS) for Lithium-ion Batteries', *J. Electrochem. Sci. Technol.*, vol. 11, no. 1, pp. 1–13, Feb. 2020, doi: 10.33961/jecst.2019.00528.
- [65] H. de Vries, T. T. Nguyen, and B. Op het Veld, 'Increasing the cycle life of lithium ion cells by partial state of charge cycling', *Microelectron. Reliab.*, vol. 55, no. 11, pp. 2247–2253, Nov. 2015, doi: 10.1016/j.microrel.2015.08.014.
- [66] T. Osaka, S. Nakade, M. Rajamäki, and T. Momma, 'Influence of capacity fading on commercial lithium-ion battery impedance', *J. Power Sources*, vol. 119–121, pp. 929–933, Jun. 2003, doi: 10.1016/S0378-7753(03)00233-7.
- [67] U. Tröltzscher, O. Kanoun, and H.-R. Tränkler, 'Characterizing aging effects of lithium ion batteries by impedance spectroscopy', *Electrochimica Acta*, vol. 51, no. 8, pp. 1664–1672, 2005, doi: 10.1016/j.electacta.2005.02.148.
- [68] K. Kato, A. Negishi, K. Nozaki, I. Tsuda, and K. Takano, 'PSOC cycle testing method for lithium-ion secondary batteries', *J. Power Sources*, vol. 117, no. 1, pp. 118–123, May 2003, doi: 10.1016/S0378-7753(03)00157-5.
- [69] D. Mukoyama, T. Momma, H. Nara, and T. Osaka, 'Electrochemical Impedance Analysis on Degradation of Commercially Available Lithium Ion Battery during Charge–Discharge Cycling', *Chem. Lett.*, vol. 41, no. 4, pp. 444–446, Apr. 2012, doi: 10.1246/cl.2012.444.
- [70] C. Lyu, T. Zhang, W. Luo, G. Wei, B. Ma, and L. Wang, 'SOH Estimation of Lithium-ion Batteries Based on Fast Time Domain Impedance Spectroscopy', in *2019 14th IEEE Conference on Industrial Electronics and Applications (ICIEA)*, Jun. 2019, pp. 2142–2147. doi: 10.1109/ICIEA.2019.8834119.
- [71] S. Schindler and M. A. Danzer, 'A novel mechanistic modeling framework for analysis of electrode balancing and degradation modes in commercial lithium-ion cells', *J. Power Sources*, vol. 343, pp. 226–236, Mar. 2017, doi: 10.1016/j.jpowsour.2017.01.026.

- [72] M. Petzl, M. Kasper, and M. A. Danzer, 'Lithium plating in a commercial lithium-ion battery – A low-temperature aging study', *J. Power Sources*, vol. 275, pp. 799–807, Feb. 2015, doi: 10.1016/j.jpowsour.2014.11.065.
- [73] Y. Zhang, C.-Y. Wang, and X. Tang, 'Cycling degradation of an automotive LiFePO<sub>4</sub> lithium-ion battery', *J. Power Sources*, vol. 196, no. 3, pp. 1513–1520, Feb. 2011, doi: 10.1016/j.jpowsour.2010.08.070.
- [74] M. Abdel Monem *et al.*, 'Lithium-ion batteries: Evaluation study of different charging methodologies based on aging process', *Appl. Energy*, vol. 152, pp. 143–155, Aug. 2015, doi: 10.1016/j.apenergy.2015.02.064.
- [75] D.-I. Stroe, M. Swierczynski, A.-I. Stroe, S. K. Kaer, and R. Teodorescu, 'Lithium-ion battery power degradation modelling by electrochemical impedance spectroscopy', *IET Renew. Power Gener.*, vol. 11, no. 9, pp. 1136–1141, Jul. 2017, doi: 10.1049/iet-rpg.2016.0958.
- [76] T. G. Zavalis, M. Klett, M. H. Kjell, M. Behm, R. W. Lindström, and G. Lindbergh, 'Aging in lithium-ion batteries: Model and experimental investigation of harvested LiFePO<sub>4</sub> and mesocarbon microbead graphite electrodes', *Electrochimica Acta*, vol. 110, pp. 335–348, Nov. 2013, doi: 10.1016/j.electacta.2013.05.081.
- [77] X. Wang, X. Wei, and H. Dai, 'Estimation of state of health of lithium-ion batteries based on charge transfer resistance considering different temperature and state of charge', *J. Energy Storage*, vol. 21, pp. 618–631, Feb. 2019, doi: 10.1016/j.est.2018.11.020.
- [78] Y. Leng *et al.*, 'Electrochemical Cycle-Life Characterization of High Energy Lithium-Ion Cells with Thick Li(Ni0.6Mn0.2Co0.2)O<sub>2</sub> and Graphite Electrodes', *J. Electrochem. Soc.*, vol. 164, no. 6, p. A1037, Mar. 2017, doi: 10.1149/2.0451706jes.
- [79] S. F. Schuster *et al.*, 'Nonlinear aging characteristics of lithium-ion cells under different operational conditions', *J. Energy Storage*, vol. 1, pp. 44–53, Jun. 2015, doi: 10.1016/j.est.2015.05.003.
- [80] X. Zhou, J. Huang, Z. Pan, and M. Ouyang, 'Impedance characterization of lithium-ion batteries aging under high-temperature cycling: Importance of electrolyte-phase diffusion', *J. Power Sources*, vol. 426, pp. 216–222, Jun. 2019, doi: 10.1016/j.jpowsour.2019.04.040.

## References

---

- [81] U. Westerhoff, K. Kurbach, F. Lienesch, and M. Kurrat, 'Analysis of Lithium-Ion Battery Models Based on Electrochemical Impedance Spectroscopy', *Energy Technol.*, vol. 4, no. 12, pp. 1620–1630, Dec. 2016, doi: 10.1002/ente.201600154.
- [82] Q. Yang, J. Xu, X. Li, D. Xu, and B. Cao, 'State-of-health estimation of lithium-ion battery based on fractional impedance model and interval capacity', *Int. J. Electr. Power Energy Syst.*, vol. 119, p. 105883, Jul. 2020, doi: 10.1016/j.ijepes.2020.105883.
- [83] P. Aurora, N. Ramaswamy, T. Han, and K. Adjemian, 'Electrochemical Impedance Spectroscopic Analysis of Lithium-Ion Battery Aging Mechanisms', *ECS Meet. Abstr.*, 2013, doi: 10.1149/MA2013-01/4/254.
- [84] M. Klett *et al.*, 'Electrode Behavior RE-Visited: Monitoring Potential Windows, Capacity Loss, and Impedance Changes in Li<sub>1.03</sub>(Ni<sub>0.5</sub>Co<sub>0.2</sub>Mn<sub>0.3</sub>)<sub>0.9702</sub>/Silicon-Graphite Full Cells', *J. Electrochem. Soc.*, vol. 163, no. 6, p. A875, Mar. 2016, doi: 10.1149/2.0271606jes.
- [85] T. P. Heins, N. Schlüter, S. T. Ernst, and U. Schröder, 'On the Interpretation of Impedance Spectra of Large-Format Lithium-Ion Batteries and Its Application in Aging Studies', *Energy Technol.*, vol. 8, no. 2, p. 1900279, 2020, doi: 10.1002/ente.201900279.
- [86] T. P. Heins, R. Leithoff, N. Schlüter, U. Schröder, and K. Dröder, 'Impedance Spectroscopic Investigation of the Impact of Erroneous Cell Assembly on the Aging of Lithium-Ion Batteries', *Energy Technol.*, vol. 8, no. 2, p. 1900288, 2020, doi: 10.1002/ente.201900288.
- [87] R. Xiong, J. Tian, H. Mu, and C. Wang, 'A systematic model-based degradation behavior recognition and health monitoring method for lithium-ion batteries', *Appl. Energy*, vol. 207, pp. 372–383, Dec. 2017, doi: 10.1016/j.apenergy.2017.05.124.
- [88] B. Stiaszny, J. C. Ziegler, E. E. Krauß, M. Zhang, J. P. Schmidt, and E. Ivers-Tiffée, 'Electrochemical characterization and post-mortem analysis of aged LiMn<sub>204</sub>-NMC/graphite lithium ion batteries part II: Calendar aging', *J. Power Sources*, vol. 258, pp. 61–75, Jul. 2014, doi: 10.1016/j.jpowsour.2014.02.019.
- [89] J. Schmitt, A. Maheshwari, M. Heck, S. Lux, and M. Vetter, 'Impedance change and capacity fade of lithium nickel manganese cobalt oxide-based batteries during calendar

- aging', *J. Power Sources*, vol. 353, pp. 183–194, Jun. 2017, doi: 10.1016/j.jpowsour.2017.03.090.
- [90] P. Shafiei Sabet, A. J. Warnecke, F. Meier, H. Witzenhausen, E. Martinez-Laserna, and D. U. Sauer, 'Non-invasive yet separate investigation of anode/cathode degradation of lithium-ion batteries (nickel–cobalt–manganese vs. graphite) due to accelerated aging', *J. Power Sources*, vol. 449, p. 227369, Feb. 2020, doi: 10.1016/j.jpowsour.2019.227369.
- [91] M. Ecker *et al.*, 'Development of a lifetime prediction model for lithium-ion batteries based on extended accelerated aging test data', *J. Power Sources*, vol. 215, pp. 248–257, Oct. 2012, doi: 10.1016/j.jpowsour.2012.05.012.
- [92] W. Waag, S. Käbitz, and D. U. Sauer, 'Experimental investigation of the lithium-ion battery impedance characteristic at various conditions and aging states and its influence on the application', *Appl. Energy*, vol. 102, pp. 885–897, Feb. 2013, doi: 10.1016/j.apenergy.2012.09.030.
- [93] D. Wong, B. Shrestha, D. A. Wetz, and J. M. Heinzel, 'Impact of high rate discharge on the aging of lithium nickel cobalt aluminum oxide batteries', *J. Power Sources*, vol. 280, pp. 363–372, Apr. 2015, doi: 10.1016/j.jpowsour.2015.01.110.
- [94] R. G. Jungst *et al.*, 'Accelerated calendar and pulse life analysis of lithium-ion cells', *J. Power Sources*, vol. 119–121, pp. 870–873, Jun. 2003, doi: 10.1016/S0378-7753(03)00193-9.
- [95] H. Sun *et al.*, 'Quantitative Analysis of Degradation Modes of Lithium-Ion Battery under Different Operating Conditions', *Energies*, vol. 14, no. 2, Art. no. 2, Jan. 2021, doi: 10.3390/en14020350.
- [96] P. Shafiei Sabet, G. Stahl, and D. U. Sauer, 'Non-invasive investigation of predominant processes in the impedance spectra of high energy lithium-ion batteries with nickel–cobalt–aluminum cathodes', *J. Power Sources*, vol. 472, p. 228189, Oct. 2020, doi: 10.1016/j.jpowsour.2020.228189.
- [97] M. Galeotti, L. Cinà, C. Giannanco, S. Cordiner, and A. Di Carlo, 'Performance analysis and SOH (state of health) evaluation of lithium polymer batteries through electrochemical impedance spectroscopy', *Energy*, vol. 89, pp. 678–686, Sep. 2015, doi: 10.1016/j.energy.2015.05.148.

## References

---

- [98] H. Popp, M. Einhorn, and F. V. Conte, 'Capacity Decrease vs. Impedance Increase of Lithium Batteries. A comparative study.', p. 6.
- [99] M. Li, J. Lu, Z. Chen, and K. Amine, '30 Years of Lithium-Ion Batteries', *Adv. Mater.*, vol. 30, no. 33, p. 1800561, 2018, doi: 10.1002/adma.201800561.
- [100] J. Illig, 'Physically based Impedance Modelling of Lithium-Ion Cells', Karlsruher Institut für Technologie, 2014.
- [101] A. Eddahech, O. Briat, H. Henry, J.-Y. Delétage, E. Woirgard, and J.-M. Vinassa, 'Ageing monitoring of lithium-ion cell during power cycling tests', *Microelectron. Reliab.*, vol. 51, no. 9, pp. 1968–1971, Sep. 2011, doi: 10.1016/j.microrel.2011.07.013.
- [102] S. Skoog and S. David, 'Parameterization of linear equivalent circuit models over wide temperature and SOC spans for automotive lithium-ion cells using electrochemical impedance spectroscopy', *J. Energy Storage*, vol. 14, pp. 39–48, Dec. 2017, doi: 10.1016/j.est.2017.08.004.
- [103] P. Verma, P. Maire, and P. Novák, 'A review of the features and analyses of the solid electrolyte interphase in Li-ion batteries', *Electrochimica Acta*, vol. 55, no. 22, pp. 6332–6341, Sep. 2010, doi: 10.1016/j.electacta.2010.05.072.
- [104] V. Agubra and J. Fergus, 'Lithium Ion Battery Anode Aging Mechanisms', *Materials*, vol. 6, no. 4, pp. 1310–1325, Mar. 2013, doi: 10.3390/ma6041310.
- [105] V. Pop, H. J. Bergveld, P. P. L. Regtien, J. H. G. O. het Veld, D. Danilov, and P. H. L. Notten, 'Battery Aging and Its Influence on the Electromotive Force', *J. Electrochem. Soc.*, vol. 154, no. 8, p. A744, May 2007, doi: 10.1149/1.2742296.
- [106] M. Dubarry, C. Truchot, and B. Y. Liaw, 'Synthesize battery degradation modes via a diagnostic and prognostic model', *J. Power Sources*, vol. 219, pp. 204–216, Dec. 2012, doi: 10.1016/j.jpowsour.2012.07.016.
- [107] C. R. Birkl, M. R. Roberts, E. McTurk, P. G. Bruce, and D. A. Howey, 'Degradation diagnostics for lithium ion cells', *J. Power Sources*, vol. 341, pp. 373–386, Feb. 2017, doi: 10.1016/j.jpowsour.2016.12.011.

- [108] E. IVERS-TIFFEE and A. Weber, 'Evaluation of electrochemical impedance spectra by the distribution of relaxation times', *J. Ceram. Soc. Jpn.*, vol. 125, no. 4, pp. 193–201, 2017, doi: 10.2109/jcersj2.16267.
- [109] G. Nagasubramanian, 'Two- and three-electrode impedance studies on 18650 Li-ion cells', *J. Power Sources*, vol. 87, no. 1, pp. 226–229, Apr. 2000, doi: 10.1016/S0378-7753(99)00469-3.
- [110] J. Ross Macdonald, 'Note on the parameterization of the constant-phase admittance element', *Solid State Ion.*, vol. 13, no. 2, pp. 147–149, May 1984, doi: 10.1016/0167-2738(84)90049-3.
- [111] M. R. Shoar Abouzari, F. Berkemeier, G. Schmitz, and D. Wilmer, 'On the physical interpretation of constant phase elements', *Solid State Ion.*, vol. 180, no. 14, pp. 922–927, Jun. 2009, doi: 10.1016/j.ssi.2009.04.002.
- [112] J. R. Macdonald, 'New aspects of some small-signal ac frequency response functions', *Solid State Ion.*, vol. 15, no. 2, pp. 159–161, Mar. 1985, doi: 10.1016/0167-2738(85)90095-5.
- [113] N. K. Karan, D. K. Pradhan, R. Thomas, B. Natesan, and R. S. Katiyar, 'Solid polymer electrolytes based on polyethylene oxide and lithium trifluoro- methane sulfonate (PEO-LiCF<sub>3</sub>SO<sub>3</sub>): Ionic conductivity and dielectric relaxation', *Solid State Ion.*, vol. 179, no. 19–20, pp. 689–696, 2008, doi: 10.1016/j.ssi.2008.04.034.
- [114] E. Barsoukov and J. R. Macdonald, *Impedance spectroscopy: theory, experiment, and applications*, Second Edition. Wiley, 2005.
- [115] T. Jacobsen and K. West, 'Diffusion impedance in planar, cylindrical and spherical symmetry', *Electrochimica Acta*, vol. 40, no. 2, pp. 255–262, Feb. 1995, doi: 10.1016/0013-4686(94)E0192-3.
- [116] J. Bisquert, 'Theory of the Impedance of Electron Diffusion and Recombination in a Thin Layer', *J. Phys. Chem. B*, vol. 106, no. 2, pp. 325–333, Jan. 2002, doi: 10.1021/jp011941g.
- [117] F. Nobili, R. Tossici, R. Marassi, F. Croce, and B. Scrosati, 'An AC Impedance Spectroscopic Study of LixCoO<sub>2</sub> at Different Temperatures', *J. Phys. Chem. B*, vol. 106, no. 15, pp. 3909–3915, Apr. 2002, doi: 10.1021/jp013569a.

## References

---

- [118] J. Bartoszek, Y.-X. Liu, J. Karczewski, S.-F. Wang, A. Mrozinski, and P. Jasinski, 'Distribution of relaxation times as a method of separation and identification of complex processes measured by impedance spectroscopy', in *2017 21st European Microelectronics and Packaging Conference (EMPC) & Exhibition*, Warsaw, Sep. 2017, pp. 1–5. doi: 10.23919/EMPC.2017.8346901.
- [119] H. He, R. Xiong, and J. Fan, 'Evaluation of Lithium-Ion Battery Equivalent Circuit Models for State of Charge Estimation by an Experimental Approach', *Energies*, vol. 4, no. 4, pp. 582–598, Mar. 2011, doi: 10.3390/en4040582.
- [120] D.-W. H. Witzenhausen, 'Elektrische Batteriespeichermodelle: Modellbildung, Parameteridentifikation und Modellreduktion', p. 276.
- [121] D. Andre, M. Meiler, K. Steiner, H. Walz, T. Soczka-Guth, and D. U. Sauer, 'Characterization of high-power lithium-ion batteries by electrochemical impedance spectroscopy. II: Modelling', *J. Power Sources*, vol. 196, no. 12, pp. 5349–5356, Jun. 2011, doi: 10.1016/j.jpowsour.2010.07.071.
- [122] J. Gomez, R. Nelson, E. E. Kalu, M. H. Weatherspoon, and J. P. Zheng, 'Equivalent circuit model parameters of a high-power Li-ion battery: Thermal and state of charge effects', *J. Power Sources*, vol. 196, no. 10, pp. 4826–4831, May 2011, doi: 10.1016/j.jpowsour.2010.12.107.
- [123] Y. Gao, J. Jiang, C. Zhang, W. Zhang, Z. Ma, and Y. Jiang, 'Lithium-ion battery aging mechanisms and life model under different charging stresses', *J. Power Sources*, vol. 356, pp. 103–114, Jul. 2017, doi: 10.1016/j.jpowsour.2017.04.084.
- [124] P. Iurilli, C. Brivio, R. E. Carrillo, and V. Wood, 'EIS2MOD: A DRT-Based Modeling Framework for Li-Ion Cells', *IEEE Trans. Ind. Appl.*, vol. 58, no. 2, pp. 1429–1439, Mar. 2022, doi: 10.1109/TIA.2021.3134946.
- [125] R. Xiong, J. Cao, Q. Yu, H. He, and F. Sun, 'Critical Review on the Battery State of Charge Estimation Methods for Electric Vehicles', *IEEE Access*, vol. 6, pp. 1832–1843, 2018, doi: 10.1109/ACCESS.2017.2780258.
- [126] R. Zhang *et al.*, 'State of the Art of Lithium-Ion Battery SOC Estimation for Electrical Vehicles', *Energies*, vol. 11, no. 7, p. 1820, Jul. 2018, doi: 10.3390/en11071820.

- [127] J. P. Rivera-Barrera, N. Muñoz-Galeano, and H. O. Sarmiento-Maldonado, ‘SoC Estimation for Lithium-ion Batteries: Review and Future Challenges’, *Electronics*, vol. 6, no. 4, Art. no. 4, Dec. 2017, doi: 10.3390/electronics6040102.
- [128] C. Brivio, V. Musolino, M. Merlo, and C. Ballif, ‘A Physically-Based Electrical Model for Lithium-Ion Cells’, *IEEE Trans. Energy Convers.*, vol. 34, no. 2, pp. 594–603, Jun. 2019, doi: 10.1109/TEC.2018.2869272.
- [129] S. Barcellona, ‘A novel lithium ion battery model: A step towards the electrochemical storage systems unification’, in *2017 6th International Conference on Clean Electrical Power (ICCEP)*, Santa Margherita Ligure, Italy, Jun. 2017, pp. 416–421. doi: 10.1109/ICCEP.2017.8004849.
- [130] N. E. Ghossein, J. P. Salameh, N. Karami, M. E. Hassan, and M. B. Najjar, ‘Survey on electrical modeling methods applied on different battery types’, in *2015 Third International Conference on Technological Advances in Electrical, Electronics and Computer Engineering (TAAECE)*, Beirut, Lebanon, Apr. 2015, pp. 39–44. doi: 10.1109/TAAECE.2015.7113597.
- [131] N. Meddings *et al.*, ‘Application of electrochemical impedance spectroscopy to commercial Li-ion cells: A review’, *J. Power Sources*, vol. 480, p. 228742, Dec. 2020, doi: 10.1016/j.jpowsour.2020.228742.
- [132] F. Ciucci, ‘Modeling electrochemical impedance spectroscopy’, *Curr. Opin. Electrochem.*, vol. 13, pp. 132–139, Feb. 2019, doi: 10.1016/j.coelec.2018.12.003.
- [133] P. Kollmeyer, A. Hackl, and A. Emadi, ‘Li-ion battery model performance for automotive drive cycles with current pulse and EIS parameterization’, in *2017 IEEE Transportation Electrification Conference and Expo (ITEC)*, Jun. 2017, pp. 486–492. doi: 10.1109/ITEC.2017.7993319.
- [134] R. Scipioni, P. S. Jørgensen, C. Graves, J. Hjelm, and S. H. Jensen, ‘A Physically-Based Equivalent Circuit Model for the Impedance of a LiFePO<sub>4</sub>/Graphite 26650 Cylindrical Cell’, *J. Electrochem. Soc.*, vol. 164, no. 9, p. A2017, Jul. 2017, doi: 10.1149/2.1071709jes.
- [135] B. A. Boukamp, ‘Distribution (function) of relaxation times, successor to complex nonlinear least squares analysis of electrochemical impedance spectroscopy?’, *J. Phys. Energy*, vol. 2, no. 4, p. 042001, Aug. 2020, doi: 10.1088/2515-7655/aba9e0.

## References

---

- [136] H. Schichlein, A. C. M. Ller, and M. Voigts, 'Deconvolution of electrochemical impedance spectra for the identification of electrode reaction mechanisms in solid oxide fuel cells', *Journal of Applied Electrochemistry*, vol. 32, pp. 875–882, Aug. 2002, doi: <https://doi.org/10.1023/A:1020599525160>.
- [137] P. Shafiei Sabet and D. U. Sauer, 'Separation of predominant processes in electrochemical impedance spectra of lithium-ion batteries with nickel-manganese-cobalt cathodes', *J. Power Sources*, vol. 425, pp. 121–129, Jun. 2019, doi: [10.1016/j.jpowsour.2019.03.068](https://doi.org/10.1016/j.jpowsour.2019.03.068).
- [138] J. P. Schmidt, P. Berg, M. Schönleber, A. Weber, and E. Ivers-Tiffée, 'The distribution of relaxation times as basis for generalized time-domain models for Li-ion batteries', *J. Power Sources*, vol. 221, pp. 70–77, Jan. 2013, doi: [10.1016/j.jpowsour.2012.07.100](https://doi.org/10.1016/j.jpowsour.2012.07.100).
- [139] IEC 62660-1:2010, 'Secondary lithium-ion cells for the propulsion of electric road vehicles - Part 1: Performance testing'. [Online]. Available: <https://webstore.iec.ch/publication/7331>
- [140] B. A. Boukamp, 'A Linear Kronig-Kramers Transform Test for Immittance Data Validation', *J. Electrochem. Soc.*, vol. 142, no. 6, p. 1885, 1995, doi: [10.1149/1.2044210](https://doi.org/10.1149/1.2044210).
- [141] J. Illig, J. P. Schmidt, M. Weiss, A. Weber, and E. Ivers-Tiffée, 'Understanding the impedance spectrum of 18650 LiFePO<sub>4</sub>-cells', *J. Power Sources*, vol. 239, pp. 670–679, Oct. 2013, doi: [10.1016/j.jpowsour.2012.12.020](https://doi.org/10.1016/j.jpowsour.2012.12.020).
- [142] M. Hahn, S. Schindler, L.-C. Triebs, and M. A. Danzer, 'Optimized Process Parameters for a Reproducible Distribution of Relaxation Times Analysis of Electrochemical Systems', *Batteries*, vol. 5, no. 2, p. 43, May 2019, doi: [10.3390/batteries5020043](https://doi.org/10.3390/batteries5020043).
- [143] A. L. Gavrilyuk, D. A. Osinkin, and D. I. Bronin, 'The use of Tikhonov regularization method for calculating the distribution function of relaxation times in impedance spectroscopy', *Russ. J. Electrochem.*, vol. 53, no. 6, pp. 575–588, Jun. 2017, doi: [10.1134/S1023193517060040](https://doi.org/10.1134/S1023193517060040).

- [144] R. Kohn, M. Smith, and D. Chan, 'Nonparametric regression using linear combinations of basis functions', *Stat. Comput.*, vol. 11, no. 4, pp. 313–322, 2001, doi: 10.1023/A:1011916902934.
- [145] T. H. Wan, M. Saccoccio, C. Chen, and F. Ciucci, 'Influence of the Discretization Methods on the Distribution of Relaxation Times Deconvolution: Implementing Radial Basis Functions with DRTtools', *Electrochimica Acta*, vol. 184, pp. 483–499, Dec. 2015, doi: 10.1016/j.electacta.2015.09.097.
- [146] M. Saccoccio, T. H. Wan, C. Chen, and F. Ciucci, 'Optimal Regularization in Distribution of Relaxation Times applied to Electrochemical Impedance Spectroscopy: Ridge and Lasso Regression Methods - A Theoretical and Experimental Study', *Electrochimica Acta*, vol. 147, pp. 470–482, Nov. 2014, doi: 10.1016/j.electacta.2014.09.058.
- [147] J. K. Hansen, J. D. Hogue, G. K. Sander, R. A. Renaut, and S. C. Popat, 'Non-negatively constrained least squares and parameter choice by the residual periodogram for the inversion of electrochemical impedance spectroscopy data', *J. Comput. Appl. Math.*, vol. 278, pp. 52–74, Apr. 2015, doi: 10.1016/j.cam.2014.09.017.
- [148] F. Ciucci and C. Chen, 'Analysis of Electrochemical Impedance Spectroscopy Data Using the Distribution of Relaxation Times: A Bayesian and Hierarchical Bayesian Approach', *Electrochimica Acta*, vol. 167, pp. 439–454, Jun. 2015, doi: 10.1016/j.electacta.2015.03.123.
- [149] M. A. Danzer, 'Generalized Distribution of Relaxation Times Analysis for the Characterization of Impedance Spectra', *Batteries*, vol. 5, no. 3, p. 53, Jul. 2019, doi: 10.3390/batteries5030053.
- [150] X. Chen, L. Li, M. Liu, T. Huang, and A. Yu, 'Detection of lithium plating in lithium-ion batteries by distribution of relaxation times', *J. Power Sources*, vol. 496, p. 229867, Jun. 2021, doi: 10.1016/j.jpowsour.2021.229867.
- [151] B. Manikandan, V. Ramar, C. Yap, and P. Balaya, 'Investigation of physico-chemical processes in lithium-ion batteries by deconvolution of electrochemical impedance spectra', *J. Power Sources*, vol. 361, pp. 300–309, Sep. 2017, doi: 10.1016/j.jpowsour.2017.07.006.

## References

---

- [152] S. Ma *et al.*, ‘Temperature effect and thermal impact in lithium-ion batteries: A review’, *Prog. Nat. Sci. Mater. Int.*, vol. 28, no. 6, pp. 653–666, Dec. 2018, doi: 10.1016/j.pnsc.2018.11.002.
- [153] B. A. Boukamp, ‘Derivation of a Distribution Function of Relaxation Times for the (fractal) Finite Length Warburg.’, *Electrochimica Acta*, vol. 252, pp. 154–163, Oct. 2017, doi: 10.1016/j.electacta.2017.08.154.
- [154] Spiegel Murray Ralph, *Laplace Transforms*. 1965.
- [155] S. Buller, E. Karden, D. Kok, and R. W. De Doncker, ‘Modeling the dynamic behavior of supercapacitors using impedance spectroscopy’, *IEEE Trans. Ind. Appl.*, vol. 38, no. 6, pp. 1622–1626, Nov. 2002, doi: 10.1109/TIA.2002.804762.
- [156] Leclanché, ‘Product specifications - GL55 Energy Cell - 936A03’. 2020.
- [157] ‘Product specifications - Battery Tester BCS-800 Series’, *Biologic*. <https://www.biologic.net/documents/hight-throughput-battery-tester-bcs-8xx-series/> (accessed Apr. 16, 2021).
- [158] Angelantoni Test Technologies, ‘Discovery climatic chambers’. <https://www.acstestchambers.com/en/environmental-test-chambers/discovery-my-climatic-chambers-for-stress-screening/> (accessed Apr. 16, 2021).
- [159] P. Iurilli, ‘CSEM/Battery\_team/easier’, *GitLab*. [https://gitlab.csem.local/battery\\_team/easier](https://gitlab.csem.local/battery_team/easier) (accessed Oct. 25, 2022).
- [160] P. Iurilli, C. Brivio, and V. Wood, ‘Detection of Lithium-Ion Cells’ Degradation through Deconvolution of Electrochemical Impedance Spectroscopy with Distribution of Relaxation Time’, *Energy Technol.*, vol. 10: 2200547, doi: 10.1002/ente.202200547.
- [161] A. Barré, B. Deguilhem, S. Grolleau, M. Gérard, F. Suard, and D. Riu, ‘A review on lithium-ion battery ageing mechanisms and estimations for automotive applications’, *J. Power Sources*, vol. 241, pp. 680–689, Nov. 2013, doi: 10.1016/j.jpowsour.2013.05.040.
- [162] D. Andre, M. Meiler, K. Steiner, Ch. Wimmer, T. Soczka-Guth, and D. U. Sauer, ‘Characterization of high-power lithium-ion batteries by electrochemical impedance spectroscopy. I. Experimental investigation’, *J. Power Sources*, vol. 196, no. 12, pp. 5334–5341, Jun. 2011, doi: 10.1016/j.jpowsour.2010.12.102.

- [163] M. Yi *et al.*, 'Detection of lithium plating based on the distribution of relaxation times', in *2021 IEEE 4th International Electrical and Energy Conference (CIEEC)*, May 2021, pp. 1–5. doi: 10.1109/CIEEC50170.2021.9510538.
- [164] L. Wildfeuer, N. Wassiliadis, A. Karger, F. Bauer, and M. Lienkamp, 'Teardown analysis and characterization of a commercial lithium-ion battery for advanced algorithms in battery electric vehicles', *J. Energy Storage*, vol. 48, p. 103909, Apr. 2022, doi: 10.1016/j.est.2021.103909.
- [165] T. Waldmann *et al.*, 'Review—Post-Mortem Analysis of Aged Lithium-Ion Batteries: Disassembly Methodology and Physico-Chemical Analysis Techniques', *J. Electrochem. Soc.*, vol. 163, no. 10, pp. A2149–A2164, 2016, doi: 10.1149/2.1211609jes.
- [166] C.-H. Chen, F. B. Planella, K. O'Regan, D. Gastol, W. D. Widanage, and E. Kendrick, 'Development of Experimental Techniques for Parameterization of Multi-scale Lithium-ion Battery Models', *J. Electrochem. Soc.*, vol. 167, no. 8, p. 080534, May 2020, doi: 10.1149/1945-7111/ab9050.
- [167] LG Chem, 'Product specification - Rechargeable Lithium Ion Battery - INR21700 M50 18.20 Wh'. Aug. 23, 2016.
- [168] J. Sturm *et al.*, 'Modeling and simulation of inhomogeneities in a 18650 nickel-rich, silicon-graphite lithium-ion cell during fast charging', *J. Power Sources*, vol. 412, pp. 204–223, Feb. 2019, doi: 10.1016/j.jpowsour.2018.11.043.
- [169] T. Waldmann, M. Kasper, and M. Wohlfahrt-Mehrens, 'Optimization of Charging Strategy by Prevention of Lithium Deposition on Anodes in high-energy Lithium-ion Batteries – Electrochemical Experiments', *Electrochimica Acta*, vol. 178, pp. 525–532, Oct. 2015, doi: 10.1016/j.electacta.2015.08.056.
- [170] J. Schmitt, M. Schindler, and A. Jossen, 'Change in the half-cell open-circuit potential curves of silicon-graphite and nickel-rich lithium nickel manganese cobalt oxide during cycle aging', *J. Power Sources*, vol. 506, p. 230240, Settembre 2021, doi: 10.1016/j.jpowsour.2021.230240.
- [171] N. Williard, B. Sood, M. Osterman, and M. Pecht, 'Disassembly methodology for conducting failure analysis on lithium-ion batteries', *J. Mater. Sci. Mater. Electron.*, vol. 22, no. 10, p. 1616, Jul. 2011, doi: 10.1007/s10854-011-0452-4.

## References

---

- [172] H. M. Dahn, A. J. Smith, J. C. Burns, D. A. Stevens, and J. R. Dahn, ‘User-Friendly Differential Voltage Analysis Freeware for the Analysis of Degradation Mechanisms in Li-Ion Batteries’, *J. Electrochem. Soc.*, vol. 159, no. 9, p. A1405, Aug. 2012, doi: 10.1149/2.013209jes.
- [173] J. C. Burns, D. A. Stevens, and J. R. Dahn, ‘In-Situ Detection of Lithium Plating Using High Precision Coulometry’, *J. Electrochem. Soc.*, vol. 162, no. 6, pp. A959–A964, 2015, doi: 10.1149/2.0621506jes.
- [174] X.-G. Yang, Y. Leng, G. Zhang, S. Ge, and C.-Y. Wang, ‘Modeling of lithium plating induced aging of lithium-ion batteries: Transition from linear to nonlinear aging’, *J. Power Sources*, vol. 360, pp. 28–40, Aug. 2017, doi: 10.1016/j.jpowsour.2017.05.110.
- [175] O. Capron, R. Gopalakrishnan, J. Jaguemont, P. Van den Bossche, N. Omar, and J. Van Mierlo, ‘On the Ageing of High Energy Lithium-Ion Batteries—Comprehensive Electrochemical Diffusivity Studies of Harvested Nickel Manganese Cobalt Electrodes’, *Materials*, vol. 11, Jan. 2018, doi: 10.3390/ma11020176.
- [176] P. Iurilli, C. Brivio, R. E. Carrillo, and V. Wood, ‘Physics-Based SoH Estimation for Li-Ion Cells’, *Batteries*, vol. 8, no. 11, Art. no. 11, Nov. 2022, doi: 10.3390/batteries8110204.
- [177] M. Armand and J.-M. Tarascon, ‘Building better batteries’, *Nature*, vol. 451, no. 7179, Art. no. 7179, Feb. 2008, doi: 10.1038/451652a.
- [178] D. Bresser, A. Moretti, A. Varzi, and S. Passerini, ‘The Role of Batteries for the Successful Transition to Renewable Energy Sources’, in *Encyclopedia of Electrochemistry*, John Wiley & Sons, Ltd, 2020, pp. 1–9. doi: 10.1002/9783527610426.bard110024.
- [179] M. Armand *et al.*, ‘Lithium-ion batteries – Current state of the art and anticipated developments’, *J. Power Sources*, vol. 479, p. 228708, Dec. 2020, doi: 10.1016/j.jpowsour.2020.228708.
- [180] Gert Berckmans, Maarten Messagie, Jelle Smekens, Noshin Omar, Lieselot Vanhaverbeke, and Joeri Van Mierlo, ‘Cost Projection of State of the Art Lithium-Ion Batteries for Electric Vehicles Up to 2030’, *Energies*, vol. 10, no. 9, p. 1314, Sep. 2017, doi: 10.3390/en10091314.

- [181] M. Marinaro *et al.*, ‘Bringing forward the development of battery cells for automotive applications: Perspective of R&D activities in China, Japan, the EU and the USA’, *J. Power Sources*, vol. 459, p. 228073, May 2020, doi: 10.1016/j.jpowsour.2020.228073.
- [182] T. Tsujikawa, K. Yabuta, M. Arakawa, and K. Hayashi, ‘Safety of large-capacity lithium-ion battery and evaluation of battery system for telecommunications’, *J. Power Sources*, vol. 244, pp. 11–16, Dec. 2013, doi: 10.1016/j.jpowsour.2013.01.155.
- [183] H. Rahimi-Eichi, U. Ojha, F. Baronti, and M.-Y. Chow, ‘Battery Management System: An Overview of Its Application in the Smart Grid and Electric Vehicles’, *IEEE Ind. Electron. Mag.*, vol. 7, no. 2, pp. 4–16, Jun. 2013, doi: 10.1109/MIE.2013.2250351.
- [184] H. Dai, B. Jiang, X. Hu, X. Lin, X. Wei, and M. Pecht, ‘Advanced battery management strategies for a sustainable energy future: Multilayer design concepts and research trends’, *Renew. Sustain. Energy Rev.*, vol. 138, p. 110480, Mar. 2021, doi: 10.1016/j.rser.2020.110480.
- [185] Q. Zhang, D. Wang, E. Schaltz, D.-I. Stroe, A. Gismero, and B. Yang, ‘Degradation mechanism analysis and State-of-Health estimation for lithium-ion batteries based on distribution of relaxation times’, *J. Energy Storage*, vol. 55, p. 105386, Nov. 2022, doi: 10.1016/j.est.2022.105386.
- [186] A. Marongiu, N. Nlandi, Y. Rong, and D. U. Sauer, ‘On-board capacity estimation of lithium iron phosphate batteries by means of half-cell curves’, *J. Power Sources*, vol. 324, pp. 158–169, Aug. 2016, doi: 10.1016/j.jpowsour.2016.05.041.
- [187] D. Anseán, G. Baure, M. González, I. Cameán, A. B. García, and M. Dubarry, ‘Mechanistic investigation of silicon-graphite/LiNi0.8Mn0.1Co0.1O2 commercial cells for non-intrusive diagnosis and prognosis’, *J. Power Sources*, vol. 459, p. 227882, May 2020, doi: 10.1016/j.jpowsour.2020.227882.
- [188] E. Schaltz, D.-I. Stroe, K. Nørregaard, L. S. Ingvardsen, and A. Christensen, ‘Incremental Capacity Analysis Applied on Electric Vehicles for Battery State-of-Health Estimation’, *IEEE Trans. Ind. Appl.*, vol. 57, no. 2, pp. 1810–1817, Mar. 2021, doi: 10.1109/TIA.2021.3052454.

## References

---

- [189] C. P. Lin, J. Cabrera, D. Y. W. Yu, F. Yang, and K. L. Tsui, 'SOH Estimation and SOC Recalibration of Lithium-Ion Battery with Incremental Capacity Analysis & Cubic Smoothing Spline', *J. Electrochem. Soc.*, vol. 167, no. 9, p. 090537, May 2020, doi: 10.1149/1945-7111/ab8f56.
- [190] X. Zhou, Z. Pan, X. Han, L. Lu, and M. Ouyang, 'An easy-to-implement multi-point impedance technique for monitoring aging of lithium ion batteries', *J. Power Sources*, vol. 417, pp. 188–192, Mar. 2019, doi: 10.1016/j.jpowsour.2018.11.087.
- [191] K. M. Carthy, H. Gullapalli, K. M. Ryan, and T. Kennedy, 'Review—Use of Impedance Spectroscopy for the Estimation of Li-ion Battery State of Charge, State of Health and Internal Temperature', *J. Electrochem. Soc.*, vol. 168, no. 8, p. 080517, Aug. 2021, doi: 10.1149/1945-7111/ac1a85.
- [192] S. Jiang and Z. Song, 'Estimating the State of Health of Lithium-Ion Batteries with a High Discharge Rate through Impedance', *Energies*, vol. 14, no. 16, Art. no. 16, Jan. 2021, doi: 10.3390/en14164833.
- [193] R. Mingant *et al.*, 'EIS Measurements for Determining the SoC and SoH of Li-Ion Batteries', *ECS Trans.*, vol. 33, no. 39, pp. 41–53, Dec. 2019, doi: 10.1149/1.3589920.
- [194] L. Chen, Z. Lü, W. Lin, J. Li, and H. Pan, 'A new state-of-health estimation method for lithium-ion batteries through the intrinsic relationship between ohmic internal resistance and capacity', *Measurement*, vol. 116, pp. 586–595, Feb. 2018, doi: 10.1016/j.measurement.2017.11.016.
- [195] S. K. Dam and V. John, 'High-Resolution Converter for Battery Impedance Spectroscopy', *IEEE Trans. Ind. Appl.*, vol. 54, no. 2, pp. 1502–1512, Mar. 2018, doi: 10.1109/TIA.2017.2771498.
- [196] X. Wang, X. Wei, Q. Chen, and H. Dai, 'A Novel System for Measuring Alternating Current Impedance Spectra of Series-Connected Lithium-Ion Batteries With a High-Power Dual Active Bridge Converter and Distributed Sampling Units', *IEEE Trans. Ind. Electron.*, vol. 68, no. 8, pp. 7380–7390, Aug. 2021, doi: 10.1109/TIE.2020.3001841.

- [197] Y. Hoshi, N. Yakabe, K. Isobe, T. Saito, I. Shitanda, and M. Itagaki, ‘Wavelet transformation to determine impedance spectra of lithium-ion rechargeable battery’, *J. Power Sources*, vol. 315, pp. 351–358, May 2016, doi: 10.1016/j.jpowsour.2016.03.048.
- [198] CSEM SA, ‘Battery system and battery management method’, WO 2022/200476 A1, Sep. 29, 2022
- [199] Infineon Technologies, ‘Evaluation Board - Infineon Technologies’. <https://www.infineon.com/cms/en/design-support/finder-selection-tools/product-finder/evaluation-board/> (accessed Sep. 22, 2022).
- [200] Infineon Technologies, ‘TLE9012DQU | Li-Ion battery monitoring and balancing IC - Infineon Technologies’. <https://www.infineon.com/cms/en/product/battery-management-ics/tle9012dqu/> (accessed Sep. 22, 2022).
- [201] P. M. Attia *et al.*, ‘Review—“Knees” in Lithium-Ion Battery Aging Trajectories’, *J. Electrochem. Soc.*, vol. 169, no. 6, p. 060517, Jun. 2022, doi: 10.1149/1945-7111/ac6d13.
- [202] W. Diao, S. Saxena, B. Han, and M. Pecht, ‘Algorithm to Determine the Knee Point on Capacity Fade Curves of Lithium-Ion Cells’, *Energies*, vol. 12, no. 15, Art. no. 15, Jan. 2019, doi: 10.3390/en12152910.
- [203] Y. Zhang, Q. Tang, Y. Zhang, J. Wang, U. Stimming, and A. A. Lee, ‘Identifying degradation patterns of lithium ion batteries from impedance spectroscopy using machine learning’, *Nat. Commun.*, vol. 11, no. 1, p. 1706, Apr. 2020, doi: 10.1038/s41467-020-15235-7.
- [204] M. Schönleber, D. Klotz, and E. Ivers-Tiffée, ‘A Method for Improving the Robustness of linear Kramers-Kronig Validity Tests’, *Electrochimica Acta*, vol. 131, pp. 20–27, Jun. 2014, doi: 10.1016/j.electacta.2014.01.034.
- [205] ‘impedance.py — impedance.py 1.4.1 documentation’. <https://impedancepy.readthedocs.io/en/latest/index.html> (accessed Oct. 11, 2022).







# Publications

## Scientific Journals

1. **Pietro Iurilli**, Claudio Brivio, Rafael E. Carrillo and Vanessa Wood (2022)

*Physics-based SoH estimation for Li-ion cells*

Batteries, vol. 8, no. 11.

2. **Pietro Iurilli**, Claudio Brivio and Vanessa Wood (2022)

*Detection of Lithium-Ion Cells' Degradation through Deconvolution of Electrochemical Impedance Spectroscopy with Distribution of Relaxation Time*

Energy Technology, 10: 2200547.

3. **Pietro Iurilli**, Claudio Brivio, Rafael E. Carrillo and Vanessa Wood (2022)

*EIS2MOD: A DRT-Based Modeling Framework for Li-Ion Cells*

IEEE Transactions on Industry Applications, 58, 2.

4. **Pietro Iurilli**, Claudio Brivio and Vanessa Wood (2021)

*On the use of electrochemical impedance spectroscopy to characterize and model the aging phenomena of lithium-ion batteries: a critical review*

Journal of Power Sources, 505.

## Other publications not related to doctoral research

1. **Pietro Iurilli**, Luigi Luppi, and Claudio Brivio (2022)

*Non-Invasive Detection of Lithium-Metal Battery Degradation*

Energies, 15, 19.

## Conference Contributions

1. **Pietro Iurilli**, Claudio Brivio and Vanessa Wood (2022). Characterization of Lithium-ion cells degradation through deconvolution of EIS. – talk & poster  
**Swiss Battery Days 2022**, Dübendorf, Switzerland
2. **Pietro Iurilli**, Claudio Brivio and Vanessa Wood (2022). EIS-based aging assessment of Li-ion cells. – talk  
**Battery Expert Forum 2022**, Frankfurt, Germany
3. **Pietro Iurilli**, Claudio Brivio and Vanessa Wood (2022). Characterization of Lithium-ion cells degradation through deconvolution of EIS. – invited talk  
**HKUST workshop – The Distribution of Relaxation Times, an application of machine learning in electrochemistry**, virtual
4. **Pietro Iurilli**, Claudio Brivio, Rafael E. Carrillo and Vanessa Wood (2021). DRT-based modelling framework for Li-ion cells. – talk  
**14<sup>th</sup> International Workshop on Impedance Spectroscopy**, virtual

## Awards

1. 3<sup>rd</sup> Best paper award (2021)  
**14<sup>th</sup> International Workshop on Impedance Spectroscopy**, virtual